6 August 2010 | $10

Science

AAAS

EDITORIAL

NEWS OF THE WEEK

NEWS FOCUS

LETTERS

BOOKS *ET AL.*

POLICY FORUM

PERSPECTIVES

BREVIA

CONTENTS continued >>

page 620

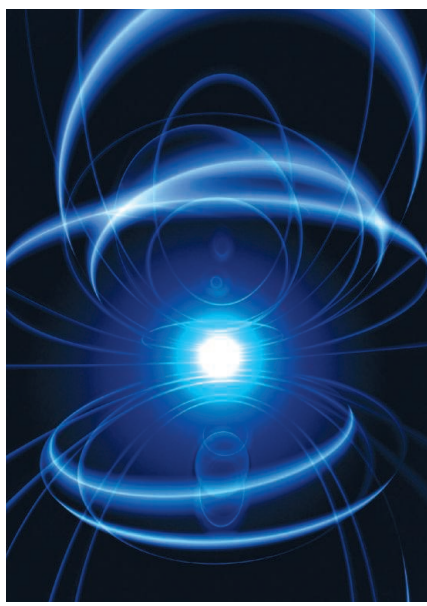

page 629

COVER

Mexican free-tailed bats roost at Bracken Cave near San Antonio, Texas. Streicker *et al.* (p. 676) describe how the spread of new forms of rabies virus is restricted between bat species; Frick *et al.* (p. 679) explain how a fungal disease of bats, white-nose syndrome, is likely to lead to local extinctions of once-common bat species.

Photo: © Merlin D. Tuttle, Bat Conservation International, www.batcon.org

DEPARTMENTS

Published by AAAS

RESEARCH ARTICLES

REPORTS

CONTENTS continued >>

page 637

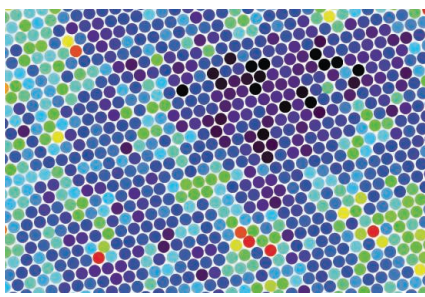

page 656

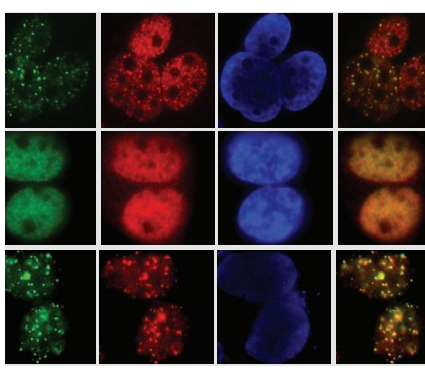

page 693

Published by AAAS

SCIENCEONLINE

SCIENCEXPRESS
www.sciencexpress.org

Strange Metal Transport Realized by Gauge/Gravity Duality
T. Faulkner et al.
Black hole theory is used to develop a mathematical description of a class of metals with unusual electronic properties.
10.1126/science.1189134

The Chlorine Isotope Composition of the Moon and Implications for an Anhydrous Mantle
Z. D. Sharp et al.
The range of chlorine isotope values of the Moon is distinct from those of Earth and meteorites, indicating that the Moon is dry.
10.1126/science.1192606
>> Science *Podcast*

Aryl Hydrocarbon Receptor Antagonists Promote the Expansion of Human Hematopoietic Stem Cells
A. E Boitano et al.
The identification of a mechanism for ex vivo amplification may facilitate clinical application of hematopoietic stem cell therapies.
10.1126/science.1191536

Structural Basis for Activation of Class Ib Ribonucleotide Reductase
A. K. Boal et al.
A single protein activates two different metallofactors by distinct chemistries.
10.1126/science.1190187

Glutamine Deamidation and Dysfunction of Ubiquitin/NEDD8 Induced by a Bacterial Effector Family
J. Cui et al.
Pathogenic bacterial proteins interfere with eukaryotic ubiquitination pathways to induce cytopathic effects.
10.1126/science.1193844

SCIENCENOW
www.sciencenow.org
Highlights From Our Daily News Coverage

Western Diet Tied to Intestinal Disease and Allergies
Gut bacteria may make people in developed countries more prone to a variety of maladies.

Orangutans Go Green
Apes are amazingly energy efficient for their size.

Marijuana Time Warp
Active ingredient in cannabis disrupts the body's internal clock.

SCIENCESIGNALING
www.sciencesignaling.org
The Signal Transduction Knowledge Environment

RESEARCH ARTICLE: HCMV-Encoded Chemokine Receptor US28 Mediates Proliferative Signaling Through the IL-6–STAT3 Axis
E. Slinger et al.

PODCAST
M. J. Smit and A. M. VanHook
A viral G protein–coupled receptor may initiate a positive feedback loop to promote tumor proliferation and vascularization.

RESEARCH ARTICLE: The Nonphagocytic NADPH Oxidase Duox1 Mediates a Positive Feedback Loop During T Cell Receptor Signaling
J. Kwon et al.
Reactive oxygen species enhance T cell receptor signaling by promoting the phosphorylation of a proximal kinase.

SCIENCECAREERS
www.sciencecareers.org/career_magazine
Free Career Resources for Scientists

Taken for Granted: Creating Their Own Credibility
B. L. Benderly
A nonprofit founded and run by a group of independent researchers has permitted decades of scientific work.

Scientist Dads Step Up
V. Venkatraman
Although women still do most of the parenting, some scientist dads are taking on the role of primary caregiver.

SCIENCETRANSLATIONAL MEDICINE
www.sciencetranslationalmedicine.org
Integrating Medicine and Science

PERSPECTIVE: PINing Down the Origin of Prostate Cancer
D. Moscatelli and E. L. Wilson
Two distinct cell types give rise to prostate cancer, which might cause differences in the resulting tumor's behavior.

PERSPECTIVE: A Microbe-Dependent Viral Key to Crohn's Box
D. A. Peterson and P. J. Turnbaugh
Multiple facets of the human microbiome must be considered when deciphering complex diseases such as Crohn's.

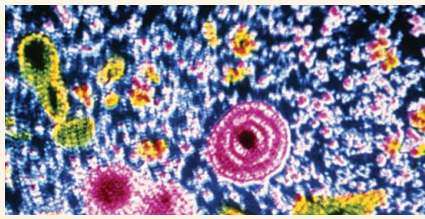

SCIENCESIGNALING
How HCMV infection promotes cancer.

RESEARCH ARTICLE: Pathway-Based Identification of Biomarkers for Targeted Therapeutics—Personalized Oncology with PI3K Pathway Inhibitors
J. N. Andersen et al.
Drug-specific modulation of an oncogenic signaling pathway can help predict tumor sensitivity to candidate drugs.

RESEARCH ARTICLE: Ferroportin and Iron Regulation in Breast Cancer Progression and Prognosis
Z. K. Pinnix et al.
An iron efflux pump is a pivotal protein in breast cancer biology and a strong and independent predictor of breast cancer prognosis.

SCIENCEPODCAST
www.sciencemag.org/multimedia/podcast
Free Weekly Show

Download the 6 August *Science* Podcast to hear about bats threatened by white-nose syndrome, Arctic methane, the water content of the Moon's interior, and more.

SCIENCEINSIDER
news.sciencemag.org/scienceinsider
Science Policy News and Analysis

SCIENCE (ISSN 0036-8075) is published weekly on Friday, except the last week in December, by the American Association for the Advancement of Science, 1200 New York Avenue, NW, Washington, DC 20005. Periodicals Mail postage (publication No. 484460) paid at Washington, DC, and additional mailing offices. Copyright © 2010 by the American Association for the Advancement of Science. The title SCIENCE is a registered trademark of the AAAS. Domestic individual membership and subscription (51 issues): $146 ($74 allocated to subscription). Domestic institutional subscription (51 issues): $910; Foreign postage extra: Mexico, Caribbean (surface mail) $55; other countries (air assist delivery) $85. First class, airmail, student, and emeritus rates on request. Canadian rates with GST available upon request, GST #1254 88122. Publications Mail Agreement Number 1069624. **Printed in the U.S.A.**

Change of address: Allow 4 weeks, giving old and new addresses and 8-digit account number. **Postmaster:** Send change of address to AAAS, P.O. Box 96178, Washington, DC 20090–6178. **Single-copy sales:** $10.00 current issue, $15.00 back issue prepaid includes surface postage; bulk rates on request. **Authorization to photocopy** material for internal or personal use under circumstances not falling within the fair use provisions of the Copyright Act is granted by AAAS to libraries and other users registered with the Copyright Clearance Center (CCC) Transactional Reporting Service, provided that $20.00 per article is paid directly to CCC, 222 Rosewood Drive, Danvers, MA 01923. The identification code for *Science* is 0036-8075. *Science* is indexed in the *Reader's Guide to Periodical Literature* and in several specialized indexes.

AAAS
ADVANCING SCIENCE, SERVING SOCIETY

CREDIT: CNRI/PHOTO RESEARCHERS, INC.

William H. Schlesinger is president of the Cary Institute of Ecosystem Studies in Millbrook, NY. E-mail: schlesingerw@caryinstitute.org.

Translational Ecology

ECOLOGY IS WELL INTO ITS SECOND CENTURY AS AN ORGANIZED SCIENTIFIC DISCIPLINE, RICH WITH observations, experiments, and a general understanding of how the natural world works. Today's environmental scientists have a powerful array of tools and techniques to measure and monitor the environment and to interpret vast and diverse data. Yet despite producing an enormous amount of new information, ecologists are often unable to convey knowledge effectively to the public and to policy-makers. Unless the discoveries of ecological science are rapidly translated into meaningful actions, they will remain quietly archived while the biosphere degrades.

Global warming, the Gulf of Mexico oil disaster, invasive species—these are but a few of the issues concerning environmental scientists and, increasingly, the public. What is needed is a new partnership between scientists and advocacy groups that conveys ecological information accurately and in ways that stakeholders (including policy-makers, resource managers, public health officials, and the general public) can understand. Just as physicians use "translational medicine" to connect the patient to new basic research, "translational ecology" should connect end-users of environmental science to the field research carried out by scientists who study the basis of environmental problems. Translational ecology requires constant two-way communication between stakeholders and scientists. It should continually alert scientists to aspects of the environment in need of study to produce new data, while clearly synthesizing what is already known from field studies and its relevance to policy. The partnership's purpose should be to ensure that all stakeholders know the implications of scientific discoveries and understand their impact on alternative ecological diagnoses.

Good examples of translational ecology involve interdisciplinary teams of scientists, engineers, public health experts, and members of the end-user community. A recent study of the environmental impacts of mountain-top–removal mining involved a collaboration between ecologists and public health experts.* Earth Justice and other nonprofit groups used this material to convince the U.S. Environmental Protection Agency (EPA) to issue new guidelines that will severely limit most such mining practices. In earlier years, research by wetland ecologists helped the EPA outline how to recognize and delineate wetlands, based on soil characteristics. Other scientists are now working with advocacy groups to help policy-makers understand the implications of human perturbations of the global nitrogen cycle. And we can be sure that scientific analysis of the impacts of deep-water petroleum extraction will also be forthcoming—in this case, unfortunately, as a retrospective.

Translational medicine grew from the recognition that basic research findings were not moving effectively into the development of drugs and treatments. To overcome this problem, in 2006 the U.S. National Institutes of Health established a Consortium for Transforming Clinical and Translational Research, which grants Clinical and Translational Science Awards. These awards have recently been increased to over $250 million for the next 5 years, expanding the consortium to 55 institutions nationwide. Translational ecology should similarly connect the end-users of environmental science with the major funders of environmental research.

This week, the Ecological Society of America concludes its annual meeting in Pittsburgh. The world's largest international organization of ecologists can play a critical role in spurring translational ecology. It has drawn together more than 3000 scientists, policy-makers, and citizens to explore the causes and consequences of this year's theme, global warming. Many of the sessions call for ecologists to take charge and improve science education and literacy, so that issues related to global warming are not misunderstood. Connecting ecology to stakeholders in these and other ways should enhance the understanding and application of ecological concepts, ensuring that scientific rigor is brought to bear on the world's many environmental challenges.

– William H. Schlesinger

10.1126/science.1195624

*M. A. Palmer *et al.*, *Science* **327**, 148 (2010).

CREDITS: (TOP) THE CARY INSTITUTE; (RIGHT) GETTY IMAGES/ISTOCKPHOTO

Downloaded from www.sciencemag.org on August 5, 2010

Published by AAAS

www.sciencemag.org

Science

1200 New York Avenue, NW
Washington, DC 20005
Editorial: 202-326-6550, FAX 202-289-7562
News: 202-326-6581, FAX 202-371-9227
Bateman House, 82-88 Hills Road
Cambridge, UK CB2 1LQ
+44 (0) 1223 326500, FAX +44 (0) 1223 326501

Subscription Services For change of address, missing issues, new orders and renewals, and payment questions: 866-434-AAAS (2227) or 202-326-6417, FAX 202-842-1065. Mailing addresses: AAAS, P.O. Box 96178, Washington, DC 20090-6178 or AAAS Member Services, 1200 New York Avenue, NW, Washington, DC 20005

Institutional Site Licenses please call 202-326-6755 for any questions or information

Reprints: Author Inquiries 800-635-7181
Commercial Inquiries 803-359-4578

Permissions 202-326-7074, FAX 202-682-0816

Member Benefits AAAS/Barnes&Noble.com bookstore www.aaas.org/bn; AAAS Online Store www.apisource.com/aaas/ code MKB6; AAAS Travels: Betchart Expeditions 800-252-4910; Apple Store www.apple.com/eppstore/aaas; Bank of America MasterCard 1-800-833-6262 priority code FAA3YU; Cold Spring Harbor Laboratory Press Publications www.cshlpress.com/affiliates/aaas.htm; GEICO Auto Insurance www.geico.com/landingpage/go51.htm?logo=17624; Hertz 800-654-2200 CDP#343457; Office Depot https://bsd.officedepot.com/portalLogin.do; Seabury & Smith Life Insurance 800-424-9883; Subaru VIP Program 202-326-6417; VIP Moving Services www.vipmayflower.com/domestic/index.html; Other Benefits: AAAS Member Services 202-326-6417 or www.aaasmember.org.

science_editors@aaas.org	(for general editorial queries)
science_letters@aaas.org	(for queries about letters)
science_reviews@aaas.org	(for returning manuscript reviews)
science_bookrevs@aaas.org	(for book review queries)

Published by the American Association for the Advancement of Science (AAAS), *Science* serves its readers as a forum for the presentation and discussion of important issues related to the advancement of science, including the presentation of minority or conflicting points of view, rather than by publishing only material on which a consensus has been reached. Accordingly, all articles published in *Science*—including editorials, news and comment, and book reviews—are signed and reflect the individual views of the authors and not official points of view adopted by AAAS or the institutions with which the authors are affiliated.

AAAS was founded in 1848 and incorporated in 1874. Its mission is to advance science, engineering, and innovation throughout the world for the benefit of all people. The goals of the association are to: enhance communication among scientists, engineers, and the public; promote and defend the integrity of science and its use; strengthen support for the science and technology enterprise; provide a voice for science on societal issues; promote the responsible use of science in public policy; strengthen and diversify the science and technology workforce; foster education in science and technology for everyone; increase public engagement with science and technology; and advance international cooperation in science.

Information for Authors
See pages 352 and 353 of the 15 January 2010 issue or access www.sciencemag.org/about/authors

EDITOR-IN-CHIEF **Bruce Alberts**
EXECUTIVE EDITOR **Monica M. Bradford**
NEWS EDITOR **Colin Norman**
MANAGING EDITOR, RESEARCH JOURNALS **Katrina L. Kelner**
DEPUTY EDITORS **R. Brooks Hanson, Barbara R. Jasny, Andrew M. Sugden**

Editorial senior editors/commentary Lisa D. Chong, Brad Wible; **senior editors** Gilbert J. Chin, Pamela J. Hines, Paula A. Kiberstis (Boston), Marc S. Lavine (Toronto), Beverly A. Purnell, L. Bryan Ray, Guy Riddihough, H. Jesse Smith, Phillip D. Szuromi (Tennessee), Valda Vinson, Jake S. Yeston; **associate editors** Kristen L. Mueller, Jelena Stajic, Nicholas S. Wigginton, Laura M. Zahn; **research associate** Alexis Wynne Mogul; **book review editor** Sherman J. Suter; **associate letters editor** Jennifer Sills; **editorial manager** Cara Tate; **senior copy editors** Jeffrey E. Cook, Cynthia Howe, Harry Jach, Lauren Kmec, Barbara P. Ordway, Trista Wagoner; **copy editor** Chris Filiatreau; **editorial coordinators** Carolyn Kyle, Beverly Shields; **publications assistants** Ramatoulaye Diop, Joi S. Granger, Emily Guise, Jeffrey Hearn, Michael Hicks, Lisa Johnson, Scott Miller, Jerry Richardson, Jennifer A. Seibert, Brian White, Anita Wynn; **editorial assistants** Emily C. Horton, Patricia M. Moore, Miriam Weinberg; **executive assistant** Alison Crawford; **administrative support** Maryrose Madrid; **editorial fellow** Melissa R. McCartney

Editorial director, web and new media Stewart Wills; **senior web editor** Tara S. Marathe; **web editor** Robert Frederick; **web development manager** Martyn Green; **web developer** Andrew Whitesell

News deputy news editors Robert Coontz, Eliot Marshall, Jeffrey Mervis, Leslie Roberts; **contributing editors** Elizabeth Culotta, Polly Shulman; **news writers** Yudhijit Bhattacharjee, Adrian Cho, Jennifer Couzin, David Grimm, Jocelyn Kaiser, Richard A. Kerr, Eli Kintisch, Greg Miller, Elizabeth Pennisi, Lauren Schenkman, Robert F. Service (Pacific NW), Erik Stokstad, Jue Wang; **interns** Kristen Minogue, Nezile Mthembu, Dolly Krishnaswamy; **contributing correspondents** Jon Cohen (San Diego, CA), Daniel Ferber, Ann Gibbons, Sam Kean, Robert Koenig, Andrew Lawler, Mitch Leslie, Charles C. Mann, Virginia Morell, Gary Taubes; **copy editors** Linda B. Felaco, Melvin Gatling, Melissa Raimondi; **administrative support** Scherraine Mack; **bureaus** San Diego, CA: 760-942-3252, FAX 760-942-4979; Pacific Northwest: 503-963-1940

Production director James Landry; **senior manager** Wendy K. Shank; **assistant manager** Rebecca Doshi; **senior specialists** Steve Forrester, Chris Redwood, Anthony Rosen; **Preflight director** David M. Tompkins; **manager** Marcus Spiegler; **specialist** Jason Hillman

Art director Yael Kats; **associate art director** Laura Creveling; **senior illustrators** Chris Bickel, Katharine Sutliff; **illustrator** Yana Greenman; **senior art associates** Holly Bishop, Preston Huey, Nayomi Kevitiyagala; **art associates** Kay Engman, Matthew Twombly; **photo editor** Leslie Blizard

***Science* International**

Europe (science@science-int.co.uk) **editorial: international managing editor** Andrew M. Sugden; **senior editor/commentary** Julia Fahrenkamp-Uppenbrink; **senior editors** Caroline Ash, Stella M. Hurtley, Ian S. Osborne, Peter Stern; **associate editor** Maria Cruz; **locum editor** Helen Pickersgill; **editorial support** Rachel Roberts, Alice Whaley; **administrative support** John Cannell, Janet Clements, Louise Hartwell; **news: europe news editor** John Travis; **deputy news editor** Daniel Clery; **contributing correspondents** Michael Balter (Paris), John Bohannon (Vienna), Martin Enserink (Amsterdam and Paris), Gretchen Vogel (Berlin); **intern** Sarah Reed

Latin America contributing correspondent Antonio Regalado

Asia Japan Office: Asca Corporation, Tomoko Furusawa, Rustic Bldg. 7F, 77 Tenjin-cho, Shinjuku-ku, Tokyo 162-0808, Japan; +81 3 6802 4616, FAX +81 3 6802 4615, inquiry@sciencemag.jp; **asia news editor** Richard Stone (Beijing: rstone@aaas.org); **contributing correspondents** Dennis Normile [Japan: +81 (0) 3 3391 0630, FAX +81 (0) 3 5936 3531; dnormile@gol.com]; Hao Xin [China: cindyhao@gmail.com]; Pallava Bagla [South Asia: +91 (0) 11 2271 2896; pbagla@vsnl.com]

EXECUTIVE PUBLISHER **Alan I. Leshner**
PUBLISHER **Beth Rosner**

Fulfillment Systems and Operations (membership@aaas.org); **director** Waylon Butler; **customer service supervisor** Pat Butler; **specialists** Latoya Casteel, LaVonda Crawford, Vicki Linton, April Marshall; **data entry supervisor** Cynthia Johnson; **specialists** Shirlene Hall, Tarrika Hill, William Jones

Business Operations and Administration director Deborah Rivera-Wienhold; **business systems and financial analysis director** Randy Yi; **manager, business analysis** Eric Knott; **manager, business operations** Jessica Tierney; **financial analysts** Priti Pamnani, Celeste Troxler; **rights and permissions: administrator** Emilie David; **associate** Elizabeth Sandler; **marketing director** Ian King; **marketing managers** Allison Pritchard, Alison Chandler, Julianne Wielga; **marketing associates** Aimee Aponte, Mary Ellen Crowley, Wendy Wise; **senior marketing executive** Jennifer Reeves; **director, site licensing** Tom Ryan; **director, corporate relations** Eileen Bernadette Moran; **publisher relations, eresources specialist** Kiki Forsythe; **senior publisher relations specialist** Catherine Holland; **publisher relations, east coast** Phillip Smith; **publisher relations, west coast** Philip Tsolakidis; **fulfillment supervisor** Iquo Edim; **fulfillment coordinator** Carrie MacDonald; **marketing manager** Christina Schlecht; **marketing associate** Laura Tutino; **electronic media: manager** Lizabeth Harman; **project manager** Trista Snyder; **assistant manager** Lisa Stanford; **senior production specialists** Ryan Atkins, Christopher Coleman, **computer specialist** Walter Jones, Kai Zhang; **production specialists** Angela Forest, Nichele Johnston, Kimberly Oster; **director, web and new media** Will Collins

advertising director, worldwide ad sales Bill Moran
commercial editor Sean Sanders: 202-326-6430
assistant commercial editor Tianna Hicklin 202-326-6463
project director, outreach Brianna Blaser

Product (science_advertising@aaas.org); **midwest** Rick Bongiovanni: 330-405-7080, FAX 330-405-7081; **east coast/e. canada** Laurie Faraday: 508-747-9395, FAX 617-507-8189; **west coast/w. canada** Lynne Stickrod: 415-931-9782, FAX 415-520-6940; **uk/europe/asia** Roger Goncalves: TEL/FAX +41 43 243 1358; **japan** ASCA Corporation, Nanako Ide +81 (0) 3 6802 4616, FAX +81 (0) 3 6802 4615; ads@sciencemag.jp; **senior traffic associate** Deiandra Simms

worldwide associate director of *Science* Careers Tracy Holmes: +44 (0) 1223 326525, FAX +44 (0) 1223 326532

Classified (advertise@sciencecareers.org); **u.s.: midwest/west coast/south central/canada** Tina Burks: 202-326-6577; **east coast/industry** Elizabeth Early: 202-326-6578; **advertising operations manager** Kate Panganiban **sales coordinators** Rohan Edmonson, Shirley Young; **europe/row sales:** Susanne Kharraz, Dan Pennington, Alex Palmer; **sales assistant** Lisa Patterson; **japan** ASCA Corporation, Jie Chin +81 (0) 3 6802 4616, FAX +81 (0) 3 6802 4615; careerads@sciencemag.jp; **advertising support manager** Karen Foote: 202-326-6740; **advertising production operations manager** Deborah Tompkins; **senior production specialist/graphic designer** Amy Hardcastle; **senior production specialist** Robert Buck; **senior traffic associate** Christine Hall

AAAS Board of Directors retiring president, chair Peter C. Agre; **president** Alice Huang; **president-elect** Nina Fedoroff; **treasurer** David E. Shaw; **chief executive officer** Alan I. Leshner; **board** Linda P. B. Katehi, Nancy Knowlton, Stephen Mayo, Cherry A. Murray, Julia M. Phillips, Sue V. Rosser, David D. Sabatini, Thomas A. Woolsey

AAAS
ADVANCING SCIENCE, SERVING SOCIETY

SENIOR EDITORIAL BOARD

John I. Brauman, *Chair, Stanford Univ.*
Richard Losick, *Harvard Univ.*
Linda Partridge, *Univ. College London*
Michael S. Turner, *University of Chicago*

BOARD OF REVIEWING EDITORS

Adriano Aguzzi, *Univ. Hospital Zürich*
Takuzo Aida, *Univ. of Tokyo.*
Sonia Altizer, *Univ. of Georgia*
David Altshuler, *Broad Institute*
Arturo Alvarez-Buylla, *Univ. of California, San Francisco*
Richard Amasino, *Univ. of Wisconsin, Madison*
Angelika Amon, *MIT*
Kathryn Anderson, *Memorial Sloan-Kettering Cancer Center*
Siv G. E. Andersson, *Uppsala Univ.*
Peter Andolfatto, *Princeton Univ.*
Meinrat O. Andreae, *Max Planck Inst., Mainz*
John A. Bargh, *Yale Univ.*
Ben Barres, *Stanford Medical School*
Marisa Bartolomei, *Univ. of Penn. School of Med.*
Jordi Bascompte, *Estación Biológica de Doñana, CSIC*
Facundo Batista, *London Research Inst.*
Ray H. Baughman, *Univ. of Texas, Dallas*
Yasmine Belkaid, *NIAID, NIH*
Stephen J. Benkovic, *Penn State Univ.*
Gregory C. Beroza, *Stanford Univ.*
Ton Bisseling, *Wageningen Univ.*
Mina Bissell, *Lawrence Berkeley National Lab*
Peer Bork, *EMBL*
Robert W. Boyd, *Univ. of Rochester*
Paul M. Brakefield, *Leiden Univ.*
Christian Büchel, *Universitätsklinikum Hamburg-Eppendorf*
Joseph A. Burns, *Cornell Univ.*
William P. Butz, *Population Reference Bureau*
Mats Carlsson, *Univ. of Oslo*
Mildred Cho, *Stanford Univ.*
David Clapham, *Children's Hospital, Boston*
David Clary, *Oxford University*
J. M. Claverie, *CNRS, Marseille*
Jonathan D. Cohen, *Princeton Univ.*
Andrew Cossins, *Univ. of Liverpool*
Robert H. Crabtree, *Yale Univ.*
Wolfgang Cramer, *Potsdam Inst. for Climate Impact Research*
F. Fleming Crim, *Univ. of Wisconsin*
Jeff L. Dangl, *Univ. of North Carolina*
Stanislas Dehaene, *Collège de France*
Edward DeLong, *MIT*
Emmanouil T. Dermitzakis, *Univ. of Geneva Medical School*
Robert Desimone, *MIT*
Claude Desplan, *New York Univ.*
Dennis Discher, *Univ. of Pennsylvania*
Scott C. Doney, *Woods Hole Oceanographic Inst.*
Jennifer A. Doudna, *Univ. of California, Berkeley*
Julian Downward, *Cancer Research UK*
Bruce Dunn, *Univ. of California, Los Angeles*
Christopher Dye, *WHO*
Michael B. Elowitz, *Calif. Inst. of Technology*
Gerhard Ertl, *Fritz-Haber-Institut, Berlin*
Mark Estelle, *Indiana Univ.*
Barry Everitt, *Univ. of Cambridge*
Paul G. Falkowski, *Rutgers Univ.*
Ernst Fehr, *Univ. of Zurich*
Tom Fenchel, *Univ. of Copenhagen*
Alain Fischer, *INSERM*
Wulfram Gerstner, *EPFL Lausanne*
Charles Godfray, *Univ. of Oxford*
Diane Griffin, *Johns Hopkins Bloomberg School of Public Health*
Christian Haass, *Ludwig Maximilians Univ.*
Steven Hahn, *Fred Hutchinson Cancer Research Center*
Gregory J. Hannon, *Cold Spring Harbor Lab.*
Niels Hansen, *Technical Univ. of Denmark*
Dennis L. Hartmann, *Univ. of Washington*
Chris Hawkesworth, *Univ. of St Andrews*
Martin Heimann, *Max Planck Inst., Jena*
James A. Hendler, *Rensselaer Polytechnic Inst.*
Janet G. Hering, *Swiss Fed. Inst. of Aquatic Science & Technology*
Ray Hilborn, *Univ. of Washington*
Michael E. Himmel, *National Renewable Energy Lab.*
Kei Hirose, *Tokyo Inst. of Technology*
Ove Hoegh-Guldberg, *Univ. of Queensland*
Lora Hooper, *UT Southwestern Medical Ctr at Dallas*
Ronald R. Hoy, *Cornell Univ.*
Jeffrey A. Hubbell, *EPFL Lausanne*
Steven Jacobsen, *Univ. of California, Los Angeles*
Peter Jonas, *Universität Freiburg*
Barbara B. Kahn, *Harvard Medical School*
Daniel Kahne, *Harvard Univ.*
Bernhard Keimer, *Max Planck Inst., Stuttgart*
Robert Kingston, *Harvard Medical School*
Hanna Kokko, *Univ. of Helsinki*
Alberto R. Kornblihtt, *Univ. of Buenos Aires*
Leonid Krugylak, *Princeton Univ.*
Lee Kump, *Penn State Univ.*
Mitchell A. Lazar, *Univ. of Pennsylvania*
David Lazer, *Harvard Univ.*
Virginia Lee, *Univ. of Pennsylvania*
Julian Lewis, *Cancer Research UK*
Olle Lindvall, *Univ. Hospital, Lund*
Marcia C. Linn, *Univ. of California, Berkeley*
John Lis, *Cornell Univ.*
Richard Losick, *Harvard Univ.*
Ke Lu, *Chinese Acad. of Sciences*
Laura Machesky, *CRUK Beatson Inst. for Cancer Research*
Andrew P. MacKenzie, *Univ. of St Andrews*
Anne Magurran, *Univ. of St Andrews*
Oscar Marin, *CSIC & Univ. Miguel Hernández*
Charles Marshall, *Univ. of California, Berkeley*
Martin M. Matzuk, *Baylor College of Medicine*
Grahma Medley, *Univ. of Warwick*
Virginia Miller, *Washington Univ.*
Yasushi Miyashita, *Univ. of Tokyo*
Richard Morris, *Univ. of Edinburgh*
Edvard Moser, *Norwegian Univ. of Science and Technology*
Sean Munro, *MRC Lab. of Molecular Biology*
Naoto Nagaosa, *Univ. of Tokyo*
James Nelson, *Stanford Univ. School of Med.*
Timothy W. Nilsen, *Case Western Reserve Univ.*
Pär Nordlund, *Karolinska Inst.*
Helga Nowotny, *European Research Advisory Board*
Stuart H. Orkin, *Dana-Farber Cancer Inst.*
Christine Ortiz, *MIT*
Elinor Ostrom, *Indiana Univ.*
Andrew Oswald, *Univ. of Warwick*
Jonathan T. Overpeck, *Univ. of Arizona*
P. David Pearson, *Univ. of California, Berkeley*
John Pendry, *Imperial College*
Reginald M. Penner, *Univ. of California, Irvine*
John H. J. Petrini, *Memorial Sloan-Kettering Cancer Center*
Simon Phillpot, *Univ. of Florida*
Philippe Poulin, *CNRS*
Colin Renfrew, *Univ. of Cambridge*
Trevor Robbins, *Univ. of Cambridge*
Barbara A. Romanowicz, *Univ. of California, Berkeley*
Jens Rostrup-Nielsen, *Haldor Topsoe*
Edward M. Rubin, *Lawrence Berkeley National Lab*
Shimon Sakaguchi, *Kyoto Univ.*
Michael J. Sanderson, *Univ. of Arizona*
Jürgen Sandkühler, *Medical Univ. of Vienna*
Randy Seeley, *Univ. of Cincinnati*
Christine Seidman, *Harvard Medical School*
David Sibley, *Washington Univ*
Joseph Silk, *Univ. of Oxford*
Montgomery Slatkin, *Univ. of California, Berkeley*
Davor Solter, *Inst. of Medical Biology, Singapore*
Allan C. Spradling, *Carnegie Institution of Washington*
Jonathan Sprent, *Garvan Inst. of Medical Research*
Elsbeth Stern, *ETH Zürich*
Yoshiko Takahashi, *Nara Inst. of Science and Technology*
Jurg Tschopp, *Univ. of Lausanne*
Bert Vogelstein, *Johns Hopkins Univ.*
Bruce D. Walker, *Harvard Medical School*
Christopher A. Walsh, *Harvard Medical School*
David A. Wardle, *Swedish Univ. of Agric Sciences*
Colin Watts, *Univ. of Dundee*
Detlef Weigel, *Max Planck Inst., Tübingen*
Jonathan Weissman, *Univ. of California, San Francisco*
Sue Wessler, *Univ. of Georgia*
Ian A. Wilson, *The Scripps Res. Inst.*
Tim Wilson, *Univ. of Virginia*
Xiaoliang Sunney Xie, *Harvard Univ.*
John R. Yates III, *The Scripps Res. Inst.*
Jan Zaanen, *Leiden Univ.*
Huda Zoghbi, *Baylor College of Medicine*
Maria Zuber, *MIT*

BOOK REVIEW BOARD

John Aldrich, *Duke Univ.*
David Bloom, *Harvard Univ.*
Angela Creager, *Princeton Univ.*
Richard Shweder, *Univ. of Chicago*
Ed Wasserman, *DuPont*
Lewis Wolpert, *Univ. College London*

Motojima: fusion's new boss
616

Methane doomsday? Not this week
620

CANCER RESEARCH

As Questions Grow, Duke Halts Trials, Launches Investigation

When biostatisticians Keith Baggerly and Kevin Coombes began poking around a cancer study back in 2006, they never imagined the furor that would eventually follow. Their questions about a prominent genetics group at Duke University in Durham, North Carolina, not only raised doubts about a popular method of tumor analysis but also led to accusations that a cancer researcher, Anil Potti, had padded his resumé. Clinical trials at Duke based on these methods have been suspended, Duke is investigating the researcher in question, and there are calls for a general review of the field.

The controversy involves the work of Potti and cancer geneticist Joseph Nevins, both of Duke. Their study of tumor genetics was first questioned by Baggerly and Coombes of the M. D. Anderson Cancer Center in Houston, Texas, in early 2007. The contretemps has gone back and forth since then. It reached a turning point this summer when *The Cancer Letter* reported that Potti's resumé identified him as a Rhodes scholar even though the Rhodes Trust does not. The Duke clinical trials were suspended, and Duke said in a statement last week that it has placed Potti on administrative leave.

Potti did not respond to an e-mail seeking comment for this story. In an e-mail message, Nevins said he would like to speak out about the research, as "the stories that have been told to date, and how they have been told, are very skewed and one-sided." But he added that because "the timing is not good" it would be best not to comment now.

The Duke project began on a hopeful note: Like many researchers interested in personalizing cancer treatment, Potti and Nevins were examining patterns of genetic behavior in tumor cells, called gene expression signatures. It has been a popular field in recent years, as physicians look for ways to give patients only the drugs that will help them the most. But the gene signatures used to define tumor types—and there are many candidates out there—have been difficult to replicate. Only a handful have seemed reliable enough to use in the clinic.

In October 2006, Potti and Nevins described in *Nature Medicine* how examining the sensitivity of cell lines to particular drugs could predict patients' responses to cancer therapies for a range of cancers. Based on this work, Duke launched three clinical trials that used the signatures to help determine which therapy patients should get.

Other clinics were just as keen to try this idea, including physicians at M. D. Anderson. But first, the physicians wanted to be sure the data were reliable, and they asked Baggerly and Coombes to give the *Nature Medicine* paper a careful look.

"We had difficulties pretty early on," Baggerly says. He and Coombes say they found errors in the 2006 paper, including genes that didn't seem to belong on the list and tumor samples that were incorrectly labeled. They were in communication with the Duke authors, Baggerly says, but "we did not receive an answer that satisfied us." In the spring of 2007, Baggerly and Coombes sent a communication to *Nature Medicine* detailing their concerns; the journal published it in November 2007. "We'd identified a problem, we'd talked with the authors, we'd written a letter to the journal, the journal was going to print our letter," Baggerly says. "We figured, okay, this is how the process of checking and calibrating should work."

Under scrutiny. Anil Potti's work using gene signatures to guide cancer treatment has been challenged.

CREDIT: DUKE PHOTOGRAPHY

But Potti and Nevins continued to publish papers using the same method. This troubled Baggerly. He became obsessed with determining why the Duke team could make their prediction models work when he and Coombes could not. In subsequent papers by the Duke group, Baggerly says he found new errors and contacted both *Lancet Oncology* and the *Journal of Clinical Oncology* (*JCO*), where they had appeared. Both declined to publish Baggerly's letters but later printed corrections covering some points.

Spokesperson Laura Livingston said that *JCO* was now in the process of tracking down this correspondence for a review of the case. *Lancet Oncology* declined to comment on the particulars.

Steven Goodman, an epidemiologist and biostatistician at Johns Hopkins University in Baltimore, Maryland, first heard Baggerly give a talk on the subject about 2 years ago and was taken aback. "This was really, really serious stuff," he says, and he told Baggerly that this needed to appear in the major journals.

Baggerly then learned that Duke was running three clinical trials using the Potti-Nevins approach to assign patients to treatment. He took a new tack: publishing a paper of his own. He and Coombes shared their critique of several papers published by Potti and Nevins with a "prominent" biological journal, he says, whose editors suggested that the paper was too negative. They then submitted it to a high-level statistical journal, the *Annals of Applied Statistics*, where it was published online 2 weeks later, last September. Within weeks, Duke suspended its trials—only to restart them in January after a review by the university gave approval. It wasn't until Potti's resumé came into question last month that the trials were stopped again.

The case threads together two tricky issues: the difficulty of correcting the scientific record and the difficulty of interpreting

Downloaded from www.sciencemag.org on August 5, 2010

Published by AAAS

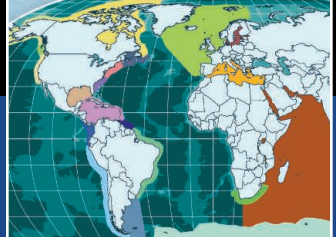

Mapping marine life
622

The power of polyploidy
623

gene expression data, in which "our intuition is actually pretty poor" about what's right and what's not, says Baggerly.

Dogged. Keith Baggerly couldn't replicate Potti's work.

"How can we do better in the future so we don't end up in this situation?" asks Sharyl Nass, who directs the Institute of Medicine's (IOM's) National Cancer Policy Forum. *The Cancer Letter* reported last week that the forum has asked IOM to give it the green light to examine clinical use of these signatures. Cancer biologists are also concerned that the Duke case will cast a shadow over gene signature research. The Duke research has "done a disservice to the community," says David Beer, who studies the molecular genetics of lung cancer at the University of Michigan, Ann Arbor. He hopes it won't tar the field.

After the allegation that Potti may have padded his resumé, Duke announced that it was launching a "full, external review of the science" behind the clinical trials. "That painted everything in a new light," says Michael Cuffe, vice dean for medical affairs at Duke's School of Medicine. Duke also announced last week that it has launched "a formal institutional investigation related to Dr. Potti's biographical claims." Adds Cuffe: "There's a substantial difference" between the resumé allegations and "a debate about data integrity." *JCO* is investigating too; *Lancet Oncology* published an Expression of Concern about the research. *The New England Journal of Medicine*, where Potti also published, and *Nature Medicine* say they're awaiting the results of the Duke inquiry.

–JENNIFER COUZIN-FRANKEL

BIOSECURITY

Defining Select Agents by DNA Sequence

To work with dangerous pathogens such as anthrax, U.S. researchers must follow strict rules governing so-called select agents, or potential bioweapons. But what about a DNA sequence ordered from a company that contains some of the genes that make anthrax deadly? Currently, such an entity—or an artificial organism designed with such DNA—would not be subject to the same regulations despite its potential as a bioweapon, simply because of the way select agents are defined.

A report by the National Academies this week recommends plugging this loophole with a new system of defining select agents based on DNA sequences. "That would provide a very sharp, bright line" to help gene-synthesis companies and their clients decide if a genomic sequence "meets the definition of a select agent or not," says Sean Eddy, a biologist at the Howard Hughes Medical Institute's Janelia Farm Research Campus in Ashburn, Virginia, and one of the report's authors. He says the proposed classification system could also help gene-synthesis companies and government officials spot potential bioterrorism plots involving novel organisms cobbled together from different pieces of custom-ordered DNA.

Concerns about artificially designed bioagents have risen with advances in synthetic biology. Many gene-synthesis companies already screen orders against known pathogenic genome sequences. Last November, the U.S. government published draft guidelines for how such screening ought to be done but did not make them mandatory.

The classification system the academies' panel recommends would clarify requirements and make them legally binding. To be called a select agent, a stretch of DNA would have to meet at least three criteria: It would have to contain a minimum number of sequences or genelike units with pathogenic functionality; these units would have to closely match known pathogenic sequences; and the stretch of DNA would have to contain other generic parts required to create a fully functional synthetic organism.

Anthrax would still be anthrax, but a synthetic construct containing pathogenic sequences from anthrax and meeting other criteria would now be defined as a select agent. A do-it-yourself bioterrorist could still piece together an agent by ordering different pathogenic sequences and generic sequences from a variety of companies; Eddy suggests addressing this concern by getting companies to share information with each other and identify a potentially troubling client.

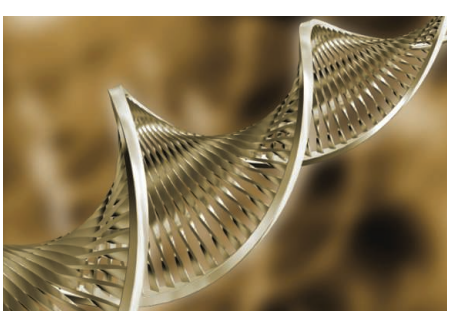

Developing the proposed select-agent system would require help from the whole community, Eddy says, and resulting classifications would have to be reviewed. For example, Eddy says, if a researcher were to point out, "You dummies, you just classified the vaccine strain of [*Bacillus*] *anthracis* as a select agent," it might require redefining a particular rule of classification.

Jonathan Tucker, a biosecurity expert at the Monterey Institute of International Studies in Washington, D.C., says implementing such a classification system could be challenging. One problem is that "a lot of these select-agent sequences have not been adequately annotated," he says. Because the consequences for researchers could be serious, he says, "the government would have to invest in a standard sequence database and a screening algorithm and make that available to researchers to prevent them from inadvertently ordering what could be a select agent."

–YUDHIJIT BHATTACHARJEE

CREDITS (TOP TO BOTTOM): COURTESY KEITH BAGGERLY; ISTOCKPHOTO

Downloaded from www.sciencemag.org on August 5, 2010

Published by AAAS

ENERGY

Fresh Start for Fusion Project as New Leader Shakes Up Management

Last week, ITER, the €16 billion international effort aiming to prove the viability of fusion as an energy source, shook off nagging worries that soaring costs and management problems, combined with Europe's economic woes, could lead to the downsizing or even killing of the experimental reactor. ITER's governing council finally approved the project's so-called Baseline, an extensive document outlining its cost, schedule, and design, and officially named Osamu Motojima, former director-general of Japan's National Institute for Fusion Science, as ITER's new leader.

The major steps forward brought almost audible sighs of relief from fusion scientists, who can now look forward to 2019, when ITER is supposed to produce its first plasma. "I was beginning to wonder if we were ever going to nail down cost and schedule. Europe had been dragging its feet," says Steven Cowley, director of the Culham Centre for Fusion Energy in Abingdon, U.K. "We're over this nasty hump. Yes, ITER is going to cost a lot of money, but we're going to do it."

That hump included a fierce debate over how the European Union which is responsible for 45% of ITER's budget, would cover a €1.4 billion shortfall in short-term funding for the increasingly expensive project. In June, E.U. member states declined to inject new money into ITER, recommending instead the use of funds already allocated to other research efforts. This outraged nonfusion scientists, and in July the European Commission rejected the advice; current plans are to take just €400 million from existing research budgets and find the rest from money allocated to agricultural subsidies and other uses.

In an attempt to forestall future budget battles, the ITER Council last week placed a cap on the overall budget of the reactor, to be built in Cadarache, France. Building ITER on time and on budget will be a "tough job," Motojima admits.

"Fusion is not a dream but a real target."

—OSAMU MOTOJIMA, ITER

He isn't moving slowly, however. The day after his appointment, Motojima announced plans to overhaul ITER's operations. A management review requested by the ITER Council had earlier this year criti-

PHYSICS

Diamond Feats Give Quantum Computing a Solid Boost

Quantum computing may finally be ready to grow up. Over the past 3 decades, physicists have learned to use the quantum behavior of atoms to store and process a handful of bits of information. But they've never managed to scale up quantum computers the way the computer industry has integrated millions of transistors on chips.

Now, a pair of new results brings that goal a step closer. Researchers in California report creating a way to vastly scale up the production of quantum bits (or qubits) in a diamond wafer, a leading contender for making a solid-state quantum computer. Meanwhile, researchers in Massachusetts have linked the quantum state of one such qubit in diamond to the quantum state of a photon, the basic particle behind light. The result may open the door to linking large amounts of quantum information in the solid state to photons of light that can carry the information over long distances.

"Both [papers] taken in isolation are extremely important contributions to being able to use diamond as a platform for doing quantum information processing in the solid state," says Ray Beausoleil, a physicist and HP fellow at HP Laboratories in Palo Alto, California. Taken together, Beausoleil adds, the papers could make it possible both to scale up quantum computers and to pass their data over a distributed quantum network.

For decades, researchers have longed to build quantum computers because of the unique way they store and process information. In conventional computers, each bit of data exists in one of two states, either a "1" or a "0." Quantum computers take bits much further. Each qubit can exist as either a 0 or a 1, or as a "superposition" of all its possible states. For example, it might be 19% 0 and 81% 1, or 65% 0 and 35% 1, or countless other in-between combinations. In carrying out its operations, a quantum computer weighs all such values simultaneously. As a result, stringing just 30 qubits together would give a quantum computer the computational power of a conventional computer running at 30 trillion operations per second.

Qubits aren't just theoretical playthings. Researchers have made them out of many different ingredients, including trapped ions and superconductors. They've also entangled multiple quantum states together so that manipulating one bit causes a predictable change in its neighbor. But they've struggled with the scaling step that has defined the success of conventional computers.

That's where diamond may have an edge. In 2006, researchers found that when they inject nitrogen atoms into a wafer of crystalline diamond, nitrogen atoms not only insert themselves in the carbon lattice but also can kick out carbon atoms. If a nitrogen atom winds up next to a vacancy, one of its electrons can form a stable qubit with a property called spin, which researchers can manipulate with radiofrequency (RF) signals, microwaves, or laser light. Nestled inside the diamond lattice, isolated from outside influences, such nitrogen-vacancy (NV) centers

CREDIT: © ITER ORGANIZATION

Downloaded from www.sciencemag.org on August 5, 2010

Published by AAAS

cized the project's governance, and several senior managers have recently departed. Motojima intends more changes. "Simplify everything; that is the only possible way to respond to the capping of the project," he says. One casualty of this streamlining will be Norbert Holtkamp, ITER's principal deputy director-general and leader of the project's construction since 2006. An ITER spokesperson confirmed that Holtkamp would soon step down and that the position would be eliminated. "We need to simplify the decision-making process," Motojima says.

Even though the approval of ITER's Baseline is supposed to signify an end to major changes, Motojima will also request that the project's scientists and engineers seek new ways to simplify the fusion reactor's design and the integration of its many components, which are being built by the project's seven international partners—China, the European Union, India, Japan, the Republic of Korea, the Russian Federation, and the United States. Motojima says the ITER Council wants him to present cost-saving plans at a meeting in November. Any such changes won't mean that ITER will produce significantly less science, Motojima emphasizes: "I'm keeping the [original] scope of ITER."

If anyone can pull that off, it may be Motojima, who is widely praised for his oversight of the construction of another fusion experiment, Japan's Large Helical Device. "He's a real machine-builder" and "also has a real directorial presence," says Cowley. Indeed, fusion scientists say that Motojima's appointment and the departure of former ITER Director-General Kaname Ikeda, a career diplomat with an engineering background, represent an acknowledgement that the project has moved on from securing funding to a phase dominated by construction. ITER's key components are now being built, Cowley notes. Even more promising, he says, industrial bids for other components are in line with cost predictions.

Although some European politicians called for killing ITER in favor of promoting more immediate renewable-energy projects, Motojima argues that fusion science has rapidly matured over the past half-century. "Some say fusion is always a dream. This is not true. … Fusion is not a dream but a real target," Motojima says.

–JOHN TRAVIS

can maintain their quantum states much longer than qubits in rival solid-state quantum-computing setups can.

Creating NV centers in diamond has been slow going, as researchers typically make them by firing nitrogen atoms through a tiny aperture one at a time. In a paper published online in *Nano Letters* on 23 July, however, researchers led by David Awschalom, a physicist at the University of California (UC), Santa Barbara, report that they created a 60 × 60 array of NV centers in diamond by shining a beam of nitrogen atoms through a thin mask containing 3600 apertures. The mask, made with a conventional high-resolution technique known as electron-beam lithography, can be scaled to any size. The UC researchers also showed that they could use RF electronics to control the quantum state of individual and neighboring NV centers, a development that sets the stage for using those neighbors to carry out complex quantum computations. "This brings the ability to do nearest-neighbor information processing much closer to realization," Beausoleil says.

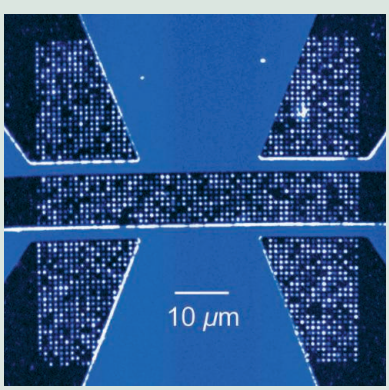

Upscale. Array of NV centers in diamond.

This week in *Nature*, meanwhile, researchers led by Harvard University physicist Mikhail Lukin report that they can reliably link quantum information in an NV center to the polarization state of photons. The feat marks the first time solid-state qubits have been linked to light, Lukin says, and it opens the way for using diamond-based qubits for long-distance quantum communication, cryptography, and distributed computing. Beausoleil cautions that it's still far too early to know whether diamond-based quantum computers will beat out their rivals. Even so, it looks as if the field is finally set to stop crawling and to start walking.

–ROBERT F. SERVICE

CREDIT: D. M. TOYLI *ET AL.*, *NANO LETTERS* (PUBLISHED ONLINE 23 JULY 2010) © 2010 AMERICAN CHEMICAL SOCIETY

*Science*Insider

From the *Science* Policy Blog

The U.S. Environmental Protection Agency (EPA) has rejected petitions asking it to halt the planned **regulation of greenhouse gases**. Some cited e-mails made public as part of the "Climategate" affair to question scientific aspects of the issue. But EPA says there's "no evidence" to suggest climate data were suspect. http://bit.ly/petition_epa

Mirroring its House of Representatives counterpart and the president's request, a Senate spending panel has proposed a $1 billion boost for the **budget of the National Institutes of Health**. The bill contains $50 million for the Cures Acceleration Network, a drug-development program that some scientific groups worry could come at the expense of funding proposals from scientists. http://bit.ly/NIH_boost

A House committee hearing explored **open access** in scientific publishing. Advocates of making papers freely available say informing the public is a noble goal, while publishers worry that expanding a 2-year-old NIH policy to more agencies will hurt the scientific enterprise. http://bit.ly/hearing_access

A Spanish National Research Council panel has recommended the **retraction of a paper** published last year in *Science* that described an enzyme-monitoring chip called the reactome array (*Science*, 9 October 2009, p. 252). But some scientists, including a Nobel laureate who conducted a blind test of the technology, maintain that the array works. http://bit.ly/reactome_debate

Senate Majority Leader Harry Reid (D–NV) has dropped a legislative mandate on the use of **alternative energy** from an energy package he introduced. The announcement came a week after Reid said that limiting carbon emissions via Senate legislation was impossible because he could not muster 60 votes. http://bit.ly/mandate_out

Dispersed oil droplets could have unknown and dangerous effects in the Gulf of Mexico, say scientists. Issues include their small size and the makeup of the dispersant molecules used by BP. http://bit.ly/drops_deadly

For more science policy news, visit **news.sciencemag.org/scienceinsider**.

Downloaded from www.sciencemag.org on August 5, 2010

Published by AAAS

INFECTIOUS DISEASE

New Map Illustrates Risk From the 'Other' Malaria

It may be the malaria you've never heard of, but nearly 3 billion people are at risk of infection with the malaria parasite *Plasmodium vivax*, according to a new analysis published this week in *PLoS Neglected Tropical Diseases*. The *P. vivax* parasite has long been considered the milder, less-dangerous cousin of *P. falciparum*. But recent studies have made clear that *P. vivax* can also cause deadly complications in infected people. A new map of areas where the parasite has been reported, and where conditions are right for mosquitoes to transmit it, should serve as a wake-up call for those who hope to eliminate malaria (*Science*, 14 May, p. 849), says epidemiologist Carlos Guerra of the University of Oxford in the United Kingdom, who developed the map with his colleagues. Although *P. vivax* does often cause milder symptoms, it can lay dormant for months or even years in patients, making it difficult to cure people and to identify carriers—thereby complicating efforts to eliminate the disease from a region.

"*P. falciparum* has traditionally received most of the attention," Guerra says, mainly because it kills so many people in sub-Saharan Africa. Globally, however, "*P. vivax* deserves equal attention, and yet there are still many fundamental gaps in our understanding of this parasite," he says. Most of the 2.85 billion people at risk—91%, according to the new analysis—live in Central and Southeast Asia. About 5.5% of at-risk people—160 million—live in the Americas, and 100 million live in Africa, Yemen, and Saudi Arabia.

The map divides regions of the world into areas of high transmission, low transmission, and areas in Africa where most of the residents carry a genetic trait that makes them less likely to be infected by *P. vivax*. The researchers started by identifying all countries in which the vivax parasite is endemic. They then looked at the number of cases per year in subregions of the countries, categorizing them as zones of stable or unstable (rare) transmission. They further refined the map by excluding areas in which temperatures are too low or conditions too dry for mosquitoes to transmit the parasite. The scientists also drew on knowledge from on-the-ground public health workers to identify additional places that could be deemed malaria-free. Finally, they determined the areas in which more than 90% of residents carry the so-called Duffy negative genetic trait, leaving them without an antigen that the parasite uses to infect cells.

> **"The renewed global effort [to eliminate malaria] needs to wake up to the persistent public health burden of vivax malaria."**
>
> **—PETER ZIMMERMAN, CASE WESTERN RESERVE UNIVERSITY**

Not everyone agrees with the methods. Richard Cibulskis of WHO's Global Malaria Programme says the spatial resolution of the map is not very high, which leads to an overestimation of the number of people at risk. "The median population size of a district in India is 1.5 million, and the whole district might be erroneously classified as at risk, whereas malaria could be occurring in only part of the district," he says.

But Peter Zimmerman of Case Western Reserve University in Cleveland, Ohio, who studies vivax malaria, says underestimation of the disease has long been a serious problem. He says that because *P. vivax* is more difficult to diagnose than *P. falciparum*, cases often go underreported, especially when people are infected with both parasites at once. "The renewed global effort [to eliminate malaria] needs to wake up to the persistent public health burden of vivax malaria," he says. "I hope that [the map] causes serious discussion among malaria researchers."

–GRETCHEN VOGEL

Areas at Risk of *Plasmodium vivax* Transmission

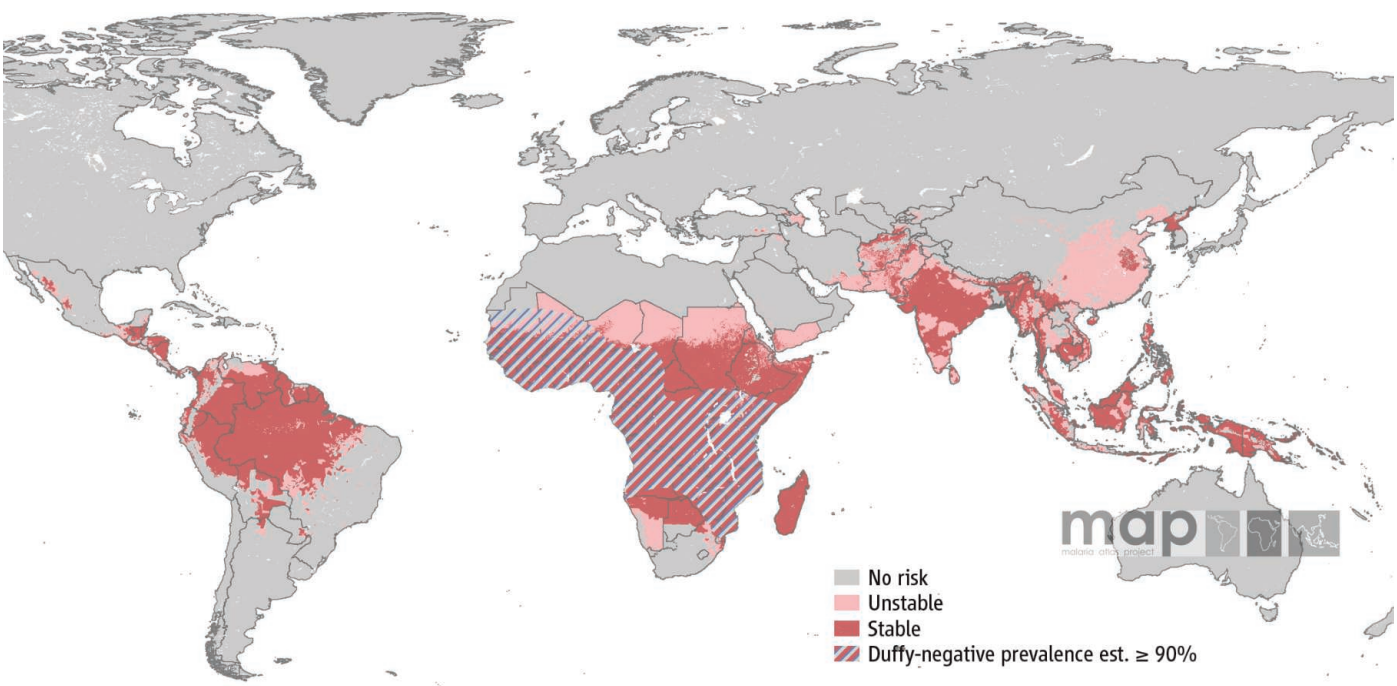

CREDIT: C. A. GUERRA *ET AL.*, *PLOS NEGLECTED TROPICAL DISEASES* 4 (AUGUST 2010)

Overlooked threat. A new analysis estimates the risk of vivax malaria across the globe, taking into account climate, public heath, and genetic data.

Downloaded from www.sciencemag.org on August 5, 2010

Published by AAAS

ScienceNOW

From *Science*'s Online Daily News Site

Traffic Jam in Orbit
Vying for geosynchronous orbit, more than 400 telecommunications satellites occupy a narrow band of space some 35,000 kilometers above Earth's equator. Now, researchers say that attaching solar sails to satellites could reduce the congestion. Computer models developed by aerospace engineer Colin McInnes and graduate student Shahid Baig of the University of Strathclyde in the United Kingdom reveal that the photons of sunlight streaming across the solar system contain sufficient energy to push a satellite arrayed with a solar sail into a stable geostationary orbit that doesn't circle Earth's equator. The satellite could also maintain its new position without the need for heavy, liquid-fueled thrusters, the pair reported in the *Journal of Guidance, Control, and Dynamics*. http://bit.ly/solar-sail

Tough Food, Better Bite
Throw a coyote a bone, and you may just change the shape of its skull. Ethologist Suzanne LaCroix of Michigan State University in East Lansing and colleagues randomly split related coyotes into two groups: one gnawed on sheep and cow femurs, and one dined exclusively on a soft diet similar to canned dog food. At 18 months old, the bone-chewing coyotes consumed rawhide treats more than three times as fast and ate nearly 1.5 times as much of a portion of beef shank as did coyotes without access to bones as pups, LaCroix reported at the 47th Annual Meeting of the Animal Behavior Society in Williamsburg, Virginia.

As adults, the bone-gnawers also had significantly shorter and wider mouth bones,

bigger chewing muscles, and a more prominent sagittal crest, the ridge of bone at the top of the skull to which these muscles attach. The researchers say this is the first time food has been shown to have such a dramatic impact on the anatomy of any animal. http://bit.ly/coyote-bite

CREDITS (TOP TO BOTTOM): CRISTINA SANTIESTEVAN/BBPP; SUZANNE LACROIX/MICHIGAN STATE UNIVERSITY

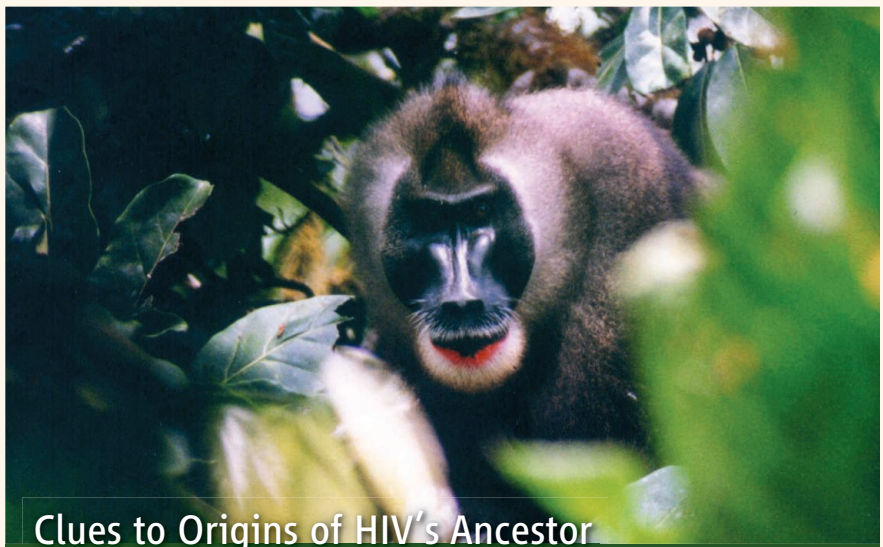

Clues to Origins of HIV's Ancestor

Monkeys on an island that separated from West Africa thousands of years ago could help unravel the puzzling origins of AIDS, according to a study presented at the 18th International AIDS Conference in Vienna.

HIV-1, the main virus driving the AIDS epidemic, likely entered humans from chimpanzees in the early 1930s. Chimps are infected with a related virus called SIVcpz, a blend of SIVs from two different monkey species. But scientists don't know when these SIVs made the leap from monkeys to chimps.

To find out, virologist Preston Marx of the Tulane National Primate Research Center in Covington, Louisiana, isolated SIVs from four different monkey species on the island of Bioko. One species, the Bioko drill (*Mandrillus leucophaeus poensis*), has a mainland counterpart that also harbors SIV. By looking at changes in the viruses' RNA, and calibrating this "molecular clock" based on the island's separation 12,000 years ago, Marx's team calculated that a virus related to the Bioko drill's SIV infected chimpanzees at least 22,000 years ago, much earlier than previous estimates. At a minimum, the SIVs are 76,000 years old, which may explain why they cause no harm in infected African monkeys, Marx noted: The hosts have had more time to evolve protective immune responses. http://bit.ly/HIV-origin

Marijuana Time Warp
People who smoke pot can feel lost in time—for some, it's part of the draw. Now researchers may have figured out one reason why.

The brain's suprachiasmatic nucleus (SCN) controls the 24-hour physiological cycle known as the circadian rhythm, using light to reset the clock. But SCN neurons also possess receptors for cannabinoids, the psychoactive compounds in marijuana. To find out what role these receptors play, a team led by Yale University circadian biologist Anthony van den Pol first housed 42 mice in total darkness for 2 weeks until they synchronized their daily internal clocks, spending 12 hours dormant and 12 hours active. Then the researchers shined a light into some of the cages shortly after the mice became active. Because mice are nocturnal, they became active about 2 hours later in the day than did mice not exposed to light. But mice given brain injections of cannabinoids before light exposure became active only 1 hour later than did the controls.

When the researchers added cannabinoids to mouse SCN cells in a petri dish, the cells fired about 50% more frequently. This increased activity likely mucks up the circadian rhythm in a live mouse, the researchers reported in *The Journal of Neuroscience*; cannabinoids may have a similar effect in humans. http://bit.ly/time-warp

Read the full postings, comments, and more at **news.sciencemag.org/sciencenow**.

Downloaded from www.sciencemag.org on August 5, 2010

Published by AAAS

Methane on ice. In winter, Arctic lake ice traps methane, but only temporarily.

'Arctic Armageddon' Needs More Science, Less Hype

Researchers agree that global warming will unleash methane stored at high latitudes, further increasing the greenhouse effect. But their concerns fall far short of the apocalyptic headlines

Downloaded from www.sciencemag.org on August 5, 2010

"MASSIVE METHANE RELEASE SPARKS global warming fears," blared the online news headline. "Arctic seabed methane stores destabilizing," warned a University of Alaska, Fairbanks (UAF), press release. Even the U.S. National Science Foundation, in another press release, found Arctic methane to be leaking off Siberian shores at "an alarming rate."

Alarm might well be warranted. Methane, chemical formula CH_4, is a powerful greenhouse gas 25 times more potent than carbon dioxide, and the ongoing global warming driven by carbon dioxide will inevitably force it out of its frozen reservoirs and into the atmosphere to amplify the warming. Such an amplifying feedback may have operated in the past, with devastating effects. If the modern version is anything like past episodes, two scientists warned in a Perspective in *Science* (24 April 2009, p. 477), it could mean that "far from the Arctic, crops could fail and nations crumble."

Yet, with bubbles of methane streaming from the warming Arctic sea floor and deteriorating permafrost, many scientists are trying to send a more balanced message. The threat of global warming amplifying itself by triggering massive methane releases is real and may already be under way, providing plenty of fodder for scary headlines. But what researchers understand about the threat points to a less malevolent, more protracted process. "It will aggravate the global change problem," says geochemist Martin Heimann of the Max Planck Institute for Biogeochemistry in Jena, Germany, "but it's not a catastrophe."

Sure looks scary

There's certainly plenty of methane out there. Beneath the sea floor, methane produced by the microbes in the sediment can become trapped in the crystalline cages of water ice to form methane hydrate, "ice that burns." No one is sure how much submarine hydrate exists worldwide, but it is on the order of several thousand petagrams (Pg) of carbon. (A petagram is 10^{15} grams, or a billion metric tons.) That's easily 1000 times the amount of methane presently in the atmosphere.

If hydrates are warmed, especially those under relatively low pressure beneath the shallow sea floor, they will melt, releasing their methane. "If you gave the planet a shake," says geochemist David Archer of the University of Chicago in Illinois, the gas "would all come out, and it would be a global catastrophe."

The other precarious source of methane is permafrost. Permanently frozen soil and sediment contains organic matter that microbes can convert to methane if the permafrost thaws and remains free of oxygen. That happens, for example, in the bottoms of the numerous arctic lakes that form in thawing permafrost. The top 3 meters of arctic permafrost are thought to hold about 1000 Pg of carbon as organic matter that could be converted to methane that would equal 300 times the methane in the atmosphere.

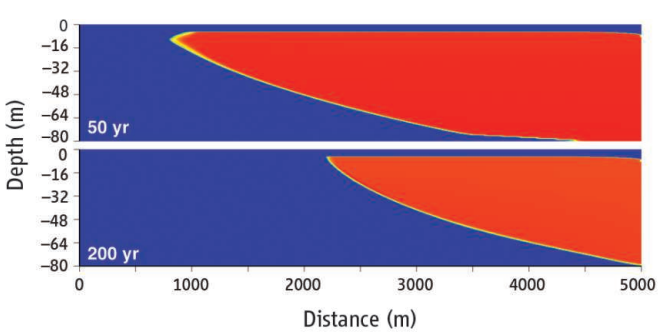

Going, going, … In a model, a methane hydrate deposit (orange) recedes as ocean warmth penetrates, much as happened off Svalbard (opposite page).

Here it comes?

This past March, oceanographer Natalia Shakhova of UAF and colleagues reported what sounded to some like the first methane gusher of many to come. The group took exhaustive samples over the East Siberian Arctic Shelf and found pervasive methane-rich waters, as they reported in the 5 March issue of *Science* (p. 1246). The methane was coming from the sea floor. The group calculated that as much

CREDITS: (TOP) KATEY WALTER ANTHONY/UAF; NSF/NASA FUNDING; (BOTTOM) M. REAGAN AND G. MORIDIS, *GEOPHYS. RES. LET.* **36** © 2009 AGU

Published by AAAS

methane was escaping from the water into the atmosphere as had been estimated to be escaping from the entire world ocean.

Alarm gripped at least some quarters of the media. But reporters failed to note—and scientists did not emphasize—one important detail: The methane was coming from permafrost thawing under the relatively warm waters that had inundated the Siberian shelf as sea level rose after the last ice age. With only 5 years of sampling, no one could tell whether the leak had started under global warming or had been going on for millennia. Many scientists lean toward millennia in this case.

A far stronger case for incipient hydrate destabilization appeared last year with less fanfare. In a paper in the 6 August 2009 issue of *Geophysical Research Letters*, marine geophysicist Graham Westbrook of the University of Birmingham in the United Kingdom and colleagues described how they used sonar to probe the shallow waters just west of Norway's Svalbard archipelago—halfway between mainland Norway and the North Pole. There, bottom waters had in fact warmed by a considerable 1°C during the previous 30 years, possibly because of global warming.

Where warmed currents brushed the Svalbard sea floor, the researchers found plumes of methane bubbles rising from the bottom. And in modeling reported in *Geophysical Research Letters* (*GRL*) on 15 December 2009 by hydrogeologists Matthew Reagan and George Moridis of Lawrence Berkeley National Laboratory in California, bottom-water warming melted the model's hydrates and released methane along the edge of the deteriorating hydrate deposit, much as seen off Svalbard. "That seems like the strongest argument for hydrates releasing methane" as they are warmed, says Archer.

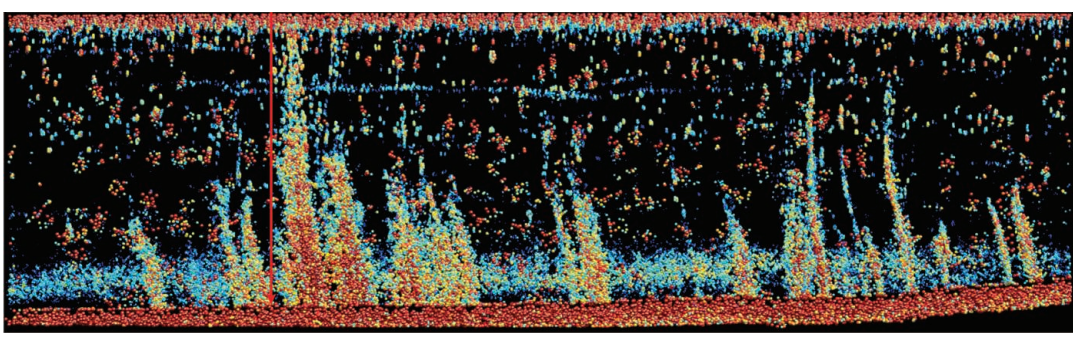

Up, up, and away. Sonar probing along 2.5 kilometers of 250-meter-deep water west of Svalbard revealed plumes of methane bubbles (multicolored) rising from the edge of a methane hydrate deposit beneath the sea floor (red-orange).

CREDIT: G. WESTBROOK *ET AL.*, *GEOPHYSICAL RESEARCH LETTERS* **36** © 2009 AMERICAN GEOPHYSICAL UNION

And more-widespread warming could be big trouble. Last year in the 8 December issue of the *Proceedings of the National Academy of Sciences*, Archer and colleagues reported on their own modeling of methane hydrate behavior, this time on a global scale. In both of their models, a 3°C warming of the ocean melts fully half of the existing hydrates. And aquatic ecologists Katey Walter Anthony of UAF and Sergey Zimov of the Northeast Science Station in Cherskii, Russia, reported at last December's meeting of the American Geophysical Union (AGU) that, according to "a very coarse estimate," the dominant type of northern permafrost would yield 50 billion tons of methane if it should thaw—10 times the current methane content of the atmosphere.

Not so fast

So at least in one high-latitude location, hydrates seemed to be newly giving up their methane, while reports of thawing permafrost and bubbly arctic lakes streamed in as well. But what did all the bubbling—seen and presumably unseen—really amount to? Atmospheric chemist Edward Dlugokencky of the National Oceanic and Atmospheric Administration's Earth System Research Laboratory in Boulder, Colorado, and colleagues analyzed NOAA measurements of atmospheric methane made on samples collected weekly from 1983 to 2008 at 46 sites around the world. Atmospheric methane had been increasing until the late 1990s, when it leveled off. Then in 2007, its abundance bumped up.

Online
sciencemag.org
Podcast interview with author Richard A. Kerr.

Taking into consideration numerous factors—including latitudinal patterns of change in atmospheric methane and shifting regional climates—Dlugokencky and his colleagues concluded that the recent methane jump was not driven by melting hydrates and permafrost. Instead, it seemed to be due to some combination of the high northern-latitude warmth in 2007 that is accelerating emissions from wetlands there; biomass burning contributing methane in the tropics; and heavy rains in Indonesia and the eastern Amazon encouraging tropical wetlands emissions. But because methane stopped increasing in the polar Northern Hemisphere in 2008, "the Arctic has not yet reached a point of sustained increased CH_4 emissions from melting permafrost and CH_4 hydrates," the group wrote in *GRL*. Dlugokencky summed up their conclusions at the AGU meeting: "Despite all the media hype, I don't think we're yet at an arctic tipping point."

Tipping points for both methane hydrates and permafrost will come, Archer predicts—but they will probably happen slowly. It takes time, he notes, to get from an atmospheric warming driven by carbon dioxide to an amplifying warming driven by atmospheric methane. It takes time for the ocean to warm. It takes time for that warmth to penetrate into hydrates. And it takes quite a bit of that penetrating heat to melt hydrates.

Once freed, the methane has to reach the atmosphere through the obvious obstacle of the overlying sediment. The ocean presents an impediment of its own. Bubbles may never reach the surface. Methane leaks out of bubbles, reacts with air dissolved in sea water, and becomes oxidized to form carbon dioxide. Even methane that reaches the atmosphere intact gets oxidized within about 10 years.

Folding all of those processes into an admittedly still-crude model, Archer and his colleagues get a warming of about 0.5°C, whether the ultimate carbon dioxide warming is a very modest 2°C or an extreme 7°C. The catch is that once the methane is converted into long-lived carbon dioxide, it prolongs that added warming for thousands of years.

So to scientists, the methane threat looks less like a catastrophe than an aggravation of a problem that already scares them. But "media people are all the time trying to have a doomsday story" about methane, says Walter Anthony. Not that scientists are blameless. "Quite a few scientists have maybe exaggerated a bit," Heimann acknowledges.

"Is now the time to get frightened?" Archer asked rhetorically on the blog Real Climate (www.realclimate.org) in March. His answer: "No. CO2 is plenty to be frightened of, while methane is frosting on the cake. … Methane sells newspapers, but it's not the big story."

–RICHARD A. KERR

Downloaded from www.sciencemag.org on August 5, 2010

Published by AAAS

MARINE BIOLOGY

Seeing Deeply Into the Sea's Biodiversity

Results from the decade-long Census of Marine Life are pouring in, providing insights into what lives where in the world's oceans

For the past 10 years, scientists from 80 nations have been creating the Census of Marine Life (*Science*, 2 June 2000, p. 1575; 31 October 2003, p. 773). Derek Tittensor of Dalhousie University in Halifax, Canada, and colleagues have now analyzed more than 6.5 million entries from the census databases, as well as other data for 11,500 marine species to create a map (*top right*) of diversity hot spots. Corals and coastal fishes are most diverse in Southeast Asia, as indicated by the outlined squares in the map, the team reported online 28 July in *Nature*.

Another analysis, drawn from field surveys and literature reviews by 360 scientists, appears in a series in the 2 August *PLoS ONE*. It looks at species diversity in 25 regions of the world and comes up with a global average of what types of species populate the oceans (see pie chart). The proportions of species that inhabit particular waters change according to location.

–ELIZABETH PENNISI

BIODIVERSITY HOT SPOTS

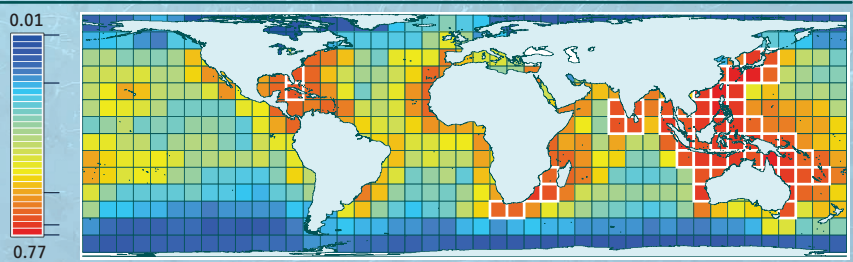

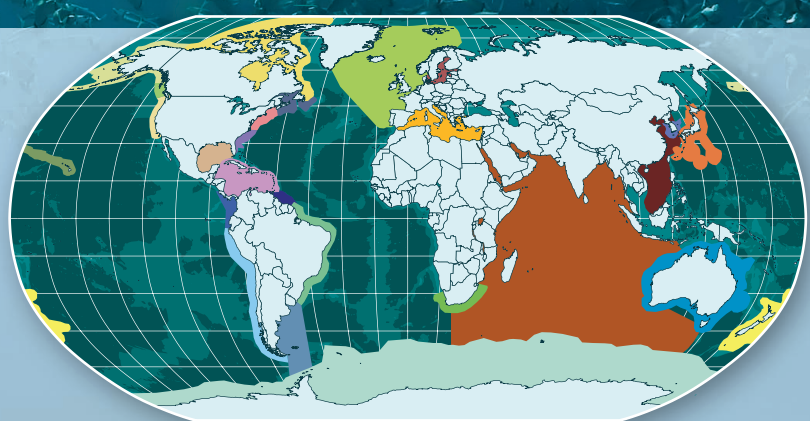

REGIONS STUDIED WITH SPECIES TOTAL

Alaska **5925**	S.A. Tropical West Atlantic **2743**	Arctic Canada **3038**	Japan **32,777**
Western Canada **2636**	Tropical East Pacific **6696**	Atlantic Europe **12,270**	South Korea **9900**
California **10,160**	Brazil Shelves **9101**	Eastern Canada **3160**	China **22,365**
Hawaii **8244**	Humboldt Current **10,186**	U.S. Northeast **5045**	Indian Ocean **23,964**
Gulf of Mexico **15,374**	Patagonia Shelf **3776**	U.S. Southeast **4229**	South Africa **12,715**
Caribbean **12,046**		Baltic **5865**	Australia **32,889**
Antarctica **8200**		Mediterranean **16,848**	New Zealand **12,780**

DISTRIBUTIONS OF BIODIVERSITY

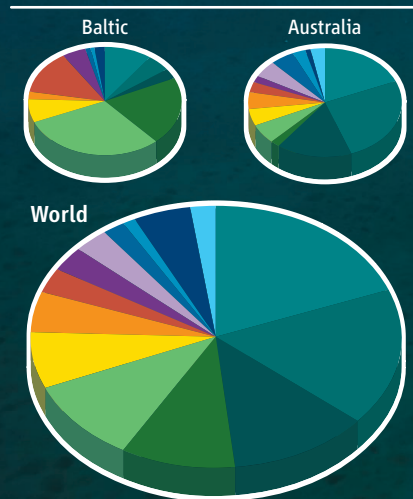


Pisces


Annelida


Echinodermata


Tunicata


Protozoa


Cnidaria


Porifera


Other Invertebrates


Crustaceans


Mollusca


Algae and Plantlike


Platyhelminthes


Bryozoa


Other Vertebrates

SOURCE: (TOP) D. TITTENSOR *ET AL.*, *NATURE* (28 JULY 2010); (MIDDLE AND BOTTOM) M. COSTELLO *ET AL.*, *PLOS ONE* **5**, ISSUE 8 (AUGUST 2010); PHOTO CREDITS: THINKSTOCK; PHOTOS.COM; WIKIPEDIA

Downloaded from www.sciencemag.org on August 5, 2010

Married, with plants. Douglas and Pamela Soltis work together in all aspects of their careers.

PROFILE: DOUGLAS AND PAMELA SOLTIS

The Power of Two

A University of Florida couple studying the evolution of flowering plants shows the value of doubled genomes—and joined careers

PULLMAN, WASHINGTON—When Pamela Soltis first joined her husband, Douglas, on the faculty at Washington State University, Pullman, they wrote separate grants and ran separate research programs. But they worked side by side in the field and in the greenhouse and read and critiqued each other's grant proposals and papers. More often than not, they also worked together in the lab. "We knew we were interested in a lot of the same things," Pam recalls. Eventually, they gave up trying to work independently.

Today, more than 25 years later, they are known collectively as the "Solti." "We're generally viewed as one person," Pam says. True, they have separate appointments at the University of Florida, Gainesville, she at the natural history museum and he in the biology department. But students, grants, courses, publications, talks, even accolades are shared. They studied in London on the same Fulbright scholarship and were co-awardees on an international prize. "Everything they do, they do together," says Michael Donoghue, an evolutionary biologist at Yale University.

"They are the most powerful, productive couple that may have ever been in botany, certainly in my generation," says John Kress, an evolutionary biologist at the Smithsonian National Museum of Natural History in Washington, D.C. The Soltises helped bring plant systematics into the molecular age, according to peers. And their innovations have led to firsts in "approaches to questions and ultimately first answers to questions," says Vaughan Symonds, a former postdoc now at Massey University in Palmerston North, New Zealand.

Early adopters of new techniques—including molecular DNA tools—as students in the 1980s, the Soltises have shown how rapid progress can be when two minds focus on a single research program. Says Jeffrey Doyle, a systematist at Cornell University, "They are so energetic and active that seeing Doug and Pam moving into your areas is a little frightening."

Doubling up is a main theme in their research as well. In their work on the evolution of flowering plants, the Soltises have shown that two genomes can be better than one. Throughout their joint career, they have studied a genus called *Tragopogon*, weedy plants with composite flowers that turn into puffballs. Hybridization of closely related *Tragopogon* species in Washington state has brought together two plant genomes in a single organism—a condition called polyploidy—yielding new species that are crowding out the parent stock. "They are weeds run amok," Doug says.

In addition, using molecular techniques to build a family tree of flowering plants, or angiosperms, the Soltises and their collaborators have determined which plants in the angiosperms are the most ancient. Early genome duplications, they learned, created genetic fodder for the great burst of diversification that followed the first appearance of flowering plants. "Using *Tragopogon* has led them to look at how important polyploidy is to angiosperms as a whole," says Jennifer Tate, a former postdoc and now a plant systematist at Massey University.

Backyard discovery

In their early days in Pullman when they were first looking into angiosperm evolution, the Soltises decided to follow up on work done by Washington State University botanist

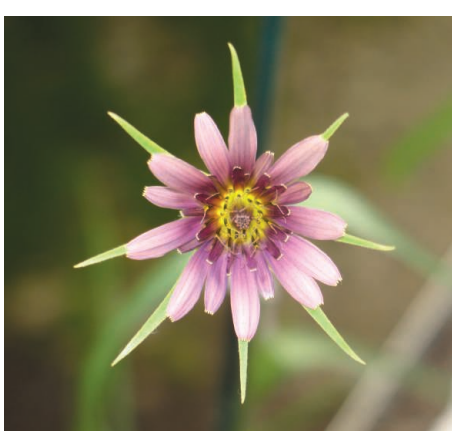

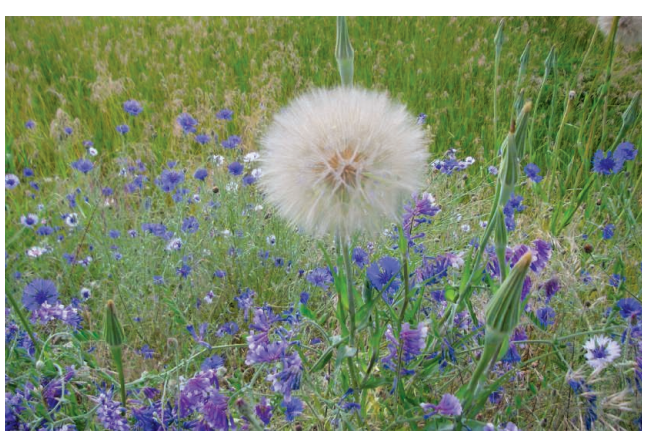

Success story. An 80-year-old new species, *Tragopogon mirus* (*right*), outcompetes its parental species, which produces smaller seed heads (*far right*).

CREDITS (TOP AND BOTTOM RIGHT): E. PENNISI/*SCIENCE*; (BOTTOM LEFT): ANDREW DOUST

Downloaded from www.sciencemag.org on August 5, 2010

Published by AAAS

Marion Ownbey. He had made a surprising discovery walking downtown from campus one day in 1949: He noticed some large, oddly colored versions of *Tragopogon*, whose sunflower-like flower heads are typically either yellow or purple. These had a yellow "eye" rimmed by purple. Ownbey found that they belonged to a new species that had arisen when two *Tragopogon* species had hybridized and produced descendents with double the usual number of chromosomes. Herbarium records showed that the two parent species were European natives that had reached Washington no earlier than 1928, which meant the new species was less than 50 years old.

Ownbey also found a second new polyploid species that involved a third *Tragopogon* parent. In 1950, he named the one with the yellow and purple flower *T. mirus* and the other, *T. miscellus*. It was the first time anyone had pinned down such a recent origin of a new organism; a few more examples have since been documented. "So often in evolutionary biology, it's like archaeology; you are looking for signs of what might have happened in the past," says Paul Wolf, a plant evolutionary geneticist at Utah State University in Logan. Now it was possible to work with a "real experimental system."

Ownbey spent much of the rest of his career tracking down local populations of the parents, hybrids, and polyploids and crossing them. He found them most often in abandoned lots, along roadsides, and other neglected places. Ownbey said these fragile populations bore watching to see how they fared over time.

The Soltises had been reading Ownbey's papers when "all of the sudden we realized we live here" right where Ownbey worked, Pam recalls. "We knew this would be a novel research opportunity." They were joined by a postdoc at Washington State, Stephen Novak, who tracked down Ownbey's notebooks. Novak, now a plant population geneticist at Boise State University in Idaho, and the Soltises spent a year going to 90 small towns—places where Ownbey had seen the new species and other nearby sites—estimating the numbers of each *Tragopogon* they found. On sunny mornings in Pullman, Doug could be found pushing a stroller—they had just had the first of their two daughters—up hillsides in search of *Tragopogon* flowers.

Doug, who had the morning child-care shift in those days, seems to be the more motivated by data-gathering of the two. He's also the big-ideas person with a drive to explore. Pam is drawn to data analysis and is more of a planner, colleagues say. They are competitive inside and outside the lab, according to friends. Before Doug's knees gave way, they played a lot of basketball and tennis together. Now she runs marathons and he does triathlons and fishes.

Speciation mania

The Soltises "were able to … bring new tools to the problem" that their predecessor grappled with, Donoghue says. Researchers used to think that a polyploid organism arose once and then spread to new places. Ownbey suspected that in *Tragopogon*'s case, the new species had formed multiple times. By comparing chloroplast DNA and other markers of the new species from different locations, the Soltises confirmed the multiple origins in spades.

Close quarters. Once they were transplanted from Europe, the purple *Tragopogon porrifolius* and yellow *T. dubius* came in close enough contact to hybridize and form a new species.

CREDIT: E. PENNISI/*SCIENCE*

A paper in the July issue of *Evolution* by Symonds and the Soltises documents the extent of these origins. "Each one of these towns is a little evolutionary experiment," Doug explains, as the new species arose independently many times. In one place, Oakesdale, there seem to be two origins of *T. mirus*: The flowers have different colors, and varied molecular markers support the suggestion that this species formed twice, with a different set of parents each time. The Soltises have argued that "multiple origins of polyploids are the rule rather than [the] exception," says Loren Rieseberg, one of their former students and an evolutionary biologist at the University of British Columbia, Vancouver, in Canada: "I think their views have now become conventional wisdom."

The Soltises and Tate, then a postdoc at the University of Florida where the Soltises went in 2000, began to create polyploid *Tragopogon* plants in the lab. People had assumed that polyploids would retain the extra genes they had acquired but turn off duplicates to keep genetic activity in balance. Instead, "we found out the *Tragopogon* polyploids were losing a lot of their genes," Tate says.

They began to think that evolution might repeat itself, with the same genes being lost as each new polyploid population formed. Indeed, that tends to be the case for *T. miscellus*, they reported last year in *BMC Plant Biology*. "We also found that there were some genes that were always maintained in duplicate," Tate says.

In addition, "weird things are happening to the chromosomes," Pam says. Even though standard biology says the chromosomes from one parent in a polyploid organism stay away from those of the other, in these plants they appear to exchange pieces. Instead of having two copies of a gene from each parent, a plant may have four copies from one and none from the other. There's an element of chance, "but there also may be a little bit of a pattern," Doug says. Certain genes are frequently lost—often those from *T. dubius*—and certain genes are always retained.

On a sunny day last month, the Soltises were back in Washington to collect seeds for an experiment they intend to run in Florida: growing the parents and the new polyploid species in the same conditions and observing DNA at work. "We want to know the effect of polyploidy on gene expression," Doug says.

They try to do most of their collecting before noon, when the flowers open for the morning sun. They work quickly and efficiently, Doug picking seed heads and putting them in envelopes, and Pam labeling them and putting them in a larger bag. They have seen that, over time, one of the polyploids has really taken off, while some of the parents seem to be struggling. In Pullman, for example, the Soltises can no longer find one of the parents, *T. pratensis*, although herbarium records show it used to be there. In contrast, *T. miscellus* has become quite common at a number of sites—its seed heads are big

Downloaded from www.sciencemag.org on August 5, 2010

Published by AAAS

and each plant has quite a few of them. "It's a poster child for why the polyploids are so successful," Doug says.

Thus in less than 80 years—the earliest date at which these new species could have formed—the polyploids have shown they are here to stay. One unresolved question is whether each separate origin should each be considered its own species. "It's one of the cool questions," Pam says.

Sequencing frenzy

"One of the things that make the Solti so successful is that they aren't afraid to dive into new territories" and tackle interesting questions, Tate says. "If they don't have the expertise themselves in a particular area, they build a team of collaborators who do."

Take DNA sequencing. When the Soltises went to California in 1988 to learn the technique from Michael Clegg, it took them 6 months to pull out eight sequences of 1700 bases apiece from the *rbcL* gene found in chloroplasts, a gene chosen because it was found in all photosynthetic plants. "People thought it was a speed record," Pam says. With these data, they were able to show that a supposed flowering plant family did not belong in a single group. They were hooked on the technology.

At the time, the map of flowering plants was a mess. With some 400,000 species, 15,000 genera, and more than 400 families, plant systematists had not been able to come up with a coherent, agreed-upon evolutionary tree. Several groups had started to collect DNA data to sort it out. At lunch one day at a conference in 1991, the Soltises and Mark Chase of the Royal Botanic Gardens, Kew, decided to pool their data; they then recruited other collaborators. "It was a novel approach for this area to get a lot of people to contribute to the same [project]," Donoghue says. "They had a vision of 'Let's try to work together to solve a large problem.' They became the ringleaders."

Two years later, Chase, the Soltises, and 40 collaborators published a tree based on 500 *rbcL* gene sequences. The tree's branching pattern generally agreed with results obtained earlier by nonmolecular methods. That agreement "gave credence to the surprises," such as putting lotuses and sycamores in the same small clade, Doug says.

Next, they came up with a tree for 220 species based on the *18s* gene, a nuclear gene, in 1997. It generally agreed with the *rbcL* gene tree. In the new analysis, they included an obscure plant from New Caledonia called *Amborella trichopoda* that happened to be in the freezers of the Smithsonian Institution, where the Soltises had done some work with Elizabeth Zimmer. Its lineage was surprisingly old: It fell out at the base of the angiosperm tree. These analyses "changed [angiosperm phylogeny] from a speculative field where personality meant a lot into a scientific field," says Gregory Plunkett, a molecular systematist at the New York Botanical Garden in Bronx, New York.

Ancient secrets. DNA from basal angiosperms such as the water lily and a plant called *Amborella* (*inset*) revealed early genome duplication in flowering plants.

On a roll, the Soltises embarked on an evolutionary tree based on three genes, the third also coming from the chloroplast genome. The sequencing was labor-intensive, and the Soltises did most of it themselves. "After we put the kids to bed at night, I would go and set up the sequencing reactions," Pam explains. "Doug would go into the lab in the morning to load the gels and then come home to see the kids before they went off to school."

In the end, their tree encompassed 560 species and included unrelated organisms—seven gymnosperms, a category that includes pines and conifers—for comparison. It clarified branches that were not well supported in the 1993 tree and "helped us figure out where more work was needed," Pam says. It was also adopted by the newly formed Angiosperm Phylogeny Group, which published its collaborative classification in 1998 and updated it in 2003 and 2009. With funding from the National Science Foundation, eight participating institutions are using 17 genes to understand "the dirty dozen" unresolved parts of the tree, in particular to sort out the flowering plants that diverged early, with a paper in the works. Today, "no other group of organisms have as good a phylogeny as flowering plants," says Mark Mort of the University of Kansas, Lawrence. Adds Kress: "It's so agreed on now that people are changing the organization of the whole herbarium."

Now the Soltises would like to expand their angiosperm tree, which has about 1000 species, to include representatives from all 15,000 genera. China has shown an interest. When the Soltises were in Shenzhen to meet with their Chinese collaborators in July 2010, they also met with the mayor to discuss the city's support of a Chinese angiosperm tree-of-life project. "If the Chinese will help fund it, it will be a big step," Doug says. They are also helping to promote a 100,000-species tree for all green plants.

In the meantime, the angiosperm phylogeny work has helped clarify which modern flowering plants represent the earliest evolving branches. To get a sense of what early angiosperm genomes were like, the Soltis group joined with Claude dePamphilis of Pennsylvania State University, University Park; Victor Albert, now at the University at Buffalo in New York; and more than a dozen other researchers to develop the Floral Genome Project.

From 2001 to 2006, this project compared the expression patterns of genes known to be important in flowering in an index plant, *Arabidopsis*, with patterns in plants at the base of the evolutionary tree they had constructed. The study found that most of the basal angiosperms used the same genes as *Arabidopsis*, but in different places at different times during development. "Basal angiosperms don't do things the way *Arabidopsis* does them," Doug says.

What's more, almost all of the genes involved with floral organization were duplicated. The Soltises and others suggested that polyploidy might be important to angiosperm evolution, enabling duplicated genes to evolve new functions and new roles. Polyploidy "might actually be instrumental to their origin," Doug says. Next, they plan to sequence *Amborella*, which should show more clearly whether genome duplication occurred 130 million years ago in the common ancestor to all living angiosperms.

The Soltises' decision to follow up on a botanist's curiosity about oddball flowers spotted on a walk into downtown Pullman is leading to a new understanding of how flowering plants evolved. **–ELIZABETH PENNISI**

CREDITS (TOP TO BOTTOM): MI-JEONG YOO

Downloaded from www.sciencemag.org on August 5, 2010

Published by AAAS

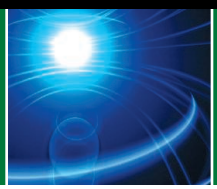

LETTERS

edited by Jennifer Sills

The Time of Young Scientists

T. BRÜCK *ET AL*. ("EMPOWERING YOUNG SCIENTISTS," EDITORIAL, 2 APRIL, P. 17) SUPPORT THE formation in various countries of young-scientist academies that younger scientists would be eligible to join, along the lines of the already-formed Global Young Academy. The latter will include an elite group of approximately 200 international young scientists around the age of 35. Although I am a proven advocate of young scientists (*1*), I found the Editorial to be off target.

The Editorial suggests that most internationally recognized scientists are senior and that "young scientists rarely receive societal recognition for their work." The reason for this discrepancy is not that young scientists are excluded; it is that most of them haven't yet produced high-impact work or that their recent discoveries need time to mature and make an impact. There are many examples of scientists less than 40 years old who have won Nobel Prizes or have been inducted into regular national academies. Consequently, there should be no reason or indications for discrimination for age, as speculated in the Editorial.

The parallel between science and sports is also off target. In sports, such as the 100-meter dash or tennis, the winner is unequivocal. The referees are only there to keep the score and/or make sure that the contestants follow rules of the game. In science, the question of "who is better" cannot be unequivocally answered because the criteria are subjective and the diversity of the scientific disciplines is enormous. It seems likely that the selection of the so-called 200 young international academicians will be based less on actual merit and more on the strength of the nominations by highly influential scientists who, predictably, will push and lobby for their own protégés.

The notion that young academicians will play major roles in national science policies is also not convincing. These highly promising young scientists would benefit more at this stage of their career from being shielded from such activities and encouraged to devote all of their time, energy, creativity, and focus on making important discoveries. There will be plenty of opportunities for them in the future to play roles in policy and management issues.

I conclude that academies for young scientists are not only unnecessary, but may damage the careers of highly promising young scientists. Necessarily, these promising future stars will need to divert at least part of their activity to conferences, policy, and management issues, which will distract them from creativity and innovation. Such activities could be easily fulfilled by more experienced senior scientists. Let us also not forget that the vast majority of senior scientists have a genuine interest in promoting the careers of younger scientists and not, as hinted in the Editorial, in grabbing their resources or stealing their societal recognition. After all, we are their natural mentors, and the importance of good mentorship has been emphasized repeatedly in this and other journals.

ELEFTHERIOS P. DIAMANDIS
Department of Pathology and Laboratory Medicine, Mount Sinai Hospital, Toronto, ON M5T 3L9, Canada. E-mail: ediamandis@mtsinai.on.ca

Reference

1. E. P. Diamandis, *Clin. Cancer Res.* **12**, 669 (2006).

Response

DIAMANDIS HAS RAISED A NUMBER OF IMPORTANT concerns about the role of young scientists in the science-policy dialogue. However, we strongly believe that his message—focus on science—runs contrary to the interests of young scientists and the broader scientific community.

In many countries, particularly less-developed countries, the value of science and scientists is underestimated. Young scientists are particularly vulnerable. The societal recognition we alluded to in our Editorial does not immediately concern the Nobel Prizes or membership in National Academies referred to by Diamandis, which are quite naturally connected with seniority. Of greater concern

Readers' Poll

The Time of Young Scientists

In their 2 April Editorial,* T. Brück *et al*. suggest that academies for young scientists (~35 years old) can help early-career researchers earn the support and recognition they deserve. E. P. Diamandis argues in a Letter that such societies will distract young scientists from their work at the bench. T. Brück *et al*. respond that the message to focus only on science "runs contrary to the interests of young scientists and the broader scientific community." In the coming years, there is likely to be a growing focus on science communication; scientists will be asked to explain their science and the scientific process to the general public and policy-makers.

How much time should the next generation of young scientists devote to nonresearch activities?

- ❒ **Less than 1%**
- ❒ **1–10%**
- ❒ **10–25%**
- ❒ **25–50%**
- ❒ **More than 50%**

Vote online at www.sciencemag.org/extra/polls/20100806-1.dtl

*T. Brück *et al.*, *Science* **328**, 17 (2010).

Polling results reflect the votes of those who chose to participate; they do not represent a random sample of the population.

Downloaded from www.sciencemag.org on August 5, 2010

Published by AAAS


Genomic imprinting
636

The light aquatic
637

are more mundane forms of recognition, such as societal leaders understanding and emphasizing the importance of young scientists for the well-being of the country, as well as academic freedom, independence, job security, and decent pay for talented young researchers. The formation of Young Academies is one important step to address and improve these issues.

Judging by the success of the Young Academies of Germany and the Netherlands (*1*), it appears that connecting the brightest across fields (including not only the natural sciences but the social sciences and humanities as well) yields novel modes of communication with society, authentic advice on science policy, and innovation in interdisciplinary fields. The last aspect directly strengthens the core business of the young scientist, which is and remains doing excellent research. The Young Academies movement represents a model of scientific creativity and achievement quite different from that advocated by Diamandis, which more closely resembles top-down learning and rituals of initiation.

We believe that all generations can contribute to science policy and management, and involving young scientists early in their career will help improve science's impact on society. For example, in Canada, young scientists have been major drivers behind a number of important recent initiatives at the science-policy interface, including the creation of a new prestigious postdoctoral fellowship program and a national forum on science policy (Canadian Science Policy Centre; http://sciencepolicy.ca).

The selection process for membership in the Global Young Academy involves rigorous peer review by both senior and young scientists. Although we share the author's concern that senior scientists may try to pack the ranks with their protégés, we will allow self-nominations to help alleviate this potential problem. The final decision on election depends on broadly accepted standards of excellence, and remains that of the Global Young Academy, not the nominators.

Our success to date owes no small debt to visionary support by senior scientists like Diamandis. We appreciate his well-documented interest in mentoring and advancing the careers of young scientists, and we hope he'll join us in recognizing and inviting to the table young academicians.

TILMAN BRÜCK,[1] CATHERINE BEAUDRY,[2] HANS HILGENKAMP,[3] REES KASSEN,[4] NITSARA KAROONUTHAISIRI,[5] HIBA SALAH EL DIN MOHAMED,[6] GREGORY A. WEISS[7]*

[1]Department of International Economics, German Institute for Economic Research (DIW Berlin) and Humboldt-University of Berlin, Mohrenstraße 58, 10117 Berlin, Germany. [2]Département de Mathématiques et de Génie Industriel, École Polytechnique de Montréal, succ. Centre-ville, Montréal, QC H3C 3A7, Canada. [3]University of Twente and Leiden University, Faculty of Science and Technology and MESA+ Institute for Nanotechnology, 7500 AE Enschede, The Netherlands. [4]Department of Biology, University of Ottawa, 30 Marie-Curie, Ottawa, ON K1S 3B5, Canada. [5]National Center for Genetic Engineering and Biotechnology, Microarray Laboratory, 113 Paholyothin Road Thailand Science Park, Pathumatani 12120, Thailand. [6]Department of Molecular Biology, The Institute of Endemic Diseases, University of Khartoum, Medical Campus, Qasser Street, Khartoum, Sudan. [7]Department of Chemistry, Molecular Biology and Biochemistry, University of California, Irvine, CA 92697, USA.
*To whom correspondence should be addressed. E-mail: gweiss@uci.edu

Reference

1. Junge Akademie Magazin (June 2010); www.diejungeakademie.de/publikationen/magazin_db/frameset_02.php?id_mag=13.

The Silver Lining of Language Loss

JUST AS ZOOLOGISTS AND BOTANISTS ARE concerned about the extinction of biological species, linguists are concerned about the rapid loss of languages ["What's lost when languages are," A. Pires, Books *et al.*, 23 April, p. 431, review of (*1*)]. We should, however, view the situation from the user's standpoint as well. In this modern and connected world, we cannot fully realize our potential unless we understand, speak, and write the language of our school, media, government, place of employment, and economic centers of power. If our mother language does not provide these connections (and most languages do not), one alternative is bilingualism or multilingualism, but many people are not able or willing to attain fluency in more than one language. The problem thus becomes a political one: Either the speakers of such a language maintain the autonomy and capability to promote enduring bilingualism, as the Catalans did, or the language takes the path toward extinction, as is happening to Occitan, Yiddish, and the native languages of North America.

We may, as outsiders, deplore such an evolution, but language is a practical tool. We do not advocate returning to the steam engine, the slide rule, or the logarithmic table. The drastic reduction of the number of languages is natural, unavoidable, and—from the viewpoint of communication and integration into a world community—desirable.

KURT F. J. HEINRICH
Rockville, MD 20850, USA. E-mail: kfjh@verizon.net

Reference

1. K. David Harrison, *When Languages Die: The Extinction of the World's Languages and the Erosion of Human Knowledge* (Oxford Univ. Press, Oxford, 2008).

Losing languages. The number of Yiddish speakers is dwindling.

Cuban Health Care: Consider the Source

I AM WRITING TO PROTEST THE EGREGIOUS misrepresentation of the Cuban health care system presented by P. K. Drain and M. Barry in their Policy Forum, "Fifty years of U.S. embargo: Cuba's health outcomes and lessons" (30 April, p. 572).

The most serious flaw in the Policy Forum is its unquestioning faith in the legitimacy

CREDIT: WIKIMEDIA COMMONS

Downloaded from www.sciencemag.org on August 5, 2010

of Cuban government health data. By basing their conclusions solely on official government sources, the authors imply that the health sector in Cuba can be analyzed apart from the rest of the government apparatus. As a result, the health sector is portrayed as an oasis of humanitarianism and egalitarianism that is completely unaffected by the surrounding problems of authoritarianism, repression of information, and grave human rights abuses that have characterized the Castro regime for most of its 50-year history.

A small but compelling array of recent publications (*1*–*5*) in the social sciences, as well as numerous informal reports (*6*–*10*) by dissident journalists and physicians, have successfully challenged these assumptions by documenting the myriad ways Cuba's systemic problems have become embedded in the organization and delivery of health care. The results of these inquiries are decidedly unflattering to the Cuban government and reveal a health system rife with corruption, authoritarianism, inequality, falsification of data, and human rights abuses. Any scholarly attempt to assess the true state of health conditions in Cuba, or the health impact of the U.S. trade embargo, should begin with a discussion of the way these systemic problems distort empirical research.

KATHERINE HIRSCHFELD
Department of Anthropology, University of Oklahoma, Norman, OK 73019, USA. E-mail: tkhirschfeld@ou.edu

References

1. O. E. Chepe, *Cuba: Revolución o Involución?* (Editorial Aduana Vieja, Valencia, Spain, 2007).
2. E. Kath, *Social Relations and the Cuban Health Miracle* (Transaction Press, New Brunswick, NJ, 2010).
3. K. Hirschfeld, *Health, Politics, and Revolution in Cuba Since 1898* (Transaction Press, New Brunswick, NJ, 2007).
4. K. Hirschfeld, *Cuban Affairs* **2**, 1 (2007).
5. A. Lago, *Can. J. Psychiatry* **39**, 129 (1994).
6. M. A. O'Grady, "Cuban doctor pays a high price for truth," *Wall Street Journal*, 31 March 2006.
7. Video testimony from Darsi Ferrer, dissident physician (www.youtube.com/watch?v=jgXP6AFo7lc), in the documentary "Cuba y los Elefantes" (Instituto Politico para la Libertad, Lima, Peru, 2009).
8. CNN story on Darsi Ferrer [in Spanish]; www.youtube.com/watch?v=8r0U7u6sTd4.
9. D. Mendoza, I. Fuentes, *Dengue!* (Center for a Free Cuba, Washington, DC, 2001).
10. Generation Y blog (www.desdecuba.com/generationy).

Letters to the Editor

Letters (~300 words) discuss material published in *Science* in the previous 3 months or issues of general interest. They can be submitted through the Web (www.submit2science.org) or by regular mail (1200 New York Ave., NW, Washington, DC 20005, USA). Letters are not acknowledged upon receipt, nor are authors generally consulted before publication. Whether published in full or in part, letters are subject to editing for clarity and space.

Cuban Health Care: Benefits Without Costs

THE SUGGESTION BY P. K. DRAIN AND M. BARRY ("Fifty years of U.S. embargo: Cuba's health outcomes and lessons," Policy Forum, 30 April, p. 572) that Cuba can provide the United States with the know-how to provide high-quality care at low cost is suspect. Cuba's system is specific to a small, centrally controlled country. This is not necessarily translatable to a large, heterogeneous nation profoundly focused on individual liberties, including the personal freedom to eschew preventive care. Many countries can provide medicine and other medical technologies at lower cost than the United States. Missing is the fact that these low-cost generics are based on discoveries mostly made in the United States and a handful of other developed nations. The United States bears the substantial burden of direct development costs as well as the general costs for development of an educational system and an infrastructure that has yielded an astounding array of medical advances over the past several decades. Others, such as Cuba, reap the benefits while avoiding most of the costs. Perhaps the authors would like to speculate on what the quality of health care in Cuba would be were it only based on discoveries and medical advances originating in Cuba.

LAWRENCE BODENSTEIN
Department of Surgery, Columbia University, New York, NY 10032, USA. E-mail: lb2126@columbia.edu

Response

HIRSCHFELD EXPRESSES A SKEPTICISM REgarding the validity of Cuban health data. Cuba has been publishing annual morbidity and mortality data by age, gender, cause of death, and geographical region since 1970 (*1*). These reports, generated from actual data collected within each polyclinic and hospital, have been presented in a timely manner and contain trends that are consistent with expected national and regional variations over time (*2*). Cuba also performs a high rate of autopsy procedures (*3*), which helps to complete their morbidity and mortality data. As a result, the rate of deaths attributed to ill-defined causes (0.7%) and estimation of under-registered deaths (2.1%) are both very low in comparison to other Latin American countries (*4*). Every year, Cuba submits data on 42 national health indicators as well as causes of mortality to the Pan American Health Organization (PAHO) (*5*). Given the completeness and consistency of Cuba's health data over the past 40 years, regular forgery of their annual reports would seem extremely improbable. By politicizing the dialogue, Hirschfeld does a disservice to all countries, including Cuba, that collect data to transform health care systems and save lives.

We agree with Bodenstein that the American medical system has yielded many astounding medical advances and discoveries, which have not come cheaply, and globalization has disseminated many of these advances to resource-poor countries, including Cuba. We have not advocated reducing funding of U.S. medical research, but rather providing better access to cost-efficient medical care, as exemplified by the Cuban health care system. For example, a large survey in 2003 found that American adults received only 55% of recommended preventive care or acute care services (*6*). In addition to providing better access to primary and preventive medical care, the U.S. medical system should also strive to streamline administrative processes, all of which Cuba has been doing well for many years. By shifting part of our focus from disease treatment to disease prevention, low-cost solutions implemented in Cuba could be applied to improve the health of Americans and help defray overall medical costs. Furthermore, eliminating the trade embargo may foster greater collaboration between American and Cuban scientists and physicians, which may lead to future medical advances and discoveries in both countries.

PAUL K. DRAIN[1]* AND MICHELE BARRY[2]
[1]Massachusetts General Hospital, 55 Fruit Street, GRJ-504, Boston, MA 02114, USA. [2]School of Medicine, Stanford University, Palo Alto, CA, 94305, USA.
*To whom correspondence should be addressed. E-mail: pkdrain@gmail.com

References

1. Ministry of Public Health, *Annual Statistical Report on Health, 2009* (Ministry of Public Health, Havana, Cuba, 2010); www.infomed.sld.cu/servicios/estadisticas/.
2. R. S. Cooper, J. F. Kennelly, P. Ordunez-Garcia, *Int. J. Epidemiol*. **35**, 817 (2006).
3. A. Espinosa-Brito, J. Viera-Yaniz, O. Chavez-Troya, R. Nieto-Cabrera, *Br. Med. J*. **328**, 66 (2004).
4. J. Silvi, *PAHO Epidemiol. Bull.* **24**, 1 (2003).
5. Pan American Health Organization, Data and Statistics (http://new.paho.org/hq/index.php?option=com_content&task=view&id=2470&Itemid=2003).
6. E. A. McGlynn *et al*., *N. Engl. J. Med.* **348**, 2635 (2003).

CORRECTIONS AND CLARIFICATIONS

News Focus: "Dams for Patagonia" by G. Vince (23 July, p. 382). The caption on p. 384 misidentified the glacier Perito Moreno as a source of water for the Baker River; the glacier feeds into Lago Argentina. Also, Hudson volcano was spelled incorrectly. In the sidebar, El Niña should be La Niña.

Letters: "Bracing for oil" by R. N. Silverstein (23 July, p. 388). Reference 1 was authored by A. H. Knap *et al*., not by Y. Loya *et al*.

Reviews: "Sea-level rise and its impact on coastal zones" by R. J. Nicholls and A. Cazenave (18 June, p. 1517). In Fig. 1, the range for Rahmstorf (2007) is attributed to the A1FI scenario, but it represents the response to the full range of SRES scenarios.

Downloaded from www.sciencemag.org on August 5, 2010

Published by AAAS

PHYSICS

Meaning in a Quantum Universe

Eric Werner

What is reality? Why is there anything at all? How did the complexity of the universe arise? What do quantum mechanics and quantum computers have to do with all this? If you have ever pondered any of these questions, then Vlatko Vedral's *Decoding Reality* is for you. Well written and engaging, the book provides a constant flow of new ideas. Vedral (a physicist at Oxford University) attempts to explain all of reality, its origins, and evolution in terms of the concept of information. He starts with Shannon's communication theory and then turns to quantum information theory and quantum computing. These are weighty topics, yet Vedral elucidates normally inaccessible concepts and theories with ease.

Decoding Reality
The Universe as Quantum Information

by Vlatko Vedral
Oxford University Press, Oxford, 2010. 239 pp. $29.95, £16.99. ISBN 9780199237692.

In the first half of the book, Vedral argues that Shannon's theory of communication is the basis for explaining social cooperation, biological information, and economics. One of the most frustrating things about Shannon's theory is that people keep trying to make it carry too heavy a load, a load Shannon never intended. That may be because of the use of the label "information." The power of his theory lies in its total disregard of meaning, but it thereby ignores the essence of social and biological information and communication. Although Shannon's theory may help to send a signal to Mars through the noisy channel of space, it will not help a robot on the planet's surface interpret the meaning of the signal (e.g., turn to left). Moreover, for two or more robots to cooperate, they must communicate strategic meanings, meanings that set up their respective intentions. These intentional, strategic states need not contain mutual information that is held in common. Instead, to achieve a goal by cooperative, social action, the strategic states have to be coordinated, be in synchrony, or coalesce. This is fundamentally different from Shannon's mutual information. As a result, Vedral's account of the role mutual information plays in social processes is misguided and misses the core of social communication.

The reviewer is at the Department of Physiology, Anatomy, and Genetics, University of Oxford, Parks Road, Oxford OX1 3PT, UK. E-mail: eric.werner@dpag.ox.ac.uk

There are similar shortcomings in Vedral's treatment of biology, which blindly follows Richard Dawkins's gene-centric view of biological information. Such a view fails to explain the central problems of developmental biology and evolution, namely the foundational role of genome control networks rather than genes. In addition, most of the content of the vast noncoding but conserved areas of genomes may be control information. As with social communication, such information has to be interpreted by the cell to give it pragmatic meaning. Hence, in this sense cells are communicating agents that possess a vast store of hard-wired strategic information in their genomes. Their status will not be explained by Shannon's communication theory nor by an extended quantum information theory. Although both theories hold, they are not relevant for understanding the reality of living, social processes.

When a cell receives a signal through a receptor, it initiates a series of steps in an internal interpretive network, which may lead a transcription factor to activate an area of its genome. This in turn may activate an entire genome network. Thus, the meaning of a signal depends on the complex interpretation carried out by the receiving cell. The signal's information content is enhanced by way of an interpretive mapping. The signal itself can be simple and, by itself, information poor.

The semantics of signals (and, more generally, languages) is governed by enrichment: Meaning enriches the information content of a signal. In adding information, it allows for extremely sophisticated responses to simple signals. The information in an intercellular message is not contained in the signal, the signal's probability of being sent, or its surprise value to the receiver. As a result, Shannon's theory is nearly irrelevant to understanding information and communication in developmental processes.

A very similar story can be told for human communication. Most animal communication involves coordinating social action. The meaning of a message is determined by how it affects the informational and intentional state of the agent. Agents coordinate their actions by using communication to adjust their respective strategies so that they cohere to achieve their interlocking goals (*1*). Again, this has little to do with the probability of a signal. Shannon's theory remains silent about meaning and understanding of language.

In the book's second half, Vedral turns from the world of living organisms to physics. He introduces the strange quantum world and argues that the universe is a quantum computer. As he recounts, the universe starts with a random event out of nothing, before there is space and time. Then, through further random events, the universe forms itself. Where the laws of the universe come from is unclear. Given that we accept that a set of consistent laws somehow came into being, the set of physical laws is a very small set. Its complexity is virtually nil compared with the complexity of the universe. Hence, the laws by themselves could not generate the space-time events that form the history of our universe. A limited set of laws can at best generate a set of universes, namely those consistent with the

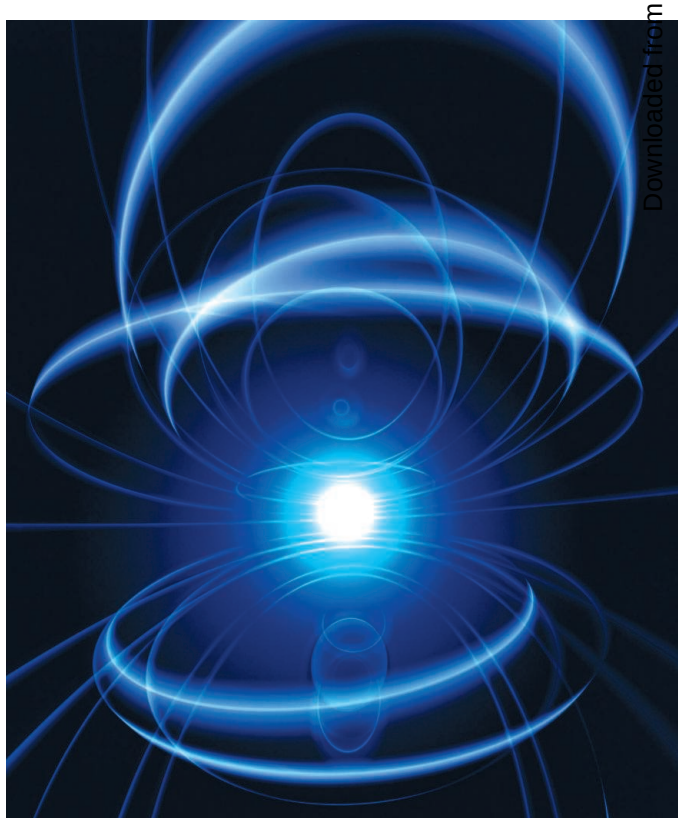

CREDIT: RYUICHI OKANO/AMANA IMAGES/GETTY IMAGES

Downloaded from www.sciencemag.org on August 5, 2010

Published by AAAS

laws. To generate a particular space-time event such as the creation of our universe, we need laws plus extra information, e.g., the initial and boundary conditions of differential equations or the program that initiates a particular Turing machine in a universal computer. As Andrey Kolmogorov implied, the complexity of a string cannot be greater than the minimal program that generates it and stops. We can abstract this to a complexity conservation principle that applies to all space-time events generated by agents using meaningful strategic and state information (*2*).

At the core of quantum computing is directive information (the program), the sequence of operators that repeatedly act on the quantum state to compute the result. The initial quantum state of the system has to be prepared. Classically, the initial state is prepared by putting data in memory, and the operator is prepared by loading a program. In quantum computing, analogous procedures are used. The quantum computer's advantage is that it can represent many states at once, through a superposition of states. This superposition can be operated on in a single step, offering an exponential increase in calculation speed over classical computers. Nonetheless, even if the universe is a quantum computer, the problem remains what (or who) wrote the program and set up the initial conditions.

Complex events such as the construction of our universe require sufficient information. One may argue that the universe resulted from random interactions constrained by the laws of physics. However, that would produce a vanishingly small probability for the generation of our particular, coherent universe. Most universes would be near-random structures. The counterargument is: Well, our universe was formed. Therefore, the laws plus random quantum processes must have generated it. But this begs the question. There is no free lunch. The information generated in the universe has to come from information. We are left puzzling over the source of our universe's ordered complexity.

Decoding Reality offers nonspecialists a powerful account of a science and its technology in the process of creation. To date, the theoretical work in quantum computing has vastly outpaced its technological realization. It took hundreds of years before Newton's calculus could be used to launch satellites and guide spacecraft to explorations of distant planets. Perhaps it will be a similarly long time before quantum computing is fully realized. Vedral guides readers into the center of the debates about the foundations of the field. And readers who hunger for additional details can turn to the more mathematical account he coauthored with Jacob Dunningham (*3*), which is also clearly written.

We still don't know why there is something rather than nothing. Vedral's book will introduce you to the fantastic world of quantum computing, teleportation, and multiple universes. Whether it decodes your reality, you must decide.

References

1. E. Werner, in *Distributed Artificial Intelligence*, vol. 2, M. Huhns, L. Gasser, Eds. (Pitman, London, 1989), pp. 3–36.
2. E. Werner, in *Applications of Multi-Agent Systems*, J. W. Perram, J.-P. Müller, Eds. (Springer Verlag, Berlin, 1996), pp. 19–39.
3. J. A. Dunningham, V. Vedral, *Introductory Quantum Physics and Relativity* (Imperial College Press, London, 2010).

10.1126/science.1192829

SOCIAL SCIENCES

Toward an Economy of Well-Being

Prashanth Ak

Happiness, for the Epicureans, was *ataraxia* (tranquility); for the Beatles, it was "a warm gun." Perhaps because of its particularity and amorphous nature, it has proven hard to discuss meaningfully. Nonetheless, happiness remains an enduring obsession and has fascinated a wide range of thinkers, including early economists.

Happiness Around the World
The Paradox of Happy Peasants and Miserable Millionaires
by Carol Graham
Oxford University Press, Oxford, 2009. 267 pp. $24.95, £14.99. ISBN 9780199549054.

In Adam Smith's weltanschauung, human activities were part of a great machine, the aim of which was the maximization of happiness. Utilitarian philosophy, which had a strong impact on economics, proposed that human goals, and the actions to achieve those goals, ought to maximize utility. They offered various definitions of utility, but in several accounts it was equated to happiness.

Happiness's position in the dismal science receded as the field's concepts and theories became increasingly precise and formalized. Eventually, more tractable and measurable quantities became stand-ins for utility in economics. Modern economics has largely taken utility to be an ordinal concept, a mathematical tool for talking about choices people make.

In the past three or four decades, happiness has made a comeback. Economists and psychologists have engaged the subject (and each other) with serious scholarly attention, which is moving happiness from the fringes to mainstream economics. However, the label "happiness" is a bit misleading, because most of the econometric studies are actually about subjective well-being, a more inclusive concept. Until recently, these studies have almost exclusively focused on the developed world. That restriction mainly reflects the paucity of data from elsewhere but also assumptions that cultures, institutional arrangements, and other conditions were far too different to allow comparisons.

Economist Carol Graham (University of Maryland and Brookings Institution) and her colleagues have been among the scholars who have grappled with these issues. *Happiness Around the World* offers a brief, well-written account of their intriguing findings. The author draws on findings from a variety of surveys across the world, but the book is not a mere compilation of interesting survey results. Graham includes original analyses of a host of factors such as macroeconomic trends, political regimes, corruption, crime, inequality, and health. Despite the complexity and nuances of the topic, her lucid text is an easy read.

Graham notes that, notwithstanding undoubted cultural variations in conceptions of happiness, on average the patterns seem remarkably consistent around the globe, across different levels of economic development, and even over time—at least in terms of correlates of happiness, such as income, employment, wealth, health, and stable relationships. In any country, the affluent tend to be happier than the less affluent. However, the Nigerians and the Chinese report about the same level of happiness as the French and the Japanese, despite large differences in gross domestic product. Afghans tend to be about as happy as Latin Americans; Kenyans seem as happy with their healthcare as the U.S. population is with its. For health satis-

The reviewer is at the Center for Systems Biology, Bloomberg Hall Extension, Institute for Advanced Study, 1 Einstein Drive, Princeton, NJ 08540, USA. E-mail: prashanth@ias.edu

Downloaded from www.sciencemag.org on August 5, 2010

Published by AAAS

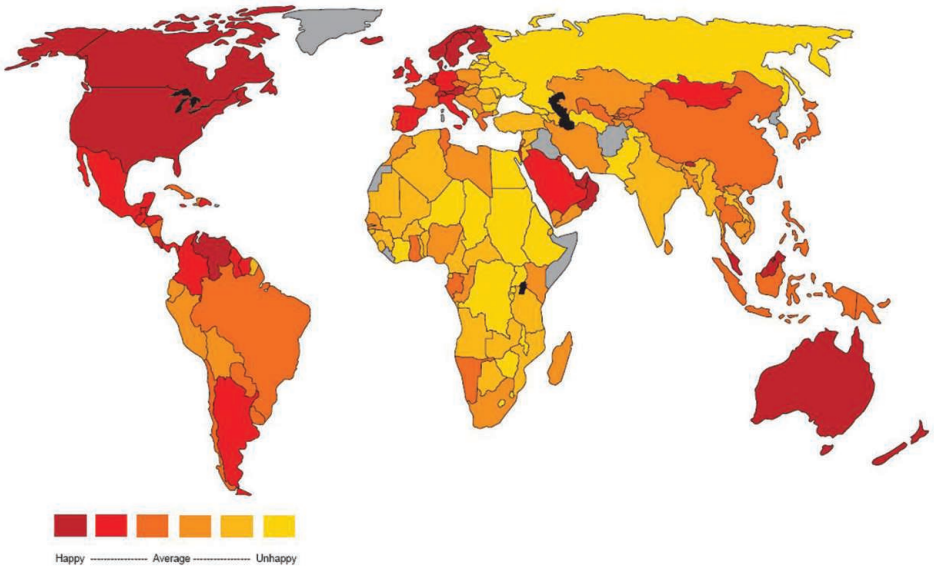

Mapping happiness. Social psychologist Adrian White drew on findings from over 100 studies to rank countries according to people's satisfaction with life.

CREDIT: ADRIAN WHITE (4)/COURTESY CARTOGRAPHIC UNIT, UNIVERSITY OF LEICESTER

faction (and, to a lesser degree, income satisfaction), variables that capture cultural differences seem to matter more than do objective conditions. Graham identifies some of these traits particular to countries and cohorts.

As the subtitle indicates, Graham also considers explanations for the "happy peasants and miserable millionaires" problem. These range from a link between rising aspirations and rising income (the "hedonic treadmill" hypothesis) to the possibility that individuals have an intrinsic "set point" of happiness, independent of external factors. People seem to adapt to both adversity and prosperity, though less well to some factors (uncertainty or income loss) than to others (petty crime and corruption or income gains).

Governments are beginning to show substantial interest in the application of such findings to public policy (*1*). Graham provides an even-handed account of the benefits such research may offer public policy as well as of the pitfalls of rushing to apply findings. Her cautious approach should be stressed: Whereas academics at least must subject their publications to the scrutiny of peer review, policy-makers face no such comparable rigor. The research itself can be ideology-free, but no such guarantee exists for applications. Such caution is especially important at this early stage of the field. Even observed correlations are still being acrimoniously debated. Suggestive evidence for causality is unclear: Do happier people earn more and enjoy better health? Or do higher incomes allow better access to healthcare and promote well-being?

We need to tread carefully rather than rush to apply happiness studies to public policy. As one expects of a young field, considerable conceptual and methodological issues remain unsettled. Data for such studies are collected primarily through surveys, and the recurrent question remains: do people mean what they say? A key aspect of these studies is their emphasis on expressed preferences (what people say they prefer) rather than revealed preferences (what people actually choose). Revealed preferences dominate conventional economics because stated preferences may not be reflected in people's actions as they typically do not involve the real-world trade-offs that occur during actual choices. Happiness economists contend that revealed preferences don't capture the gamut of optimal human responses (*2*); choices people make are circumscribed by available options. In addition, people often make perverse, suboptimal choices when driven by factors such as addictions or norms.

To take one reason for caution, a good deal hinges on the order in which survey questions are posed. When undergraduates were asked (*3*) how many dates they had the previous month followed by how happy they were with their lives in general, the correlation between the questions was high ($r = 0.66$). However, when the order of the questions was reversed, the correlation nearly vanished ($r = -0.12$). As Graham's research shows, Afghans place above the world average in happiness when asked open-ended happiness questions (generally speaking, how happy are you with your life?). But they fall well below average when asked the "best possible life" question (what is the best possible life you can imagine, and where do you rate your life on that scale?).

A multitude of other psychosocial factors can also affect responses. Some can be controlled for through the increasing sophistication of survey design and econometric procedures. A degree of validation exists in that answers to surveys of subjective well-being have been shown to be correlated with physiological and psychological measures such as heart rate, cortisol levels, brain scans, rate of smiling, sociability, and so on, but these measures in themselves are still not unambiguous. A somewhat better degree of validation exists in the correlation between a subject's answers and friends' reports of the subject's well-being. Many studies use standard econometric methods with some adaptations for the ordinal nature of the data (e.g., ordered probit or logit rather than standard regression equations), but analysis procedures continue to evolve. Graham briefly touches on some of these issues. A more-detailed exposition would have been handy for the consideration of policy applications. However, the book's brevity is one of its charms. Graham does not intend it to be a comprehensive tome on happiness economics, and in any case her account is well annotated.

Currently, the results of the sorts of surveys Graham discusses yield more questions than answers. Although that is intellectually stimulating, these questions need to be clarified before they can help guide intelligent policy applications. Were different levels of happiness reported for Afghanistan because the two surveys probed different aspects of a single concept? Is one aspect subsumed within the other, broader idea? Or did the results reflect two related but different concepts? The survey questions generally did not presume any specific notion of happiness, which allowed for comparisons across groups. But specific definition matters for public policy. What kind of happiness should our policies attempt to maximize? Does future happiness warrant current sacrifices? What, really, is happiness?

With more data being collected and analyzed with increasing sophistication, we have the tantalizing possibility of gaining a better understanding of age-old questions. *Happiness Around the World* offers a welcome, thought-provoking, and engaging snapshot of this emerging field.

References and Notes

1. See, for example, the French government's initiative at www.stiglitz-sen-fitoussi.fr/en/index.htm.
2. D. Kahneman, in *Choices, Values, and Frames*, D. Kahneman, A. Tversky, Eds. (Russell Sage, New York, 2000), pp. 758–774.
3. F. Strack, L. L. Martin, N. Schwarz, *Eur. J. Soc. Psychol.* **18**, 429 (1988).
4. A. White, *PsychTalk* **56**, 17 (2007).

10.1126/science.1191273

Downloaded from www.sciencemag.org on August 5, 2010

Published by AAAS

INTELLECTUAL PROPERTY

China's Innovation Landscape

A growing, domestic, private-sector and geographic diffusion of capacity mark the first two decades of China's patent system.

Kenneth G. Huang

The People's Republic of China has experienced three decades of sustained, strong annual economic growth as it transitions from a centrally planned economy to a free market. Currently the world's second largest economy (*1*), China recognizes scientific and technological innovation as an increasingly important strategy to fuel the next phase of its productivity growth (*2*). However, the drivers and trajectories of China's scientific and technological growth remain underinvestigated. To understand elements of China's innovative activities, particularly in science and technology, an analysis of comprehensive patent data provided by the State Intellectual Property Office (SIPO) of China is presented here.

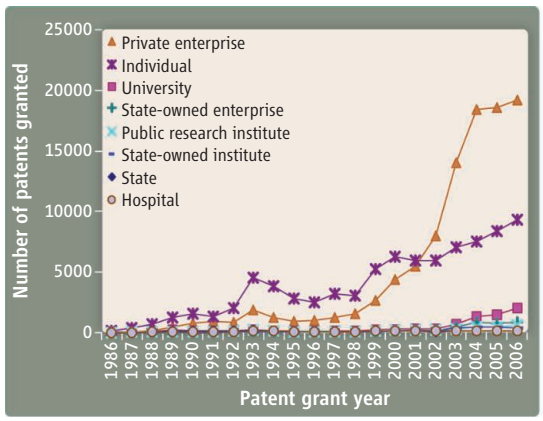

SIPO patents granted in 12 major science and technology classes by assignee sector.

Patents and Innovation

Patents play a central role in empirical research on innovation, despite their limitations as measures of the introduction of new products, processes, and services (*3*). They identify the inventors, assignees (i.e., patent holders), location, date, and innovative characteristics of every filed invention over long periods of time (*4*, *5*).

Although previous patent-based studies sought to examine determinants of national innovative capacity (*6*–*9*), economic growth and government policy (*10*, *11*), and the impact of geographic localization of knowledge exchange and diffusion (*12*), they focused primarily on developed North American and European nations. The few studies that sought to understand the technological development of China and East Asian countries were constrained to the limited number of patents awarded by the U.S. Patent and Trademark Office (USPTO) to Chinese entities (*9*, *13*). These studies were hindered by (i) selection bias, as the sample of Chinese firms willing and able to file a patent with the USPTO is severely restricted compared with the entire population of Chinese firms, particularly start-ups; and (ii) underrepresentation of government-related organizations, regulatory agencies, universities, or research institutes, because these organizations largely file patents within China.

The present analysis provides an overview of China's overall innovative activities using more than 1.1 million SIPO-granted invention and utility model patents (*14*) from grant years 1986 to 2006. These patents are awarded from over 2 million SIPO patent applications (*15*), which include all 129 classes of the International Patent Classification (IPC) of the World Intellectual Property Organization (WIPO) and all eight assignee sectors from application year 1985, when the Chinese patent system started to process patent applications, to 2006 (*16*). The assignee sectors are private enterprise, individual, university, state-owned (or -run) enterprise, public research institute, state-owned (or -run) institute, state, and hospital (table S1).

The analysis then focuses on over 200 thousand granted patents in 12 major science and technology classes, also across all eight assignee sectors. These important classes are drawn from a large body of literature (*17*–*21*), based on the IPC. They range from chemical and life sciences (i.e., organic chemistry, organic macromolecular compounds, biochemistry, microbiology, and genetics) and medical and pharmaceutical sciences to optics, computing, information and communication technology, electronics, semiconductors, microstructural technology, and nanotechnology (table S2).

Private, Domestic Growth

Patents granted across all patent classes and assignee sectors increased over 13% per year, on average, from 1986 to 2006 (fig. S1), despite China's relatively weak intellectual property (IP) environment, especially in terms of effectiveness in patent enforcement (*22*, *23*). This may reflect the growth of direct foreign investment in China (*24*). Foreign firms with expanding activities in China demonstrated the strategic importance of patent rights against competitors, providing opportunities for domestic firms to learn and innovate. This may have prompted Chinese firms to apply for and subsequently receive more patents. Clarification of IP laws favoring patent protection and better align-

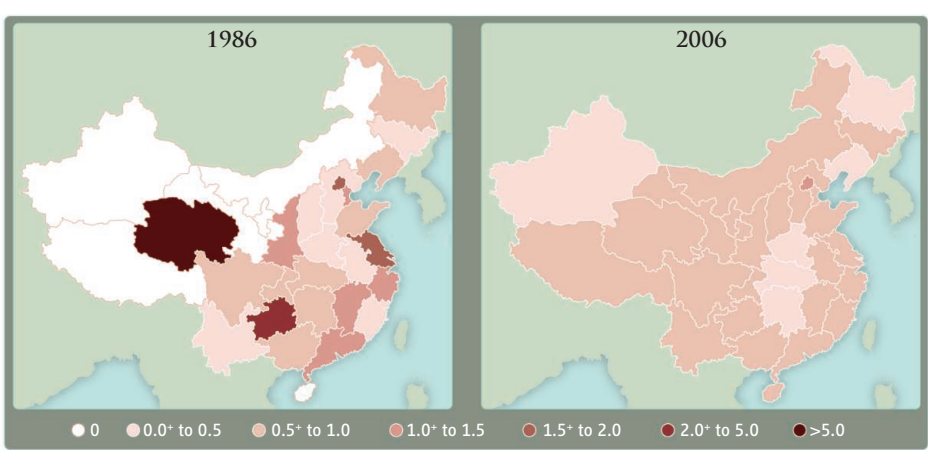

Regional relative scientific and technological advantage by patent grant year. The regions are 22 Chinese provinces, five autonomous regions [Tibet (Xizang), Guangxi, Xinjiang, Inner Mongolia, and Ningxia], and four municipalities (Beijing, Tianjin, Chongqing, and Shanghai). The two special administrative regions (Hong Kong and Macau) are not considered part of domestic China because of differences in their historical and technological developments, patent filing, and reporting systems.

Lee Kong Chian School of Business, Singapore Management University, Singapore 178899, Singapore.
E-mail: kennethhuang@smu.edu.sg

Downloaded from www.sciencemag.org on August 5, 2010

Published by AAAS

ment with international standards, as well as increased domestic investment in research and development (R&D) also may also have played roles (*24*).

In the 12 major science and technology classes, private enterprises—such as domestic firms and multinational corporations—steadily ascended to dominance after 2001 (see the first figure). This trend and the diminishing relative share of patents granted to individual inventors could be due to an increase in sophistication and cost of the R&D and technologies being patented, with firms likely to have more resources compared with individuals to develop such novel technologies. The SIPO patents granted in these 12 classes, led by medical sciences, semiconductors, communications, and computing (fig. S2), have grown from 12% of all patents in 1986 to over 20% of all patents in 2006 (table S3). They equal nearly one-fifth the number of USPTO patents granted in the same classes and time period; over 53% of all USPTO patents were in these 12 classes in 2006 (table S4).

Patents assigned to Chinese entities from 1986 to 2006 account for over 58% of the total patents in the 12 classes, followed by Japan (12%), Taiwan (11%), U.S. (7%), Korea (3%), and Germany (2%) (fig. S3). The annual growth rate of SIPO patents assigned to Chinese entities averaged 33% during this period. U.S. assignees contribute about 55% of total USPTO patents in the 12 classes from 1986 to 2006; non-U.S. assignees from advanced economies like Japan's (24%), Germany's (5%), and Korea's (3%) largely make up the remaining (fig. S4). The annual growth rate of USPTO patents assigned to U.S. entities during this period averaged around 7%.

Geographic Diffusion

A relative scientific and technological advantage (RSTA) index (*13*, *25*, *26*) can reflect how scientific and technological capabilities in these 12 classes evolve over time across geographic regions. This index is defined here as a region's share of SIPO patents across the 12 major science or technology classes, divided by that region's share of SIPO patents across all classes. For example, a region responsible for 20% of patents in the 12 classes, but only 10% of all patents, has a RSTA of 2, suggesting relative strength in the 12 key classes.

The RSTA at the province level in 1986 and 2006 is shown in the second figure. The scientific and technological advantages of key regions such as Shaanxi, Guangdong, Shanghai, Tianjin, Beijing, Jiangsu, Shandong, and other coastal provinces have diminished over time relative to the central and interior regions.

Conclusion and Future Research

Three key trends stand out. First, the increasing dominance of private firms over individuals, universities, and state-affiliated institutes suggests a fundamental shift in contribution to China's innovation landscape toward the private sector as China liberalizes its markets. Second, the surge in patents granted to domestic Chinese entities versus foreign entities across the 12 major science and technology classes suggests a rise in China's indigenous innovative capabilities, which have been well established in regions of major economic and social developments, such as Beijing, Shanghai, Tianjin, Guangdong, and Jiangsu. Third, the evening-out of regional RSTA suggests that scientific and technological capabilities have systematically diffused inward across the provinces to enhance China's overall innovative capacity. Although this pattern contrasts with previous empirical evidence from the United States suggesting that diffusion of knowledge and innovation are geographically localized (*12*) and concentrated in major cities rather than outside (*27*), it could provide some validation to the goals of the Chinese government's policy to coordinate and develop the central and interior regions (*16*). Such a centrally enforced strategy has the potential to promote innovation diffusion.

Evaluation of patterns of the evolution of innovative capabilities across geographic regions, technological classes, and ownership sectors could enable effective and targeted public policies to address specific regional and sectoral needs. For firms, identifying and matching their core scientific and technological competencies and trajectories to appropriate location choices is crucial for optimal exchange and application of knowledge, skills, and other resources.

Future research should untangle the complex relations linking spatial and temporal patterns of scientific and technological developments to investment environments and government policies. In addition, it will be important to investigate the strategic role of IP rights in shaping innovation and entrepreneurial ventures in China. Such valuable insights could stimulate sustainable R&D and entrepreneurship as China continues to transform from a manufacturing and industrial powerhouse into a knowledge-based economy.

References and Notes

1. Based on gross domestic product (GDP) purchasing power parity (PPP) calculations published by the International Monetary Fund (IMF), World Economic Outlook database (2009) and World Bank World Development Indicators database (2008).
2. Chinese president Hu Jintao called for greater emphasis on "technological advances and innovation to drive the good and fast development of the economy and society" at the opening ceremony of the member general assemblies of the Chinese Academy of Sciences and the Chinese Academy of Engineering on 5 June 2006.
3. Patents, which represent only a fraction of all inventions, are constructed within complex institutional frameworks by strategic actors who use patents in different ways to strengthen competitive positions. Thus, not all patents are of equal importance and value (*28*); analyses of their use entail assumptions, for example, in patent examination, granting, and follow-on citation behaviors. Patents are critical for investment and product development in chemical, biomedical, pharmaceutical, and life sciences (*17*–*20*), whereas in electronics and semiconductor industries, patents are important for strategic and defensive reasons, e.g., as cross-licensing bargaining chips or to fend off litigation (*21*). These patterns are more industry-specific than country-specific, although a weak IP environment can mitigate the propensity to apply for a patent (*22*, *23*).
4. Z. Griliches, *J. Econ. Lit.* **27**, 1661 (1990).
5. M. Trajtenberg, *Rand J. Econ.* **21**, 172 (1990).
6. B. Lundvall, Ed., *National Innovation Systems: Towards a Theory of Innovation and Interactive Learning* (Pinter Publishers, London, 1992)
7. J. L. Furman, M. E. Porter, S. Stern, *Res. Policy* **31**, 899 (2002).
8. M.-C. Hu, J. A. Mathews, *Res. Policy* **34**, 1322 (2005).
9. M.-C. Hu, J. A. Mathews, *Res. Policy* **37**, 1465 (2008).
10. A. B. Jaffe, M. Trajtenberg, *Patents, Citations, and Innovations: A Window on the Knowledge Economy* (MIT Press, Cambridge, MA, 2002).
11. K. G. Huang, F. E. Murray, *Res. Policy* **39**, 567 (2010).
12. A. B. Jaffe *et al.*, *Q. J. Econ.* **108**, 577 (1993).
13. I. P. Mahmood, J. Singh, *Res. Policy* **32**, 1031 (2003).
14. SIPO invention and utility model patents provide legal protection of 20 and 10 years, respectively, and are comparable with USPTO "basic" and "improvement" utility patents, respectively. A basic patent is usually a pioneering type of patent, e.g., for the first radio communication device. An improvement patent modifies or builds on the technology of the basic patent, e.g., enhancements to the device.
15. The patent applications include only patents that have been published by the SIPO, typically 18 months after the earliest priority date of the application. Before publication, the patent application is confidential to SIPO. Some applications received by SIPO may be pending publication or abandoned before publication. A subset of patents applied and published is eventually granted.
16. Further notes on data, China's patent system, and government policy are available as supporting material on *Science* Online.
17. E. Mansfield, *Manage. Sci.* **32**, 173 (1986).
18. R. Levin *et al.*, *Brookings Pap. Econ. Act.* **1987**, 783 (1987).
19. W. M. Cohen *et al.*, *Natl. Bur. Econ. Res. Work. Pap. Ser.* no. 7552 (2000); www.nber.org/papers/w7552.
20. K. G. Huang, F. E. Murray, *Acad. Manage. J.* **52**, 1193 (2009).
21. B. H. Hall, R. H. Ziedonis, *Rand J. Econ.* **32**, 101 (2001).
22. M. Zhao, *Manage. Sci.* **52**, 1185 (2006).
23. K. G. Huang, *Academy of Management Best Papers: Proceedings of the 2009 Academy of Management Annual Meeting*, Chicago, 7 to 11 August 2009, pp. 1–6.
24. A. G. Hu, G. H. Jefferson, *J. Dev. Econ.* **90**, 57 (2009).
25. L. Soete, *Res. Policy* **16**, 101 (1987).
26. D. Archibugi, M. Pianta, *The Technological Specialization of Advanced Countries* (Kluwer Academic Publishers, Dordrecht, 1992).
27. M. P. Feldman, D. B. Audretsch, *Eur. Econ. Rev.* **43**, 409 (1999).
28. M. Gittelman, *Acad. Manage. Perspect.* **22**, 21 (2008).

29. The author thanks A. Guglani and C. Lee for their excellent research assistance. This research is funded by grant 08-C207-SMU-003 from the Office of Research, Singapore Management University.

Supplementary Online Material

www.sciencemag.org/cgi/content/full/329/5992/632/DC1

10.1126/science.1190212

Downloaded from www.sciencemag.org on August 5, 2010

Published by AAAS

EPIDEMIOLOGY

Bats, in Black and White

Two bat studies tackle the "black box" of cross-species virus transmission and the impact of white-nose syndrome.

Peter Daszak

Over the years, disease researchers have fingered bats as the reservoir for a series of high-profile lethal agents, including rabies, Ebola, Hendra, Nipah, and severe acute respiratory syndrome (SARS) (*1*). Predicting when an infectious disease might jump from a host species such as bats to other wildlife or humans, however, has been a tough task. On page 676 of this issue, Streicker *et al*. draw on a study of rabies in bats to provide some important insights into the complex dynamics of cross-species transmission (*2*). Ironically, these bat-inspired insights come as Frick *et al*. report on page 679 that an emerging fungal disease seriously threatens bat populations in the Northeastern United States (*3*). The two studies demonstrate the value and importance of monitoring wildlife diseases, which can have major impacts on both human health and ecosystems.

Viruses that originate in animals and spread to humans have caused the most significant recent emerging infectious disease (EID), HIV/AIDS, and two recent pandemics (SARS and Influenza AH1N1). Predicting the emergence of the next new infectious disease has become a sort of Holy Grail quest for disease biologists, and one beset with challenges. First, we don't know what viruses are waiting to emerge from other animals. Second, we don't know where to target our research resources. Finally, even when we discover a new virus in wildlife, we can't predict how likely it is to "spill over" into people, become transmissible, and emerge as a pandemic.

We're beginning to deal with the first two problems. Researchers are mapping the unknown virome in wildlife with high throughput sequencing and genomics (*4*), and conducting "smart surveillance" in regions believed to be high-risk hotspots for EIDs (*5*). But the third issue—determining the likelihood that a new pathogen from one species will be infectious in another—has been a black box.

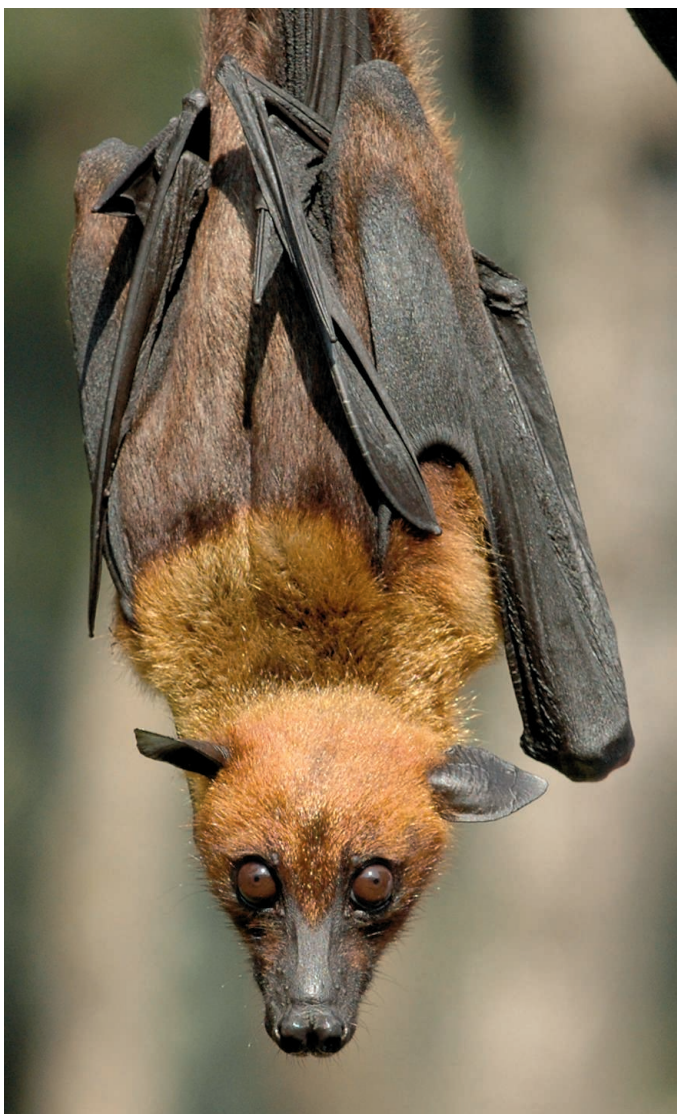

Understanding disease. Studies of bats, like this Indian flying fox (*Pteropus giganteus*), can provide important insights into disease agents that threaten both humans and wildlife.

Streicker *et al*. begin to chip away at the darkness in this issue. The authors use decades of surveillance data on bat rabies, virus sequence data, and information on bat ecology and traits to ask a fundamental question: What information is most important in predicting the likelihood of cross-species transmission of RNA viruses such as rabies? Although RNA viruses have high mutation rates that can help them move between species, Streicker *et al*. show that the phylogenetic similarity of different host species can be more important in predicting transmission than host ecological traits. More phylogenetically distant hosts are likely to have a far lower probability of swapping pathogens. To explain this, they propose that the innate similarity in immune defenses of closely related species favors viral exchange. The physical proximity or overlap in geographic range of hosts is also important, but to a lesser extent than evolutionary similarity.

Streicker *et al*.'s findings could have great relevance for better targeting surveillance of species most likely to be hosts for new emerging diseases affecting people. Perhaps future research based on these bat studies will reveal a phylogenetic "signal" that could help prevent the emergence of a new pandemic. To grasp the full complexity of cross-species disease transmission, however, researchers will need to consider the interactions of many other factors, including social, behavioral, and ecological traits, and issues such as stress, pregnancy, and seasonality.

If bats are to help us understand disease, however, we will have to do our part to protect them from emerging threats like white-nose syndrome (WNS). Investigators first implicated this fungal disease in bat die-offs in New York state in 2006. Although a growing list of bat species appears to be susceptible to WNS, researchers had not yet presented convincing evidence that this pathogen causes catastrophic population declines or has the potential to cause extinction. Frick *et al*. do both. Using long-term population data, they reveal dramatic population declines (up to 99% loss) occurring synchronously at multiple sites across the Northeastern United States. They also use data on bat population growth before the appearance of WNS and a

EcoHealth Alliance (formerly Wildlife Trust), 460 West 34th Street, New York, NY 10001, USA. E-mail: daszak@wildlifetrust.org

CREDIT: JON EPSTEIN/ECOHEALTH ALLIANCE (FORMERLY WILDLIFE TRUST) COPYRIGHT 2010

Downloaded from www.sciencemag.org on August 5, 2010

Published by AAAS

population model to estimate a 99% chance of the regional extinction of the little brown bat, *Myotis lucifugus*, within 16 years.

WNS is not the first documented EID of wildlife, nor the first case of potential extinction by infection. Amphibians, for instance, have experienced global decline (and multispecies extinction) largely due to the introduced fungal disease chytridiomycosis (*6*). It took disease ecologists two decades, however, to publish the first valid evidence of fungus-related declines in amphibians. It took a further decade to convince the research community that the disease could cause extinction and to develop a global policy response (*7*). In contrast, Frick *et al*. heralds a shift in how rapidly scientists and conservationists can now mobilize scant resources to identify the cause of a major environmental problem.

Let us hope that this work garners public interest and galvanizes government action to monitor, study, and address WNS and other wildlife diseases. In addition to better funding for this field, we need to rewrite the rules on who tracks and manages disease risks to wildlife. That task currently falls through the gaps between many U.S. agencies (*8*), is beyond the remit of international agencies such as the World Health Organization and the Food and Agriculture Organization, and is only partly covered by the World Organization for Animal Health (*9*). We need a new international body focused on global wildlife disease, perhaps under the auspices of the International Union for the Conservation of Nature.

Bats have a poor public image, in part due to their association with disease, and in part because of the general lack of knowledge of their critical role as pollinators and predators of agricultural pests. As we work to illuminate the links between wildlife and emerging diseases, let us remember that it was bats that gave us some of the first, critical rays of light.

References

1. K. Halpin *et al.*, Henipavirus Ecology Research Group, *Clin. Infect. Dis.* **44**, 711 (2007).
2. D. Streicker *et al.*, *Science* **329**, 676 (2010).
3. W. F. Frick *et al.*, *Science* **329**, 679 (2010).
4. W. I. Lipkin, *PLoS Pathog.* **4**, e1000002 (2008).
5. USAID (2010), "USAID Launches Emerging Pandemic Threats Program," URL last accessed July 15th 2010: www.usaid.gov/press/releases/2009/pr091021_1.html
6. K. R. Lips *et al.*, *Proc. Natl. Acad. Sci. U.S.A.* **103**, 3165 (2006).
7. L. M. Schloegel, P. Daszak, A. A. Cunningham, R. Speare, B. Hill, *Dis. Aquat. Organ.*, published online 13 January 2010; 10.3354/dao02140.
8. K. F. Smith *et al.*, *Science* **324**, 594 (2009).
9. T. Kuiken *et al.*, *Science* **309**, 1680 (2005).

10.1126/science.1194089

CHEMISTRY

The Give and Take of Alcohol Activation

Catalysts make alcohols more reactive by taking away hydrogen to create carbonyl compounds and then returning the hydrogen to the final products.

Andrew J. A. Watson and Jonathan M. J. Williams

Alcohols are relatively common starting materials for chemical reactions, even though they are quite unreactive. For example, reactions that would substitute another functional group (a nucleophile) for OH often fail because the hydroxide group (HO^-) is difficult to displace—it is a poor leaving group. Alcohols are usually activated by turning the hydroxide into a better leaving group, either by protonating the alcohol or by converting it into a sulfonate or halide. However, both of these activation methods have some disadvantages (*1*). The acidic environment required for protonating the alcohol also protonates and deactivates the incoming nucleophile, especially amines. Conversion of the alcohol into a sulfonate or halide can lead to toxicity problems; many alkyl halides and alkyl sulfonates are mutagenic.

Many chemical transformations could be more efficient and more environmentally friendly if there were improved ways of making alcohols more reactive. An alternative approach to alcohol activation is being developed that uses a catalyst to remove hydrogen, which oxidizes the alcohol to form a more reactive carbonyl group. The carbonyl group then undergoes a transformation, such as reaction with an amine to form an imine with the loss of water as the only waste product, and then the catalyst returns the hydrogen. This approach has been termed "borrowing hydrogen" (*2*), and its use in amine formation is summarized in the figure.

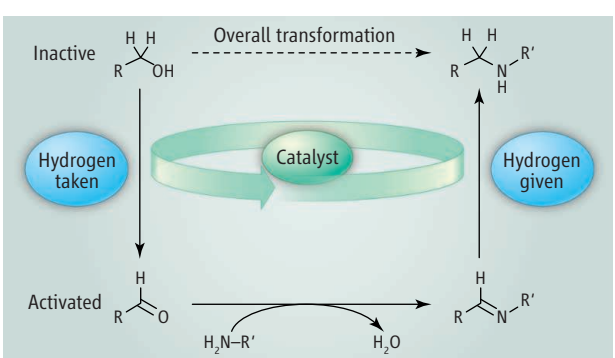

Borrowing hydrogen for alcohol activation. Transition metal catalysts can activate normally unreactive alcohols by temporary removal of hydrogen. The inactive alcohol (where R is a side-chain group) is converted into an aldehyde by taking hydrogen away. The more reactive aldehyde undergoes reaction, in this case a condensation reaction with an amine (with a different side-chain group R′). The hydrogen is returned to yield the product.

Typical catalysts for this reaction are ruthenium or iridium complexes, and the first examples of homogeneous catalysts were reported in the early 1980s (*3*, *4*). These early methods were limited by low yields and the requirement for high temperatures. Recent developments in catalyst design have allowed these reactions to be run at temperatures down to 70°C, usually in an organic solvent, although they have been performed in water in some cases (*5*). Fujita and Yamaguchi have used a pentamethylcyclopentadienyl iridium complex as a catalyst for a wide variety of amine formation reactions (*6*). Beller and co-workers have used a simple ruthenium carbonyl cluster activated with a bulky phosphine ligand (*7*), whereas Williams and co-workers have used (arene)ruthenium complexes with bidentate phosphines (*8*), to prepare more than 100 amines with excellent selectivity. Even deactivated aromatic amines (anilines) undergo reac-

Department of Chemistry, University of Bath, Claverton Down, Bath, BA2 7AY, UK. E-mail: ajaw20@bath.ac.uk; chsjmjw@bath.ac.uk

Downloaded from www.sciencemag.org on August 5, 2010

Published by AAAS

tion readily, typically at 100° to 110°C. Iridium complexes with either bidentate ligands bearing phosphorus or nitrogen atoms (*9*), or *N*-heterocyclic carbenes (*10*), have also shown high reactivity.

The borrowing-hydrogen pathway allows the number of groups attached to the nitrogen atom of the amine to be controlled easily, which is often not the case when amines react with alkyl halides. Ammonia can be converted selectively into a primary amine by reaction with an alcohol (*11*), and secondary and tertiary amines can also be prepared by using suitable amines and alcohols as starting materials. Cyclic amines have been prepared by reacting an amine with a molecule bearing OH groups at both ends, such as 1,5-pentanediol (*12*). Several pharmaceutical drugs have been prepared on a small scale by reacting alcohols with amines using the borrowing-hydrogen methodology, including the analgesic fentanyl and the antihistamine chlorpheniramine (*12*). Other nitrogen-containing compounds, including sulfonamides, have been alkylated with alcohols in the presence of ruthenium catalysts, and less expensive copper catalysts have also been used for this reaction (*13*, *14*).

Alcohols can also be used as starting materials for the formation of carbon-carbon bonds. The reaction follows a similar mechanism to the one shown in the figure, where hydrogen is taken away from the alcohol to give an aldehyde. This aldehyde then reacts by an aldol condensation (*15*) or Wittig reaction (*16*) to form an alkene, which has hydrogen given back to produce the C–C bond. Recent reviews of borrowing hydrogen methodology covering both C–N and C–C bond formation provide further details of the scope of these reactions (*17*, *18*).

An elegant alternative strategy to alcohol activation by temporary oxidation to an aldehyde has been developed by Krische and co-workers (*19*). Ruthenium or iridium complexes oxidize the alcohol and then activate the reacting partner by addition of the metal and a hydrogen to generate a nucleophilic organometallic species that adds to the aldehyde. This strategy has allowed dienes and other unsaturated substrates to react with alcohols and form new C–C bonds (*20*).

The ability to alkylate amines without the need for conventional mutagenic alkylating agents is being recognized by pharmaceutical manufacturers as an appealing new strategy in the synthesis of drug compounds. There are many further opportunities that could be exploited by using the borrowing-hydrogen strategy, such as deprotonation of the intermediate carbonyl compound to give an enolate that can then act as a nucleophile. Although the currently used ruthenium and iridium catalysts are effective, they have so far been unsuccessful at room temperature. The development of more reactive catalysts, as well as ones that avoid the use of noble metals, will be a welcome addition in this area.

References

1. R. N. Salvatore, C. H. Yoon, J. W. Jung, *Tetrahedron* **57**, 7785 (2001).
2. M. G. Edwards *et al.*, *Chem. Commun. (Camb.)* **1**, 90 (2004).
3. R. Grigg, T. R. B. Mitchell, S. Sutthivaiyakit, N. Tongpenyai, *J. Chem. Soc. Chem. Commun.* **12**, 611 (1981).
4. Y. Watanabe, Y. Tsuji, Y. Ohsugi, *Tetrahedron Lett.* **22**, 2667 (1981).
5. O. Saidi, A. J. Blacker, M. M. Farah, S. P. Marsden, J. M. Williams, *Chem. Commun. (Camb.)* **46**, 1541 (2010).
6. K.-I. Fujita, R. Yamaguchi, *Synlett* **4**, 560 (2005).
7. D. Hollmann, A. Tillack, D. Michalik, R. Jackstell, M. Beller, *Chem. Asian J.* **2**, 403 (2007).
8. M. H. S. A. Hamid, J. M. J. Williams, *Chem. Commun. (Camb.)* **7**, 725 (2007).
9. B. Blank, S. Michlik, R. Kempe, *Chemistry* **15**, 3790 (2009).
10. A. Prades, R. Corberán, M. Poyatos, E. Peris, *Chemistry* **14**, 11474 (2008).
11. C. Gunanathan, D. Milstein, *Angew. Chem. Int. Ed.* **47**, 8661 (2008).
12. M. H. S. A. Hamid *et al.*, *J. Am. Chem. Soc.* **131**, 1766 (2009).
13. F. Shi *et al.*, *Angew. Chem. Int. Ed.* **48**, 5912 (2009).
14. A. Martínez-Ascencio, D. J. Ramón, M. Yus, *Tetrahedron Lett.* **51**, 325 (2010).
15. R. Martínez *et al.*, *Tetrahedron* **62**, 8988 (2006).
16. M. G. Edwards, J. M. J. Williams, *Angew. Chem. Int. Ed.* **41**, 4740 (2002).
17. T. D. Nixon, M. K. Whittlesey, J. M. J. Williams, *Dalton Trans.* **5**, 753 (2009).
18. G. Guillena *et al.*, *Chem. Rev.* **110**, 1611 (2010).
19. J. F. Bower *et al.*, *Org. Lett.* **10**, 1033 (2008).
20. R. L. Patman, V. M. Williams, J. F. Bower, M. J. Krische, *Angew. Chem. Int. Ed.* **47**, 5220 (2008).

10.1126/science.1191843

Downloaded from www.sciencemag.org on August 5, 2010

DEVELOPMENTAL BIOLOGY

Which Parental Gene Gets the Upper Hand?

Maternal and paternal influences on gene expression play a surprisingly large role in the epigenetic regulation of mammalian brain function.

Lawrence S. Wilkinson

Things used to be relatively straightforward when it came to parental influences on gene action. Mom and Dad passed on one copy (or allele) of each autosomal gene to their progeny and overall, the expression and function of genes inherited by the offspring were indifferent to which parent they came from. When imprinted genes were discovered, this simple picture changed. That is because chemical modifications of DNA that occur early during development of the female and male germ line (the cells that form the egg and sperm) epigenetically mark imprinted genes for differential expression, depending on whether the gene is of maternal or paternal origin (*1*). In some cases, such imprinting suppresses expression from the maternal allele, leading to sole (or predominate) expression of the paternal copy of the gene. For other imprinted genes, the opposite is true and expression is solely or predominately from the maternal allele. On pages 643 and 682 of this issue, Gregg *et al*. (*2*, *3*) provide new findings that influence current thinking about the scale and complexity of genomic imprinting and place parental influences on gene expression as a major player in the epigenetic regulation of brain function.

In both studies, Gregg *et al*. used a combination of "new generation" sequencing methods for high-resolution screening of the transcriptome (all the RNA molecules transcribed from a genome) in mouse brain tissue, and a model that allowed them to identify whether gene expression was from the male or female parental allele. The first striking result is the sheer number of genes in brain that showed parental bias in expression—over 1300 protein coding and putative noncoding RNAs, representing a factor of about 10 increase over current knowledge and expectations. How could so many candidate

Behavioural Genetics Group, Cardiff MRC Centre for Neuropsychiatric Genetics and Genomics, Cardiff University Neuroscience and Mental Health Research Institute, Schools of Medicine and Psychology, Cardiff University, Cardiff CF10 3AT, UK. E-mail: wilkinsonl@cardiff.ac.uk

Published by AAAS

Offspring genes. There is strong parental bias in genes expressed in the mouse brain. Whether this is true in humans is not yet known.

CREDIT: PHOTOS.COM

imprinted loci have gone unrecognized? Presumably, enhanced resolution of the molecular screen is the reason, a testimony to the transforming powers of new-generation sequencing. Another fundamental issue is the shifting definition of what an imprinted gene actually is. The improved sensitivity of the methods used by Gregg *et al*. dictates that a proportion of the newly identified imprinted candidate genes are based on relatively marginal expression biases. It can be argued that a "true" imprinted gene shows a profound, almost complete silencing of one or the other parental allele. It is likely that full acceptance of the substantially enlarged list of imprinted gene candidates as bona fide imprinted genes will await supporting evidence of the precise epigenetic mechanisms underlying the parent-of-origin expression biases.

The mammalian brain is extremely complex in terms of its development, connectivity, and cellular composition, and previous work has demonstrated a measure of matching complexity to imprinted gene expression. For example, some imprinted genes show a parental bias in expression only at specific stages of development, whereas others show such expression only in certain cell types, with biallelic expression elsewhere in the brain. However, the findings of Gregg *et al*. reveal a hitherto unanticipated level of complexity and subtlety to the factors controlling parental influences on gene expression biases, showing sensitivity to stage of development, brain area, and cell type, but also to the sex of the individual and even to different versions (isoforms) of products from the same gene.

Furthermore, Gregg *et al*. provide evidence for the emergence of larger-scale organization. For example, in the embryonic mouse brain, there is an overall preferential maternal contribution to gene expression, which switches to a preferential paternal contribution in the adult. Things get even more interesting and complicated when taking sex into account. Here, there is evidence for a preponderance of candidate autosomal imprinted gene loci in females that is present in the hypothalamus but not in other brain regions, such as the medial prefrontal cortex. Such findings open up new avenues for the way in which parental influences, through genomic imprinting, may be directed selectively toward daughters or sons.

The main message from the new findings of Gregg *et al*. is that far from being some arcane sideshow, parental bias in gene expression constitutes a major component of epigenetic regulation in the mammalian brain. The studies raise numerous questions. How is widespread dynamic control of parental bias in gene expression achieved? Also, the extent to which such control is "hard-wired" or sensitive to environmental changes is not yet clear. Presumably, the underlying molecular mechanisms will involve interactions, yet to be determined, between developmentally controlled epigenetic marks and cell-type–specific gene promoters and enhancers. Another question is the extent to which such data obtained in mice are relevant to humans, as genomic imprinting is suggested to play an important role in human brain function and behavior (*4*).

As for the many and varied evolutionary theories surrounding genomic imprinting, such as "genomic conflict" (maternal and paternal genomes act antagonistically) (*5*) and "coadaptation" (imprinted genes coevolve to optimize parental care of offspring) (*6*), the findings of Gregg *et al*. do not add overwhelming weight to one idea or the other. But irrespective of the choppy waters surrounding evolutionary arguments, the findings of Gregg *et al*. provide new insight into the relevance and importance of parental influences on gene expression in the brain, and bolster the evidence that such effects need to be taken into account in the etiology of complex brain disorders, such as autism and schizophrenia (*7*).

References

1. W. Reik, J. Walter, *Nat. Rev. Genet.* **2**, 21 (2001).
2. C. Gregg *et al*., *Science* **329**, 643 (2010); published online 8 July 2010 (10.1126/science.1190830).
3. C. Gregg, J. Zhang, J. E. Butler, D. Haig, C. Dulac, *Science* **329**, 682 (2010); published online 8 July 2010 (10.1126/science.1190831).
4. A. R. Isles, *Trends Genet.* **25**, 495 (2009).
5. J. F. Wilkins, D. Haig, *Nat. Rev. Genet.* **4**, 359 (2003).
6. E. B. Keverne, J. P. Curley, *Front. Neuroendocrinol.* **29**, 398 (2008).
7. L. S. Wilkinson, W. Davies, A. R. Isles, *Nat. Rev. Neurosci.* **8**, 832 (2007).

10.1126/science.1194692

ENVIRONMENTAL SCIENCE

When UV Meets Fresh Water

Craig E. Williamson and Kevin C. Rose

Ultraviolet radiation has detrimental and beneficial effects in freshwater ecosystems.

Ultraviolet radiation (UV)—the shortest-wavelength, highest-energy solar radiation that passes through the atmosphere—is a potent force affecting life on Earth. Exposure to UV, which reaches Earth's surface at wavelengths between 290 and 400 nm, can damage DNA and impair an organism's ability to reproduce, sense its environment, and resist disease. Ozone concentrated in the stratosphere shields living organisms from the most damaging wavelengths of UV, known as UV-B (280 to 320 nm). In the 1980s and 1990s, observations that this protective layer was becoming depleted, and that a seasonal ozone "hole" over the Antarctic was expanding, generated serious concerns about the potential negative effects of increased UV on aquatic ecosystems (*1*). More recently, however, it has become clear that even the shortest-wavelength, highest-energy UV reaching Earth has beneficial as well as detrimental effects on individual organisms and thus on natural ecosystems (*2*).

Many organisms, including humans, cannot see UV, but a wide variety of fish, birds, spiders, insects, zooplankton, and other

Department of Zoology, Miami University, Oxford, OH 45056, USA. E-mail: craig.williamson@muohio.edu; rosekc@muohio.edu

Downloaded from www.sciencemag.org on August 5, 2010

Published by AAAS

organisms use UV in orientation, communication, navigation, foraging, and mate selection. For example, the spectral composition of underwater light plays a key role in mate selection and speciation in African cichlids because it affects how the fish perceive body colors (*3*). Color-based reproductive isolation has contributed to the evolution of more than 500 species of cichlids from a single ancestor in Lake Victoria in less than 13,000 years. Recently, UV receptors have been discovered in some African cichlids (*4*), and UV has been demonstrated to be important in mate selection of other freshwater fish, such as guppies (*5*). These observations suggest that UV may be an important part of the Lake Victoria cichlid story. There is also growing evidence that UV allows some fish to attract mates but not predators, because some predatory fish cannot see UV (*6*).

In clear, cold-water lakes, high levels of UV transparency may also help maintain the integrity of fish communities by protecting them from invasive warmwater fish. For example, in Lake Tahoe, the invasive warmwater bluegill (*Lepomis macrochirus*) reproduces in shallow nearshore waters where temperatures are warm enough to support successful spawning. At undisturbed sites where the water is very clear, however, high UV exposure levels preclude spawning due to lethal DNA damage (*7*). Bluegill are thus restricted to spawning in sites where natural or human disturbances reduce water transparency, providing a refuge from UV damage. The potential for UV damage in surface waters may also force zooplankton into deeper, colder, suboptimal habitats with potentially negative consequences (*8*). Researchers have also found that UV at longer wavelengths of 320 to 400 nm (UV-A) can

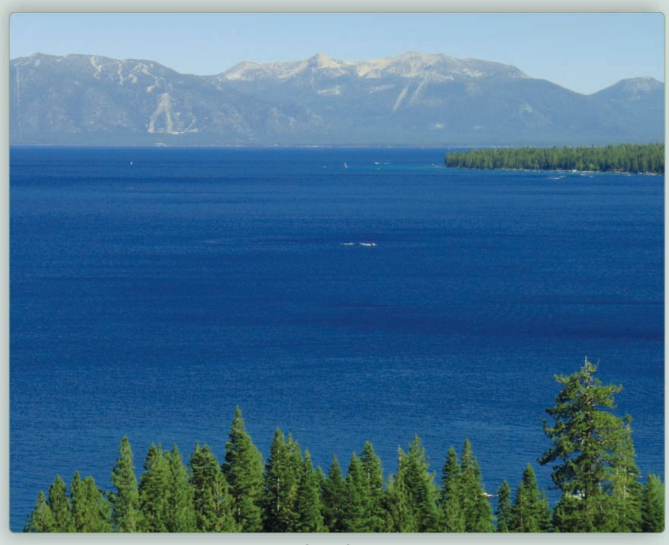

Lake Tahoe

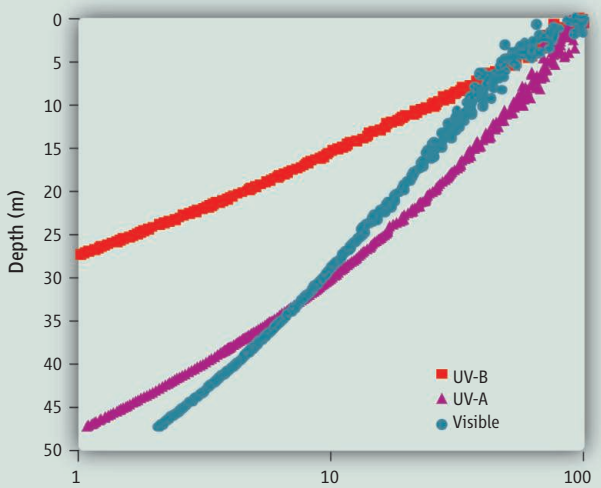

Lake Lacawac

Getting deep. Some fish and zooplankton respond behaviorally to UV-A, which usually penetrates much deeper into lakes than UV-B (graph, **center**). In some clear lakes with low CDOM, such as Tahoe in California and Nevada (**top**), UV-A attenuation is similar to that of visible light (*12*). In many smaller lakes with higher CDOM, such as Lake Lacawac in Pennsylvania (**bottom**), both UV-A and UV-B are absorbed within less than 1 m of the surface.

enhance the foraging ability of some juvenile fish that have UV-A receptors only early in their lives (*9*).

In most aquatic ecosystems, CDOM, the color-absorbing component of dissolved organic matter (DOM), acts as the ozone of the underwater world by selectively removing the shorter wavelengths of UV. In some of the world's clearest lakes, where DOM concentrations are low, 1% of incident UV penetrates to depths of many tens of meters (see the figure); in systems with higher DOM, the UV is absorbed within a fraction of a meter (*10*). Although changes in water transparency to visible light have been documented in response to disturbances ranging from acidification to eutrophication and climate change, changes in UV transparency related to the quality (color) and quantity of DOM provide an even more responsive sentinel of environmental change (*11*).

The Environmental Effects Assessment Panel of the United Nations Environment Programme is monitoring how stratospheric ozone, and the beneficial and damaging effects of UV, are changing over time (*12*). Recently observed trends of increasing and, in some cases, decreasing DOM concentrations in inland waters across North America and Europe (*13*) indicate that underwater UV exposure is changing as well. Levels of UV radiation found in natural sunlight have been shown

PHOTO CREDITS: CRAIG E. WILLIAMSON

Downloaded from www.sciencemag.org on August 5, 2010

Published by AAAS

to kill waterborne human pathogens such as *Cryptosporidium* under environmentally realistic conditions (*14*, *15*). The potential for recently observed increases in DOM to reduce the solar UV exposure levels of these pathogens suggests a need for continued vigilance in monitoring the UV transparency of inland and coastal waters. The contrasting effects of UV, combined with a changing UV environment, have important implications for the freshwater ecosystems on which humans depend.

References and Notes

1. L. Roberts, *Science* **244**, 288 (1989).
2. R. L. McKenzie, J. B. Liley, L. O. Björn, *Photochem. Photobiol.* **85**, 88 (2009).
3. O. Seehausen *et al.*, *Nature* **455**, 620 (2008).
4. R. Jordan *et al.*, *J. Fish Biol.* **68**, 1291 (2006).
5. A. Kodric-Brown, S. C. Johnson, *Anim. Behav.* **63**, 391 (2002).
6. U. E. Siebeck, A. N. Parker, D. Sprenger, L. M. Mäthger, G. Wallis, *Curr. Biol.* **20**, 407 (2010).
7. A. J. Tucker *et al.*, *Ecology* **91**, 882 (2010).
8. S. L. Cooke, C. E. Williamson, D. M. Leech, W. J. Boeing, L. Torres, *Can. J. Fish. Aquat. Sci.* **65**, 1144 (2008).
9. D. M. Leech, W. J. Boeing, S. L. Cooke, C. E. Williamson, L. Torres, *Limnol. Oceanogr.* **54**, 1152 (2009).
10. K. C. Rose, C. E. Williamson, J. E. Saros, R. Sommaruga, J. M. Fischer, *Photochem. Photobiol. Sci.* **8**, 1244 (2009).
11. K. C. Rose, C. E. Williamson, S. G. Schladow, M. Winder, J. T. Oris, *J. Geophys. Res. Biogeosci.* **114**, G00D03 (2009).
12. A. Andrady *et al.*, United Nations Environment Programme, Environmental Effects Assessment Panel, *Photochem. Photobiol. Sci.* **9**, 275 (2010).
13. J. Zhang *et al.*, *Limnol. Oceanogr.* **55**, 30 (2010).
14. S. J. Connelly, E. A. Wolyniak, C. E. Williamson, K. L. Jellison, *Environ. Sci. Technol.* **41**, 7101 (2007).
15. B. J. King *et al.*, *Appl. Microbiol.* **104**, 1311 (2008).

16. We acknowledge support from the NSF (DEB-IRCEB 0552283, DEB 0734277, and DGE IGERT 0903560).

10.1126/science.1191192

PHYSICS

In Praise of Exact Quantization

Magnetic impurities in a topological insulator provide a route to control its electronic properties.

Marcel Franz

In science, great value is placed on quantities that are exact. In physics, it is crucial for our understanding of the world around us to know that the values of fundamental physical constants, such as the mass and charge of an electron (or any other elementary particle), remain precisely the same no matter the circumstance. In solid-state physics, where we deal with complicated systems of many particles, such comforting exactness is hard to come by. A piece of iron will have electrical resistance that can vary greatly with temperature, impurity content, and other factors; the same is true of most of its other measurable properties. There are notable exceptions to this rule, such as when large numbers of particles act in a way that leads to emergence of exactness on a macroscopic scale (*1*, *2*). Two celebrated examples of this phenomenon are quantization of magnetic flux in superconductors and quantization of Hall conductance in quantum Hall fluids. On page 659 of this issue, Chen *et al*. (*3*) report findings that may soon establish another entry in this short list. The venue here is the surface of dibismuth triselenide (Bi_2Se_3), which belongs to the recently discovered class of solids called topological insulators (*4*–*6*).

Underlying the exactness in all known many-body systems is the notion of topological order. Crudely speaking, this means that some property of the system is completely insensitive to changes in the microscopic conditions (such as impurity content or temperature) as long as they are applied continuously and within certain bounds. In a superconductor, the magnetic flux threading a hole will remain precisely quantized in units of the flux quantum, $\Phi_0 = hc/2e$ (where h is Planck's constant, c is the speed of light, and e is the charge of an electron), independent of temperature, hole shape, or even the material type, as long as the system stays in the superconducting state. Similarly, the Hall conductance σ_{Hall} in integer quantum Hall fluids, realized in a two-dimensional electron gas (2DEG) in a strong magnetic field, remains pinned to an integer multiple of the conductance quantum e^2/h for a range of conditions. The remarkable aspect of these phenomena is that the quantization is truly exact, so much so that the most precise values of e and h come from measurements performed on superconductors and 2DEGs. Thus, finding a new form of exact quantization in a solid-state context is a big deal, and this is where topological insulators may come in.

As the name suggests, these materials possess topological order. In three-dimensional topological insulators, such as the recently discovered Bi_xSb_{1-x} alloys and Bi_2Se_3 and Bi_2Te_3 crystals, the physical manifestation of the topological order comes in the form of protected, gapless, surface states. In the bulk of an insulator, all electronic states are gapped; that is, an energy gap exists between the occupied and empty states, and this is what makes an insulator insulating. Some insulators have gapless surface states, meaning that their surfaces

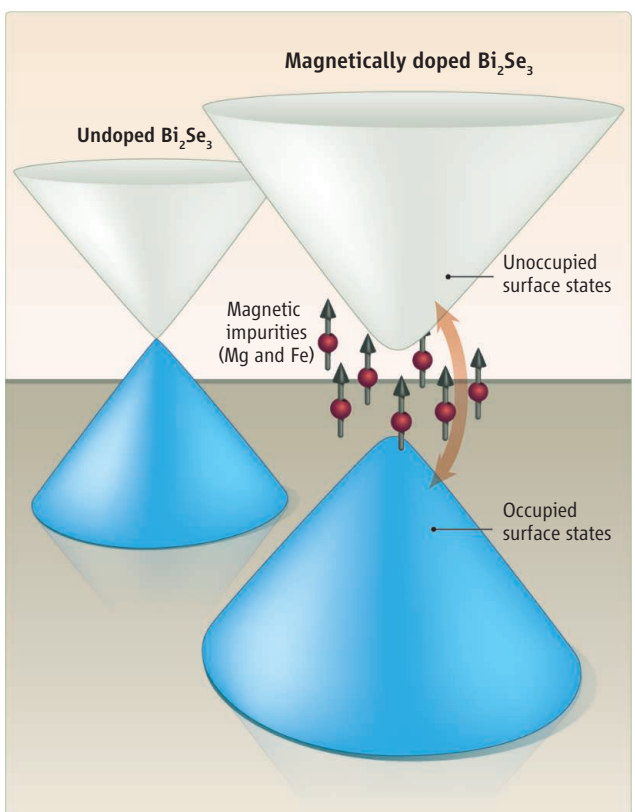

Divide and conquer. Doping a topological insulator with magnetic impurities breaks time reversal symmetry and opens up a gap between the Dirac cones of the surface states, as found by Chen *et al*. (*3*), thereby providing a way to control the electronic properties.

CREDIT: P. HUEY/*SCIENCE*

Department of Physics and Astronomy, University of British Columbia, Vancouver, BC V6T 1Z1, Canada. E-mail: franz@physics.ubc.ca

Downloaded from www.sciencemag.org on August 5, 2010

Published by AAAS

behave as two-dimensional metals and conduct electric current. In ordinary insulators, such surface states are typically fragile and can be destroyed by coarsening the surface. In topological insulators, however, the surface states are robust, and according to theory they should essentially persist—despite damaging the surface by chemical or mechanical means, altering its shape or orientation with respect to the crystal lattice, or even disordering the bulk—as long as such changes are applied in moderation. The conducting surface states can be destroyed only by changes that also destroy the insulating character of the bulk.

The above statements are subject to an important caveat: They apply exclusively to systems that respect time reversal symmetry (TRS)—that is, nonmagnetic topological insulators in zero external magnetic field. When TRS is broken, all bets are off, and even a weak magnetic perturbation can open up a gap in the spectrum of the topologically protected surface states. Chen *et al*. exploit this point to show that the gapless surface states of the pristine topological insulator Bi_2Se_3 become gapped upon introducing magnetic impurities (Mg and Fe) into the crystal.

Although this finding confirms one of the basic predictions of the theory underlying the physics of topological insulators, it also raises several new questions. Perhaps the most interesting concerns the nature of magnetism in Mg/Fe-doped Bi_2Se_3. It might be expected that gapping of the surface state would require a "uniform" breaking of TRS, whereby the magnetic moments of the dopant atoms all point in the same direction, with a component perpendicular to the surface. Whether such ordering occurs in the bulk (or on the surface only) is currently unknown, as is the mechanism behind this ordering.

Where does the exact quantization fit into this picture described above? According to theory (*4*–*6*), when the gap opens as the result of a magnetic perturbation, the resulting surface is no ordinary insulator; instead, it is a quantum Hall insulator, with properties similar to those of the familiar quantum Hall systems realized in 2DEGs. Its Hall conductance is predicted to be $(2n + 1)e^2/2h$, where n is an integer and $2n + 1$ corresponds to the (odd) number of gapless surface states in the underlying pristine topological insulator. In Bi_2Se_3 there is a single surface state ($n = 0$), and one thus expects $\sigma_{Hall} = e^2/2h$. The appearance of such a "fractional" value of quantized conductance (due to the factor of 2 in the denominator) in a weakly interacting system of electrons is itself very interesting, as is the fact that it should appear in the absence of an externally applied magnetic field. These two features set this effect apart from the conventional quantum Hall effects in 2DEGs and make it a likely new candidate for the list of solid-state systems exhibiting the phenomenon of exact quantization.

As yet, direct experimental measurement of the quantized surface Hall conductance in a topological insulator remains elusive. But once observed, aside from testing a fundamental physical paradigm, it will offer possibilities for future practical applications, such as the proposed dissipationless switching of magnetic moments that can be of use in the magnetic recording industry (*7*, *8*).

References

1. P. W. Anderson, *Science* **177**, 393 (1972).
2. R. B. Laughlin, *Rev. Mod. Phys.* **71**, 863 (1999).
3. Y. L. Chen *et al*., *Science* **329**, 659 (2010).
4. J. E. Moore, *Nature* **464**, 194 (2010).
5. X.-L. Qi, S.-C. Zhang, *Phys. Today* **63**, 33 (2010).
6. M. Z. Hasan, C. L. Kane, http://arxiv.org/abs/1002.3895 (2010).
7. T. Yokoyama, Y. Tanaka, N. Nagaosa, *Phys. Rev. B* **81**, 121401(R) (2010).
8. I. Garate, M. Franz, *Phys. Rev. Lett.* **104**, 146802 (2010).

10.1126/science.1194123

DEVELOPMENTAL BIOLOGY

Versatile Germline Genes

When do germ cells establish their separate, independent identity during animal development?

Celina Juliano[1] and Gary Wessel[2]

Animal germline cells ultimately produce eggs and sperm, providing an immortal link to the next generation. Establishing and maintaining the germline requires a conserved gene set (*1*), but traditionally classified "germline genes" may have a broader role in development than originally anticipated. Recent findings from less well-studied animal models suggest that in some taxa, germline genes appear to specify a multipotent cell lineage during embryogenesis, the fates of which include both somatic cells and the germ line.

During animal embryogenesis, the germ line is segregated from somatic cells (*2*), but this lineage dichotomy is not universal in animals. Studies exploring this segregation have primarily focused on organisms from two major animal groups, the vertebrates and the ecdysozoans, including the model organisms *Drosophila melanogaster* (fruit fly), *Caenorhabditis elegans* (roundworm), *Mus musculus* (mouse), *Danio rario* (zebrafish), *Xenopus laevis* (frog), and *Ambystoma mexicanum* (axolotl). In these animals, the germ line separates from the rest of the embryo prior to gastrulation, an early developmental stage in which cells organize into specific layers that will establish the animal's body plan. Thus, the development of these segregated cells in vivo is absolute and limited to a germ cell fate. In the fly, worm, zebrafish, and frog, the germ line is established autonomously by the inheritance of cytoplasm during cell division that contains specification factors, such as the RNA-binding proteins encoded by the genes *vasa*, *nanos*, and *piwi*. Alternatively, the mouse and axolotl segregate their germ line during embryogenesis through inductive cell-to-cell interactions, yet a highly similar gene set is involved.

However, in other animal taxa, germline segregation occurs after gastrulation. In these animals, long-term multipotent precursor cells are established during embryogenesis, from which the germ line separates after embryonic development is completed. For example, in the marine annelid *Platynereis dumerilii* (a lophotrochozoan), one of the embryonic cells (the 4d lineage) gives rise to proliferating cells that express *vasa*, *nanos*, and *piwi*. However, after embryogenesis is complete, these cells contribute both to the somatic mesodermal tissues of the developing adult segments and to the germ line (*3*). Similarly, in the snail *Ilyanassa* (a lophotrochozoan), the 4d lineage, which expresses *vasa* and *nanos*, gives rise to multipotent cells during embryogenesis that later contribute to the germ line and to mesoderm and endoderm of the adult (*4*, *5*). Furthermore, *nanos* is required to maintain

[1]Department of Cell Biology, Stem Cell Center, Yale University, New Haven, CT 06520, USA. [2]Department of Molecular Biology, Cell Biology, and Biochemistry, Brown University, Providence, RI 02912, USA. E-mail: gary_wessel@brown.edu

Downloaded from www.sciencemag.org on August 5, 2010

Published by AAAS

the fate of the snail 4d lineage; loss of *nanos* function results in a loss of all 4d-derived adult structures (*4*). Thus, similar to the marine annelid germ line, the snail germ line segregates from multipotent descendants after embryogenesis, and these multipotent cells likely depend on conserved "germline" genes such as *vasa*, *nanos*, and *piwi* for their establishment and maintenance.

The germ line of the echinoderm *Strongylocentrotus purpuratus* (sea urchin) also segregates from the soma well after embryogenesis. Sea urchin embryogenesis culminates in the formation of a swimming larva. At metamorphosis, a juvenile sea urchin emerges and larval tissues are destroyed. Cells of the small micromere lineage, which are specified at the 32-cell embryo stage, are multipotent but contribute only to adult tissues and not to the larva (*6*, *7*). This small micromere lineage expresses *vasa*, *nanos*, and *piwi*; loss of *nanos* function disrupts formation of the juvenile, and metamorphosis does not occur (*6*, *8*, *9*). Thus, similar to the snail and the marine annelid germ lines, the sea urchin germ line segregates after embryogenesis and arises from a long-term multipotent precursor cell that is established during embryogenesis through the functions of genes originally ascribed only to the germ line.

Many adult flatworms, cnidarians, and sponges contain multipotent or totipotent stem cells that give rise to various adult cell types, including the germ line. These animals continually segregate germ line from stem cells throughout adulthood. The lophotrochozoan flatworms, such as planarians, contain totipotent cells (neoblasts) that express *piwi*, *vasa*, *tudor*, and *pumilio*, and give rise to all tissue types. These genes are required for neoblast function, but were first identified as germline genes in *Drosophila* (*10*). Several members of the phylum Cnidaria, the sister group to the Bilateria, contain adult multipotent stem cells (I-cells) that give rise to both somatic cells and germ cells. In adult *Hydra*, for example, I-cells selectively express *vasa* and *nanos*, but their functions are not yet known (*11*, *12*). Similar to the cnidarians, members of the phylum Porifera (sponges) are non-Bilateria and segregate their germ line continuously from adult stem cells. Adult sponges contain a totipotent stem cell (the archeocyte) that gives rise to somatic cells and to germ cells. *Piwi* is selectively expressed in the archeocytes of the sponge *Ephydatia fluviatilis*, suggesting the presence of a conserved gene program in the cnidarian, echinoderm, and lophotrochozoan multipotent germline precursors (*13*).

The timing of germline segregation in animals appears to occur along a continuum, with onset at embryogenesis and continuously throughout adulthood at the extremes (see the figure). In all cases, germline segregation requires that a population of cells, either multipotent or germline limited, be established in the embryo. Given that germline segregation from a multipotent precursor occurs after embryogenesis in the lophotrochozoans, echinoderms, cnidarians, and sponges, it is parsimonious to conclude that it is the ancestral mechanism of establishing a germline. This would predict that embryonic germline segregation evolved independently in vertebrates and ecdysozoans. It may be that the germline molecular program, which includes genes such as *vasa*, *nanos*, and *piwi*, originated in multipotent cells, and was subsequently coopted by more specialized, embryonic germ cells. However, it will be necessary to collect more functional data from animals spanning diverse taxa to reveal the most ancient and essential portions of such a multipotency molecular program.

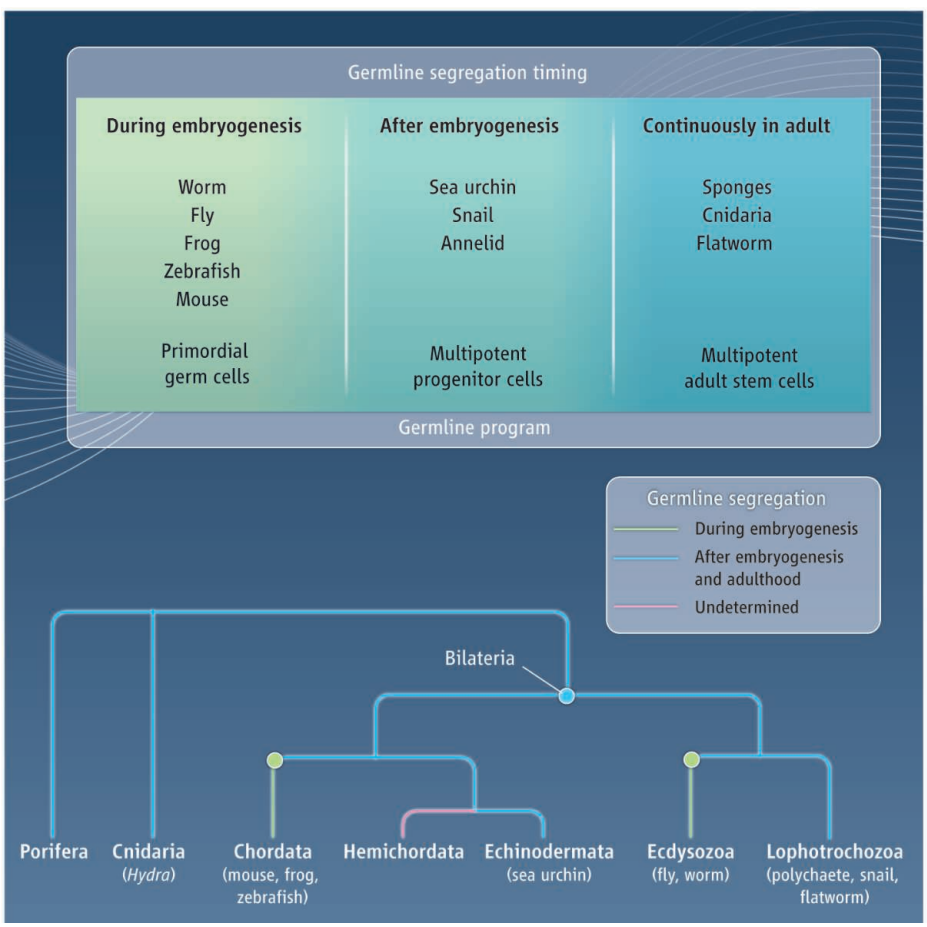

CREDIT: Y. GREENMAN/SCIENCE

Germline segregation in animals. (**Top**) The timing of germline segregation from somatic cells varies, from early embryogenesis to continuously in the adult. The same underlying molecular program may operate in all cases. In segregation during embryogenesis, primordial germ cells migrate to the somatic gonad to give rise to germ cells. In segregation after embryogenesis, a long-term multipotent precursor is established in the embryo from which the germline segregates during larval development or adulthood. (**Bottom**) If germline segregation that occurs after embryogenesis (blue line) is the ancestral mechanism, then embryonic germline segregation (green line) must have evolved independently in vertebrates and ecdysozoans.

Downloaded from www.sciencemag.org on August 5, 2010

References

1. B. Ewen-Campen, E. E. Schwager, C. G. Extavour, *Mol. Reprod. Dev.* **77**, 3 (2010).
2. E. E. Saffman, P. Lasko, *Cell. Mol. Life Sci.* **55**, 1141 (1999).
3. N. Rebscher, F. Zelada-González, T. U. Banisch, F. Raible, D. Arendt, *Dev. Biol.* **306**, 599 (2007).
4. J. S. Rabinowitz, X. Y. Chan, E. P. Kingsley, Y. Duan, J. D. Lambert, *Curr. Biol.* **18**, 331 (2008).
5. S. Z. Swartz, X. Y. Chan, J. D. Lambert, *Dev. Genes Evol.* **218**, 107 (2008).
6. C. E. Juliano, M. Yajima, G. M. Wessel, *Dev. Biol.* **337**, 220 (2010).
7. S. Tanaka, K. Dan, *Dev. Growth Differ.* **32**, 145 (1990).
8. C. E. Juliano *et al.*, *Dev. Biol.* **300**, 406 (2006).
9. E. Voronina *et al.*, *Dev. Biol.* **314**, 276 (2008).
10. N. Shibata, L. Rouhana, K. Agata, *Dev. Growth Differ.* **52**, 27 (2010).
11. K. Mochizuki, C. Nishimiya-Fujisawa, T. Fujisawa, *Dev. Genes Evol.* **211**, 299 (2001).
12. K. Mochizuki, H. Sano, S. Kobayashi, C. Nishimiya-Fujisawa, T. Fujisawa, *Dev. Genes Evol.* **210**, 591 (2000).
13. N. Funayama, *Dev. Growth Differ.* **52**, 1 (2010).

10.1126/science.1194037

Published by AAAS

Vanadium Nitrogenase Reduces CO

Chi Chung Lee, Yilin Hu,* Markus W. Ribbe*

The Haber-Bosch (HB) and Fischer-Tropsch (FT) syntheses are important industrial processes for fertilizer and fuel production: The former converts a mixture of dinitrogen (N_2) and hydrogen (H_2) gases into ammonia (NH_3), whereas the latter converts a mixture of carbon monoxide (CO) and H_2 gases into liquid hydrocarbons. Both reactions involve the hydrogenation of isoelectronic small molecules on late transition metal catalysts under high temperature and pressure (*1*, *2*). Yet despite these common traits, the two processes are rarely compared because of the clear distinction between their respective products. Here, we report an unanticipated link between these two formal reactions through a natural source, the vanadium nitrogenase of *Azotobacter vinelandii*.

Like the *nif*-encoded molybdenum nitrogenase, the *vnf*-encoded V nitrogenase is composed of a specific reductant and a catalytic component (*3*). Both nitrogenases use a catalytic mechanism that involves adenosine triphosphate (ATP)–dependent electron transfer from a reductant (i.e., *nifH*- or *vnfH*-encoded Fe protein) to the catalytic component (i.e., *nifDK*-encoded MoFe protein or *vnfDGK*-encoded VFe protein) and the reduction of N_2 at the cofactor site (i.e., FeMoco or FeVco) of the latter. Unlike the HB process, the nitrogenase-based NH_3 synthesis involves addition of separated protons and electrons (rather than intact H_2) across the N_2 triple bond, and H_2 is liberated as a side product (*4*, *5*). In the absence of N_2, H_2 is the sole electron-accepting product of nitrogenase catalysis. Such H_2 evolution by Mo nitrogenase is unaffected by CO, yet the activity of H_2 evolution by V nitrogenase is reduced by an average of 35% in the presence of 100% CO (fig. S1).

We observed that the rates of ATP hydrolysis by Mo and V nitrogenases were comparable under CO, which reflected a similar flux of electrons through the two nitrogenases (fig. S1). One question naturally follows: Could the diminished H_2 evolution by V nitrogenase originate from the diversion of electrons toward CO reduction?

Indeed, we detected ethylene (C_2H_4), ethane (C_2H_6), and propane (C_3H_8) by gas chromatography–mass spectrometry (GC-MS) analysis of the reaction catalyzed by V nitrogenase under 100% CO (Fig. 1, red) (*6*). In contrast, no alkane or alkene formation was observed in the reaction catalyzed by Mo nitrogenase (Fig. 1, black). Isotopic labeling confirmed CO as the carbon source in these products by showing mass shifts of 2, 2, and 3, respectively, of C_2H_4, C_2H_6, and C_3H_8 upon substitution of ^{12}CO with ^{13}CO (Fig. 1).

Like the concomitant evolution of H_2, the reduction of CO required the presence of both component proteins of V nitrogenase, the hydrolysis of ATP, and dithionite as an in vitro electron source (fig. S2). Furthermore, CO reduction by V nitrogenase was inhibited by the addition of increasing amounts of H_2, a well-established inhibitor for N_2 reduction by nitrogenase (fig. S3). The latter observation implies that the reaction mechanism likely involves proton (and electron) transfer to CO rather than direct hydrogenation of CO, in a similar manner to the native N_2 reduction.

The ability of V nitrogenase to catalyze both CO and N_2 reductions suggests a potential link between the evolution of carbon and nitrogen cycles. It has been shown that abiotic substances, such as minerals on submarine vents and nebular dust, are capable of catalyzing FT- and HB-type reactions under extreme conditions (*7*). Perhaps this dual catalytic capacity was assimilated by ancient microbes through a primitive form of nitrogenase (*8*), which evolved solely toward nitrogen fixation following the rise of photosynthesis for carbon fixation.

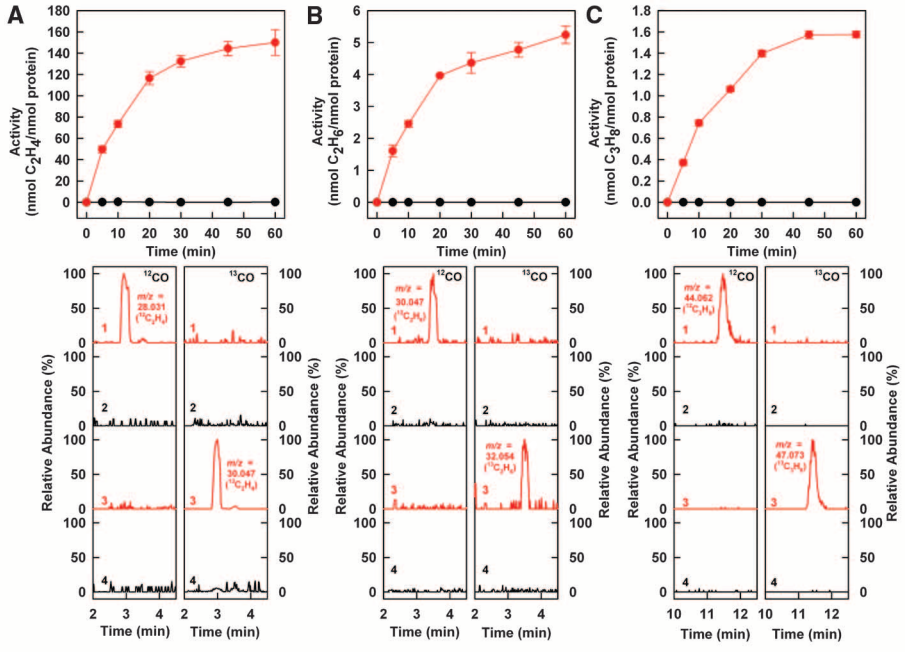

Fig. 1. CO-reducing activity of V nitrogenase. (Top) Time courses of C_2H_4 (**A**), C_2H_6 (**B**), and C_3H_8 (**C**) formation by V (red) and Mo (black) nitrogenases in the presence of 100% CO [data are presented as mean ± SD (N = 5)]. (Bottom) GC-MS analyses of C_2H_4 (A), C_2H_6 (B), and C_3H_8 (C) formed by V and Mo nitrogenases in the presence of 100% CO. The products were analyzed with ^{12}CO or ^{13}CO as the substrate and traced at the following mass-to-charge ratios (*m/z*): (A) 1 and 2, 28.031; 3 and 4, 30.047; (B) 1 and 2, 30.047; 3 and 4, 32.054; (C) 1 and 2, 44.062; 3 and 4, 47.073.

References and Notes

1. C. K. Rofer-DePoorter, *Chem. Rev.* **81**, 447 (1981).
2. R. Schlögl, *Angew. Chem. Int. Ed. Engl.* **42**, 2004 (2003).
3. R. L. Robson *et al.*, *Nature* **322**, 388 (1986).
4. B. K. Burgess, D. J. Lowe, *Chem. Rev.* **96**, 2983 (1996).
5. Alternative substrates of Mo nitrogenase include alkynes, cyanides, nitriles, and nitrogen oxides, whereas alternative substrates of V nitrogenase have not been studied extensively (*4*).
6. Materials and methods are detailed in supporting material on *Science* Online.
7. H. G. M. Hill, J. A. Nuth, *Astrobiology* **3**, 291 (2003).
8. V nitrogenase is likely more ancient than Mo nitrogenase (*9*), which may explain why V nitrogenase retains the CO-reducing ability.
9. A. D. Anbar, A. H. Knoll, *Science* **297**, 1137 (2002).
10. We thank D. C. Rees of Caltech (Pasadena) for help on the GC-MS analysis. This work was supported by Herman Frasch Foundation grant 617-HF07 (M.W.R.) and NIH grant GM-67626 (M.W.R.).

Supporting Online Material

www.sciencemag.org/cgi/content/full/329/5992/642/DC1
Materials and Methods
Figs. S1 to S3
References

26 April 2010; accepted 17 June 2010
10.1126/science.1191455

Department of Molecular Biology and Biochemistry, University of California, Irvine, CA 92697–3900, USA.

*To whom correspondence should be addressed. E-mail: yilinh@uci.edu (Y.H.); mribbe@uci.edu (M.W.R.)

Downloaded from www.sciencemag.org on August 5, 2010

High-Resolution Analysis of Parent-of-Origin Allelic Expression in the Mouse Brain

Christopher Gregg,[1,2]*† Jiangwen Zhang,[3]* Brandon Weissbourd,[1,2] Shujun Luo,[5] Gary P. Schroth,[5] David Haig,[4] Catherine Dulac[1,2]†

Genomic imprinting results in preferential expression of the paternal or maternal allele of certain genes. We have performed a genome-wide characterization of imprinting in the mouse embryonic and adult brain. This approach uncovered parent-of-origin allelic effects of more than 1300 loci. We identified parental bias in the expression of individual genes and of specific transcript isoforms, with differences between brain regions. Many imprinted genes are expressed in neural systems associated with feeding and motivated behaviors, and parental biases preferentially target genetic pathways governing metabolism and cell adhesion. We observed a preferential maternal contribution to gene expression in the developing brain and a major paternal contribution in the adult brain. Thus, parental expression bias emerges as a major mode of epigenetic regulation in the brain.

Parent-of-origin effects influence gene expression and trait inheritance in offspring. Genomic imprinting is a form of epigenetic regulation that results in the preferential expression of the paternally or maternally inherited allele of certain genes (*1*). Currently, fewer than 100 imprinted genes have been identified, and the evolutionary pressures that underlie imprinting are debated (*2*, *3*). Clinical and experimental data suggest roles for imprinting in regulating brain development and function (*4*). In humans, Prader-Willi syndrome (PWS) and Angelman syndrome (AS) result from a deletion of the paternal or maternal copy of 15q11-q13, respectively. PWS is associated with hyperphagia, stubbornness, and compulsive traits (*5*), whereas AS is associated with absent speech, happy affect, and inappropriate laughter (*6*). Further, studies of parthenogenetic (PG) and androgenetic (AG) chimeras in the mouse have suggested preferential maternal contribution to the development of the cortex, but preferential paternal contribution to the hypothalamus (*7*, *8*). Such biased roles have yet to be clearly demonstrated. Moreover, despite tantalizing reports, our understanding of the neural systems governed by imprinted genes and of the scope and features of imprinted loci expressed in the brain is very limited.

Imprinting refers to functional differences between the maternal and paternal chromosomes or alleles (*9*) and is also used more strictly to define complete allele-specific silencing (*10*). Known imprinted genes have been shown to display all-or-none and biased allelic expression according to the gene and tissue considered (*11*, *12*). We report here a genome-wide analysis of parental allelic effects involving complete silencing or parental biases in gene expression in the murine embryonic day 15 (E15) brain, and in the adult male and female cortex [medial prefrontal cortex (mPFC)] and hypothalamus [preoptic area (POA)]. Together with a companion study (*13*), our data suggest that substantial maternal and paternal biases in gene expression originate from the X chromosomes and autosomes, respectively. These results may shed light on gene regulatory processes underlying brain function, evolution, and disease.

Imprinted gene expression in the adult CNS. To gain insight into neural systems affected by imprinting, we performed an in silico study of the expression pattern of known imprinted genes in the adult brain (*14*). The expression pattern of 45 known imprinted genes was investigated across 118 distinct adult brain regions in the Allen Brain Atlas (Fig. 1 and fig. S1). A heat map based on the relative number of known imprinted genes expressed in a given brain region identified 26 out of 118 brain regions as hotspots for the expression of imprinted genes, whereas the expression hotspots of 20 randomly selected control genes with known biallelic expression were located mainly in cortical and olfactory regions and appeared entirely distinct from that of imprinted genes (Fig. 1 and fig. S1). Brain regions predicted from earlier studies to be enriched for imprinted gene expression indeed emerged as hotspots, such as the medial preoptic area (MPOA), which regulates mating, maternal behavior, and thermoregulation (*15*). From our data, aminergic systems and neural systems associated with feeding and motivated behaviors constituted the largest source of imprinting hotspots. These included the arcuate nucleus, dorsal raphe, substantia nigra pars compacta, ventral tegmental area, dorsal hypothalamic area, locus ceruleus, and nucleus accumbens (*16*, *17*). These findings enticed us to perform a more detailed and large-scale analysis to characterize and compare parent-of-origin effects governing gene expression in distinct brain regions.

A high-resolution approach to analyze imprinting. We used Illumina RNA-sequencing (RNA-Seq) technology to characterize the transcriptome of brain tissues from F_1 hybrids resulting from reciprocal crosses of CAST/EiJ (CAST) and C57BL/6J (C57) mice [F_1 initial cross (F_1i): CAST mother × C57 father; F_1 reciprocal cross (F_1r): C57 mother × CAST father]. Single-nucleotide polymorphisms (SNPs) were identified by separately sequencing the CAST and C57 transcriptomes of the original parents (or parental strains for the E15 brains), and the subsequent base calls were used to distinguish transcription from maternal and paternal alleles in F_1i and F_1r [table S1 and figs. S2 and S3 and supporting online material (SOM) (*14*)]. We characterized parent-of-origin effects governing gene expression in the E15 brain, as well as the adult male and female mPFC and POA. For the current study, male and female samples were treated as biological replicates. This approach is appropriate for the detection of parental effects that are independent of the sex of the offspring.

Imprinting was assessed by chi-square tests in both initial and reciprocal crosses as described in the SOM. The total number of SNP sites exhibiting a significant parent-of-origin effect was determined for a range of chi-square *P*-value cutoffs (0.001 to 0.2) and compared with the number expected by chance (Fig. 2A). We selected a cutoff of $P < 0.05$ for each cross [E15 false-discovery rate (FDR) = 0.06, POA FDR = 0.1, mPFC FDR = 0.1]. Our approach yields highly accurate and reproducible results, as demonstrated by multiple controls detailed in the SOM (*14*). Scatter plots of the –log (*P*) for the F_1i and F_1r data for each SNP site clearly indicated exclusive selection of paternally and maternally expressed loci relative to the total data set (Fig. 2B and fig. S4). Overall, SNPs identified by our approach (excluding mitochondrial and X-chromosome SNP sites) exhibited a robust parental expression bias with a mean of 87 ± 15% (mean ± SD). Parent-specific biases emerged as a continuum from the data set, which suggested that imprinting may manifest as relative allele-specific expression bias, rather than strict monoallelic transcription, or that allelic bias is cell-type specific and is partially masked by cellular heterogeneity in

[1]Department of Molecular and Cellular Biology, Harvard University, Cambridge, MA 02138, USA. [2]Howard Hughes Medical Institute, Harvard University, Cambridge, MA 02138, USA. [3]FAS Research Computing, Harvard University, Cambridge, MA 02138, USA. [4]Department of Organismic and Evolutionary Biology, Harvard University, Cambridge, MA 02138, USA. [5]Illumina, Inc., Hayward, CA 94545, USA.

*These authors contributed equally to this study.
†To whom correspondence should be addressed. E-mail: dulac@fas.harvard.edu (C.D.); cgregg@mcb.harvard.edu (C.G.)

Downloaded from www.sciencemag.org on August 5, 2010

brain samples (Fig. 2B and fig. S4). As our approach includes sequencing of transcriptomes from parents and hybrid offspring, as well as increased sequence depth, this likely contributes to differences in results between our study and previous studies (*18*, *19*).

Genome-wide analysis of imprinting. Imprinted genes and genes with imprinted features were identified by the presence of one or more SNP sites exhibiting a significant paternal or maternal expression bias, as described above. This approach enabled us to identify 1308 candidate imprinted loci, among which were 824 genes annotated in the University of California Santa Cruz genome database (UCSC) (5.7% of the ~14,520 genes assessed) (Fig. 2C and table S2) and 484 putative noncoding RNAs (ncRNAs) annotated in the functional RNA database (fRNAdb) (4.1% of the 11,545 ncRNAs assessed) (Fig. 2C and table S3). Of these, 604 have known human orthologs. Of the 86 previously known imprinted genes, 72 were expressed in one or more brain regions and contained SNPs above the 10-read minimum cutoff. Among those, 47 were called imprinted, whereas the remaining 25 exhibited biallelic expression in all brain regions tested. Of the 484 ncRNAs associated with parental allelic effects on the basis of alignments to the fRNAdb, we classified 82 as "known" based on genomic positions directly or closely associated with previously known imprinted ncRNAs, including *Apeg3*, *Copg2as*, *Air*, *Nespas*, *H19*, *Peg12*, *Snurf/Snrpn/Ube3aas*, *Gtl2*, and *Rian* (*20*).

A gene ontology analysis revealed that biological processes associated with parental allelic effects are mostly related to metabolic processes in the developing brain (e.g., primary metabolic process, FDR = 4.11E-14), and to cell adhesion in the adult brain (e.g., cell adhesion, FDR = 1.45E-8) (table S4). These findings are striking in light of previous work that identified roles for imprinted genes in growth, feeding, metabolism, and thermoregulation (*2*). We report here and in our companion study (*13*) parental allelic effects at key conserved regulators of metabolism, such as interleukin-18 (*Il18*) (*13*) and the mitochondrial ribosomal protein *Mrpl48* (*21*), as well as cell adhesion, such as cadherin 15 (*cdh15*).

Characterization of gene clusters with parent-of-origin allelic effects. Analysis of the genomic

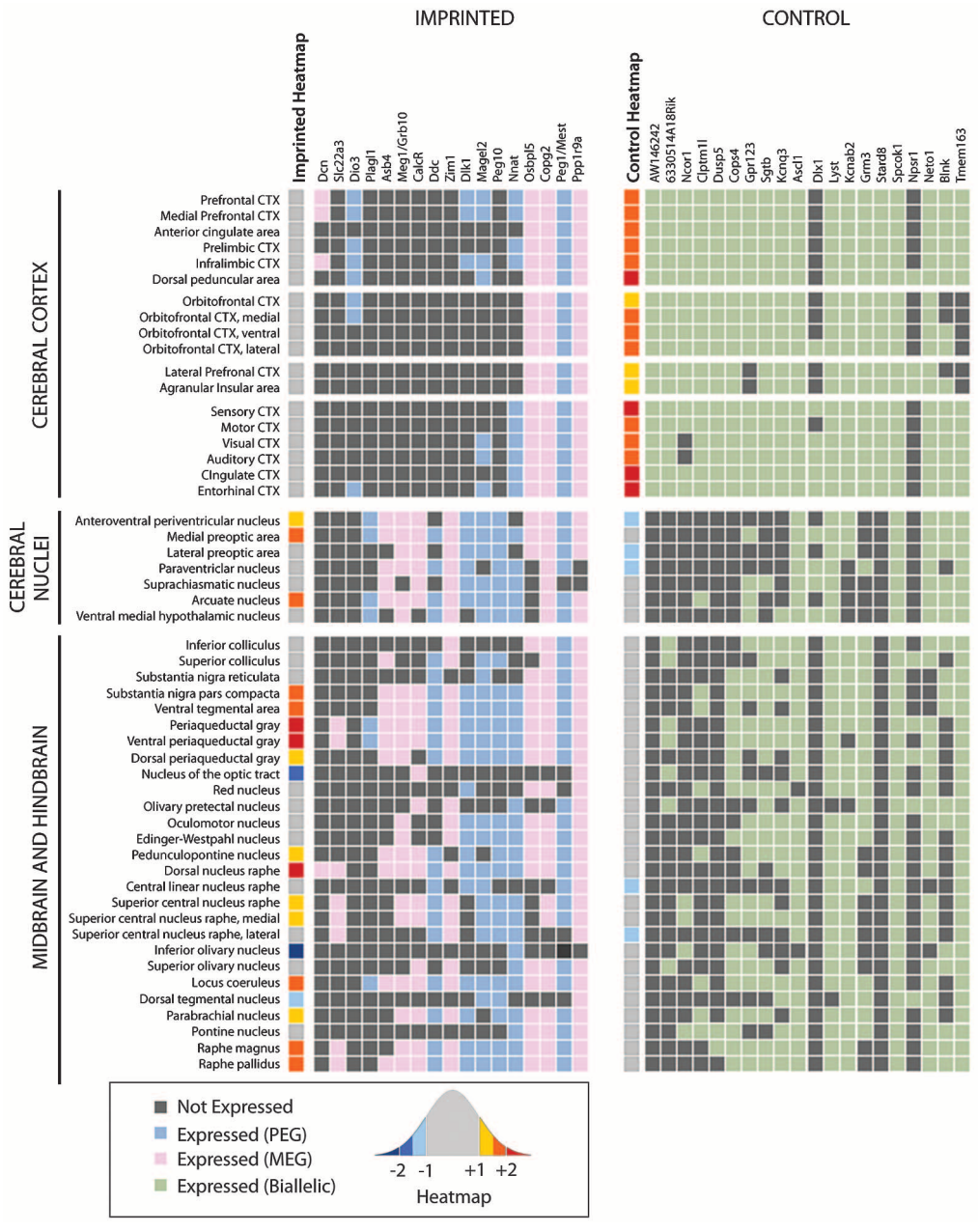

Fig. 1. A map of imprinted gene expression in the adult CNS identifies distinctive hot- and coldspots. Presence (colored squares) versus absence (dark gray squares) of imprinted gene expression was mapped in a representative subset of brain regions (full map in fig. S1). Randomly selected biallelic control genes are indicated by green squares. The heat map was assigned for each brain region according to the number of standard deviations from the mean for the number of imprinted genes expressed [cooler to warmer (standard deviations): <–2, <–1.5, <–1, >+1, >+1.5, >+2].

Downloaded from www.sciencemag.org on August 5, 2010

distribution of all loci identified in our study shows a scattered distribution across all chromosomes (fig. S5). An algorithm was applied that searched for >2 imprinted genes and/or ncRNAs residing within a 1-Mb window. This window size correctly identified previously characterized imprinted gene clusters (e.g., *H19-IGF2*, *Mest-Copg2*, and *Dlk1-Gtl2*), with the exception of the 4-Mb-long PWS-AS cluster that splits into two clusters (table S5). This analysis identified 204 putative imprinted gene clusters, which encompass 65% of the genes and ncRNAs identified in our study. The presence of imprinted ncRNAs has been demonstrated to play a critical role in the regulation of imprinting for many known imprinted gene clusters (*1*), and 106 (52%) of these candidate clusters contained both coding and putative noncoding loci (table S5). For a summary of data for known imprinted gene clusters, see fig. S6.

Our approach identified features in imprinted gene clusters known to be associated with brain functions and disorders. For example, *Peg13* and *Kcnk9* [linked to Birk-Barel mental retardation (*22*)] were found to be part of a larger cluster that includes *1810044A24Rik* [also called *Trappc9* and linked to mental retardation (*23*)], several maternally expressed ncRNAs, and a maternally expressed gene (MEG), *Eif2c2* (*argonaute2*) (Fig. 3, A and B). From our data, it appears that *1810044A24Rik* undergoes isoform-specific imprinting, which is revealed by SNPs within the unique exon and 3′ untranslated region (3′UTR) of the uc007wbn.1 isoform, that are all paternally expressed. SNPs located in the exons shared by all other isoforms (uc007wbp.1, uc007wbm.1, and uc007wbl.1) are maternally expressed.

In the PWS-AS cluster, we uncovered a large region between *Snrpn* and *Ndn* that hosts numerous paternally expressed imprinted ncRNAs, including two predicted microRNAs (mir-344 and mir-344-2) (Fig. 3C). Sequenom DNA analysis of allele-specific expression with an independent cohort of animals replicated the Illumina RNA-Seq results and clearly revealed strict paternal expression of the *DOKist4* gene within this region (Fig. 3D).

Brain region– and developmental stage–specific parent-of-origin allelic effects. A total of 553 UCSC genes associated with parental allelic effects were uncovered in the E15 brain, compared with 256 in the adult POA ($P < 0.001$; χ^2 analysis) and 153 in the adult mPFC ($P < 0.0001$; χ^2 analysis) (Fig. 4, A and B). Sixty-one percent of genes identified in the E15 brain were MEGs, which revealed a significant maternal bias in the developing brain [paternally expressed genes (PEGs), 215; MEGs, 338; $P < 0.0001$; χ^2 analysis) (Fig. 4A). In contrast, a paternal bias was observed in both the adult POA (PEGs, 172; MEGs, 84; $P < 0.0001$; χ^2 analysis) and the adult mPFC (PEGs, 109; MEGs, 44; $P < 0.0001$; χ^2 analysis), such that ~70% of genes identified in the adult brain were PEGs. The observed parental allelic biases were statistically significant through a range of different *P*-value cutoffs ($P < 0.03$, $P < 0.05$, and $P < 0.1$) that increased the total number of genes by more than threefold, which indicated a robust signal-to-noise ratio in the data. The biases were not present at higher *P*-value cutoffs ($P < 0.9$).

Of the 824 UCSC annotated genes associated with parental allelic effects in the E15 brain, POA, or mPFC, 769 (93%) were expressed and had SNP site read depths above the cutoff of 10 in all of the three target brain tissues. However, most demonstrated a significant parental expression bias in only one of the target tissues (Fig. 4B). A majority was found exclusively in the E15 brain, including 73% of all MEGs. Further, only five PEGs were shared between the adult POA and mPFC, and 74% of the genes imprinted in all three samples were PEGs. These results suggest that parental influence over gene expression is highly spatially and temporally regulated in the brain.

Two examples of this phenomenon are detailed here and in the SOM (figs. S7 and S8). The *Igf2-H19* locus has been linked to colorectal and other forms of cancers (*24*), Beckwith-Wiedemann syndrome (BWS) (*24*), and Silver-Russell syndrome (*25*). *H19* is a maternally expressed ncRNA (*26*), and *Igf2* is a canonical PEG that promotes placental and embryonic growth (*2*). In endodermal and mesodermal cell lineages, the reciprocal parental expression of the two genes is due to a competition for promoter access to a shared set of enhancers located downstream of *H19* (*27*, *28*). Maternal *H19* expression is directly involved in regulating the paternal expression of *Igf2* (*29*). Previous studies have suggested that imprinting at this locus is more complex in the brain (*29*–*31*).

Our data document maternal expression of *H19* and paternal bias of *Igf2* in the E15 brain (Fig. 4, C and D). *H19* is not expressed in the adult mPFC or POA, and 80% of *Igf2* transcription in the adult male and female POA and mPFC originates from the maternal allele (Fig. 4, C and D). These data were confirmed by Sequenom DNA analysis on a distinct cohort of animals (Fig. 4D). Similarly, a gene cluster encompassing *Grb10* and dopa (3,4-dihydroxyphenylalanine) decarboxylase (*Ddc*) displays spatiotemporally regulated parental allelic effects (figs. S7 and S8).

These examples, and the reproducibility of the parental allelic biases in independent male, female samples, and by Sequenom DNA analysis, highlight the extraordinary complexity of parental influence over transcription in the CNS.

Complex parent-of-origin allelic effects in the brain. Three general categories of genes with parent-of-origin expression bias emerged from our analysis in known loci, as well as newly identified loci, which we term consensus, complex, and single SNP loci (Fig. 5A and tables S6 to S12). Consensus loci have multiple SNPs, at

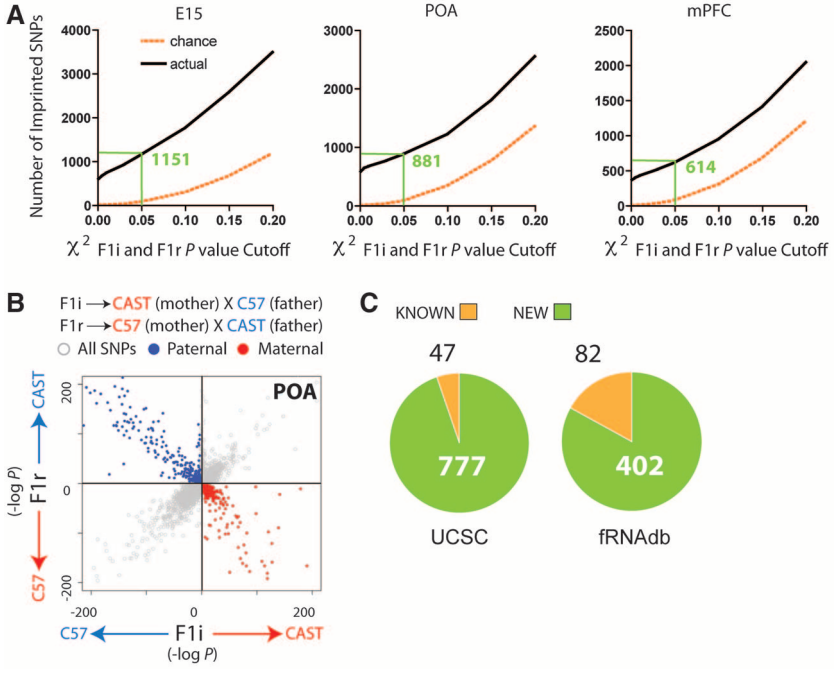

Fig. 2. Identification of loci exhibiting parent-of-origin allelic effects in the embryonic and adult CNS using Illumina RNA-Seq. (**A**) Plots of the number of SNP sites exhibiting parental expression bias identified by sequencing (black) compared to chance expectations (orange) at various chi-square *P*-value cutoffs. Green values indicate number of imprinted SNPs detected at $P < 0.05$. (**B**) Scatter plot of the –log (*P*) of the two-tailed chi-square probability (*P*) for individual SNP sites for the F_1i versus the F_1r cross (POA shown). SNP sites identified by $P < 0.05$ cutoff in each cross are indicated by red and blue dots. (**C**) Numbers of known and uncovered genes associated with parental allelic effects.

Downloaded from www.sciencemag.org on August 5, 2010

least one SNP site above the *P*-value cutoff of 0.05 in each cross, and 100% of SNPs agree with the direction of the parental expression bias in both the F_1i and F_1r cross. Complex loci have multiple SNPs, with one or more SNPs above the *P*-value cutoff and one or more SNP sites that differ (i.e., biallelic expression, strain, or opposite parental bias). Finally, a subset of genes had a single SNP site or multiple SNPs within 32 base pairs of each other (the size of a single read). Thirty-five of the 47 previously known imprinted genes displayed consensus imprinting in at least one brain region (table S6). However, several of these same genes also exhibited complex imprinting in other samples, such that 41 known imprinted genes were identified as complex in one or more brain regions. Seven known imprinted genes were identified on the basis of a single SNP site (Fig. 5A). Detailed analysis of the positions of SNPs with parental allelic bias within complex loci revealed genes in which monoallelic SNPs are confined to a specific exon (195 genes), to the 3′UTR (final exon) (57 genes), or to both a specific exon and the 3′UTR region (39 genes) (Fig. 5B), which suggests that, in these genes, the parental allelic effect is restricted to only one or a few transcript isoforms. In a subset of these cases, the same parental bias is confirmed by multiple SNPs in the exon or 3′UTR (Fig. 5B). A large proportion of the genes exhibited parental effects in the last exon (including 3′UTR region), but involved disagreements between SNP sites in the same region of the gene [classified as "other" (560 genes)]. In some cases, as detailed below, these disagreements appear to be related to the fact that only a subset of the SNPs for a given complex gene are able to distinguish a specific imprinted isoform from other overlapping transcripts arising from the same locus.

Cadherin 15 (*cdh15*), a gene prospectively linked to intellectual disability in humans (*32*), emerges as a consensus imprinted locus, in which

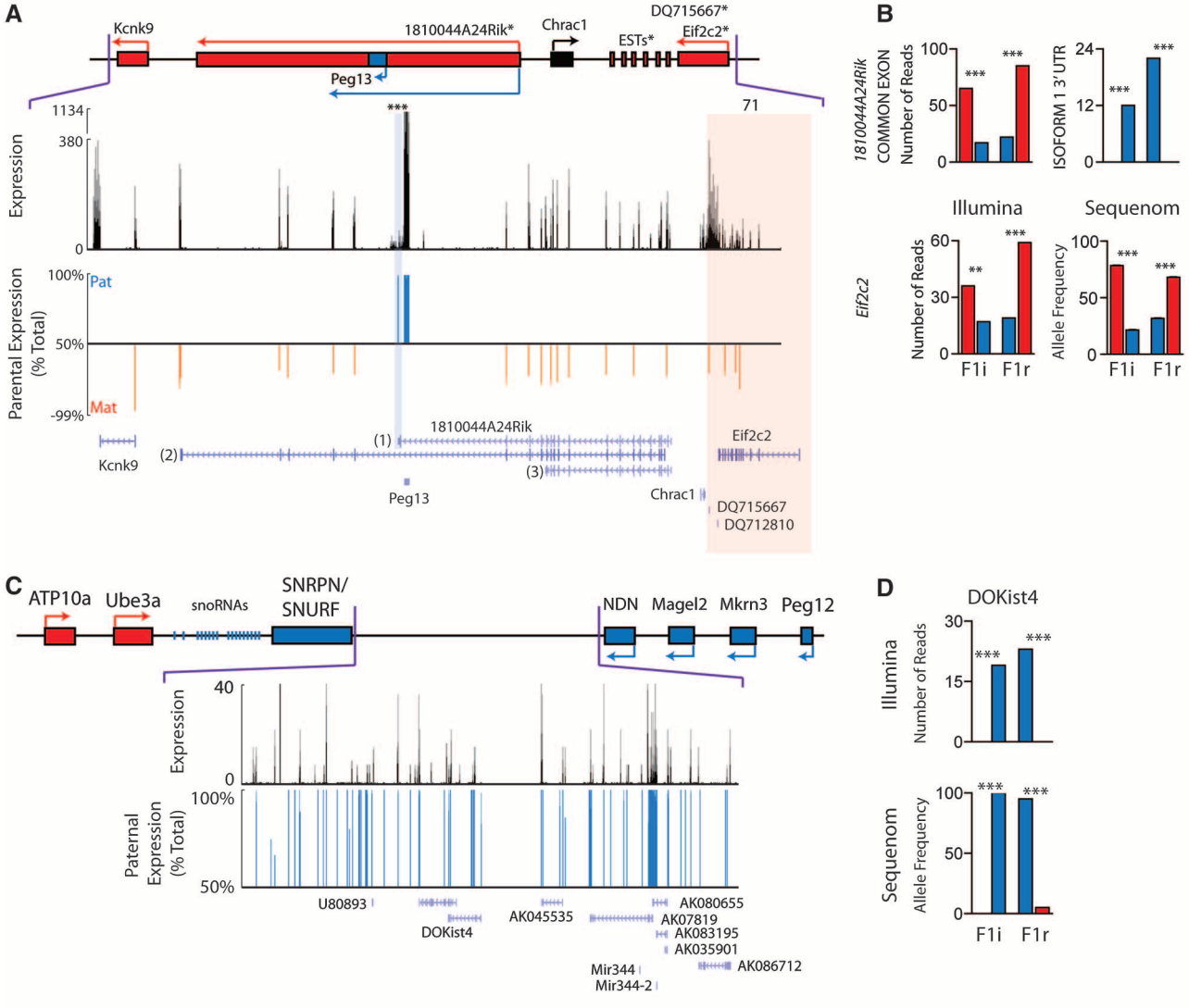

Fig. 3. Features of imprinted gene clusters associated with neurological disorders and diseases. (**A**) UCSC browser tracks indicate all reads aligning uniquely to the genome (expression, black) and the percentage of transcriptome aligned reads at SNP sites that were assigned to the paternal (blue, positive) versus maternal allele (red, negative). Analysis of *1810044A24Rik* isoforms [(1) uc007wbn.1, (2) uc007wbl.1 (uc007wbm.1 not shown), and (3) uc007wbp.1] revealed mixed isoform-specific imprinting at this locus. A paternally expressed isoform (uc007wbn.1) was identified by SNPs located in the unique 3′ exon and UTR. (**B**) Parental bias for SNP sites located in a *1810044A24Rik* shared exon (SNP_ID: uc007wbl.1_1339), the 3′UTR of the uc007wbn.1 isoform (SNP_ID: uc007wbn.1_4207), and *Eif2c2* (SNP_ID: uc007wbu.1_1944). Sequenom DNA analysis validated maternal expression of *Eif2c2* (E15 brain). Highlighted regions in browser tracks (A) red, *Eif2c2*; blue, *1810044A24Rik*) indicate regions detailed in bar graphs. (***P<0.001 and **P< 0.01; χ^2 analysis). (**C**) A large region of paternally biased transcription was uncovered in the PWS-AS gene cluster between the *SNRPN/SNURF* locus and *Ndn*. (**D**) Sequenom validation of paternally biased expression by DOKist4 in the PWS-AS cluster (SNP_ID: uc009hex.1_3057).

Downloaded from www.sciencemag.org on August 5, 2010

all three SNPs display preferential expression of the paternal allele in independent male and female samples (Fig. 5C) and by Sequenom DNA analysis on an independent cohort of animals (Fig. 5C). Other notable consensus imprinted genes include *Bcl2l1*, a major regulator of apoptosis linked to cancer (*33*), and *Eif2c2* (also called *argonaute2*), involved in microRNA and short-interfering RNA (siRNA)–mediated gene silencing (*34*) (table S6).

Detailed analysis of complex loci revealed remarkable and so far unsuspected features of

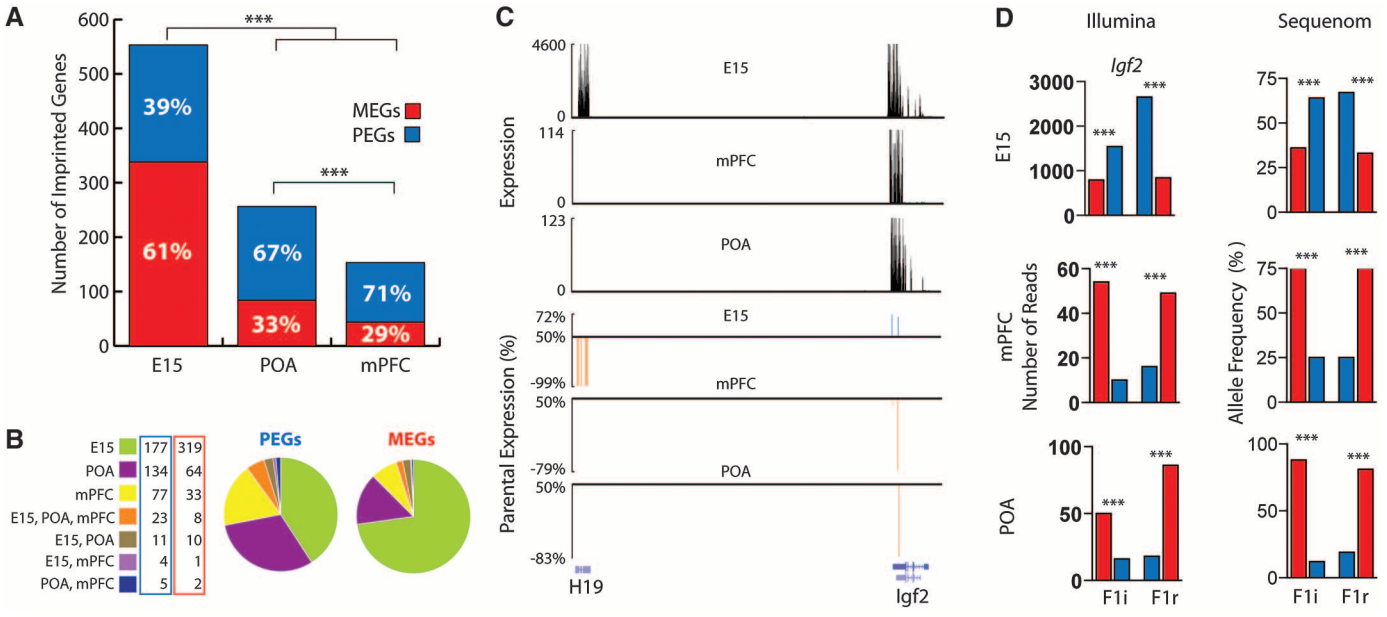

Fig. 4. Parent-of-origin allelic effects influence gene expression in a developmental and region specific manner in the CNS. (**A**) Comparison of the total numbers of UCSC annotated genes with parent-of-origin allelic effects in the E15 brain, adult POA, and mPFC. Red and blue bars indicate MEGs and PEGs identified in each sample, respectively. (**B**) Proportion of PEGs and MEGs identified in the E15 brain, mPFC, and POA. (**C**) Spatiotemporal regulation of imprinting at the *H19-Igf2* locus revealed by UCSC Browser tracks of raw expression data (black) and parental expression bias (blue, paternal; red, maternal) at identified SNP sites in *H19* and *Igf2*. (**D**) Igf2 allele-specific expression inversion confirmed by Illumina RNA and Sequenom DNA analyses (SNP_ID: uc009kod.1_2313). Raw expression tracks of reads uniquely aligning to the genome are shown below in black. (***P<0.001; **P< 0.01; *P< 0.05; χ^2 analysis).

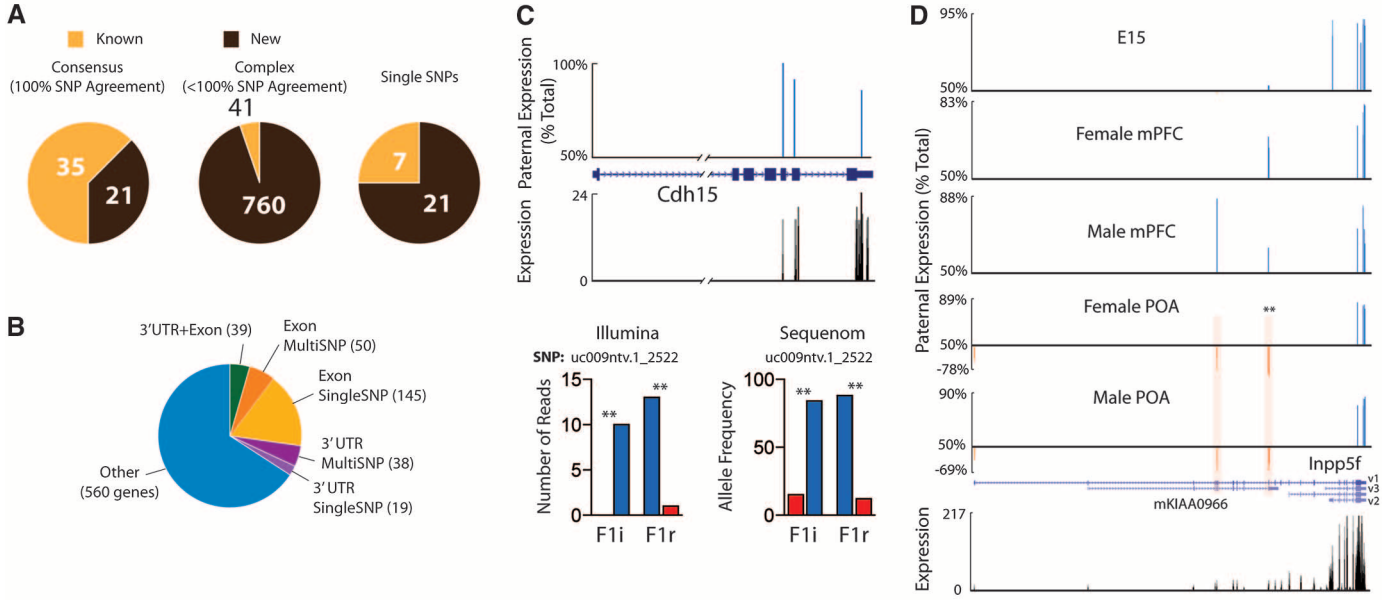

Fig. 5. Characterization of complex genes associated with parental allelic effects in the CNS transcriptome. (**A**) Numbers of previously known and newly uncovered consensus, complex, or single SNP imprinted genes. (**B**) Proportions of complex genes with parent-of-origin allelic effects localized to one or more exons (Exon), the 3′UTR (last exon), or 3′UTR+Exons, or other outcomes (i.e., disagreements between SNPs in the same exon or 3′UTR). Exons or 3′UTRs with more than one SNP for evidence are indicated separately (multiSNP). (**C**) UCSC browser tracks at the *cdh15* locus indicate preferential expression of the paternal allele (paternal allele expression bias in blue, POA data shown). Illumina RNA and Sequenom DNA analyses confirmed preferential expression of the paternal allele for *cdh15* (SNP_ID: uc009ntv.1_2522). (**D**) Complex spatiotemporal and isoform-specific imprinting at the *Inpp5f* locus. A significant maternal bias was observed specifically in the region of *Inpp5f_v1* that overlaps with *mKIAA0966* in adult POA. Highlighted SNP sites of particular interest are statistically significant in both crosses by (***P<0.001; **P< 0.01; *P< 0.05; χ^2 analysis).

Downloaded from www.sciencemag.org on August 5, 2010

parent-of-origin transcription bias (tables S7 to S11). In the *Inpp5f* locus, three isoforms have previously been described (Fig. 5D) with preferential paternal expression of *Inpp5f_v2* and *Inpp5f_v3*, while *Inpp5f_v1* was reported biallelic (*35*). In our analysis, SNP sites aligning to the *Inpp5f_v2* and *Inpp5f_v3* isoforms confirmed strict paternal expression. Four SNP sites located in exons shared by the *Inpp5f_v1* isoform and an overlapping UCSC annotated transcript (mKIAA0966) indicated a modest and nonsignificant paternal bias in expression in the adult mPFC and E15 brain. However, in the adult male and female POA, 73% of transcription at these sites ($P < 0.01$, in F_1i and F_1r cross) originated from the maternal allele. A single SNP found in the first exon of *Inpp5f_v1* indicated a modest, nonsignificant maternal expression bias in POA. Thus, our approach resolved complex regional-, developmental stage– and isoform-specific parental bias in the transcriptome.

Recently, a highly complex form of imprinting has been described for the gene *H13*, such that some *H13* isoforms are maternally expressed, whereas others are paternally expressed (*36*). Our analysis confirmed these results (fig. S9). Here we find that *Herc3*, a host gene for the known PEG *Nap1l5*, showed features indicative of isoform-specific imprinting in a manner similar to that for *H13* (fig. S10). Additional examples of complex parent-of-origin effects in the CNS transcriptome are presented in the SOM for *Lsm14a*, *Pafah1b3*, and *Ndel1* (fig. S11). Other notable complex loci include *cdh2* (neuronal-cadherin), which plays a central role in brain morphogenesis (*37*), as well as *arnt2* (*aryl hydrocarbon receptor nuclear translocator 2*), a gene with multiple isoforms that regulates hypothalamic development in concert with other imprinted genes, such as *Ndn* (*38*). Many genes identified in our analysis exhibited complex patterns of parental allelic effects for which the underlying mechanism and functional significance are not yet clear.

Finally, several loci in our data set did not display the classical pattern associated with parent-of-origin expression biases but, instead, displayed significant differences in the relative expression of the maternal and paternal alleles in F_1i versus F_1r offspring, which we refer to as cross-effects. These effects were analyzed separately, and the findings are detailed in the supplemental data (fig. S12).

Discussion. Our study documents over ~1300 protein-coding genes and putative ncRNAs associated with parental allelic effects in expression in the brain. The resolution and reproducibility of our approach is highlighted by the correct detection of maternally inherited mtDNA and male X-linked loci, highly correlated parental bias among male and female samples from the same adult brain regions, and, finally, by independent confirmation using Sequenom DNA analysis for select examples. From our study, parent-of-origin effects in the brain emerges as a complex and widespread form of epigenetic regulation characterized by brain region-, developmental stage–, and isoform-specific parental allelic effects. These findings build substantially on earlier studies that identified imprinted genes in which monoallelic expression is restricted to a developmental stage (*32*, *39*), tissue (*40*, *41*), or cell type (*42*). Such complex regulation is likely to involve the combined effects of specific parent-of-origin allelic DNA methylation patterns and histone modifications, as well as tissue- and cell type–specific promoters and enhancers (*41*, *43*). Recent work suggests that alternative polyadenylation sites may also contribute to the generation of distinct maternal and paternal isoforms (*36*). It will be of interest to determine whether other emerging epigenetic mechanisms that appear to influence the expression of alternative exons and 3′UTRs in the transcriptome, such as nucleosome positioning and histone modifications (*44*, *45*), might be relevant to the complex parent-of-origin effects uncovered in our data.

Early studies of imprinting gave rise to the concept of a maternal influence centered in the cortex and a paternal influence centered in the hypothalamus (*7*, *8*). A slightly different picture emerged from our study, such that significant maternal influence was uncovered in the embryonic brain, whereas a robust paternal bias was observed in both adult cortex (mPFC) and hypothalamus (POA). Our companion study suggests maternal control over adult brain gene expression residing on the X chromosome (*13*). Our findings may provide insights into brain evolution, function, and neurological disease due to the prominent involvement of X-linked genes in neurological function (*46*) and the unique susceptibility of imprinted loci to mutation and dysregulation (*47*).

References and Notes

1. W. Reik, J. Walter, *Nat. Rev. Genet.* **2**, 21 (2001).
2. D. Haig, *Annu. Rev. Genet.* **38**, 553 (2004).
3. E. B. Keverne, *Horm. Behav.* **40**, 146 (2001).
4. L. S. Wilkinson, W. Davies, A. R. Isles, *Nat. Rev. Neurosci.* **8**, 832 (2007).
5. S. B. Cassidy, D. J. Driscoll, *Eur. J. Hum. Genet.* **17**, 3 (2009).
6. G. Van Buggenhout, J. P. Fryns, *Eur. J. Hum. Genet.* **17**, 1367 (2009).
7. N. D. Allen *et al.*, *Proc. Natl. Acad. Sci. U.S.A.* **92**, 10782 (1995).
8. E. B. Keverne, R. Fundele, M. Narasimha, S. C. Barton, M. A. Surani, *Brain Res. Dev. Brain Res.* **92**, 91 (1996).
9. J. G. Hall, *Am. J. Hum. Genet.* **46**, 857 (1990).
10. M. S. Bartolomei, S. M. Tilghman, *Annu. Rev. Genet.* **31**, 493 (1997).
11. A. Hernandez, S. Fiering, E. Martinez, V. A. Galton, D. St Germain, *Endocrinology* **143**, 4483 (2002).
12. R. Ono *et al.*, *Genome Res.* **13**, 1696 (2003).
13. C. Gregg, J. Zhang, J. E. Butler, D. Haig, C. Dulac, *Science* **329**, 682 (2010); published online 8 July 2010 (10.1126/science.119031).
14. Materials and methods are available as supporting material on *Science* Online.
15. E. B. Keverne, *Adv. Genet.* **59**, 217 (2007).
16. Q. Gao, T. L. Horvath, *Annu. Rev. Neurosci.* **30**, 367 (2007).
17. S. E. Hyman, R. C. Malenka, E. J. Nestler, *Annu. Rev. Neurosci.* **29**, 565 (2006).
18. T. Babak *et al.*, *Curr. Biol.* **18**, 1735 (2008).
19. X. Wang *et al.*, *PLoS ONE* **3**, e3839 (2008).
20. R. Schulz *et al.*, *Epigenetics* **3**, 89 (2008).
21. E. C. Koc *et al.*, *J. Biol. Chem.* **276**, 43958 (2001).
22. O. Barel *et al.*, *Am. J. Hum. Genet.* **83**, 193 (2008).
23. G. H. Mochida *et al.*, *Am. J. Hum. Genet.* **85**, 897 (2009).
24. W. Chao, P. A. D'Amore, *Cytokine Growth Factor Rev.* **19**, 111 (2008).
25. K. Delaval, A. Wagschal, R. Feil, *Bioessays* **28**, 453 (2006).
26. M. S. Bartolomei, S. Zemel, S. M. Tilghman, *Nature* **351**, 153 (1991).
27. M. S. Bartolomei, A. L. Webber, M. E. Brunkow, S. M. Tilghman, *Genes Dev.* **7**, 1663 (1993).
28. A. L. Webber, R. S. Ingram, J. M. Levorse, S. M. Tilghman, *Nature* **391**, 711 (1998).
29. P. A. Leighton, R. S. Ingram, J. Eggenschwiler, A. Efstratiadis, S. M. Tilghman, *Nature* **375**, 34 (1995).
30. J. F. Hu, T. H. Vu, A. R. Hoffman, *Mol. Endocrinol.* **9**, 628 (1995).
31. M. Hemberger *et al.*, *Dev. Genes Evol.* **208**, 393 (1998).
32. K. Bhalla *et al.*, *Am. J. Hum. Genet.* **83**, 703 (2008).
33. R. Beroukhim *et al.*, *Nature* **463**, 899 (2010).
34. J. Liu *et al.*, *Science* **305**, 1437 (2004).
35. A. J. Wood, D. Bourc'his, T. H. Bestor, R. J. Oakey, *Nucleic Acids Res.* **35**, 7031 (2007).
36. A. J. Wood *et al.*, *Genes Dev.* **22**, 1141 (2008).
37. M. Kadowaki *et al.*, *Dev. Biol.* **304**, 22 (2007).
38. A. Caqueret, C. Yang, S. Duplan, F. Boucher, J. L. Michaud, *Horm. Res.* **64**, 222 (2005).
39. Y. Wang *et al.*, *Mol. Cell. Biol.* **24**, 270 (2004).
40. M. A. Smit *et al.*, *Mamm. Genome* **16**, 801 (2005).
41. P. Arnaud *et al.*, *Hum. Mol. Genet.* **12**, 1005 (2003).
42. Y. Yamasaki *et al.*, *Hum. Mol. Genet.* **14**, 2511 (2005).
43. K. R. McEwen, A. C. Ferguson-Smith, in *Genomic Imprinting: A Model for Roles of Histone Modifications in Epigenetic Control*, A. C. Ferguson-Smith, J. M. Greally, R. A. Martienssen, Eds. (Springer, Berlin, 2009), pp. 235–258.
44. H. Tilgner *et al.*, *Nat. Struct. Mol. Biol.* **16**, 996 (2009).
45. N. Spies, C. B. Nielsen, R. A. Padgett, C. B. Burge, *Mol. Cell* **36**, 245 (2009).
46. D. K. Nguyen, C. M. Disteche, *Brain Res.* **1126**, 46 (2006).
47. R. L. Jirtle, M. K. Skinner, *Nat. Rev. Genet.* **8**, 253 (2007).

48. We thank L. Luo, T. Maniatis, R. Losick, S. Hippenmeyer, and members of the Maniatis and Dulac labs for critical comments on the manuscript. We thank R. Hellmiss for help with figures and R. Jaenisch for X^{egfp} mice. This work was supported by the Klarman Foundation for Eating Disorders and the Howard Hughes Medical Institute (HHMI). C.G. is supported by a Human Frontiers long-term fellowship and Alberta Heritage Foundation for Medical Research Incentive Award. C.D. is an HHMI investigator. All data can be found in GEO: GSE22131.

Supporting Online Material

www.sciencemag.org/cgi/content/full/science.1190830/DC1
Materials and Methods
SOM Text
Figs. S1 to S12
Tables S1 to S12
References

13 April 2010; accepted 24 June 2010
Published online 8 July 2010;
10.1126/science.1190830
Include this information when citing this paper.

Downloaded from www.sciencemag.org on August 5, 2010

Role of Secondary Sensory Cortices in Emotional Memory Storage and Retrieval in Rats

Tiziana Sacco[1] and Benedetto Sacchetti[1,2]*

Visual, acoustic, and olfactory stimuli associated with a highly charged emotional situation take on the affective qualities of that situation. Where the emotional meaning of a given sensory experience is stored is a matter of debate. We found that excitotoxic lesions of auditory, visual, or olfactory secondary sensory cortices impaired remote, but not recent, fear memories in rats. Amnesia was modality-specific and not due to an interference with sensory or emotional processes. In these sites, memory persistence was dependent on ongoing protein kinase Mζ activity and was associated with an increased activity of layers II–IV, thus suggesting a synaptic strengthening of corticocortical connections. Lesions of the same areas left intact the memory of sensory stimuli not associated with any emotional charge. We propose that secondary sensory cortices support memory storage and retrieval of sensory stimuli that have acquired a behavioral salience with the experience.

During an emotional experience, sensory stimuli such as odors, sounds, and colors are associated with the affective qualities of that situation. Despite recent advances (*1*, *2*), the question of how and where the brain stores permanent emotional memories remains elusive. Because memories involve the representation of past sensory and emotional events, they may be stored, in part, within the sensory cortex (*3*, *4*). Nonetheless, lesions of sensory cortices do not prevent the formation of emotional memories (*5*–*11*). However, such lesions have been performed before (*5*, *6*, *10*, *11*) or shortly after (*7*–*9*) learning, a time interval in which thalamus-amygdala circuits support the functional absence of sensory cortices (*6*, *12*). No data are available on the involvement of the sensory cortex in long-term storage and retrieval of emotional memories. Therefore, we addressed two related questions: Are sensory cortices necessary for the storage and retrieval of remote fear memories? And if so, what is the role played by these sites?

Role of auditory cortices in fear memory. We first analyzed the involvement of the auditory neocortex in remote fear memories. Rats were trained to associate seven acoustic stimuli (i.e., conditioned stimuli, CSs) to an aversive unconditioned stimulus (US). The primary auditory cortex was lesioned 1 month later; this lesion was centered in area Te1 (*13*–*15*). Reconstructions of the smallest and largest extents of damage are shown in Fig. 1A [see also (*15*) and fig. S1]. Memory retention was assessed by measuring freezing behavior elicited by CSs previously paired with the US (Fig. 1B). During CS presentation, lesioned- and sham-operated animals

[1]Department of Neuroscience, University of Turin, Corso Raffaello 30, I-10125 Turin, Italy. [2]National Institute of Neuroscience, I-10125 Turin, Italy.

*To whom correspondence should be addressed. E-mail: benedetto.sacchetti@unito.it

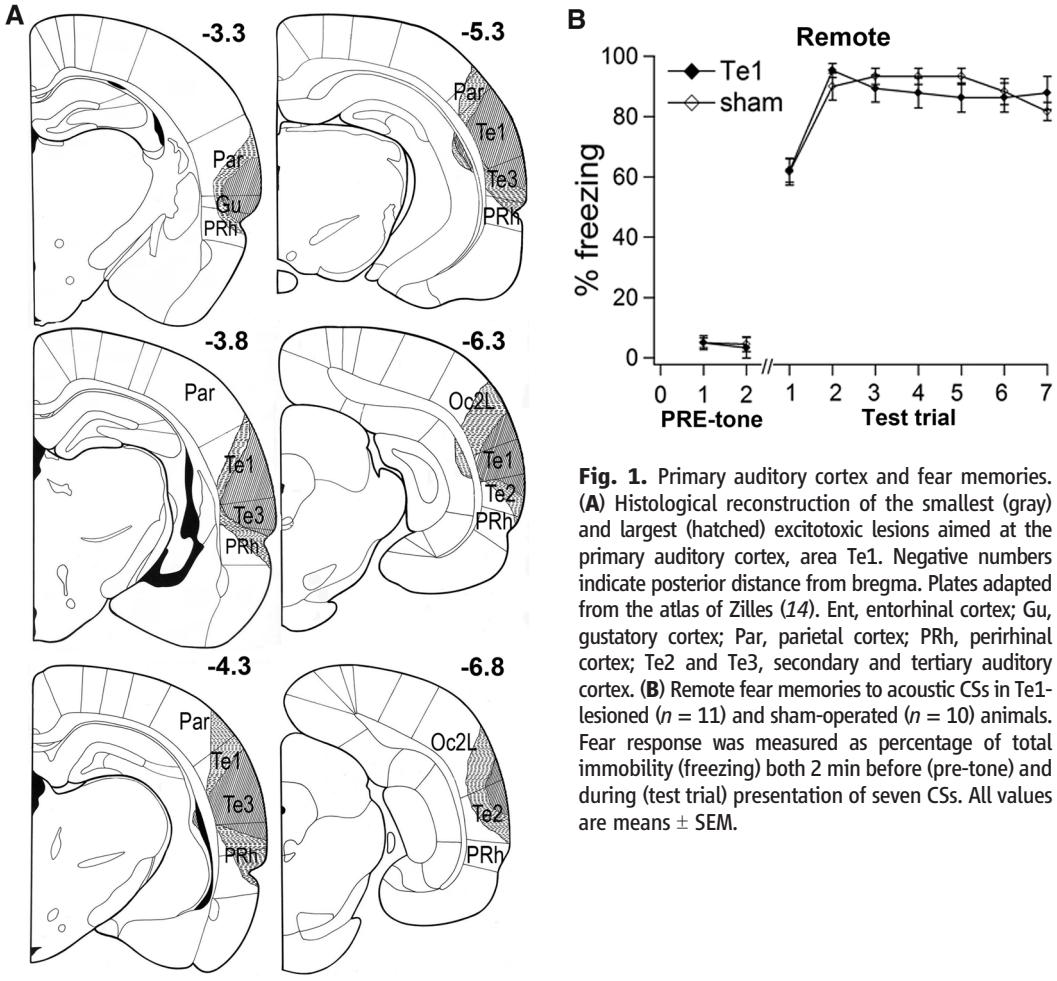

Fig. 1. Primary auditory cortex and fear memories. (**A**) Histological reconstruction of the smallest (gray) and largest (hatched) excitotoxic lesions aimed at the primary auditory cortex, area Te1. Negative numbers indicate posterior distance from bregma. Plates adapted from the atlas of Zilles (*14*). Ent, entorhinal cortex; Gu, gustatory cortex; Par, parietal cortex; PRh, perirhinal cortex; Te2 and Te3, secondary and tertiary auditory cortex. (**B**) Remote fear memories to acoustic CSs in Te1-lesioned (n = 11) and sham-operated (n = 10) animals. Fear response was measured as percentage of total immobility (freezing) both 2 min before (pre-tone) and during (test trial) presentation of seven CSs. All values are means ± SEM.

Downloaded from www.sciencemag.org on August 5, 2010

showed equivalent freezing [mixed-design analysis of variance (ANOVA), $F_{1,19} = 0.42$, $P > 0.05$; group × trial interaction, $P > 0.05$].

The primary auditory cortex is surrounded by a belt region that constitutes the secondary auditory area (*13*, *14*). We therefore examined whether the secondary auditory cortex participates in remote fear memory storage and retrieval. The lesion was centered in the Te2 area (*14*) (Fig. 2, A and B, and fig. S2). Because Te2 is just above the posterior perirhinal cortex, and because a previous study reported that lesions of the entire perirhinal cortex abolished fear memories (*9*), in an additional group we disrupted the posterior perirhinal, but not Te2, cortex (fig. S1). In the latter case, sham-operated animals were those used in Te2 experiments. Figure 2C depicts freezing scores during a memory retention test in the lesioned and sham-operated rats. A mixed ANOVA revealed a significant effect for groups ($F_{2,36} = 68.66$, $P < 0.05$) and a significant group × trial interaction ($F_{12,216} = 1.83$, $P = 0.044$). A Newman-Keuls test showed that Te2-lesioned animals differed from the other two groups ($P < 0.05$). Collectively, the results indicate that lesions of the secondary auditory cortex, but not of the posterior perirhinal cortex or primary cortex, affect long-term fear memory.

Because previous findings showed that pretraining lesions of the entire auditory area do not prevent CS-US association (*5*, *6*), we then asked whether Te2-lesioned rats can form new fear memories. The animals that displayed amnesia underwent an additional CS-US training and 2 days later were tested for CS retention. All animals could reacquire CS-US association (Fig. 2C) (*15*). Finally, we tested whether a Te2 lesion hampers recent fear memories. Te2 was lesioned 1 day after CS-US pairing. During a memory retention test, there were no differences between groups ($F_{1,23} = 1.719$, $P > 0.05$) and no significant group × trial interaction ($P > 0.05$) (Fig. 2D); that is, post-acquisition lesion of the auditory cortex does not abolish recent fear memories (*7*).

Secondary sensory visual and olfactory cortices and emotional memories. To formulate a broader functional conceptualization of the involvement of secondary sensory cortices in emotional memories, we examined whether a lesion of secondary visual cortex affects fear memories related to visual CSs and whether a lesion of the posterior piriform cortex impairs olfactory fear memories. The secondary visual cortex lesion was centered in the lateral Oc2 (Oc2L) area (*14*) (Fig. 3A and fig. S3). During CS presentation, there were differences between groups ($F_{1,19} = 24.31$, $P < 0.05$) and a significant group × trial interaction ($F_{6,114} = 3.73$, $P < 0.05$) (Fig. 3B); hence, Oc2L lesions hamper remote memories. Lesioned animals could form new conditioned fear responses ($F_{1,19} = 0.627$, $P > 0.05$) (*10*, *11*) (Fig. 3B). Finally, lesions of Oc2L performed 1 day after training did not impair recent fear memory ($F_{1,20} =$

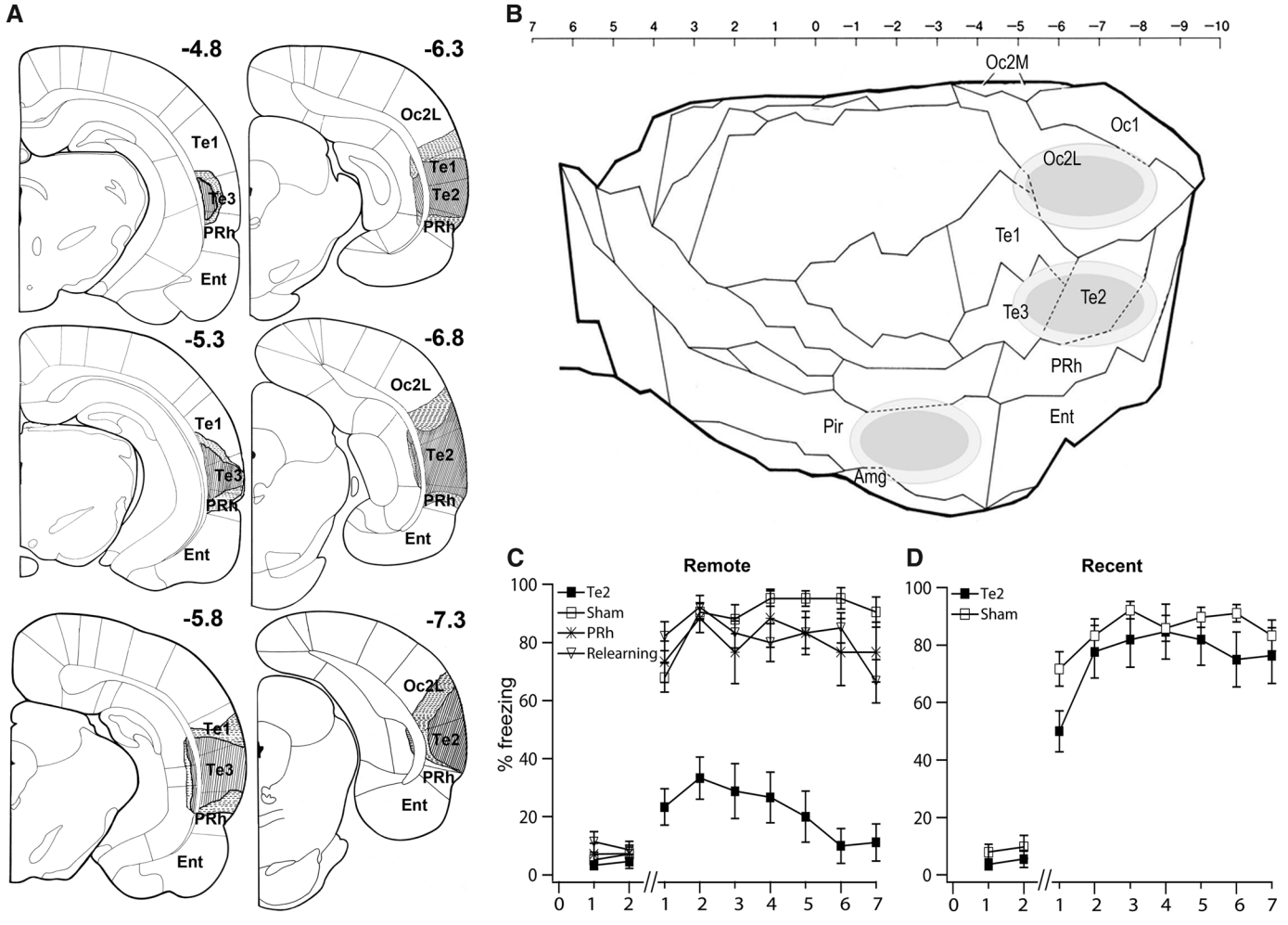

Fig. 2. Secondary auditory cortex and emotional memories. (**A**) Histological reconstruction of the excitotoxic lesions aimed at the Te2 area. Gray and hatched areas represent the smallest and the largest extent of the lesions, respectively. Negative numbers indicate posterior distance from bregma. Plates adapted from (*14*). (**B**) Schematic representation of the secondary sensory cortices included in the present study. The upper scale indicates positive and negative distances from bregma. Plate adapted from (*14*). (**C**) Remote fear memories in Te2-lesioned ($n = 15$), posterior perirhinal–lesioned (PRh, $n = 10$), and sham-operated ($n = 14$) animals. Te2-lesioned rats were able to reacquire CS-US association, as demonstrated by freezing levels comparable to those of control animals ($F_{1,27} = 2.083$, $P > 0.05$). (**D**) Recent fear memories in Te2-lesioned ($n = 12$) and sham-operated ($n = 13$) animals. Amg, amygdala; Ent, entorhinal cortex; Oc1, primary visual cortex; Oc2L and M, secondary occipital visual cortex; Pir, piriform cortex; Te3, tertiary auditory cortex.

Downloaded from www.sciencemag.org on August 5, 2010

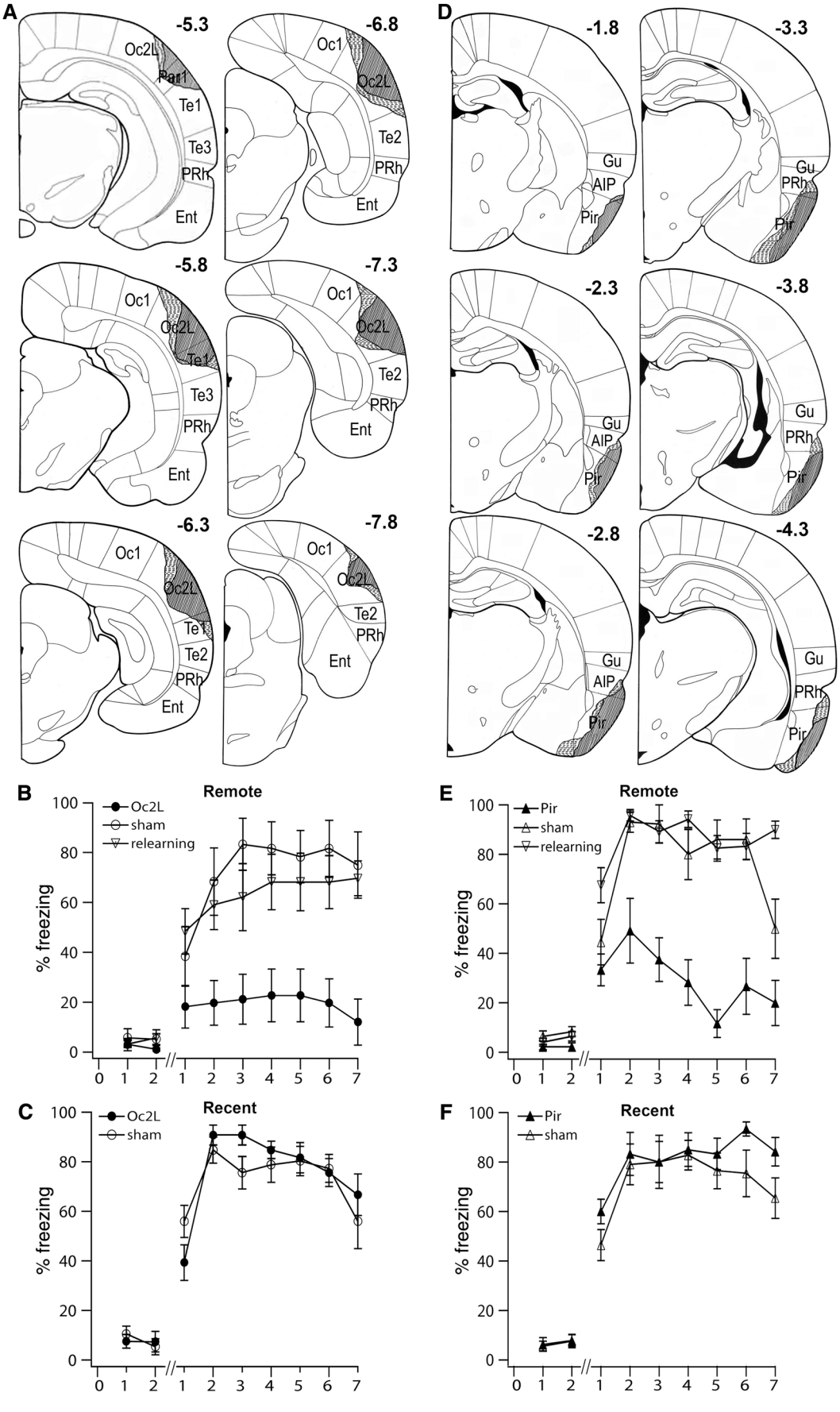

Fig. 3. Lesions of secondary visual cortex or of posterior piriform cortex impair remote fear memories. (**A**) Extent of Oc2L lesions. (**B**) Remote fear memories to visual CSs in lesioned (n =11) and sham-operated (n = 10) animals and in those retrained. (**C**) Recent emotional memories in Oc2L-lesioned (n = 11) and sham-operated (n = 11) rats. (**D**) Extent of posterior piriform cortical lesions. (**E**) Animals with posterior piriform cortex lesions (Pir, n = 12) are impaired in retention of remote memories relative to sham animals (n = 13). Lesioned animals were able to relearn CS-US association ($F_{1,23}$ = 2.225, P > 0.05). (**F**) Posterior piriform cortex lesions do not affect recent fear memories ($F_{1,21}$ = 1.775, P > 0.05; group × trial interaction, P > 0.05). Plates adapted from (*14*); perirhinal cortex (PRh) extent from (*40*). AIP, agranular posterior insular cortex; Ent, entorhinal cortex; Gu, gustatory cortex; Oc1, primary visual cortex; Te2 and Te3, secondary and tertiary auditory cortex.

Downloaded from www.sciencemag.org on August 5, 2010

0.754, $P > 0.05$; group × trial interaction, $P > 0.05$) (Fig. 3C).

The piriform cortex represents the most extensive olfactory area. In it, information is represented in a topographic fashion, with more sensory representations maintained in the anterior part and more associative representations in the posterior part (*16*, *17*). Therefore, we lesioned the posterior part of the piriform cortex 1 month after olfactory fear learning (Fig. 3D and fig. S4). These lesions disrupted remote fear memories ($F_{1,23} = 48.872$, $P < 0.05$; group × trial interaction ($F_{6,138} = 2.82$, $P < 0.05$) (Fig. 3E) but did not impair the capacity of relearning CS-US association (Fig. 3E) and did not affect recent fearful memories (Fig. 3F and fig. S5).

Collectively, the data indicate that lesions of the secondary cortices affect remote fear memories, whereas recent memories are left intact. These results suggest that amnesia, when present, is specifically related to memory impairment and is not secondary to sensory or motor disturbance. To more fully address this issue, we used the cell-permeable zeta inhibitory peptide (ZIP). ZIP inactivates protein kinase Mζ (PKMζ), an autonomously active protein kinase C isoform that is required for encoding long-term memory traces in several brain sites (*18*, *19*). ZIP injection elicits amnesia without interfering with basal synaptic activity and without inducing large-scale neuronal damage (*18*, *19*). Indeed, amnesia is still present when the peptide has been eliminated (*18*).

We injected ZIP into Te2, Oc2L, or piriform cortex 1 day or 1 month after fear learning. Memory was tested 2 days after injection. Controls received the scrambled inactive version of ZIP (Fig. 4, A and B). ZIP injection into Te2 impaired remote fear memories ($F_{1,19} = 22.98$, $P < 0.05$; group × trial interaction, $P > 0.05$), but not recent fear memories ($F_{1,14} = 0.10$, $P > 0.05$; group × trial interaction, $P > 0.05$) (Fig. 4, A and B, and fig. S6). PKMζ inactivation may disrupt remote memory storage, in which case the effect of ZIP would be persistent, or information retrieval, in which case the effect would be transient (*18*–*20*). We thus continued testing ZIP-treated animals 2 weeks after injection, to unveil memory spontaneous recovery. No evidence for spontaneous recovery was observed in ZIP-injected rats (Fig. 4C and fig. S6), thus suggesting that ZIP effects on long-term memories are durable. Immunocytochemistry after injections of biotin-labeled ZIP showed that the peptide diffused specifically within the Te2 without spreading to adjacent brain regions (fig. S7A). Histological analysis revealed no large-scale damage in ZIP-injected rats (fig. S7B). Similar results were obtained by injecting ZIP in Oc2L (Fig. 4, D to F, and figs. S6 and S7) and in the posterior piriform cortex (Fig. 4, G to I, and figs. S6 and S7).

Modality-specific involvement of sensory cortices in fear memories. The involvement of secondary sensory cortices in memory storage raises the question of whether each cortex encodes memories specifically related to the sensory modality elaborated by the area, or whether these sites play a general role in memory processes irrespective of the diverse sensory modalities present during the emotional experience. We therefore investigated the effect of lesions of each sensory cortex on fear memories related to CSs of different sensory modalities. Figure 5A illustrates freezing elicited by acoustic CSs in rats with a lesion in Oc2L or in the posterior piriform cortex, as well as in unoperated animals. ANOVA indicated no differences among groups ($F_{2,25} = 0.171$, $P > 0.05$) and a nonsignificant group × trial interaction ($P > 0.05$) (see also fig. S6). Figure 5B shows freezing to visual CSs in Te2-lesioned, posterior piriform–lesioned, and unoperated animals. Te2-lesioned animals froze less than did posterior piriform–lesioned and unoperated rats ($F_{2,24} = 18.168$, $P < 0.05$; group × trial interaction, $P > 0.05$). In rodents, the lateral posterior nucleus of the visual thalamus projects to Te2 (*13*, *21*, *22*), and this pathway may be involved in fear con-

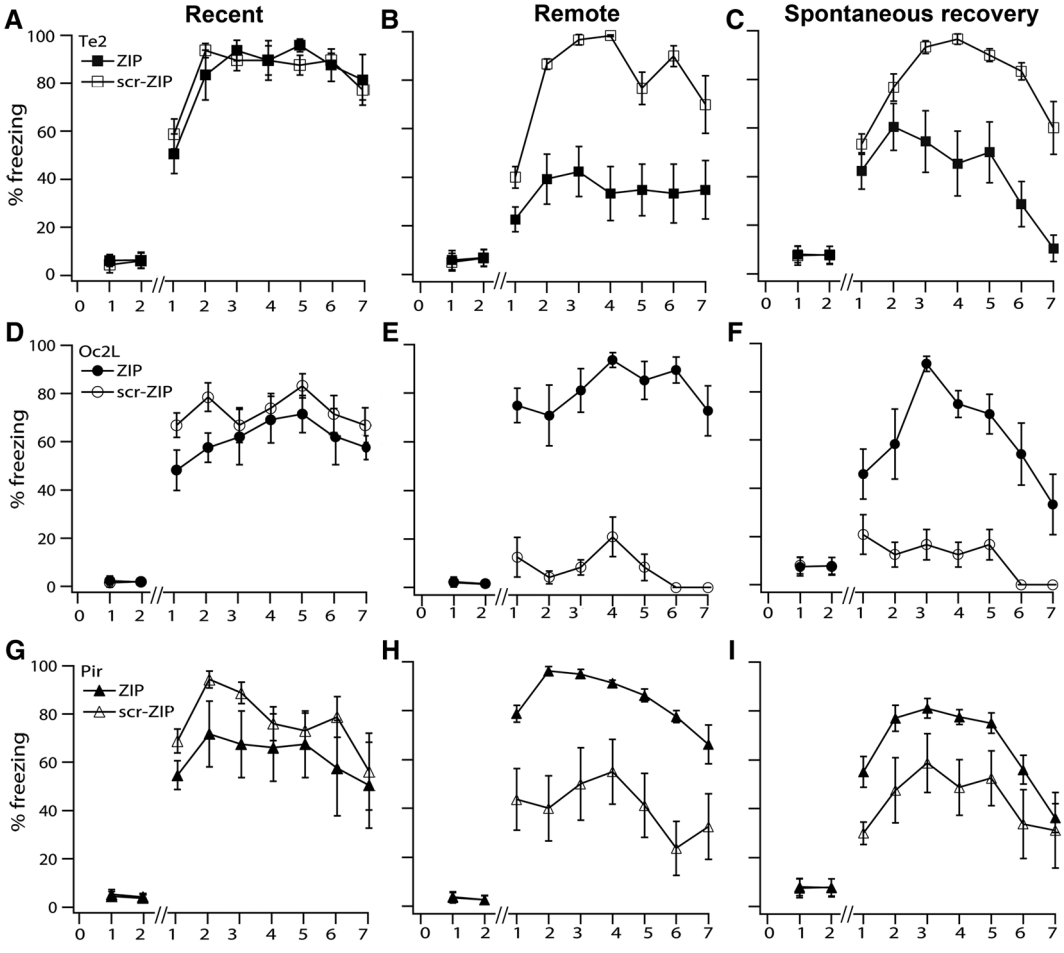

Fig. 4. Impairment of remote fear memories after injection of the PKMζ inhibitor ZIP. (**A**) ZIP ($n = 8$) or the scrambled version of ZIP (scr-ZIP, $n = 8$) was injected into Te2 1 day after training. (**B**) ZIP injection into Te2 ($n = 11$) 1 month after training hampered remote memory relative to control ($n = 10$) animals. (**C**) ZIP-treated rats did not show memory spontaneous recovery ($F_{1,19} = 17.26$, $P < 0.05$; group × trial interaction, $F_{6,114} = 3.88$, $P < 0.05$). (**D**) Recent memory to visual CSs was similar in rats infused with ZIP ($n = 7$) or scr-ZIP ($n = 7$) ($F_{1,12} = 2.91$, $P > 0.05$). (**E** and **F**) ZIP administration into Oc2L ($n = 8$) affected remote memories relative to control ($n = 8$) animals tested 2 days ($F_{1,14} = 95.26$, $P < 0.05$) (E) and 2 weeks ($F_{1,14} = 46.86$, $P < 0.05$) (F) after injection. (**G**) Recent olfactory fear memories were similar in ZIP-treated ($n = 7$) and control ($n = 7$) rats ($F_{1,12} = 1.29$, $P > 0.05$). (**H** and **I**) ZIP injection into posterior piriform cortex (Pir, $n = 8$) impaired remote memory both 2 days ($F_{1,14} = 23.41$, $P < 0.05$) (H) and 2 weeks ($F_{1,14} = 7.47$, $P < 0.05$) (I) after injection.

Downloaded from www.sciencemag.org on August 5, 2010

ditioning to visual stimuli (*9*, *22*). Furthermore, Te2 neurons are also activated by visual stimuli (*23*) and objects (*24*) as well as by polymodal auditory-visual stimulation (*23*). On the other hand, the Te2 lesion also extends to part of Oc2L (Fig. 2A). Figure 5C depicts freezing to olfactory CSs in rats with lesions in Te2 or Oc2L and in the unoperated group. There were no differences among groups ($F_{2,26} = 0.396$, $P > 0.05$; group × trial interaction, $P > 0.05$).

Collectively, these results indicate that each secondary sensory cortex is involved in emotional memories related to a specific sensory modality. The modality-specific involvement of sensory cortices suggests that lesions of these sites do not affect innate fear behavior. To address this further, we tested animals in two well-established models of anxiety—the open field and elevated plus maze tests—and also tested their unconditioned fear in the presence of a predator odor. No differences were detected among groups in all cases (*15*) (fig. S8).

Role of secondary sensory cortices in fear memories. Secondary sensory cortices may encode the physical features of the sensory stimuli ("recognition memory"). Alternatively, these sites may store the emotional meaning acquired by sensory stimuli during an emotional experience. To discriminate between the two possibilities, we tested whether lesions of secondary cortices impair long-term recognition memory of stimuli not associated with any overt emotional consequences. If lesions of sensory cortices do not affect such memories, we can reliably exclude the proposition that these sites play a crucial role in encoding the physical features of sensory stimuli. Sudden auditory stimuli elicit a startle response; if the stimuli are presented repeatedly, startle response habituates across days and this habituation is retained for weeks. Long-term habituation memory relies on the memory of the sensory stimuli presented repeatedly. Therefore, we tested whether Te2 lesions affect such recognition memory.

Four weeks after training, animals were lesioned in Te2 or sham-operated. Figure 5D presents mean startle amplitude measured during memory retention trial. A mixed ANOVA revealed differences between the first day of training and the day of testing ($F_{1,22} = 12.32$, $P < 0.05$). Thus, recognition memory is still present 1 month after training. There were no differences between groups ($F_{1,22} = 1.36$, $P > 0.05$; group × trial interaction, $P > 0.05$). We also analyzed the startle reflex in Te2-lesioned animals not submitted to the habituation training. In these rats, startle response was measured 4 weeks before the lesion and shortly after it (Fig. 5D). The two measurements did not differ significantly ($F_{1,9} = 1.08$, $P > 0.05$), thus indicating that (i) Te2 lesions did not affect startle reaction, and (ii) the decrement in startle amplitude observed in the habituated animals is produced by the habituation protocol and is not due to the mere passage of time. During the retention trial, one-way ANOVA showed differences among groups ($F_{2,31} = 6.13$, $P < 0.05$). A Newman-Keuls test individuated differences between the untrained group and the other groups ($P < 0.05$), but not between the sham-habituated and Te2-habituated animals. Thus, Te2 lesion did not affect long-term habituation memory. After the memory test, we measured startle response to a new sound never before experienced in order to verify the capacity of the animals to discriminate between novel and familiar stimuli (Fig. 5D). One-way ANOVA showed no differences among habituated and untrained animals ($F_{1,9} = 0.4$, $P > 0.05$).

The acoustic stimuli used in the habituation paradigm differed from those presented in the fear conditioning experiments (a white noise versus a pure tone). Therefore, we verified the impact of Te2 lesion on remote fear memories produced by the association of white noises (CSs) with footshock (US) (Fig. 5E). ANOVA showed differences between lesioned and control animals ($F_{1,14} = 58.18$, $P < 0.05$; group × trial interaction, $P > 0.05$). Thus, a Te2 lesion hampered emotional memories irrespective of the type of acoustic stimuli used. Again, lesioned animals could relearn CS-US association (Fig. 5E).

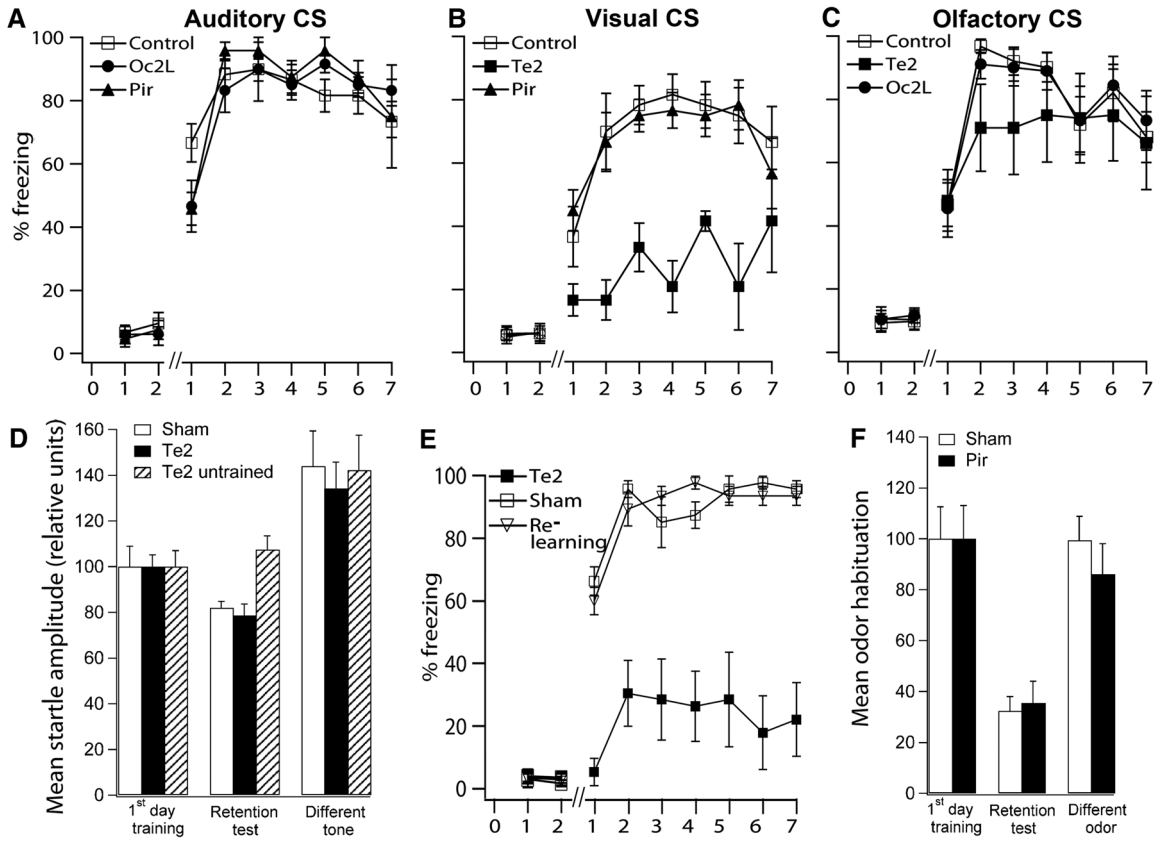

Fig. 5. Role of sensory cortices in emotional memory. (**A**) Acoustic fear memories in control ($n = 10$), Oc2L-lesioned ($n = 10$), and posterior piriform cortex–lesioned (Pir, $n = 8$) rats. (**B**) Visual fear memory in control ($n = 9$), Te2-lesioned ($n = 8$), or posterior piriform–lesioned (Pir, $n = 10$) animals. (**C**) Olfactory fear memory in control ($n = 12$), Te2-lesioned ($n = 8$), or Oc2L-lesioned ($n = 9$) rats. (**D**) Startle habituation during the first day of training, during the retention trial, and during the presentation of a new tone in Te2-lesioned ($n = 12$) and sham-operated ($n = 12$) rats and in those untrained ($n = 10$). (**E**) Remote fear memories to white-noise CSs were impaired in Te2-lesioned ($n = 8$) rats relative to sham-operated animals ($n = 8$). Te2-lesioned animals could form new fear memories ($F_{1,14} = 0.007$, $P > 0.05$). (**F**) Olfactory habituation in the posterior piriform–lesioned animals (Pir, $n = 8$) and in sham-operated animals ($n = 10$).

Downloaded from www.sciencemag.org on August 5, 2010

We then examined whether a lesion of the posterior piriform cortex affects long-term habituation to an olfactory stimulus (Fig. 5F). A mixed ANOVA indicated differences between the first day of training and the day of testing ($F_{1,16}$ = 56.98, $P < 0.05$); that is, long-term habituation was present 1 month after training. The same statistical analysis showed no difference between lesioned and sham-operated rats ($F_{1,16} = 0.91$, $P > 0.05$; group × trial interaction, $P > 0.05$), thus suggesting that a posterior piriform lesion did not affect habituation memory. Student's t test confirmed the lack of difference between lesioned and control groups during the retention trial (t_{16} = –0.81, $P > 0.05$). Control and lesioned animals were also similar in their capacity to discriminate between familiar and novel odors (t_{16} = –0.01, $P > 0.05$) (Fig. 5F).

Cortical activity related to recent or remote aversive memories. An alternative method to investigate the involvement of neural sites in memory processes is based on the analysis of expression of early genes such as *cfos* and *zif268*. Such genes are required for synaptic plasticity and are used as an index of neuronal activation (*25*, *26*). We tracked the level of the proteins encoded by *zif268* in Te2 to investigate (i) whether this site is recruited by recent and/or remote fear memories, (ii) whether it is engaged by emotional and/or sensory memory, and (iii) the cortical layer(s) activated. We first analyzed zif268 expression in animals retrieving remote fear memory. zif268 was measured after the presentation of a tone in three different groups. In the first group, the tone was paired with the US 1 month before its presentation ("fear conditioned memory"); in the second group, 1 month before its presentation, the tone was presented unaccompanied by any emotional stimuli ("recognition memory"). The third group consisted of animals that had never perceived the tone previously. zif268 expression was analyzed separately in the different cortical layers without experimenter knowledge of the experimental condition (Fig. 6A). One-way ANOVA showed a significant difference among groups in layers II–III ($F_{2,41}$ = 11.929, $P < 0.05$) and IV ($F_{2,41}$ = 7.466, $P < 0.05$) but not in layers V ($F_{2,41}$ = 2.621, $P > 0.05$) or VI ($F_{2,41}$ = 0.827, $P > 0.05$). In all cases, a Newman-Keuls test showed that zif268 labeling increased in the conditioned groups ($P < 0.05$) (Fig. 6C). No differences were found between animals naïve to the sound and those that had perceived it previously, thus suggesting that cortical layers II–III ($F_{2,22}$ = 0.58, $P > 0.05$), IV ($F_{2,22}$ = 0.13, $P > 0.05$), V ($F_{2,22}$ = 0.57, $P > 0.05$), and VI ($F_{2,22}$ = 0.89, $P > 0.05$). (**E** to **G**) After remote memory test, zif268 was also analyzed in the lateral, basal, and central nuclei of the amygdala. Scale bars, 230 μm. (**H**) Lateral (LA) and central (Ce), but not basal (B), amygdala activity was significantly enhanced after remote memory retrieval mainly in the tone-conditioned group. All data are means ± SEM.

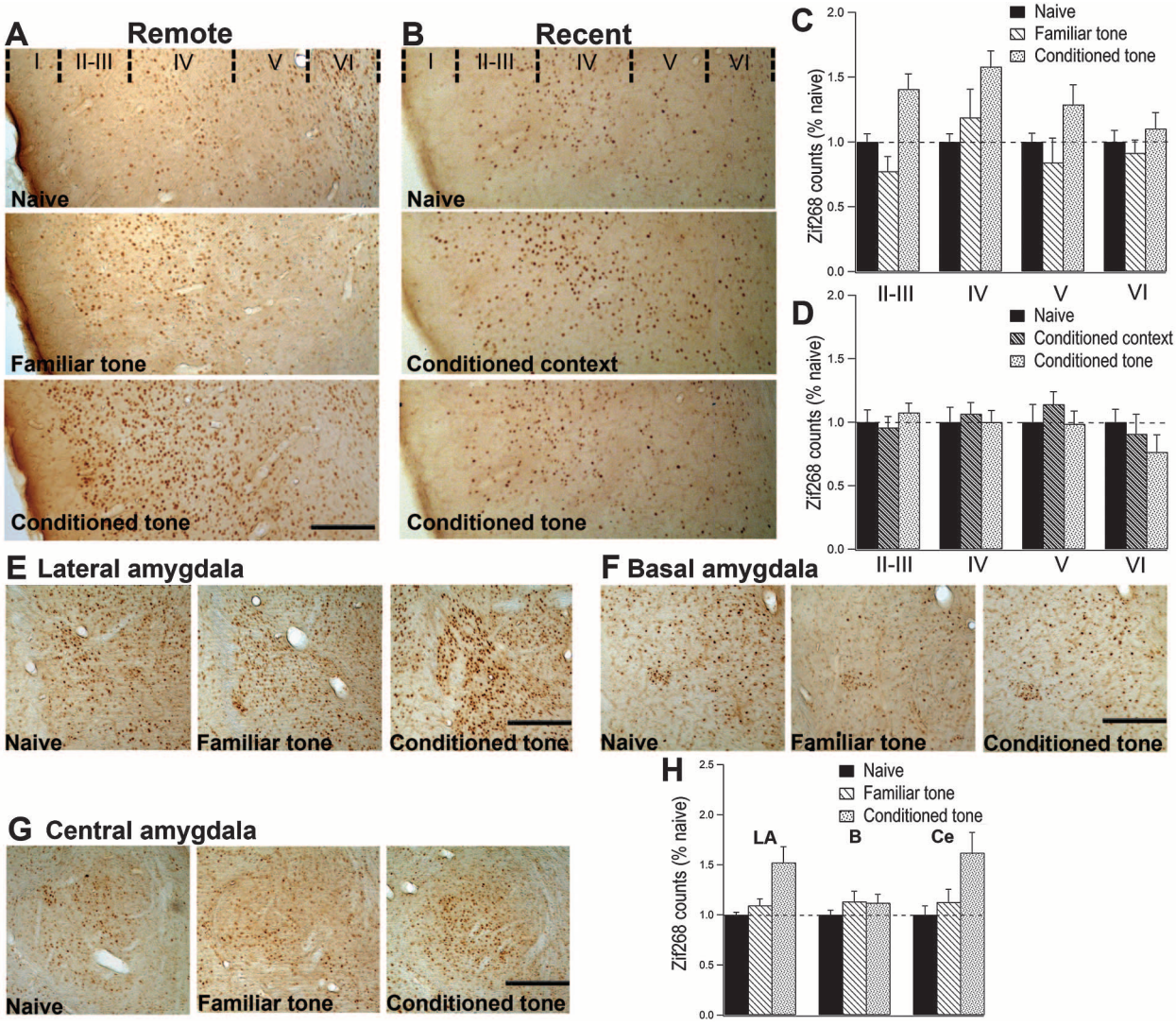

Fig. 6. zif268 protein expression in sensory neocortex and in the amygdala. (**A** and **B**) Photomicrographs of zif268 staining within Te2 cortical layers I–VI after testing for remote (A) or recent (B) fearful memory. Scale bar, 150 μm. (**C**) After remote memory test, zif268 counts relative to naïve animals significantly increased in conditioned rats in layers II–III and IV. (**D**) After recent fear memory test, zif268 analysis revealed no difference among groups in Te2

Downloaded from www.sciencemag.org on August 5, 2010

gesting that novel and familiar acoustic stimuli activated Te2 in a similar manner. Laminae II–IV are intensely connected with the other cortices and with the thalamus (*13*, *25*, *26*). An increased activity in these layers has previously been reported in parietal layers after remote spatial memory retrieval. In that case, the authors suggested that such a laminar activity reflects the formation of corticocortical neural assemblies (*26*). Our data extend these findings to secondary sensory cortices and to fear memory, perhaps suggesting that memory storage and retrieval in the cortex engages superficial layers as a general rule.

Te2 is reciprocally connected with the amygdala (*6*, *9*, *13*), a crucial site for fear-related processes (*1*, *2*). Therefore, we investigated whether the lateral, basal, and central regions of the amygdala are recruited by remote fearful memories. Analysis of zif268 expression revealed that lateral ($F_{2,31} = 9.94$, $P < 0.05$) and central ($F_{2,31} = 5.30$, $P < 0.05$) regions, but not the basal nucleus ($F_{2,31} = 0.03$, $P > 0.05$), were significantly activated by remote fear memory test (Fig. 6, E to H).

The increase of zif268 activity may be reflective of a mnemonic code but may also be a bias imparted by the expression of fear behavior displayed mainly by conditioned animals. To discriminate between the two possibilities, we examined zif268 proteins in the posterior piriform cortex, a region not engaged by acoustic fear learning. One-way ANOVA showed no differences between groups in all layers ($P > 0.05$) (fig. S9). Thus, zif268 activity was increased specifically in the brain regions engaged in acoustic fear memory.

We next proceeded to track zif268 protein expression in animals retrieving recent fear memories. To isolate auditory memory processes from nonspecific effects that may arise from a training procedure performed 24 hours before memory reactivation, we also examined zif268 activity in animals conditioned to the experimental context but not to the tone ("conditioned context"). In Te2 cortex, one-way ANOVA showed no differences among naïve, "conditioned context," and "conditioned tone" groups in all layers ($P > 0.05$) (Fig. 6, B and D). The results indicate that the secondary sensory cortices are preferentially involved in processing remote, rather than recent, fear memories. The distinct patterns of zif268 expression after recent and remote memory tests confirm that the activity of early genes in Te2 is not simply a correlate of fear-related behaviors, because freezing levels were similar at both time points (fig. S9). zif268 counts revealed a marked increase in the activity of lateral ($F_{2,19} = 5.69$, $P < 0.05$), basal ($F_{2,19} = 5.79$, $P < 0.05$), and central ($F_{2,19} = 3.92$, $P < 0.05$) amygdala in the "conditioned tone" group (fig. S10), thus suggesting that the amygdala is also involved in the early stage of memory formation (*1*, *2*, *5*–*7*).

Several observations indicate that the amnesia we observed is related specifically to interference with memory processes. As previously discussed, impairment in sensory perception or in the innate fear behavior can be reliably ruled out. Another effect that could have reduced learned fear might have resulted from deafferentiation or cell death in the amygdala or thalamic nuclei produced by cortical lesions of neurons that directly innervate these sites. However, amygdala or thalamic dysfunctions prevent CS-US association and impair recent fear memories (*6*, *7*, *27*–*29*), in marked contrast to our data. In addition, amygdala lesions hampered emotional memories irrespective of the sensory modality used as CS, in contrast to the modality-specific memory deficit that we observed. The modality-specific amnesia also allows us to rule out any "mass action effect," in which amnesia would be produced by a large cortical disruption independent of the area lesioned. The latter possibility is also ruled out by the fact that primary cortex lesions that were larger than the secondary cortex disruption did not abolish fear memories. Finally, amnesia may be due to the involvement of sensory cortices in the transmission of sensory information to the amygdala. However, in this case, memory impairment should have been present both immediately and 1 month after conditioning. Indeed, ZIP peptide is thought to interfere with synaptic plasticity and not with basal synaptic transmission (*18*).

Sensory cortical lesions do not impair recent memories or learning of a new memory trace (*5*–*11*), thus suggesting that other regions are important in these early stages. Previous (*1*, *2*, *5*, *6*) and present data indicate that the lateral and central regions of the amygdala support the formation of recent fear memories. The lateral region is the recipient of afferents from thalamus and sensory cortices (*1*). Plastic changes related to memory formation occur in both thalamic (*3*) and lateral amygdala (*1*) neurons. The central nucleus, which receives extensive connections from the lateral amygdala and projects to several brainstem regions, may be involved in the organization of specific autonomic and behavioral responses. At this early stage, the cerebellum is also recruited to set the more appropriate responses to new stimuli and/or situations (*30*, *31*). As fear memories mature, they become dependent on sensory cortices. Because previous (*28*, *29*) and present results also support a role for the amygdala in the retrieval of remote memories, it may be that permanent memories are widely distributed across sensory cortices and amygdala neurons (as well as other sites). However, because of its anatomical and functional connections, the amygdala may provide the necessary link between neural sites that encode memory and autonomic or motor effectors. Our data do not allow us to discriminate between these possibilities; they indicate only that the amygdala alone is not sufficient to support permanent fear memories.

The anterior cingulate cortex also participates in the storage of permanent fear memories (*25*). This site plays an integrative role in emotional and cognitive control processes (e.g., attention, error detection and correction). In addition, it may also encode information about the aversive components of an emotional experience (*32*). Indeed, it may interact with sensory cortices to provide the integration among the multiple representations occurring in sensory cortices during memory storage.

Both previous and present data support the view that secondary cortices encode the emotional valence acquired by sensory stimuli with the experience. Previous findings have shown that plasticity related to long-term acoustic habituation takes place in the lower auditory system (i.e., brainstem and auditory nuclei) but not in the auditory cortex (*33*, *34*), and that olfactory long-term habituation is related to olfactory bulb activity (*35*). Novel and familiar sounds determine a similar Te2 neuronal activation [(*36*) and present results], whereas Te2 activity increases significantly if the sounds have acquired a behavioral value (*34*). Finally, Te2 neurons show conditioning-induced changes in firing probability in response to CSs (*37*) and predict behavioral responses in a conditioned task (*38*). Also in the posterior piriform cortex, neurons exhibit activity according to the valence acquired with the experience by an odor cue (*17*, *39*).

Collectively, our data provide the basis for a new conceptual framework for the storage of emotional memories. Visual, acoustic, and olfactory stimuli associated with a highly charged emotional situation take on the affective qualities of that situation. Secondary cortices that perform high-level sensory analysis combine sensory processing and memory plasticity to encode the behavioral salience of perceiving stimuli. Such information becomes widely distributed throughout the cortex, each secondary sensory cortex coding the valence of stimuli of a specific modality. Such a memory storage mechanism results in a synaptic strengthening of corticocortical connections that may provide the integrated view of the whole emotional experience during memory recall.

Downloaded from www.sciencemag.org on August 5, 2010

References and Notes

1. J. E. LeDoux, *Annu. Rev. Neurosci.* **23**, 155 (2000).
2. J. L. McGaugh, *Annu. Rev. Neurosci.* **27**, 1 (2004).
3. N. M. Weinberger, *Nat. Rev. Neurosci.* **5**, 279 (2004).
4. C. M. Chavez, J. L. McGaugh, N. M. Weinberger, *Neurobiol. Learn. Mem.* **91**, 382 (2009).
5. L. M. Romanski, J. E. LeDoux, *Neurosci. Lett.* **142**, 228 (1992).
6. L. M. Romanski, J. E. LeDoux, *J. Neurosci.* **12**, 4501 (1992).
7. T. W. Jarrell, C. G. Gentile, L. M. Romanski, P. M. McCabe, N. Schneiderman, *Brain Res.* **412**, 285 (1987).
8. J. B. Rosen *et al.*, *J. Neurosci.* **12**, 4624 (1992).
9. S. Campeau, M. Davis, *J. Neurosci.* **15**, 2312 (1995).
10. J. E. LeDoux, L. Romanski, A. Xagoraris, *J. Cogn. Neurosci.* **1**, 238 (1989).
11. W. A. Falls, M. Davis, *Behav. Neural Biol.* **60**, 259 (1993).
12. J. A. Boatman, J. J. Kim, *Eur. J. Neurosci.* **24**, 894 (2006).
13. B. Kolb, R. C. Tees, *The Cerebral Cortex of the Rat* (MIT Press, Cambridge, MA, 1990).
14. K. Zilles, *The Cortex of the Rat* (Springer-Verlag, Berlin, 1985).

15. See supporting material on *Science* Online.
16. L. B. Haberly, *Chem. Senses* **26**, 551 (2001).
17. D. J. Calu, M. R. Roesch, T. A. Stalnaker, G. Schoenbaum, *Cereb. Cortex* **17**, 1342 (2007).
18. E. Pastalkova *et al.*, *Science* **313**, 1141 (2006).
19. R. Shema, T. C. Sacktor, Y. Dudai, *Science* **317**, 951 (2007).
20. B. Sacchetti, T. Sacco, P. Strata, *Eur. J. Neurosci.* **25**, 2875 (2007).
21. J. Coleman, W. J. Clerici, *Brain Res.* **194**, 205 (1980).
22. C. Shi, M. Davis, *J. Neurosci.* **21**, 9844 (2001).
23. D. S. Barth, N. Goldberg, B. Brett, S. Di, *Brain Res.* **678**, 177 (1995).
24. X. O. Zhu, M. W. Brown, B. J. McCabe, J. P. Aggleton, *Neuroscience* **69**, 821 (1995).
25. P. W. Frankland, B. Bontempi, L. E. Talton, L. Kaczmarek, A. J. Silva, *Science* **304**, 881 (2004).
26. T. Maviel, T. P. Durkin, F. Menzaghi, B. Bontempi, *Science* **305**, 96 (2004).
27. B. Sacchetti, C. A. Lorenzini, E. Baldi, G. Tassoni, C. Bucherelli, *J. Neurosci.* **19**, 9570 (1999).
28. G. D. Gale *et al.*, *J. Neurosci.* **24**, 3810 (2004).
29. Y. Lee, D. Walker, M. Davis, *Behav. Neurosci.* **110**, 836 (1996).
30. B. Sacchetti, E. Baldi, C. A. Lorenzini, C. Bucherelli, *Proc. Natl. Acad. Sci. U.S.A.* **99**, 8406 (2002).
31. B. Sacchetti, B. Scelfo, F. Tempia, P. Strata, *Neuron* **42**, 973 (2004).
32. E. L. Malin, J. L. McGaugh, *Proc. Natl. Acad. Sci. U.S.A.* **103**, 1959 (2006).
33. F. Gonzalez-Lima, T. Finkenstädt, J. P. Ewert, *Brain Res.* **489**, 67 (1989).
34. A. Poremba, D. Jones, F. Gonzalez-Lima, *Eur. J. Neurosci.* **10**, 3035 (1998).
35. D. A. Wilson, C. Linster, *J. Neurophysiol.* **100**, 2 (2008).
36. H. Wan *et al.*, *Eur. J. Neurosci.* **14**, 118 (2001).
37. D. M. Diamond, N. M. Weinberger, *Behav. Neurosci.* **98**, 189 (1984).
38. A. E. Villa, I. V. Tetko, B. Hyland, A. Najem, *Proc. Natl. Acad. Sci. U.S.A.* **96**, 1106 (1999).
39. W. Li, J. D. Howard, T. B. Parrish, J. A. Gottfried, *Science* **319**, 1842 (2008).
40. G. Paxinos, C. Watson, *The Rat Brain in Stereotaxic Coordinates* (Academic Press, New York, 1986).
41. We thank J. L. McGaugh for critical comments on the manuscript and L. Milano, A. Renna, D. Germano, V. Pastrone, D. Tonello, and G. Benvenuti for technical assistance. Supported by grants from the Italian Ministry of University.

Supporting Online Material

www.sciencemag.org/cgi/content/full/329/5992/649/DC1
Materials and Methods
SOM Text
Figs. S1 to S10
References

12 October 2009; accepted 18 June 2010
10.1126/science.1183165

REPORTS

Normal Modes and Density of States of Disordered Colloidal Solids

D. Kaya,[1] N. L. Green,[2] C. E. Maloney,[3] M. F. Islam[1,2]*

The normal modes and the density of states (DOS) of any material provide a basis for understanding its thermal and mechanical transport properties. In perfect crystals, normal modes are plane waves, but they can be complex in disordered systems. We have experimentally measured normal modes and the DOS in a disordered colloidal crystal. The DOS shows Debye-like behavior at low energies and an excess of modes, or Boson peak, at higher energies. The normal modes take the form of plane waves hybridized with localized short wavelength features in the Debye regime but lose both longitudinal and transverse plane-wave character at a common energy near the Boson peak.

Normal modes provide a framework for understanding the dynamical excitations of a system in diverse fields ranging from architecture to molecular biology. The normal modes are those degrees of freedom which, at least for small perturbations away from equilibrium, do not interact with each other. Each mode oscillates independently of the others with its own characteristic frequency. The distribution of these frequencies, known as the density of states (DOS), and the structure of the modes are used as a starting point to calculate the heat capacity, thermal conductivity, and elastic constants in solids (*1*).

In a perfect crystal, due to the translational symmetry, the normal modes must be plane waves. Once disorder is introduced into a perfect crystal, the modes become more complicated, and the related DOS and thermodynamical properties begin to deviate from those in the perfect system. The disorder can be geometrical in nature, as in the case of structural glasses (*2*). Even geometrically perfect crystals can become disordered if the interactions between nearest neighbors or the masses of the particles are not uniform (*3*). In fact, disordered crystals are often used as a simple theoretical framework to understand generic emergent behavior in other types of disordered systems, such as structural glasses (*4*–*6*). In theoretical models of both disordered crystals and structural glasses, the key features that emerge are a Debye-like regime with hybridization of localized regions of low shear modulus with the low-frequency (long wavelength) plane waves, and an excess in the DOS at higher frequencies known as the Boson peak (*4*, *5*, *7*–*9*). Normal modes and the DOS have not been directly measured experimentally in a disordered system, in part because for the case of disordered atomic systems, directly tracking the dynamics of individual atoms is not experimentally feasible.

Colloidal suspensions have been used as model systems to study various phenomena that occur in other condensed matter systems, such as atomic liquids, crystals, and glasses (*10*–*15*). In colloidal systems, one may use optical microscopy to observe individual particle motions within the interior of a system (*10*, *14*, *13*). With traditional hard-sphere colloidal particles such as silica spheres, one may readily produce a crystal or an amorphous structural glass. However, the perfect crystals produced with these conventional particles show spatially homogeneous fluctuations (*16*–*20*). Here, we studied a face-centered-cubic (fcc) crystal made of deformable microgel colloidal particles with essentially perfect geometrical order yet strongly heterogeneous fluctuations. The heterogeneity may be caused by particle-to-particle variations in the microgel stiffness and is a novel characteristic of the deformable microgel colloids (*15*).

Normal mode energies of perfect colloidal crystals are usually obtained by assuming a plane-wave form for the modes and then measuring the amplitudes of the plane waves (*16*, *17*, *20*), much as

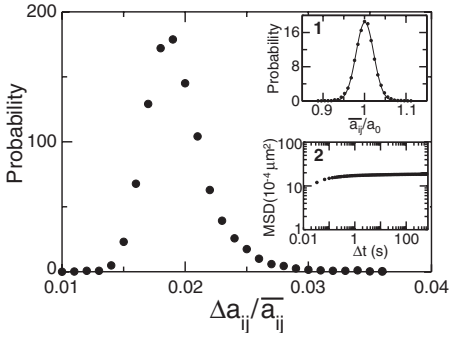

Fig. 1. Probability distribution of temporal fluctuations in nearest-neighbor spacing $\Delta a_{ij}/\overline{a}_{ij}$. The distribution is quite wide, with an average of about 1.9% and an RMS width of about 0.23%. (**Inset 1**) Probability distribution of nearest-neighbor spacing in the equilibrium configuration, $\overline{a}_{ij}/a_0$. The relative spatial fluctuations in $\overline{a}_{ij}$ were about 2.1%. The solid line is a Gaussian fit through the data. The spatial fluctuations in Δa_{ij} were ~5 times as large as the spatial fluctuations in $\overline{a}_{ij}$. (**Inset 2**) MSD averaged over particles reaches a well-defined plateau.

[1]Department of Materials Science and Engineering, Carnegie Mellon University, 5000 Forbes Avenue, Pittsburgh, PA 15213–3890, USA. [2]Department of Chemical Engineering, Carnegie Mellon University, 5000 Forbes Avenue, Pittsburgh, PA 15213–3890, USA. [3]Department of Civil and Environmental Engineering, Carnegie Mellon University, 5000 Forbes Avenue, Pittsburgh, PA 15213–3890, USA.

*To whom correspondence should be addressed. E-mail: mohammad@cmu.edu

Downloaded from www.sciencemag.org on August 5, 2010

one obtains the dispersion curves in an atomic system through scattering experiments (*1*). However, for any disordered system with heterogeneity, such as our system, one cannot assume, a priori, that the normal modes are plane waves. Therefore, we developed an approach to measure the correlations in particle displacements to determine the normal modes themselves and their DOS (*21*). The anomalous normal mode structure and DOS of our microgel colloidal system exhibited some theoretically predicted universal features of both disordered crystals (*4*, *5*) and structural glasses (*7*–*9*) and provided insights into the origin of the Boson peak. Moreover, our approach is quite general and can also be used to directly reconstruct the normal modes of other colloidal systems such as structural glasses, perfect crystals with isolated point or line defects, and the like.

The degree of geometrical order of the equilibrium configuration and the spatial heterogeneity of the fluctuations away from equilibrium in our system are shown in Fig. 1. Time-averaged positions, $\overline{\vec{r}_i}$, of the particles were computed from the tracks, and particle displacements were calculated as $\vec{u}_i(t) = \vec{r}_i(t) - \overline{\vec{r}_i}$. The resolution in particle displacements was less than 5 nm (*22*, *23*). Single-particle displacement distributions were Gaussian, with an anisotropy of less than 0.07. The nearest-neighbor separations, $\overline{a}_{ij} = |\overline{\vec{r}_i} - \overline{\vec{r}_j}|$, between the time-averaged positions of the centers of all particles were more or less homogeneous throughout the system (fig. S2). The spatial average value of $\overline{a}_{ij}$, denoted as a_0, was 1.18 μm. The normalized probability distribution of $\overline{a}_{ij}/a_0$, shown in inset 1 of Fig. 1, had a relative root mean square (RMS) variation of 2.1%. This demonstrates the relatively high degree of geometrical order in our system. The average mean squared displacement (MSD) with a clear plateau indicating solid-like behavior and the absence of diffusion are shown in inset 2 of Fig. 1.

We then focused on the temporal fluctuations in the instantaneous nearest-neighbor separations, $a_{ij}(t) = |\vec{r}_i(t) - \vec{r}_j(t)|$, to determine the degree of disorder in our system. The time-dependent fluctuations of $a_{ij}(t)$ for four random pairs of particles are shown in fig. S3. Because the fluctuations in $a_{ij}(t)$ (fig. S3) and the average RMS particle displacements (inset 2 of Fig. 1) were significantly larger than the experimental resolution in particle displacements, our subsequent analyses are not limited by experimental resolution (*24*). The temporal RMS fluctuations for each pair, $\Delta a_{ij} = \sqrt{\overline{(a_{ij}(t) - \overline{a}_{ij})^2}}$, are shown in fig. S4, and the probability distribution of the normalized values, $P(\Delta a_{ij}/\overline{a}_{ij})$, is shown in the main plot of Fig. 1. Without heterogeneous interactions between the particles, in a geometrically ordered colloidal crystal like ours, the Δa_{ij} would necessarily be identical and $P(\Delta a_{ij}/\overline{a}_{ij})$ would be very narrow. It is the internal degrees of freedom corresponding to the stiffness of individual hydrogel particles that can allow for these particle-to-particle variations in our system. The values of Δa_{ij} for any given pair defined over intermediate time windows were relatively steady over the entire duration of data collection and did not depend on time-averaging. The average $\Delta a_{ij}/\overline{a}_{ij}$ was about 1.9%, and the width of the distribution was 0.23%, which shows that the spatial fluctuations in Δa_{ij} were approximately five times as large as the spatial fluctuations in a_{ij}. We verified that there was virtually no correlation between Δa_{ij} and $\overline{a}_{ij}$ for any given pair (i.e., there was little correlation between figs. S2 and S4), indicating that the heterogeneous dynamics was due to nonuniform interactions between particles rather than geometrical irregularities in the crystal. The local MSDs of individual particles were also spatially heterogeneous, giving further indication of the presence of nonuniform interactions. We have performed molecular dynamics simulations with crystals of soft particles of spatially uncorrelated stiffness that showed regions of correlated dynamical fluctuations (fig. S5) similar to the ones observed here (fig. S4), despite the underlying uncorrelated particle stiffness (*21*).

Next, we determined the normal modes from the observed particle displacement fields (*25*). In a harmonic system governed by equipartition of energy, the two-point correlations, $G_{i\alpha j\beta} \doteq \langle u_{i\alpha} u_{i\beta} \rangle$ (where the Latin letters index particles and the Greek letters index Cartesian components with an implicit Einstein summation convention), are given in terms of the normal modes as (*26*): $G_{i\alpha j\beta} = \sum_p (\psi^p_{i\alpha} \psi^p_{j\beta}) k_B T/\lambda_p$, where $\psi^p_{i\alpha}$ is the p-th normal mode, λ_p is the p-th energy eigenvalue, k_B is the Boltzmann constant, and T is the temperature. That is, the normal modes are those degrees of freedom that appear uncorrelated with a mean squared amplitude of $k_B T/\lambda_p$. We emphasize that no assumptions are made about the underlying dynamics beyond that they give the appropriate probability for observing a given fluctuation away from the equilibrium configuration. If one knows the structure of the $\psi^p_{i\alpha}$ a priori, for example in a homogeneous perfect crystal where the $\psi^p_{i\alpha}$ must be plane waves, one may decompose $u_{i\alpha}$ onto the known

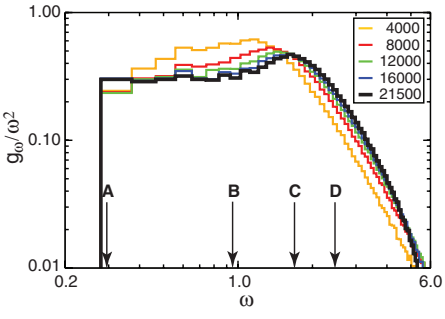

Fig. 2. g_ω, divided by ω^2. The different colored curves correspond to different statistical ensemble size, that is, the total number of statistically independent images used to compute the sample covariance. The DOS shows Debye-like behavior, constant g_ω/ω^2, at low energy with a Boson peak at higher energy. Points A to D correspond to the ω values of four modes shown in detail in Fig. 3.

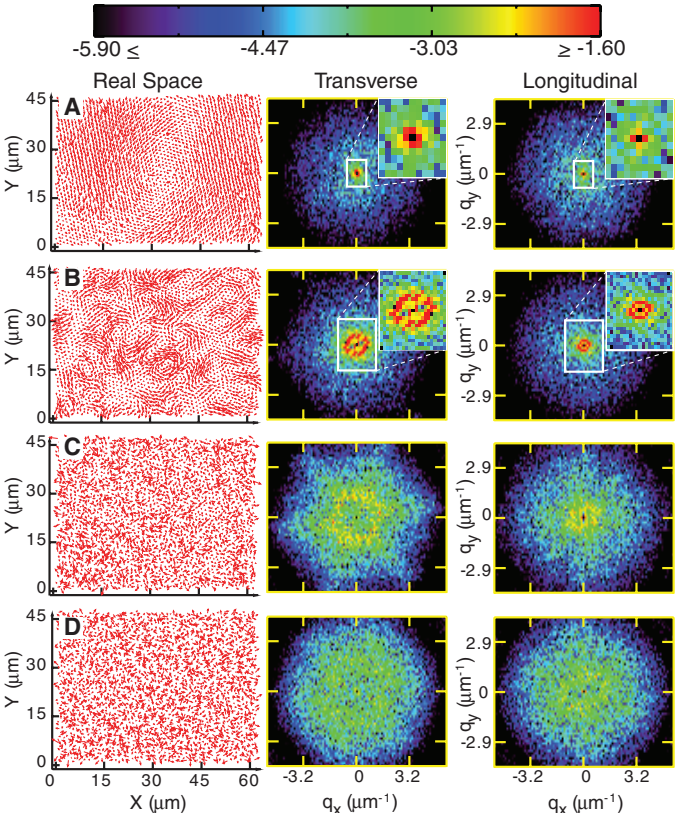

Fig. 3. (**A** to **D**) Four normal modes taken from various regimes indicated in Fig. 2. For each mode, we show the normalized mode vectors in real space along with the squared amplitude of the projection onto transverse and longitudinal plane waves. In the Debye regime, the intensity is peaked in Fourier space around a characteristic wavevector, q_0. Above the Boson peak, the intensity distribution is uniform throughout the Brillouin zone.

Downloaded from www.sciencemag.org on August 5, 2010

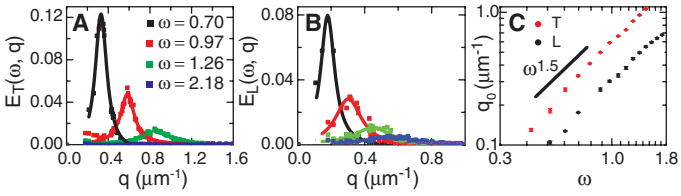

Fig. 4. The ω and *q*-averaged Fourier decompositions of the normal modes along (**A**) the transverse (T) and (**B**) the longitudinal (L) plane waves versus *q* for a few ω values. The solid lines are Lorentzian fits through the data. (**C**) q_0, obtained from the Lorentzian peak location, plotted against ω shows that $q_0 \sim \omega^{3/2}$.

$\psi^p_{i\alpha}$ and use these mode amplitudes to estimate (*17*) $\lambda_p/k_BT = \langle(\sum_i u_{i\alpha}\psi^p_{i\alpha})^2\rangle^{-1}$.

When one does not know the $\psi^p_{i\alpha}$ a priori, such as for disordered systems like ours, other methods are necessary to estimate the λ_p and the ψ_{ip} themselves. To do this, one may diagonalize the observed two-point correlations, $\hat{G}_{ij}$, the so-called sample covariance, to obtain the ψ_{ip}. This procedure has been used to infer normal modes in simulations of small molecular systems (*27*), but care must be taken when applying it to larger systems. It is known that the procedure is highly sensitive to the number of independent observations (*28*). However, we have observed that the spectrum of energy eigenvalues converged by about 20,000 independent observations of the displacement field.

In conventional studies of disordered systems, one generally normalizes the observed DOS by the Debye prediction (*4*, *5*, *7*–*9*), where a plateau is obtained at low energy. Because we observed a two-dimensional (2D) slice of a 3D system, we first determined the appropriate normalization factor for our observed DOS. At low ω, where $\omega = \sqrt{\mathrm{MSD}\lambda/(k_BT)}$, the DOS, $g_\omega = dN/d\omega$, exhibited a power-law regime for almost a decade where $dN/d\omega \sim \omega^2$ and *N* is the index of the mode. We therefore normalized g_ω by ω^2. Here, we introduce ω to make connections with theoretical work where one usually works with $\sqrt{\lambda}$ rather than λ.

In Fig. 2, we show g_ω/ω^2. Each histogram corresponds to a sample covariance obtained using a different total number of independent displacement field observations: 4000, 8000, 12,000, 16,000, and 21,500, indicating that the spectrum has converged. Below $\omega \approx 1.2$, g_ω/ω^2 shows a Debye-like plateau. At higher ω, g_ω/ω^2 rises to a Boson peak at $\omega \sim 1.7$ before rapidly falling. This general behavior is consistent with that seen generically in numerical models of structural glasses (*29*, *7*, *8*, *30*, *31*, *9*) and elastically disordered lattices (*5*, *4*).

To analyze the spatial structure of the modes, we decomposed them onto longitudinal and transverse plane waves using standard Fourier analysis techniques. Figure 3 shows four modes taken from various regions of the spectrum, as indicated in Fig. 2. In the Debye regime, the modes, shown in Fig. 3, A and B, were composed primarily of plane waves with a single dominant wavevector, q_0, which were hybridized with localized short-wavelength features. On approach to the Boson peak, q_0 saturated at q_{BP}, which corresponds to about five to six particle diameters for the transverse plane waves and about twice that wavelength for the longitudinal plane waves. Above the Boson peak, the intensity was distributed broadly throughout the Brillouin zone, and all plane-wave character was lost (Fig. 3, C and D, and movie S1). Near the Boson peak, the effects of the lattice became noticeable, and the mode shown in Fig. 3C had pronounced broken symmetry with intensity accumulating around the six-fold symmetric crystal axes.

Our observation of the $g_\omega \sim \omega^2$ scaling of the DOS at low ω implies a relationship between q_0 and ω. Simply counting the number of plane waves in 2D gives $dN/dq \sim q$ (*1*). Then $d\omega/dq \sim (d\omega/dN)(dN/dq) \sim \omega^{-2}q$, which gives $q_0 \sim \omega^{3/2}$. To test this prediction and to quantitatively determine q_0 near q_{BP}, we determined q_0 as a function of ω. We first averaged the Fourier decompositions along transverse and longitudinal plane waves over a small range (~10%) of ω. Then the ω-averaged Fourier decompositions were averaged over angles (again, ~10% in *q*) to obtain $E_T(\omega, q)$ and $E_L(\omega, q)$, where subscripts *T* and *L* were contributions along the directions of transverse and longitudinal plane waves. For each ω, we found that, below the Boson peak, $E_T(\omega, q)$ and $E_L(\omega, q)$ could be fit to a Lorentzian profile. Several of these $E_T(\omega, q)$ and $E_L(\omega, q)$ with the Lorentzian fits (solid lines) at various ω are shown in Fig. 4, A and B. The location of the Lorentzian peak then gave q_0 for a given ω. Our analysis showed that $q_0 \sim \omega^{3/2}$, as shown in Fig. 4C. We also found that the point at which a Lorentzian fit became unfeasible was at an ω near the Boson peak, and this was true for both the longitudinal and transverse contributions.

In numerical models of structural glasses (*9*), only the transverse plane waves become overdamped near the Boson peak, and there was little correlation with the longitudinal modes. In contrast, in our system of disordered crystals, the sharply peaked contribution to the normal modes goes away for both longitudinal and transverse plane waves at the Boson peak. This raises the question of how the emergent properties of various kinds of disordered solids depend on the nature of the disorder.

In conclusion, we have determined the normal modes and DOS of a strongly disordered colloidal crystal composed of deformable microgel particles. This type of disorder is similar to that used in theoretical models. We have established that Debye-like behavior at low energy with a Boson peak at higher energy are generic features of disordered solids, whereas the nature of the vanishing of the plane-wave character near the Boson peak may depend on particular details of the disorder. The general procedure presented here will be an important tool to identify the impacts, at a particle-scale level, of different types of disorder on the structure of the normal modes and elasticity that are present in various atomic, molecular, and colloidal crystals and glasses.

References and Notes

1. N. W. Ashcroft, N. D. Mermin, *Solid State Physics* (Saunders College, Philadelphia, 1976).
2. S. R. Elliott, *Physics of Amorphous Materials* (Longmans, New York, 1990).
3. R. J. Elliott, J. A. Krumhansl, P. L. Leath, *Rev. Mod. Phys.* **46**, 465 (1974).
4. S. N. Taraskin, Y. L. Loh, G. Natarajan, S. R. Elliott, *Phys. Rev. Lett.* **86**, 1255 (2001).
5. W. Schirmacher, G. Diezemann, C. Ganter, *Phys. Rev. Lett.* **81**, 136 (1998).
6. A. Souslov, A. J. Liu, T. C. Lubensky, *Phys. Rev. Lett.* **103**, 205503 (2009).
7. H. R. Schober, *J. Phys. Condens. Matter* **16**, S2659 (2004).
8. H. R. Schober, C. Oligschleger, *Phys. Rev. B* **53**, 11469 (1996).
9. H. Shintani, H. Tanaka, *Nat. Mater.* **7**, 870 (2008).
10. W. K. Kegel, A. van Blaaderen, *Science* **287**, 290 (2000).
11. D. G. A. L. Aarts, M. Schmidt, H. N. W. Lekkerkerker, *Science* **304**, 847 (2004).
12. U. Gasser, E. R. Weeks, A. Schofield, P. N. Pusey, D. A. Weitz, *Science* **292**, 258 (2001).
13. A. M. Alsayed, M. F. Islam, J. Zhang, P. J. Collings, A. G. Yodh, *Science* **309**, 1207 (2005).
14. E. R. Weeks, J. C. Crocker, A. C. Levitt, A. Schofield, D. A. Weitz, *Science* **287**, 627 (2000).
15. J. Mattsson *et al.*, *Nature* **462**, 83 (2009).
16. Z. Cheng, J. Zhu, W. B. Russel, P. M. Chaikin, *Phys. Rev. Lett.* **85**, 1460 (2000).
17. P. Keim, G. Maret, U. Herz, H. H. von Grünberg, *Phys. Rev. Lett.* **92**, 215504 (2004).
18. H. H. von Grünberg, P. Keim, K. Zahn, G. Maret, *Phys. Rev. Lett.* **93**, 255703 (2004).
19. J. Baumgartl, M. Zvyagolskaya, C. Bechinger, *Phys. Rev. Lett.* **99**, 205503 (2007).
20. D. Reinke *et al.*, *Phys. Rev. Lett.* **98**, 038301 (2007).
21. Materials and methods are available on *Science* Online.
22. J. C. Crocker, D. G. Grier, *J. Colloid Interface Sci.* **179**, 298 (1996).
23. J. C. Crocker, B. D. Hoffman, *Methods Cell Biol.* **83**, 141 (2007).
24. A. Ghosh *et al.*, *Soft Matter* **6**, 3082 (2010).
25. A. Ghosh, V. K. Chikkadi, P. Schall, J. Kurchan, D. Bonn, *Phys. Rev. Lett.* **104**, 248305 (2010).
26. P. M. Chaikin, T. C. Lubensky, *Principles of Condensed Matter Physics* (Cambridge Univ. Press, Cambridge, 2000).
27. A. Strachan, *J. Chem. Phys.* **120**, 1 (2004).
28. N. Meinshausen, P. Buhlmann, *Ann. Stat.* **34**, 1436 (2006).
29. B. B. Laird, H. R. Schober, *Phys. Rev. Lett.* **66**, 636 (1991).
30. S. N. Taraskin, S. R. Elliott, *Phys. Rev. B* **56**, 8605 (1997).
31. S. I. Simdyankin, S. N. Taraskin, M. Elenius, S. R. Elliott, M. Dzugutov, *Phys. Rev. B* **65**, 104302 (2002).

32. We acknowledge M. Widom, A. D. Dinsmore, and J. C. Crocker for valuable discussions. This work was supported by NSF through grants DMR-0645596 and DMR-0619424 (M.F.I.), the Sloan Foundation (M.F.I.), and American Chemical Society Petroleum Research Fund (M.F.I.).

Supporting Online Material

www.sciencemag.org/cgi/content/full/329/5992/656/DC1
Materials and Methods
Figs. S1 to S5
References
Movie S1

5 February 2010; accepted 29 June 2010
10.1126/science.1187988

Downloaded from www.sciencemag.org on August 5, 2010

Massive Dirac Fermion on the Surface of a Magnetically Doped Topological Insulator

Y. L. Chen,[1,2,3] J.-H. Chu,[1,2] J. G. Analytis,[1,2] Z. K. Liu,[1,2] K. Igarashi,[4] H.-H. Kuo,[1,2] X. L. Qi,[1,2] S. K. Mo,[3] R. G. Moore,[1] D. H. Lu,[1] M. Hashimoto,[2,3] T. Sasagawa,[4] S. C. Zhang,[1,2] I. R. Fisher,[1,2] Z. Hussain,[3] Z. X. Shen[1,2]*

In addition to a bulk energy gap, topological insulators accommodate a conducting, linearly dispersed Dirac surface state. This state is predicted to become massive if time reversal symmetry is broken, and to become insulating if the Fermi energy is positioned inside both the surface and bulk gaps. We introduced magnetic dopants into the three-dimensional topological insulator dibismuth triselenide (Bi_2Se_3) to break the time reversal symmetry and further position the Fermi energy inside the gaps by simultaneous magnetic and charge doping. The resulting insulating massive Dirac fermion state, which we observed by angle-resolved photoemission, paves the way for studying a range of topological phenomena relevant to both condensed matter and particle physics.

Topological insulators are a state of matter that may serve as a platform for both fundamental physics phenomena and technological applications, such as spintronics and quantum information processing. Since their discovery in two-dimensional (2D) HgTe quantum wells (*1*, *2*), topological insulators have been at the core of a very active research area (*3*–*11*). Recently, a class of 3D compounds—Bi_2Te_3, Bi_2Se_3, and Sb_2Te_3—were identified (*12*–*14*) with the surface state consisting of a single Dirac cone. The conducting surface states of topological insulators are immune to localization as long as the disorder potential does not violate time reversal symmetry (TRS) (*4*, *5*, *9*), and one way to destroy this robust surface metallicity is to break the TRS by introducing magnetic order (*5*). In the bulk, a topological insulator doped with magnetic impurities can have a long-range magnetic order both in the metallic (*15*, *16*) and insulating (*17*) phases; on the surface, such a long-range magnetic order can also be formed independent of the bulk magnetic ordering, as the Ruderman-Kittel-Kasuya-Yosida (RKKY) interaction induced by the Dirac fermions is generally ferromagnetic when the Fermi energy (E_F) is close to the Dirac point (*18*). Both effects can lead to the breaking of TRS, resulting in a gap opening at the Dirac point that makes the surface Dirac fermion mas-

[1]Stanford Institute for Materials and Energy Sciences, SLAC National Accelerator Laboratory, 2575 Sand Hill Road, Menlo Park, CA 94025, USA. [2]Geballe Laboratory for Advanced Materials, Departments of Physics and Applied Physics, Stanford University, Stanford, CA 94305, USA. [3]Advanced Light Source, Lawrence Berkeley National Laboratory, Berkeley, CA 94720, USA. [4]Materials and Structures Laboratory, Tokyo Institute of Technology, Kanagawa 226-8503, Japan.

*To whom correspondence should be addressed. E-mail: zxshen@stanford.edu

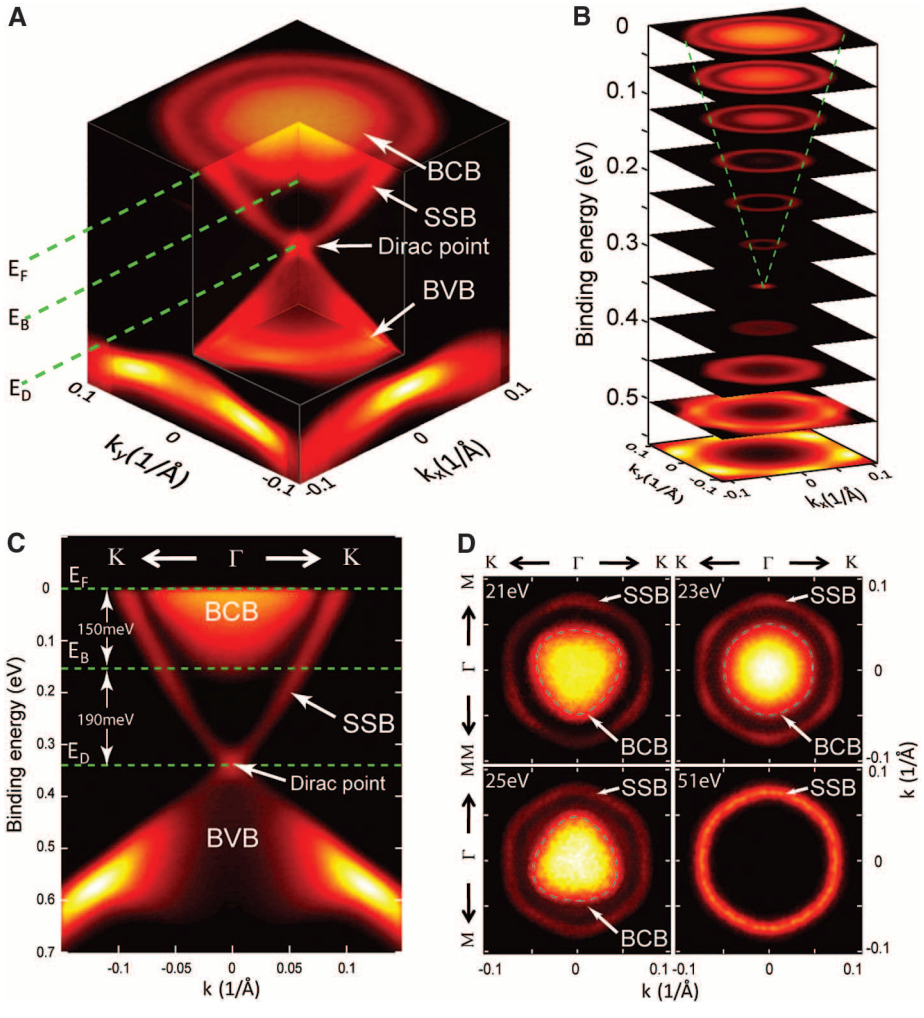

Fig. 1. Electronic band structure of undoped Bi_2Se_3 measured by ARPES. (**A**) The bulk conduction band (BCB), bulk valence band (BVB), and surface-state band (SSB) are indicated, along with the Fermi energy (E_F), the bottom of the BCB (E_B), and the Dirac point (E_D). (**B**) Constant-energy contours of the band structure show the SSB evolution from the Dirac point to a hexagonal shape (green dashed lines). (**C**) Band structure along the K-Γ-K direction, where Γ is the center of the hexagonal surface Brillouin zone (BZ), and the K and M points [see (D)] are the vertex and the midpoint of the side of the BZ, respectively (*14*). The BCB bottom is ~190 meV above E_D and 150 meV below E_F. (**D**) Photon energy–dependent FS maps (symmetrized according to the crystal symmetry). Blue dashed lines around the BCB FS pocket indicate their different shapes.

Downloaded from www.sciencemag.org on August 5, 2010

sive; indeed, we find that the Dirac gap can be observed in magnetically doped samples with or without bulk ferromagnetism (*19*). Furthermore, if E_F can be tuned into this surface-state gap, an insulating massive Dirac fermion state is formed; this state may support many striking topological phenomena, such as the image magnetic monopole induced by a point charge (*20*, *21*), the half quantum Hall effect on the surface with a Hall conductance of $e^2/2h$, and a topological contribution to the Faraday and Kerr effects (*5*). In addition, this state is a concrete realization of the "θ vacuum" state of axion physics in a condensed matter system (*5*), and thus has implications for particle physics and cosmology (*22*). Finally, a tunable energy gap at the surface Dirac point provides a means to control the surface electric transport, which is of great importance for applications.

The insulating massive Dirac fermion state is challenging to realize, because there are two critical requirements that must be simultaneously

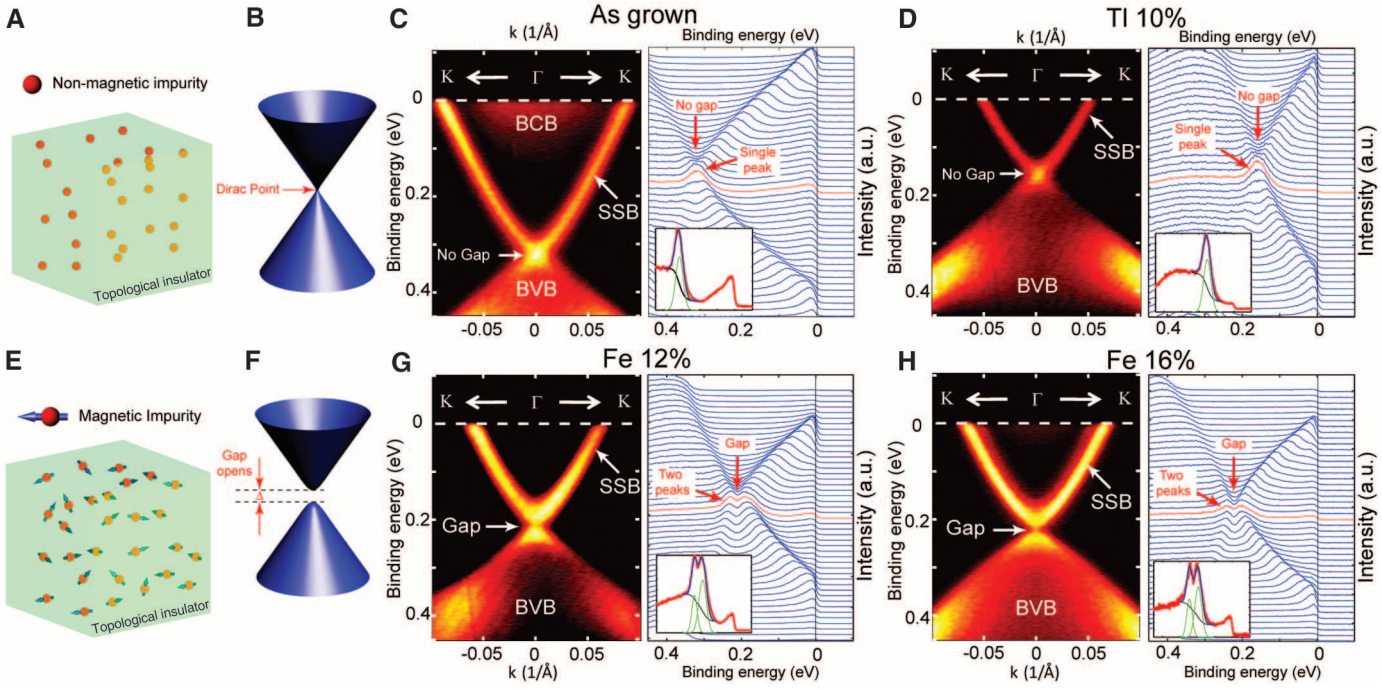

Fig. 2. (**A** and **B**) A nonmagnetically doped topological insulator with a Dirac point connecting the upper and lower Dirac cones as in the undoped case. (**C**) Band structure along the K-Γ-K direction of undoped Bi_2Se_3. Left and right subpanels show the ARPES spectral intensity plot and a stacking plot of the energy distribution curves (EDCs), respectively. The red curve in the right subpanel indicates the EDC at the Γ point. Inset: EDC at the Γ point (red), fitted with a Lorentzian peak (green) on the Shirley background (black); the total fitting function is shown in blue. The same convention is used in (D), (G), and (H). (**D**) Band structure for a Tl-doped sample, $(Bi_{0.9}Tl_{0.1})_2Se_3$. The Dirac point remains continuous. (**E** and **F**) A magnetically doped topological insulator with a broken Dirac point and a gap separating the upper and lower Dirac cones. (**G** and **H**) Band structure of two Fe-doped samples from two growth batches with melt composition $(Bi_{0.88}Fe_{0.12})_2Se_{3.7}$ and $(Bi_{0.84}Fe_{0.16})_2Se_{3.7}$, respectively. At the Dirac point, the reduced spectral intensity (left subpanels) and the twin-peak structure in the EDCs (right subpanels) indicate a gap formation.

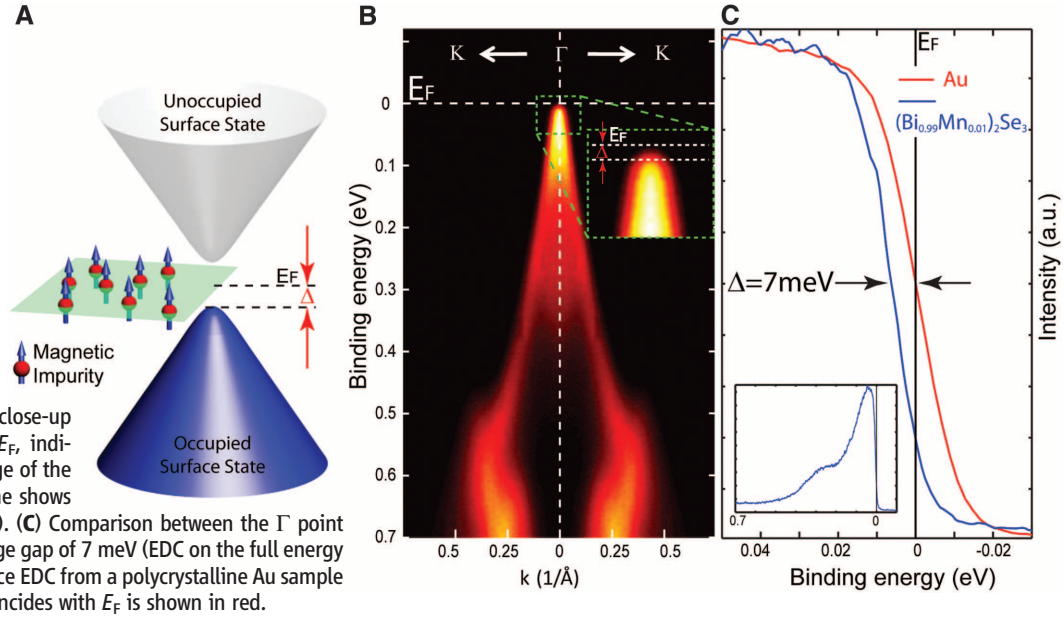

Fig. 3. Realization of the insulating massive Dirac fermion state by simultaneous magnetic and charge doping. (**A**) Gap formation at the Dirac point (caused by magnetic impurities on the surface) and the in-gap E_F position. The occupied and unoccupied Dirac cones are shown in blue and gray, respectively; Δ is the energy difference between the top of the occupied Dirac cone and E_F. (**B**) ARPES spectra intensity plot of the band structure along the K-Γ-K direction of Mn-doped sample $(Bi_{0.99}Mn_{0.01})_2Se_3$ showing the E_F inside the surface Dirac gap. Inset: close-up of the dispersion in the vicinity of E_F, indicating a gap between the leading edge of the SSB and E_F. Vertical white dashed line shows the location of the EDC plotted in (C). (**C**) Comparison between the Γ point EDC (blue) and E_F shows a leading-edge gap of 7 meV (EDC on the full energy scale is plotted in the inset). A reference EDC from a polycrystalline Au sample whose leading edge, as expected, coincides with E_F is shown in red.

Downloaded from www.sciencemag.org on August 5, 2010

satisfied: (i) A gap should open at the Dirac point of the topological surface state (as a result of the breaking of TRS); (ii) the E_F of the system must reside inside both the surface and bulk gaps. We report the realization of this state with simultaneous fulfillment of both requirements in the topological insulator Bi_2Se_3 by introducing an exact amount of magnetic dopants to break the TRS and precisely controlling the E_F position.

We performed angle-resolved photoemission spectroscopy (ARPES) to investigate the electronic structures of intrinsic, nonmagnetically doped, and magnetically doped Bi_2Se_3 (*19*). Figure 1 illustrates the measured band structure of undoped Bi_2Se_3. Similar to Bi_2Te_3 (*14*), besides the Fermi surface (FS) pocket from the surface-state band (SSB), there is also a FS pocket from the bulk conduction band (BCB) (Fig. 1, A to D) due to the Se deficiencies and the Bi-Se intersite defects. The bottom of the BCB is located at 190 meV above the Dirac point (Fig. 1, A and C), indicating a direct bulk gap (*19*). The in-gap Dirac point makes Bi_2Se_3 a better candidate for realizing the insulating massive Dirac fermion state than Bi_2Te_3, in which the Dirac point is below the top of the bulk valence band (BVB) (*14*), thus demanding a much larger surface energy gap for E_F to reside inside both the surface and bulk gaps. The cross-sectional plot of the band structure (Fig. 1B) shows how the SSB evolves from the Dirac point to a hexagonal shape at E_F. Unlike the Bi_2Te_3 band structure, where the SSB FS starts being warped at energies close to the BCB minimum (*14*) and becomes a concave hexagram, the SSB FS of Bi_2Se_3 remains convex hexagonal even in the presence of the BCB. This difference will be reflected in other experiments, such as scanning tunneling microscopy/spectroscopy (STM/STS), where the surface quasi-particle interference around defects can be suppressed in Bi_2Se_3 but not in Bi_2Te_3, where the concave SSB FS shape favors such scattering along specific directions (*23*–*27*).

The surface nature of the hexagonal SSB FS was confirmed by the photon energy–dependent ARPES (Fig. 1D), where its nonvarying shape with different excitation photon energies indicates its 2D nature. By contrast, the shape and the existence of the inner BCB FS pocket changes markedly because of its 3D nature with strong k_z dispersion.

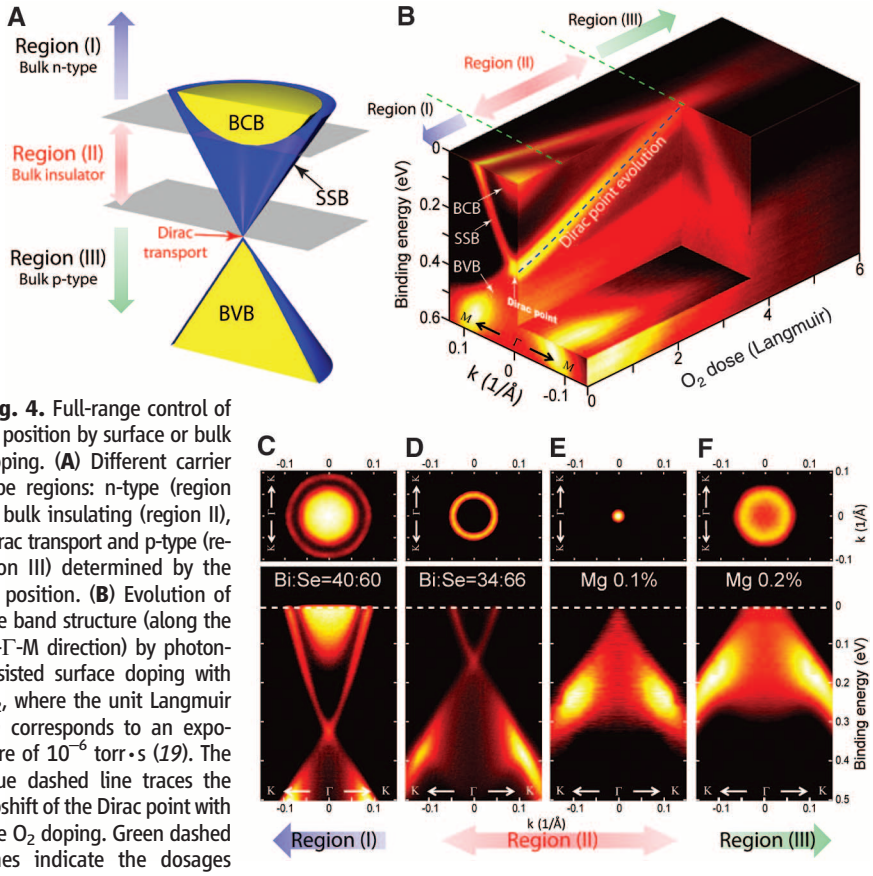

Fig. 4. Full-range control of E_F position by surface or bulk doping. (**A**) Different carrier type regions: n-type (region I), bulk insulating (region II), Dirac transport and p-type (region III) determined by the E_F position. (**B**) Evolution of the band structure (along the M-Γ-M direction) by photon-assisted surface doping with O_2, where the unit Langmuir (L) corresponds to an exposure of 10^{-6} torr·s (*19*). The blue dashed line traces the upshift of the Dirac point with the O_2 doping. Green dashed lines indicate the dosages that separate the three doping regions shown in (A): At 0.95L O_2 dosage, the BCB bottom reaches E_F; at 3.6L, the Dirac point reaches E_F; and beyond 3.6L, the Dirac point is above E_F. (**C** to **F**) Bulk doping: the FS and the band structure of (C) nominally undoped Bi_2Se_3, showing the coexistence of BCB and SSB FS pockets; (D) Se-rich sample (melt composition $Bi_{1.7}Se_{3.3}$) with only an SSB FS, and E_F residing inside the bulk gap ($E_F - E_D = 145$ meV); (E) Mg-doped $(Bi_{0.999}Mg_{0.001})_2Se_3$ sample with a point-like FS and E_F precisely at the Dirac point; and (F) more richly Mg-doped $(Bi_{0.998}Mg_{0.002})_2Se_3$ sample driven into p-type, with a p-type FS and the Dirac point above E_F.

In the presence of TRS, the SSB of Bi_2Se_3 is degenerate at the Dirac point, which connects the upper- and lower-surface Dirac cone (Fig. 2B) even if the system is perturbed by nonmagnetic dopants (Fig. 2A). This is confirmed by the ARPES measurements (Fig. 2, C and D), where the band structures of an intrinsic sample and a nominally 10% Tl-doped sample are shown, respectively. In both cases, the continuity at the Dirac point is indicated by the strong spectral intensity (left subpanels) and the single-peak structure of the energy distribution curve (EDC) at the Dirac point (right subpanels). In Fig. 2D, the charge doping effect of Tl is clearly shown by the marked shift of E_F into the bulk gap ($E_F - E_D = 160$ meV). Nonetheless, the topology of the SSB remains the same with a continuous Dirac point (*19*).

The TRS protection of the Dirac point can be lifted by magnetic dopants (Fig. 2E), resulting in a gap that separates the upper and lower branches of the Dirac cone (Fig. 2F). This is illustrated in the band structure (Fig. 2, G and H) of two Fe-doped samples. Unlike nonmagnetically doped samples, for both Fe-doped samples, the SSB dispersion at the Dirac point is broken, as indicated by the suppressed intensity regions in the spectral density plots (left subpanels) and the twin-peak structure around the Dirac point in the EDC plots (right subpanels). The data have sufficient *k*-space sampling density to reveal the qualitative difference between the nonmagnetic and magnetic dopants: One always finds a single-peak structure in as-grown and nonmagnetically doped samples, whereas the twin-peak structure is present only in magnetically doped samples (*19*). By fitting the twin-peak structure with two Lorentzian peaks (insets in EDC plots of Fig. 2, G and H), the gap size can be acquired, showing a larger value (~50 meV) in Fig. 2H than that (~44 meV) in Fig. 2G. This trend (*19*) is consistent with the increase of the magnetic moment upon increasing the magnetic dopant concentration.

The SSB gap formation at the Dirac point with broken TRS is the first step in realizing the insulating massive Dirac fermion state; the second step is to tune the E_F into this gap. In the Fe-doped Bi_2Se_3, however, E_F was found to always reside above the Dirac point (similar to undoped Bi_2Se_3), making the material n-type (Fig. 2, G and H). To remove these excess n-type carriers while maintaining the magnetic doping effect, we changed the dopant from Fe to Mn, another magnetic material with one less valence electron than Fe. Indeed, Mn dopants not only introduce magnetic moments into the system, but also naturally p-dope the samples. The measurements on an optimally doped sample (*19*) show E_F residing just inside the SSB gap (Fig. 3B). By comparing the leading edge of the EDC at the Γ point to E_F (Fig. 3C; also shown is an Au reference spectrum), we found a 7-meV difference, indicating a SSB Dirac gap of at least 7 meV (Fig. 3A). Such a gap suggests a ferromagnetic order of the Mn dopants on the surface, which can be induced by the ferromagnetic spin-spin interaction mediated by the

Downloaded from www.sciencemag.org on August 5, 2010

surface states (*18*). This optimally doped sample thus fully realizes the insulating massive Dirac fermion state and provides a model system for studying striking topological phenomena (*5*, *20*–*22*).

To maintain this insulating massive Dirac fermion state at higher temperatures requires a further increase of the Dirac gap (while keeping E_F inside it). However, because of the hole-doping effect of Mn dopants, one cannot simply increase the Mn concentration in $(Bi_{1-\delta}Mn_\delta)_2Se_3$ to acquire a larger Dirac gap, as the system will become p-type before the gap magnitude increases appreciably (*19*). However, we found that it was possible to introduce many Fe dopants into Bi_2Se_3 to increase the gap size without substantially altering the E_F position relative to the undoped Bi_2Se_3; if we can then move E_F into the gap by introducing additional p-type dopants, we can achieve a larger gap while preserving the insulating nature of the state.

Figure 4 demonstrates the full range of E_F tuning by introducing such p-type doping, with three doping regions and the topological transport point (where E_F coincides with the Dirac point) shown in Fig. 4A. By either surface doping [Fig. 4B and (*19*)] or bulk doping (Fig. 4, C to F), we were able to tune the E_F to any of the regions defined in Fig. 4A. The ability to convert the original n-type sample to p-type by surface doping (Fig. 4B, region III) is critical for applications requiring both types of carriers or p-n junctions. On the other hand, full-range bulk doping (Fig. 4, C to F) has advantages over surface doping in bulk applications.

References and Notes

1. B. A. Bernevig, T. L. Hughes, S.-C. Zhang, *Science* **314**, 1757 (2006).
2. M. König *et al.*, *Science* **318**, 766 (2007); published online 20 September 2007 (10.1126/science.1148047).
3. X. L. Qi, S. C. Zhang, *Phys. Today* **63**, 33 (2010).
4. L. Fu, C. L. Kane, E. J. Mele, *Phys. Rev. Lett.* **98**, 106803 (2007).
5. X. L. Qi, T. L. Hughes, S. C. Zhang, *Phys. Rev. B* **78**, 195424 (2008).
6. A. P. Schnyder, S. Ryu, A. Furusaki, A. W. Ludwig, *Phys. Rev. B* **78**, 195125 (2008).
7. L. Fu, C. L. Kane, *Phys. Rev. Lett.* **102**, 216403 (2009).
8. A. R. Akhmerov, J. Nilsson, C. W. J. Beenakker, *Phys. Rev. Lett.* **102**, 216404 (2009).
9. J. E. Moore, L. Balents, *Phys. Rev. B* **75**, 121306(R) (2007).
10. R. Roy, *Phys. Rev. B* **79**, 195321 (2009).
11. B. Seradjeh, J. E. Moore, M. Franz, *Phys. Rev. Lett.* **103**, 066402 (2009).
12. H. Zhang *et al.*, *Nat. Phys.* **5**, 438 (2009).
13. Y. Xia *et al.*, *Nat. Phys.* **5**, 398 (2009).
14. Y. L. Chen *et al.*, *Science* **325**, 178 (2009); published online 11 June 2009 (10.1126/science.1173034).
15. J. Choi *et al.*, *Phys. Status Solidi B* **241**, 1541 (2004).
16. Y. S. Hor *et al.*, *Phys. Rev. B* **81**, 195203 (2010).
17. R. Yu *et al.*, *Science* **329**, 61 (2010); published online 3 June 2010 (10.1126/science.1187485).
18. Q. Liu, C. X. Liu, C. K. Xu, X. L. Qi, S. C. Zhang, *Phys. Rev. Lett.* **102**, 156603 (2009).
19. See supporting material on *Science* Online.
20. X.-L. Qi, R. Li, J. Zang, S.-C. Zhang, *Science* **323**, 1184 (2009); published online 29 January 2009 (10.1126/science.1167747).
21. J. Zang, N. Nagaosa, *Phys. Rev. B* **81**, 245125 (2010).
22. F. Wilczek, *Nature* **458**, 129 (2009).
23. L. Fu, *Phys. Rev. Lett.* **103**, 266801 (2009).
24. X. Zhou, C. Fang, W. F. Tsai, J. P. Hu, *Phys. Rev. B* **80**, 245317 (2009).
25. W. C. Lee, C. Wu, D. P. Arovas, S. C. Zhang, *Phys. Rev. B* **80**, 245439 (2009).
26. Z. Alpichshev *et al.*, *Phys. Rev. Lett.* **104**, 016401 (2010).
27. T. Zhang *et al.*, http://arxiv.org/abs/0908.4136 (2009).

28. Supported by the Department of Energy, Office of Basic Energy Science, under contract DE-AC02-76SF00515.

Supporting Online Material

www.sciencemag.org/cgi/content/full/329/5992/659/DC1
Materials and Methods
SOM Text
Figs. S1 to S6
Movies S1 to S3
References

22 March 2010; accepted 16 June 2010
10.1126/science.1189924

Quantum Correlations in Optical Angle–Orbital Angular Momentum Variables

Jonathan Leach,[1] Barry Jack,[1] Jacqui Romero,[1] Anand K. Jha,[2] Alison M. Yao,[3] Sonja Franke-Arnold,[1] David G. Ireland,[1] Robert W. Boyd,[2] Stephen M. Barnett,[3] Miles J. Padgett[1]*

Entanglement of the properties of two separated particles constitutes a fundamental signature of quantum mechanics and is a key resource for quantum information science. We demonstrate strong Einstein, Podolsky, and Rosen correlations between the angular position and orbital angular momentum of two photons created by the nonlinear optical process of spontaneous parametric down-conversion. The discrete nature of orbital angular momentum and the continuous but periodic nature of angular position give rise to a special sort of entanglement between these two variables. The resulting correlations are found to be an order of magnitude stronger than those allowed by the uncertainty principle for independent (nonentangled) particles. Our results suggest that angular position and orbital angular momentum may find important applications in quantum information science.

In 1935, Einstein, Podolsky, and Rosen (EPR) proposed a Gedanken experiment that was intended to show that quantum mechanics is incomplete (*1*). Their proposal supposes the existence of two spatially separated particles that are perfectly correlated in both position and momentum. Measurement of the position (or alternatively the momentum) of one particle would then determine instantaneously the position (or momentum) of the second particle. The ability to infer either the position or the momentum of the second particle from a distant measurement on the first seems to imply that both of these quantities must have been predetermined. However, quantum theory (and specifically the uncertainty principle) does not allow the simultaneous, exact knowledge of two noncommuting observables, such as position and momentum, as seems to be required for the second particle. A demonstration of EPR correlations establishes either that quantum mechanics is incomplete, in that systems possess additional hidden variables, or that quantum mechanics is nonlocal, in that measurement of the position or momentum of either particle results in an instantaneous uncertainty of the momentum or position, respectively, of both (*2*).

In 1964, Bell deduced an inequality that distinguishes the predictions of quantum theory from those of any local hidden variable theory (*3*, *4*). Since that time, many experiments have been performed that have decided strongly in favor of quantum theory (*5*, *6*). These Bell-type tests apply only to discrete state-spaces, originally of two dimensions or, more recently, to three or higher dimensions (*7*–*9*). In contrast, EPR correlations provide a demonstration of entanglement both for discrete and continuous variables, such as energy and time (*10*), position and linear momentum (*11*), spatial modes (*12*, *13*), and images (*14*).

In addition to linear momentum, light may also carry angular momentum. The spin angular momentum is manifest as the polarization of light and is described completely within a two-dimensional Hilbert space. However, light beams can also carry a measurable orbital angular momentum that results from their helical phase structure. This phase structure can be described by $\exp(i\ell\phi)$(*15*, *16*), where ϕ is the azimuthal angle and ℓ can take any integer value, corresponding to an orbital angular momentum in the direction of propagation of $L_z = \ell\hbar$ per photon, where $\hbar$ is Planck's constant h divided by 2π. For restricted subspaces of two or three dimensions, the orbital angular momentum variable has previously been shown to be an entangled property of down-converted photon pairs (*17*, *18*) and to violate a

[1]Department of Physics and Astronomy, Scottish Universities Physics Alliance (SUPA), University of Glasgow, Glasgow, G12 8QQ, UK. [2]Institute of Optics, University of Rochester, Rochester, NY 14627, USA. [3]Department of Physics, SUPA, University of Strathclyde, Glasgow, G4 0NG, UK.

*To whom correspondence should be addressed. E-mail: m.padgett@physics.gla.ac.uk

Downloaded from www.sciencemag.org on August 5, 2010

Bell-type inequality (*19*, *20*). However, these present measurements are different in that they are performed in conjunction with the measurement of angular position, the variable conjugate to angular momentum, and hence demonstrate the existence of EPR correlations.

The probability distributions for linear momentum and position are simply Fourier transforms of each other, and the relationship between the standard deviations of their distributions is expressed in the familiar Heisenberg uncertainty relation $\Delta x \Delta p \geq \hbar/2$. In contrast, angle is 2π periodic, and so the Fourier relation between angular position and angular momentum has a different form (*21*, *22*). The periodic, and therefore bounded, angular variable is expressed as a discrete and unbounded Fourier series of angular momenta. Indeed, it is this angular periodicity that gives the quantized—that is, discrete—nature of angular momentum.

We established experimentally that entanglement, as manifest by EPR correlations, exists for angular variables (*23*). Our apparatus is based on parametric down-conversion, in which a quasi-continuous-wave, mode-locked ultraviolet pump beam at 355 nm is incident on a 3-mm length of nonlinear crystal [β-barium borate (BBO)] (Fig. 1) (*24*).

Key to our approach is that just as the spatial light modulator (SLM) can be programmed to transform the fundamental near-Gaussian mode emitted from a fiber into any complex spatial mode of choice, if operated in reverse the same hologram can efficiently couple the same complicated mode distribution back into a fiber. In this configuration, the SLM acts as a mode filter, allowing the transverse spatial state of the down-converted photons to be inferred. Although SLMs have previously been used to measure the orbital angular momentum of down-converted photons (*25*, *26*), we used a spatial variation in the blazing function (*27*) to also measure the angular position of the down-converted photons. The advantage of SLMs over static holographic components, or other phase filters, is that they can be electronically programmed to switch among different arbitrary measurement states.

To measure the orbital angular momentum state ℓ of the detected photon, we used the typical forked diffraction grating that has been widely implemented for beam generation (*28*) and single-photon measurement (*17*, *25*). The SLM is programmed with a spatial phase variation $\Phi(x, y)$, centered at $x = 0$, $y = 0$, given by

$$\Phi(x,y) = |\ell(\arctan\, x/y) + 2\pi\Lambda x|_{\mathrm{mod}2\pi} \quad (1)$$

where Λ is the period of the linear grating, to separate the first-order diffracted beam. Changing the order ℓ of the fork dislocation in the center of the hologram allows sequential measurement of an arbitrarily wide range of orbital angular momentum states. Alternatively, to measure the angular position we defined a Gaussian-profile, angular-sector transmission aperture that can be varied both in its width θ and orientation ϕ. A narrower aperture gives an inherently more precise measurement of angular position but with a commensurately lower signal. The SLM is programmed with a spatial phase variation $\Phi(x, y)$ given by

$$\Phi(x,y) = |2\pi\Lambda x|_{\mathrm{mod}2\pi} \times \mathrm{sinc}^2\left(\pi\left(1 - \left(\exp\frac{-(\arctan(x/y) - \phi)^2}{\theta^2}\right)\right)\right) \quad (2)$$

where the sinc term effectively sets the depth of the blazing to produce the desired intensity mask (*27*). The angle $(\arctan(x/y) - \phi)$ is taken to be equal to the offset from the center of the aperture of width θ (we circumvented the numerical ambiguity in the vicinity of the angular origin). Although the Gaussian profile does correspond strictly to the minimum uncertainty state (*29*), the precise profile and minimum width of the sector apertures are not central to our argument nor to the results.

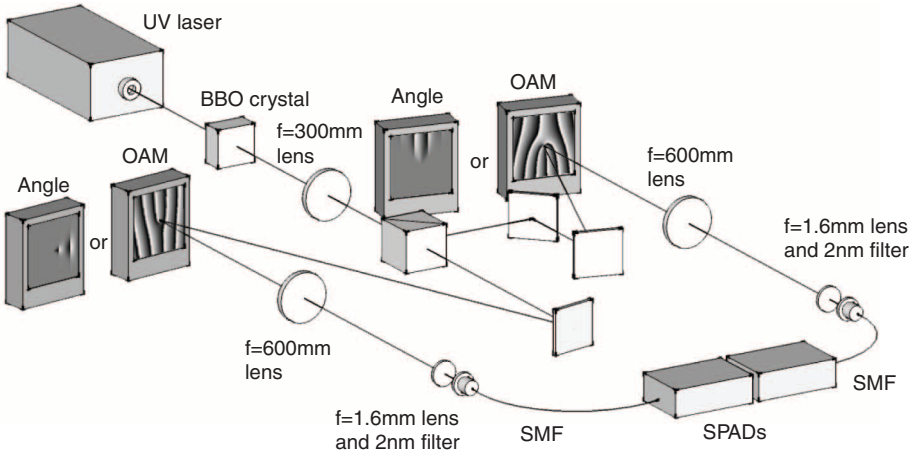

Fig. 1. Schematic of the experiment. The nonlinear BBO crystal is imaged onto two SLMs, one in the signal arm and one in the idler arm. The SLMs are then imaged onto single-mode fibers, coupling the light to SPAD detectors (single-photon avalanche photo-diodes) from which the signals are routed to coincidence-counting electronics. The SLMs can be used to measure either the angular correlations or the orbital angular momentum (OAM) correlations of the entangled fields.

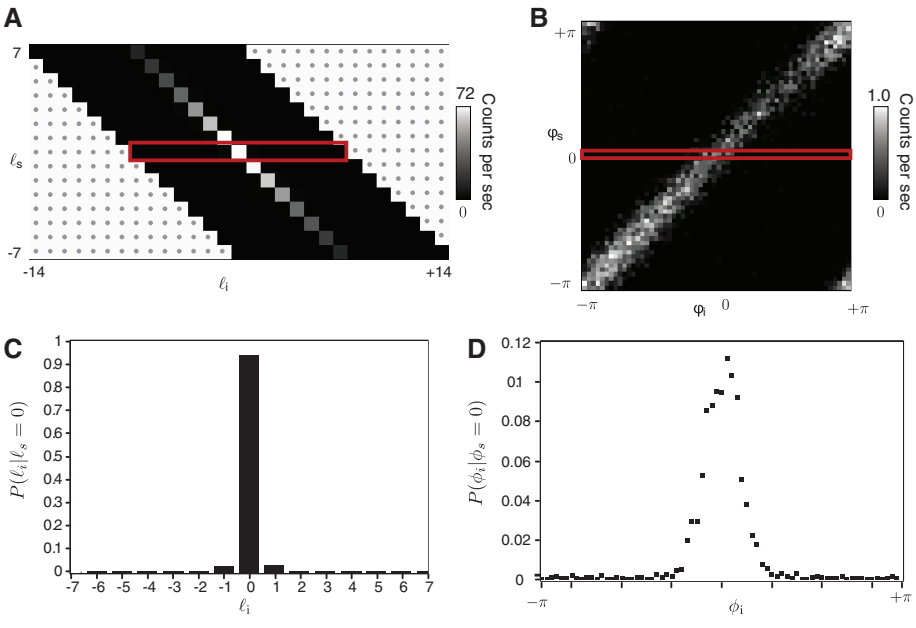

Fig. 2. Experimental results. (**A**) The coincidence count rate as a function of the measured orbital angular momentum in the signal and idler arms (corresponding to ≈20 hours of data collection). (**B**) The coincidence count rate as a function of the orientation of the sector apertures in the signal and idler arms (corresponding to ≈200 hours of data). (**C**) Conditional probability distribution of the orbital angular momentum of the idler photon for the case $\ell_s = 0$, corresponding to the row highlighted in red in (A). (**D**) Similarly, the conditional probability of the angular position ϕ_i is shown for $\phi_s = 0$.

Downloaded from www.sciencemag.org on August 5, 2010

When either the signal or idler beam is viewed independently, the lack of constraint on its phase structure implies that a spatially coherent pump beam creates spatially incoherent down-converted light (*30*), with a speckle size dictated by the phase-matching bandwidth of the crystal. The size of this speckle with respect to the pump beam sets the modal spatial bandwidth of the incoherent output. For a plane-wave or Gaussian pump beam, conservation of orbital angular momentum between the signal and idler photons results in a high coincidence count rate whenever $\ell_s + \ell_i = 0$. However, the strength is modulated by the envelope of the generated modal bandwidth (*31*) and further modified by the relative detection efficiency of the different states. Similarly, for measurements made in an image plane of the crystal the coincidence count rate for angular measurements is highest whenever $\phi_s - \phi_i = 0$.

In practice, perfect correlations in both orbital angular momentum and angular position of the down-converted pairs are unobtainable. In order to demonstrate EPR correlations, we used the more experimentally useful criterion that is based on measuring the conditional probability of finding a particular outcome in one system given a measurement in the other (*32*). Angular momentum is discrete, and angular position is periodic. However, for narrow apertures the Fourier relationship between their variances is the same as for the unbounded continuous case (*22*), and we can write the EPR-Reid criterion as a violation of the inequality

$$(\Delta_{\text{inf}}\ell_s)^2(\Delta_{\text{inf}}\phi_s)^2 \geq 1/4 \qquad (3)$$

The measured angular momentum and angle correlations are shown in Fig. 2, A and B. In both cases, the actual value of the angular momentum or position in the signal and idler beams is not important; rather, it is the difference between measurements in the signal and idler beams that determines the widths of the probability distributions. Also, the precise form of the angular aperture is not important; rather, it is the width of the measured correlation made with respect to the central position of the two apertures.

For the orbital angular momentum states, we measured all combinations of ℓ_s from –7 to +7 and ℓ_i from $\ell_s - 7$ to $\ell_s + 7$, corresponding to the approximate spiral bandwidth of our system. For the angular states, we used an angular aperture width of $\theta = \pi/15$ and measured all combinations of ϕ_s and ϕ_i in 60 equally spaced angular bins. The measured correlations shown in Fig. 2, A and B, are maximal whenever $\ell s + \ell_i = 0$ or $\phi_s - \phi_i = 0$, respectively. Shown in Fig. 2, C and D, are single sections through this data, illustrating the strength of the angular momentum and angle correlations.

As with all experimental data, small amounts of random noise can adversely affect the statistical estimate of the variance of a distribution. We minimized this noise by running the experiment at a low flux (≈20,000 photon pairs s^{-1}), which minimizes the number of accidental coincidence counts arising from classical correlations.

Without any background subtraction, we obtained $(\Delta_{\text{inf}}\ell_s)^2 = 0.348 \pm 0.022$ and $(\Delta_{\text{inf}}\phi_s)^2 = 0.456 \pm 0.012$, giving a variance product of 0.159 ± 0.011, which is approximately half of the lower bound of 0.25 required by the EPR argument.

We can also calculate the strength of the correlations when we subtract our best estimate of the background counts. For each measured number of coincidence counts N, we inferred the number of true coincidences C and accidental coincidences B so that $B + C = N$. Using the expected number of accidentals, calculated from $S_sS_i\Delta t$, the probability of a count being an accidental coincidence is taken to be $r = \text{Min}[1, S_sS_i\Delta t/N]$, so that the maximum probability is unity. The expectation value of B is then $\langle B\rangle = Nr$. This enables a subtraction of accidental counts but ensures that we obtain nonnegative values for the calculation of probability or entropy.

Subtracting this calculated background to remove accidental coincidences, we obtained $(\Delta_{\text{inf}}\ell_s)^2 = 0.171 \pm 0.018$ and $(\Delta_{\text{inf}}\phi_s)^2 = 0.140 \pm 0.007$, giving a variance product of 0.024 ± 0.004, approximately one tenth of the lower bound required by the EPR argument, hence showing a strong demonstration of the effect.

We also adopted an alternative EPR criterion that is based on entropy rather than variance (*33*–*37*). This approach has a number of advantages. First, the entropic uncertainty relation does not require the calculation of a variance, and the calculation of entropy does not require us to deal with the complications associated with the cyclic nature of the angular variable (*38*, *39*). Secondly, the inequality is state-independent (*35*, *36*), which makes it possible to make a quantitative comparison of our EPR experiment with those reported for different physical systems. Finally, the entropic approach relates the strength of the correlations to the quantum information content of the system (*37*). The entropic uncertainty relation for angular position and angular momentum is (*35*, *36*)

$$H(\ell) + H(\phi) \geq \log_2(2\pi) \qquad (4)$$

where $H(\ell) = -\sum_{\ell} P(\ell)\log_2 P(\ell)$ and $H(\phi) = -\int_{-\pi}^{\pi} d\phi P(\phi)\log_2 P(\phi)$ are the Shannon entropies for the discrete angular momentum variable ℓ and the continuous angle variable ϕ, respectively. We measured the angle in discrete segments, with N segments filling the 2π interval. Direct comparison with our data, therefore, requires us to write our angle entropy in terms of the measured probabilities for these discrete segments ϕ^m as (*36*)

$$H(\phi) = -\sum_m P(\phi_s^m)\log_2 P(\phi^m) - \log_2\left(\frac{N}{2\pi}\right) \qquad (5)$$

A demonstration of EPR correlations corresponds to a violation of the entropic uncertainty relation for the inferred values, which is a violation of the inequality

$$H_{\text{inf}}(\ell_s) + H_{\text{inf}}(\phi_s) = -\sum_{\ell_s,\ell_i} P(\ell_i)P(\ell_s|\ell_i)\log_2 P(\ell_s|\ell_i) - \int_{-\pi}^{\pi} d\phi_i \int_{-\pi}^{\pi} d\phi_s P(\phi_i)P(\phi_s|\phi_i)\log_2 \times P(\phi_s|\phi_i) \geq \log_2(2\pi) \qquad (6)$$

Using the data presented in Fig. 2, A and B, we obtained values of 1.548 ± 0.017 and 0.887 ± 0.018 for $H_{\text{inf}}(\ell_s) + H_{\text{inf}}(\phi_s)$, without and with background subtraction, respectively. Both of these values are significantly below the EPR limit of 2.651.

The results confirm that the EPR conclusion, namely that quantum mechanics is incomplete or nonlocal, applies not only to position and momentum but also to angular position and angular momentum. Unlike demonstrations of Bell-type inequalities, which are restricted to discrete state spaces, EPR correlations simultaneously span an extended range of orbital angular momentum states and the continuous state space of angular position. The demonstration of angular EPR correlations establishes that angular position and angular momentum are suitable variables for applications in quantum information processing, notably in protocols for quantum key distribution (*40*).

Downloaded from www.sciencemag.org on August 5, 2010

References and Notes

1. A. Einstein, B. Podolsky, N. Rosen, *Phys. Rev.* **47**, 777 (1935).
2. M. D. Reid *et al.*, *Rev. Mod. Phys.* **81**, 1727 (2009).
3. J. S. Bell, *Physics* **1**, 195 (1964).
4. J. S. Bell, *Speakable and Unspeakable in Quantum Mechanics* (Cambridge Univ. Press, New York, 1987).
5. S. J. Freedman, J. F. Clauser, *Phys. Rev. Lett.* **28**, 938 (1972).
6. A. Aspect, P. Grangier, G. Roger, *Phys. Rev. Lett.* **49**, 91 (1982).
7. A. Vaziri, G. Weihs, A. Zeilinger, *Phys. Rev. Lett.* **89**, 240401 (2002).
8. N. K. Langford *et al.*, *Phys. Rev. Lett.* **93**, 053601 (2004).
9. D. Collins, N. Gisin, N. Linden, S. Massar, S. Popescu, *Phys. Rev. Lett.* **88**, 040404 (2002).
10. P. G. Kwiat, A. M. Steinberg, R. Y. Chiao, *Phys. Rev. A* **47**, R2472 (1993).
11. J. C. Howell, R. S. Bennink, S. J. Bentley, R. W. Boyd, *Phys. Rev. Lett.* **92**, 210403 (2004).
12. K. Wagner *et al.*, *Science* **321**, 541 (2008).
13. M. Lassen, G. Leuchs, U. L. Andersen, *Phys. Rev. Lett.* **102**, 163602 (2009).
14. V. Boyer, A. M. Marino, R. C. Pooser, P. D. Lett, *Science* **321**, 544 (2008).
15. L. Allen, M. W. Beijersbergen, R. J. Spreeuw, J. P. Woerdman, *Phys. Rev. A* **45**, 8185 (1992).
16. S. Franke-Arnold, L. Allen, M. J. Padgett, *Laser Photon. Rev.* **2**, 299 (2008).
17. A. Mair, A. Vaziri, G. Weihs, A. Zeilinger, *Nature* **412**, 313 (2001).
18. J. B. Pors *et al.*, *Phys. Rev. Lett.* **101**, 120502 (2008).
19. A. Vaziri, G. Weihs, A. Zeilinger, *Phys. Rev. Lett.* **89**, 240401 (2002).
20. J. Leach *et al.*, *Opt. Express* **17**, 8287 (2009).

21. S. M. Barnett, D. T. Pegg, *Phys. Rev. A* **42**, 6713 (1990).
22. S. Franke-Arnold *et al*., *N. J. Phys.* **6**, 103 (2004).
23. J. Götte, S. M. Barnett, S. Franke-Arnold, *J. Mod. Opt.* **53**, 627 (2006).
24. Materials and methods are available as supporting material on *Science* Online.
25. E. Yao, S. Franke-Arnold, J. Courtial, M. J. Padgett, S. M. Barnett, *Opt. Express* **14**, 13089 (2006).
26. M. Stotz, S. Gröblacher, T. Jennewein, A. Zeilinger, *Appl. Phys. Lett.* **90**, 261114 (2007).
27. J. Leach, M. Dennis, J. Courtial, M. Padgett, *N. J. Phys.* **7**, 55 (2005).
28. V. Bazhenov, M. Vasnetsov, M. Soskin, *JETP Lett.* **52**, 429 (1990).
29. D. T. Pegg, S. M. Barnett, R. Zambrini, S. Franke-Arnold, M. Padgett, *N. J. Phys.* **7**, 62 (2005).
30. J. Arlt, K. Dholakia, L. Allen, M. Padgett, *Phys. Rev. A* **59**, 3950 (1999).
31. J. Torres, A. Alexandrescu, L. Torner, *Phys. Rev. A* **68**, 050301 (2003).
32. M. D. Reid, *Phys. Rev. A* **40**, 913 (1989).
33. S. P. Walborn, B. G. Taketani, A. Salles, F. Toscano, R. L. de Matos Filho, *Phys. Rev. Lett.* **103**, 160505 (2009).
34. S. P. Walborn, A. Salles, R. M. Gomes, F. Toscano, P. H. Souto Ribeiro, "An Entropic Einstein-Podolsky-Rosen Criterion" available at arXiv:0907.4263v1 (2009).
35. I. Bialynicki-Birula, J. Mycielski, *Commun. Math. Phys.* **44**, 129 (1975).
36. A. Rojas-Gonzales, J. A. Vaccaro, S. M. Barnett, *Phys. Lett. A* **205**, 247 (1995).
37. S. M. Barnett, S. J. D. Phoenix, *Phys. Rev. A* **40**, 2404 (1989).
38. S. M. Barnett, D. T. Pegg, *J. Mod. Opt.* **36**, 7 (1989).
39. G. M. Forbes, M. A. Alonso, A. E. Siegman, *J. Phys. Math. Gen.* **36**, 1 (2003).
40. F. Grosshans, N. J. Cerf, *Phys. Rev. Lett.* **92**, 047905 (2004).
41. This work is supported by the UK Engineering and Physical Sciences Research Council. S.F.A. is a Research Councils UK Research Fellow. S.M.B. and M.J.P. thank the Royal Society and the Wolfson Foundation. We thank J. Götte and D. Oi for useful discussions. We acknowledge the financial support of the Future and Emerging Technologies (FET) program within the Seventh Framework Programme for Research of the European Commission, under the FET Open grant agreement HIDEAS number FP7-ICT-221906. We would like to thank Hamamatsu for their support of this work. A.K.J. and R.W.B. were supported by a U.S. Department of Defense Multidisciplinary University Research Initiative award. The experiment was devised by J.L., M.J.P., and A.K.J. and performed by J.L., B.J., and J.R. D.I. designed the coincidence-counting electronics. S.M.B. and A.M.Y. formulated the inequalities. The results were interpreted and the manuscript drafted by M.J.P., S.M.B., A.M.Y., J.L., R.W.B., and S.F.A., with further inputs from all authors.

Supporting Online Material
www.sciencemag.org/cgi/content/full/329/5992/662/DC1
Materials and Methods

6 April 2010; accepted 22 June 2010
10.1126/science.1190523

Downloaded from www.sciencemag.org on August 5, 2010

MESSENGER Observations of Extreme Loading and Unloading of Mercury's Magnetic Tail

James A. Slavin,[1]* Brian J. Anderson,[2] Daniel N. Baker,[3,4] Mehdi Benna,[5,6] Scott A. Boardsen,[1,6] George Gloeckler,[7,8] Robert E. Gold,[2] George C. Ho,[2] Haje Korth,[2] Stamatios M. Krimigis,[2,9] Ralph L. McNutt Jr.,[2] Larry R. Nittler,[10] Jim M. Raines,[7] Menelaos Sarantos,[1,6] David Schriver,[11] Sean C. Solomon,[10] Richard D. Starr,[12] Pavel M. Trávníček,[11,13] Thomas H. Zurbuchen[7]

During MESSENGER's third flyby of Mercury, the magnetic field in the planet's magnetic tail increased by factors of 2 to 3.5 over intervals of 2 to 3 minutes. Magnetospheric substorms at Earth are powered by similar tail loading, but the amplitude is lower by a factor of ~10 and typical durations are ~1 hour. The extreme tail loading observed at Mercury implies that the relative intensity of substorms must be much larger than at Earth. The correspondence between the duration of tail field enhancements and the characteristic time for the Dungey cycle, which describes plasma circulation through Mercury's magnetosphere, suggests that such circulation determines the substorm time scale. A key aspect of tail unloading during terrestrial substorms is the acceleration of energetic charged particles, but no acceleration signatures were seen during the MESSENGER flyby.

Magnetospheric substorms are space weather disturbances powered by the rapid release of magnetic energy stored in the lobes of planetary magnetic tails (*1*). The loading and unloading of Earth's tail occurs on time scales of ~1 hour and is closely correlated with a southward component of the interplanetary magnetic field (IMF) (i.e., opposite to the planetary magnetic field at the nose of the magnetosphere), a geometry that transports magnetic flux into the tail via magnetic reconnection between the IMF and the dayside geomagnetic field (*2*). During a substorm, the accumulated magnetic energy is unloaded through reconnection of the oppositely directed magnetic fields in the tail lobes, resulting in the ejection of plasmoids, high-speed sunward and antisunward jetting of hot plasma, acceleration and injection of charged particles into the inner magnetosphere, and field-aligned currents flowing between the tail and the high-latitude atmosphere where aurorae are produced (*3*). Here, we report observations by the MErcury Surface, Space ENvironment, GEochemistry, and Ranging (MESSENGER) spacecraft of substorm-like magnetic tail-loading events at Mercury.

This circulation of plasma, magnetic flux, and energy from the dayside X-line at the terrestrial magnetopause to the nightside X-line in the cross-tail current layer and, later, back to the dayside magnetosphere constitutes the Dungey cycle (*4*), whose energy is drawn from the solar wind. The large magnetic field component normal to the magnetopause measured during the second MESSENGER flyby of Mercury, when the IMF was southward, implied a cross-magnetosphere electric potential of ~30 kV or a mean dawn-to-dusk electric field of ~2 mV/m (*5*). This electric field implies a Dungey cycle time (i.e., time to drift in response to the dawn-to-dusk magnetospheric electric field from local noon to midnight in the polar cap, or from the northern boundary of the tail down to the cross-tail current sheet) at Mercury of ~2 min. The ~1-hour Dungey cycle time at Earth is believed to be the underlying reason for the ~1- to 3-hour duration of terrestrial substorms (*1*, *4*).

MESSENGER's third flyby of Mercury occurred on 29 September 2009. The IMF immediately preceding the flyby of Mercury had a variable north-south orientation and a magnitude of ~28 nT, ~50% stronger than for the previous encounters. Like the other MESSENGER flybys, the M3 trajectory was near equatorial, and the spacecraft entered the magnetosphere through the downstream dusk magnetosheath and exited just forward of the dawn terminator (Fig. 1). The inbound bow shock (BS) and (average) magnetopause (MP) crossing times were 20:56:06 and 21:27:45 UTC, respectively. The MESSENGER spacecraft autonomously terminated science observations and entered a "safe hold" at 21:48:37 UTC, so no outbound boundary crossings were measured. A fit to the MESSENGER and Mariner 10 averaged boundary crossings using methods and functional forms recently applied to Mercury (*6*–*9*) yielded mean subsolar bow shock and magnetopause planetocentric distances of 1.7 and

[1]Heliophysics Science Division, NASA Goddard Space Flight Center, Greenbelt, MD 20771, USA. [2]Johns Hopkins University Applied Physics Laboratory, Laurel, MD 20723, USA. [3]Laboratory for Atmospheric and Space Physics, University of Colorado, Boulder, CO 80303, USA. [4]Department of Physics and Astrophysical and Planetary Sciences Department, University of Colorado, Boulder, CO 80303, USA. [5]Solar System Exploration Division, NASA Goddard Space Flight Center, Greenbelt, MD 20771, USA. [6]Goddard Earth Science and Technology Center, University of Maryland, Baltimore County, Baltimore, MD 21228, USA. [7]Department of Astronomy, University of Maryland, College Park, MD 20742, USA. [8]Department of Atmospheric, Oceanic and Space Sciences, University of Michigan, Ann Arbor, MI 48109, USA. [9]Academy of Athens, Athens 11527, Greece. [10]Department of Terrestrial Magnetism, Carnegie Institution of Washington, Washington, DC 20015, USA. [11]Institute of Geophysics and Planetary Physics, University of California, Los Angeles, CA 90024, USA. [12]Department of Physics, Catholic University of America, Washington, DC 20064, USA. [13]Astronomical Institute, Academy of Sciences of the Czech Republic, Prague 14131, Czech Republic.

*To whom correspondence should be addressed. E-mail: james.a.slavin@nasa.gov

1.3 R_M, respectively, where R_M is Mercury's radius (Fig. 1).

After the magnetopause crossing, Magnetometer data (*10*) spanning the dusk-side tail were acquired as the spacecraft moved from X_{MSO} = –1.85 to –1.29 R_M and Y_{MSO} = 2.40 to 0.16 R_M. Within the magnetosphere, the magnetic field data (Fig. 2) show a strong negative B_X component, indicating that the spacecraft entered Mercury's magnetic tail through the southern lobe and remained there for about 20 min. There were several brief encounters with the plasma sheet, during which the field strength was temporarily depressed.

During the four intervals labeled events 1, 2, 3, and 4 in Fig. 2, each lasting 2 to 3 min, the magnitude of the magnetic field in Mercury's tail increased and then decreased by factors of ~2 to 3.5. Events 2 to 4 corresponded to higher $|B_Y/B_X|$ than the intervening periods, indicating increased flaring of the magnetic tail. The magnetic field in the tail is in pressure equilibrium with the external solar wind. The tail magnetic field increases because of either enhanced external solar wind pressure or loading of the tail with additional magnetic flux. The latter process forces the magnetopause to flare outward and increase the angle of incidence of the solar wind on the tail magnetopause. The $|B_Y/B_X|$ signatures of greater tail flaring imply that the field increases were due to flux loading of the tail (*2*).

Event 1, observed at the outer edge of the tail, was marked by an overall increase in the tail magnetic field strength to 56 nT followed by a decrease to ~20 nT (Fig. 2). Coinciding with event 1 were more than a dozen transitions between the magnetosheath and magnetosphere, most likely the signature of large-amplitude Kelvin-Helmholtz boundary waves (*11*). These boundary waves are observed in similar regions at Earth (*12*), and, although not previously seen at Mercury, they have been predicted by simulations (*13*). Event 2 was similar in duration (~2 min) to event 1 but larger in amplitude, with the magnetic field increasing from ~20 nT to 70 nT before decreasing (Fig. 3). Events 3 and 4 (Fig. 2) were also similar in duration and had peak magnetic field intensities of 83 and 70 nT, respectively.

Intense substorms in the terrestrial magnetosphere are associated with increases in tail magnetic field of ~25% (*14*, *15*). Given that magnetic energy density is proportional to the square of the field magnitude, and neglecting changes in tail diameter, the increase in Earth's tail magnetic energy content during a loading event is less than a factor of ~1.6, whereas the present observations imply that Mercury's tail magnetic energy content increased by factors as great as ~10.

The amount of magnetic flux threading each tail-loading event, neglecting the small contribution from the plasma sheet, may be estimated from

$$\Phi_{TAIL} = 0.5\pi B_{TAIL} R_{TAIL}^2 \qquad (1)$$

where B_{TAIL} is the field strength in the lobe region and R_{TAIL} is the cross-sectional radius of the tail.

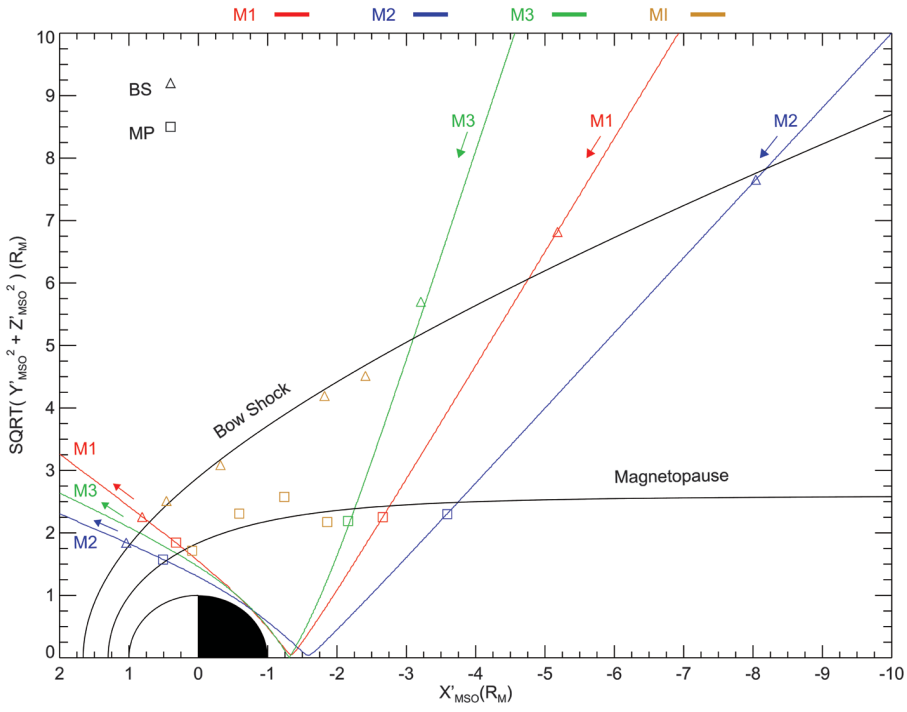

Fig. 1. MESSENGER Mercury flyby trajectories are displayed in solar-wind-aberrated cylindrical MSO coordinates (*8*). In Mercury solar orbital (MSO) coordinates, X_{MSO} is directed from the center of the planet toward the Sun, Z_{MSO} is normal to Mercury's orbital plane and positive toward the north celestial pole, and Y_{MSO} is positive in the direction opposite to orbital motion. Averaged Mariner 10 and MESSENGER inbound and outbound bow shock (BS) and magnetopause (MP) crossings are shown as triangles and squares, respectively. Model boundary surfaces fit to all of the crossings are also displayed (*6*–*9*).

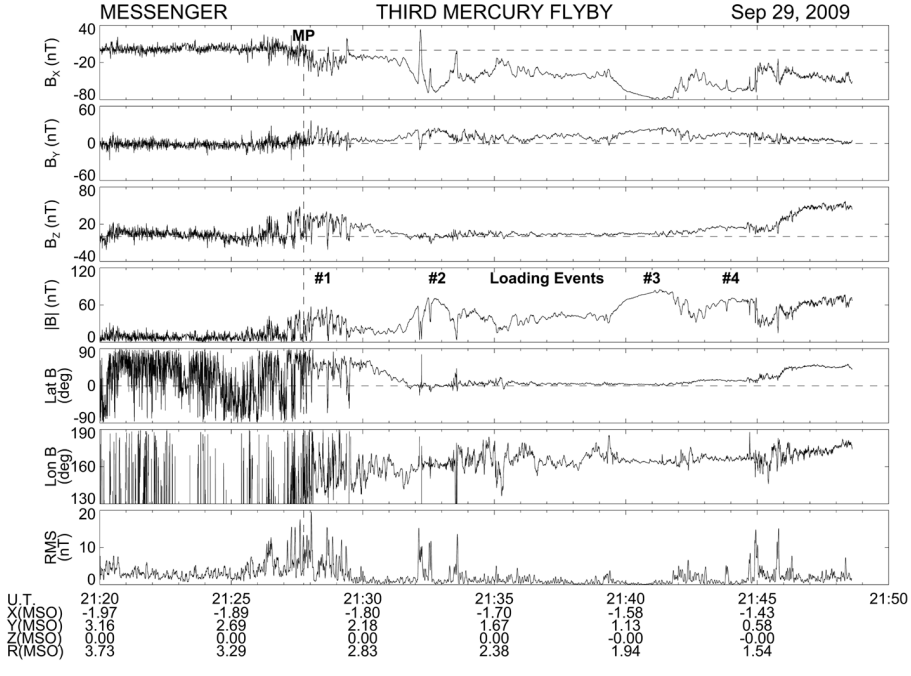

Fig. 2. Overview of magnetospheric measurements taken by MESSENGER's Magnetometer (MAG). The crossing from the magnetosheath into the magnetic tail at Mercury's magnetopause (MP) is marked with a vertical dashed line. Closest approach was at an altitude of 228 km at 21:54:58 UTC. The MAG observations of magnetic field in MSO coordinates, the field magnitude, the latitude and longitude direction angles, and the root-mean-squared (RMS) variance calculated over 3-s intervals are displayed top to bottom in the seven panels. The longitude angle of the magnetic field is defined to be 0° toward the Sun and increases counterclockwise looking down from the north celestial pole. The magnetic field latitude is +90° when directed northward and 0° when it is in the X_{MSO}-Y_{MSO} plane. The four tail-loading events discussed here are labeled.

Downloaded from www.sciencemag.org on August 5, 2010

Event 1 occurred during multiple magnetopause crossings, indicating that $R_{TAIL} \approx 2.4\ R_M$ at $X_{MSO} = -1.8\ R_M$. From the peak magnetic field, 56 nT, we computed a tail flux content of 3.0 MWb. For the other three events, the peak tail field intensities were 70, 83, and 70 nT, respectively. The increased radius of the tail accompanying these loading events was not measured by MESSENGER because the spacecraft was too deep in the tail to encounter the magnetopause. The pressure balances along the magnetopause (*2*), the peak loading field intensities, and the solar wind conditions predicted from a magnetohydrodynamic model of the inner heliosphere driven by solar magnetic field observations (*16*) imply a tail flaring angle relative to the sunward direction of ~30° for the strongest loading episode, event 3, in contrast to ~10° for the much weaker event 1. Such strong flaring implies a substantial enhancement of tail radius relative to the first loading event. Guided by these simulations and given the magnetospheric dimensions and the intensity of the inferred flaring, the radius of the tail for event 3 may have reached 3.5 R_M, corresponding to a peak tail flux content of 9.5 MWb. This value is ~50% more than predicted by a recently developed model of Mercury's magnetosphere (*17*) at the time of the second flyby, during which no tail-loading events were observed.

Closer inspection of the magnetic field record for event 2 (Fig. 3) reveals six intervals of several seconds each when the total magnetic field weakened, indicating entry into a region with high plasma thermal pressure and low magnetic field pressure. These minima in field magnitude coincide with either rapid northward-then-southward or just southward variations in B_Z, followed by a slower recovery back to $B_Z \approx 0$, as can be seen in the latitude angle of the field (Fig. 3). These characteristics are signatures of plasmoids moving antisunward over the spacecraft (*18*–*20*). The field near the peak of event 3 does not show marked intensity decreases, but a series of compressions is observed coincident with southward-then-northward tilting of the lobe magnetic field. These are signatures of traveling compression regions (TCRs) produced by the lobe magnetic field draping about sunward-moving flux ropes (*21*, *22*). A transition from plasmoids being ejected tailward to sunward-moving TCRs closer to Mercury indicates the location of the region of most intense tail reconnection (*1*, *2*), the near-Mercury neutral line (NMNL). The NMNL was observed near $X_{MSO} = -2.6\ R_M$ during MESSENGER's second flyby (*5*), but it was closer to the planet, near $X_{MSO} \approx -1.6\ R_M$, for this flyby. The third flyby results therefore suggest that the NMNL develops much closer to the planet when the magnetic tail is heavily loaded with magnetic flux, such as during events 2 and 3.

The total magnetic flux emanating from Mercury's surface can be calculated for a simple centered dipole:

$$\Phi_M = 2\pi B_{eq} R_M^2 \qquad (2)$$

where B_{eq} is the strength of the magnetic field at Mercury's equator. Given $B_{eq} \approx 250$ nT (*23*, *24*), the corresponding value of Φ_M is 9.5 MWb. As closed magnetic flux in the dayside magnetosphere is opened by reconnection at the magnetopause, it is pulled back into the tail lobes by the solar wind. For moderate loading of the tail, the dayside magnetopause contracts to lower altitudes, and the north and south magnetic cusps are displaced equatorward (Fig. 4B). In the asymptotic limit that 100% of the planet's magnetic flux is transferred to the tail, the closed dayside magnetosphere disappears, the magnetopause flares strongly, and the north and south cusps merge into a single broader cusp at the equator (Fig. 4C). This extreme configuration is expected to be highly unstable and to quickly lead to substorm-associated reconnection in the tail to rapidly transfer magnetic flux back to the dayside magnetosphere on the observed Dungey cycle

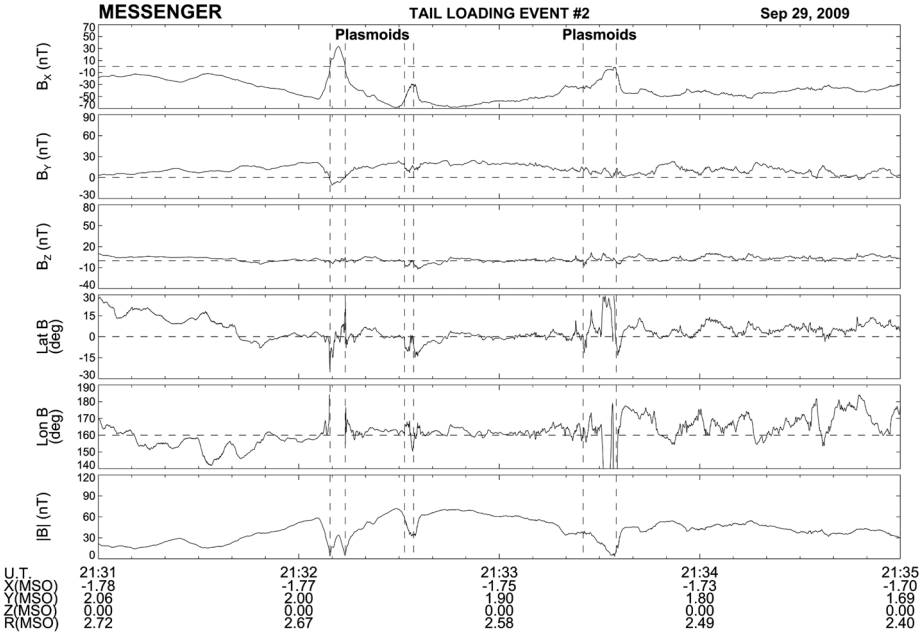

Fig. 3. Magnetometer observations of tail-loading event 2 during MESSENGER's third flyby. Vertical dashed lines mark the occurrence of tailward-moving plasmoids.

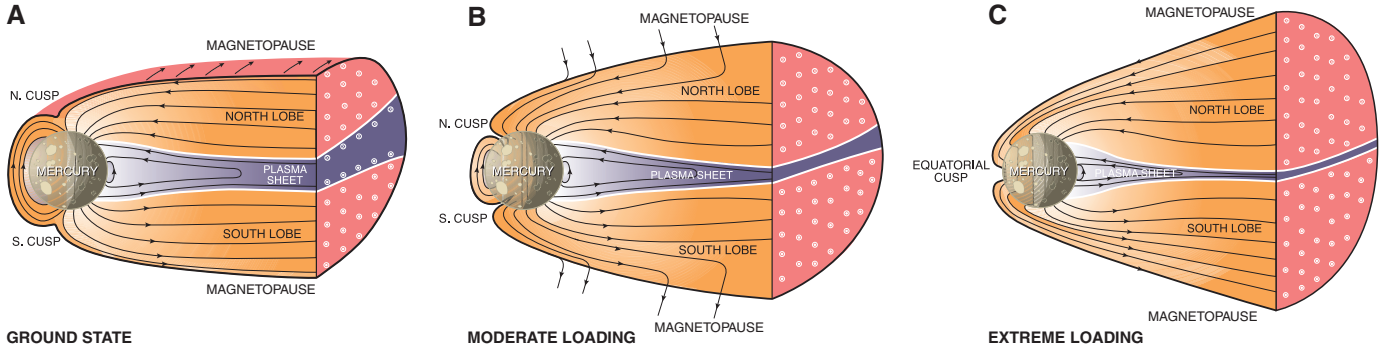

Fig. 4. Schematic view of Mercury's magnetosphere in its ground state (**A**) and during moderate (**B**) and extreme (**C**) tail loading observed by MESSENGER on 29 September 2009.

Downloaded from www.sciencemag.org on August 5, 2010

time scale, ~2 min. The tail flux contents at the time of the peak loading events measured by MESSENGER correspond to at least ~30%, and for the most intense event possibly 100%, of the available magnetic flux from Mercury. Such an extreme magnetospheric configuration has never been observed or inferred to be present on the basis of space measurements at Earth or at other planets. The typical fraction of Earth's total magnetic flux that is contained in the tail during loading events that produce intense substorms is only ~10 to 12% (*14*). If Mercury's dayside magnetosphere is fully depleted by reconnection, which may have occurred during event 3, the entire dayside surface would map to open magnetic field lines and be exposed to the shocked solar wind of the magnetosheath.

The close correspondence between the 2- to 3-min duration of the tail-loading and tail-unloading events observed during the third flyby and the ~2-min Dungey cycle time at Mercury suggests not only that Earth-like substorms occur at Mercury but also that plasma circulation times determine the temporal scale for substorms at both planets. Further, the relative variation in tail energy content observed during loading and unloading at Mercury was an order of magnitude larger than at Earth, implying that the relative energy release in substorms at Mercury must be large compared to terrestrial substorms. The high rate of reconnection inferred from the large magnetopause-normal magnetic fields seen during MESSENGER's second flyby (*5*), the large flux transfer events (FTEs) observed just outside Mercury's magnetopause (*25*) by MESSENGER during its earlier flybys (*5*), and the expected low electrical conductivity of Mercury's crust—which should greatly limit line-tying effects (*26*) and allow rapid magnetic flux transfer between the dayside magnetosphere and the tail—are the most likely causes of this intense tail loading. For example, 10 FTEs comparable to the largest flux transfer events measured during the second flyby concentrated over a period of ~1 to 2 min, or 1 FTE every 6 to 12 s, would contribute ~2 MWb to the tail loading, a substantial fraction of the flux addition marking the events during MESSENGER's third flyby. The intense fluxes of higher-energy electrons reported by Mariner 10 (*27*, *28*) and the observations of strong tail loading and unloading and plasmoid ejection reported here, which we attribute to substorm behavior, make the lack of energetic charged particles with energies above 36 keV in the MESSENGER observations for this and earlier flybys (*29*) very surprising. The production of energetic particle acceleration events at Mercury, such as that observed by Mariner 10, evidently requires conditions not yet encountered by MESSENGER.

References and Notes

1. D. N. Baker, T. I. Pulkkinen, V. Angelopoulos, W. Baumjohann, R. L. McPherron, *J. Geophys. Res.* **101**, 12975 (1996).
2. C. T. Russell, R. L. McPherron, *Space Sci. Rev.* **15**, 205 (1973).
3. V. Angelopoulos *et al.*, *Science* **321**, 931 (2008).
4. G. L. Siscoe, N. F. Ness, C. M. Yeates, *J. Geophys. Res.* **80**, 4359 (1975).
5. J. A. Slavin *et al.*, *Science* **324**, 606 (2009).
6. J.-H. Shue *et al.*, *J. Geophys. Res.* **102**, 9497 (1997).
7. Magnetopause crossings were fit to the model of Shue *et al.* (*6*), with $\alpha = 0.5$ and $R_o = 1.3\ R_M$, where α is the surface flaring parameter and R_o is the distance to the subsolar magnetopause.
8. J. A. Slavin *et al.*, *Geophys. Res. Lett.* **36**, L02101 (2009).
9. Bow-shock crossings were fit to the model of Slavin *et al.* (*8*), with $X_o = 0.475$, $\varepsilon = 1.04$, and $L = 2.59\ R_M$, where X_o is the location of the hyperbola's focus along the aberrated X_{MSO} axis, ε is the surface's eccentricity, and L is the semi-latus rectum.
10. B. J. Anderson *et al.*, *Space Sci. Rev.* **131**, 417 (2007).
11. S. A. Boardsen *et al.*, *Geophys. Res. Abstr.* **12**, EGU2010-5198-1 (2010).
12. H. Hasegawa *et al.*, *Nature* **430**, 755 (2004).
13. P. M. Trávníček *et al.*, *Icarus* 10.1016/j.icarus.2010.01.008 (2010).
14. S. E. Milan *et al.*, *J. Geophys. Res.* **109**, A04220 (2004).
15. C.-S. Huang, A. D. DeJong, X. Cai, *J. Geophys. Res.* **114**, A07202 (2009).
16. D. Odstrcil *et al.*, *Eos* **90** (fall meet. suppl.), abstract P24A-02 (2009).
17. I. I. Alexeev *et al.*, *Icarus* 10.1016/j.icarus.2010.01.024 (2010).
18. E. W. Hones Jr. *et al.*, *Geophys. Res. Lett.* **11**, 5 (1984).
19. J. A. Slavin *et al.*, *J. Geophys. Res.* **108**, 10.1029/2002JA009557 (2003).
20. A. Kidder, R. M. Winglee, E. M. Harnett, *J. Geophys. Res.* **113**, A09223 (2008).
21. M. B. Moldwin, W. J. Hughes, *J. Geophys. Res.* **98**, 81 (1993).
22. J. A. Slavin *et al.*, *J. Geophys. Res.* **110**, A06207 (2005).
23. B. J. Anderson *et al.*, *Science* **321**, 82 (2008).
24. B. J. Anderson *et al.*, *Space Sci. Rev.* **154**, 307 (2010).
25. J. A. Slavin *et al.*, *Geophys. Res. Lett.* **37**, L02105 (2010).
26. K.-H. Glassmeier, *Planet. Space Sci.* **45**, 119 (1997).
27. D. N. Baker, J. A. Simpson, J. H. Eraker, *J. Geophys. Res.* **91**, 8742 (1986).
28. S. P. Christon, J. Feynman, J. A. Slavin, in *Magnetotail Physics*, A. T. Y. Lui, Ed. (Johns Hopkins Univ. Press, Baltimore, 1987), pp. 393–400.
29. R. D. Starr *et al.*, *Eos* **90** (fall meet. suppl.), abstract P21A-1195 (2009).

30. We thank all those who contributed to the success of the MESSENGER flybys of Mercury. We thank J. Feggans and M. Marosy for data visualization and graphics support. The MESSENGER project is supported by the NASA Discovery Program under contracts NAS5-97271 to the Johns Hopkins University Applied Physics Laboratory and NASW-00002 to the Carnegie Institution of Washington. Small parts of the work were supported by an NSF Center for Integrated Space Weather Modeling grant.

8 February 2010; accepted 25 May 2010
Published online 15 July 2010;
10.1126/science.1188067
Include this information when citing this paper.

Evidence for Young Volcanism on Mercury from the Third MESSENGER Flyby

Louise M. Prockter,[1]* Carolyn M. Ernst,[1] Brett W. Denevi,[2] Clark R. Chapman,[3] James W. Head III,[4] Caleb I. Fassett,[4] William J. Merline,[3] Sean C. Solomon,[5] Thomas R. Watters,[6] Robert G. Strom,[7] Gabriele Cremonese,[8] Simone Marchi,[9] Matteo Massironi[10]

During its first two flybys of Mercury, the MESSENGER spacecraft acquired images confirming that pervasive volcanism occurred early in the planet's history. MESSENGER's third Mercury flyby revealed a 290-kilometer-diameter peak-ring impact basin, among the youngest basins yet seen, having an inner floor filled with spectrally distinct smooth plains. These plains are sparsely cratered, postdate the formation of the basin, apparently formed from material that once flowed across the surface, and are therefore interpreted to be volcanic in origin. An irregular depression surrounded by a halo of bright deposits northeast of the basin marks a candidate explosive volcanic vent larger than any previously identified on Mercury. Volcanism on the planet thus spanned a considerable duration, perhaps extending well into the second half of solar system history.

Images obtained by the MErcury Surface, Space ENvironment, GEochemistry, and Ranging (MESSENGER) spacecraft (*1*) during its first and second flybys of Mercury in 2008 established the presence and diversity of volcanism on Mercury early in the planet's history and indicated an association with ancient impact basins. A key missing element in our understanding of Mercury's global thermal evolution is the temporal extent of volcanic activity and, in particular, the timing of most recent activity (*2*). Previous analyses of the duration of geological activity led to the conclusion (*3*) that volcanism ended before the beginning of Mercury's Mansurian Period, ~3.5 to 1.0 Ga (billion years ago). Here, we report on images obtained during MESSENGER's third Mercury flyby on 29 September 2009 of what may be among the youngest volcanic deposits on the planet.

Downloaded from www.sciencemag.org on August 5, 2010

During that most recent flyby, a ~290-km-diameter peak-ring (double-ring) impact basin, centered at 27.6°N, 57.6°E, was recognized (Fig. 1) (*4*). In terms of size, morphology, and state of preservation, the basin, named Rachmaninoff, closely resembles the 265-km-diameter Raditladi peak-ring basin (27°N, 119°E) that was imaged during MESSENGER's first Mercury flyby (*5*) and may have formed as recently as 1 Ga (*6*). Peak-ring basins are characterized by an outermost basin rim and an interior ring of contiguous peaks and are transitional in form between complex craters and large multiring basins, which contain three or more rings. Peak-ring basins are common on Mercury (*7*), which has the highest density of peak-ring basins among the Moon, Earth, Mars, and Venus (*8*). Rachmaninoff may be transitional between a peak-ring basin and a multiring basin in that it has a partial third ring to the southwest, spanning an arc of about 120°. The inner ring of Rachmaninoff is about 130 km in diameter and slightly elongated in the north-south direction. The basin is surrounded by a continuous ejecta deposit and numerous secondary crater chains. Although it has no visible rays, its ejecta deposit, rim crest, wall terraces, and peaks are crisp and well preserved. On these grounds, the basin is younger than most other basins on Mercury and likely formed well after the end of the late heavy bombardment of the inner solar system at about 3.8 Ga (*3*, *6*, *9*).

The floor of Rachmaninoff basin contains several distinct plains units (Fig. 1). A smooth, relatively bright, high-reflectance plains unit has filled much of the floor within the peak ring (inner smooth plains, pink in Fig. 1B), and three relatively lower-reflectance plains units with broadly similar color characteristics are found within the annulus between the peak ring and the rim (annular smooth plains, green in Fig. 1B; annular hummocky plains, dark blue; and annular low-reflectance plains, purple; collectively hereafter grouped as "annular plains"). The bright, high-reflectance properties of the inner smooth plains are nearly identical to those of a large expanse of smooth plains located to the northeast of the basin that embay and are thus younger than Rachmaninoff ejecta. Although smooth plains with similar color properties are common within craters and basins elsewhere on Mercury (*10*), only one other example has been found to date where these types of plains appear confined within a basin's central peak ring (the 225-km-diameter Renoir basin).

There is no apparent difference in color and reflectance between the annular plains units and the basin peak ring and terrace material (peak-ring material, light gray, and terrace material, light blue; Fig. 1B), all of which are up to 28% lower in reflectance than the inner smooth plains (Fig. 1C). These characteristics are consistent with those of low-reflectance material observed elsewhere on Mercury both as scattered deposits and concentrated in the central peaks and ejecta deposits of craters and basins such as Tolstoj (*10*, *11*) (16°S, 195°E).

The geological characteristics of these units (Fig. 1B) provide further information on their origin. The plains units in the annulus between the peak ring and the basin wall are similar to typical rough-textured, hummocky units that characterize the floors of complex craters and basins on the Moon and Mercury (*7*, *12*, *13*). During the

[1]Johns Hopkins University Applied Physics Laboratory, Laurel, MD 20723, USA. [2]School of Earth and Space Exploration, Arizona State University, Tempe, AZ 85251, USA. [3]Southwest Research Institute, 1050 Walnut Street, Boulder, CO 80302, USA. [4]Department of Geological Sciences, Brown University, Providence, RI 02912, USA. [5]Department of Terrestrial Magnetism, Carnegie Institution of Washington, Washington, DC 20015, USA. [6]Center for Earth and Planetary Studies, National Air and Space Museum, Smithsonian Institution, Washington, DC 20013, USA. [7]Lunar and Planetary Laboratory, University of Arizona, Tucson, AZ 85721, USA. [8]Instituto Nazionale di Astrofisica–Astronomical Observatory of Padova, 35122 Padova, Italy. [9]Department of Astronomy, University of Padova, 35137 Padova, Italy. [10]Department of Geoscience, University of Padova, 35137 Padova, Italy.

*To whom correspondence should be addressed. E-mail: Louise.Prockter@jhuapl.edu

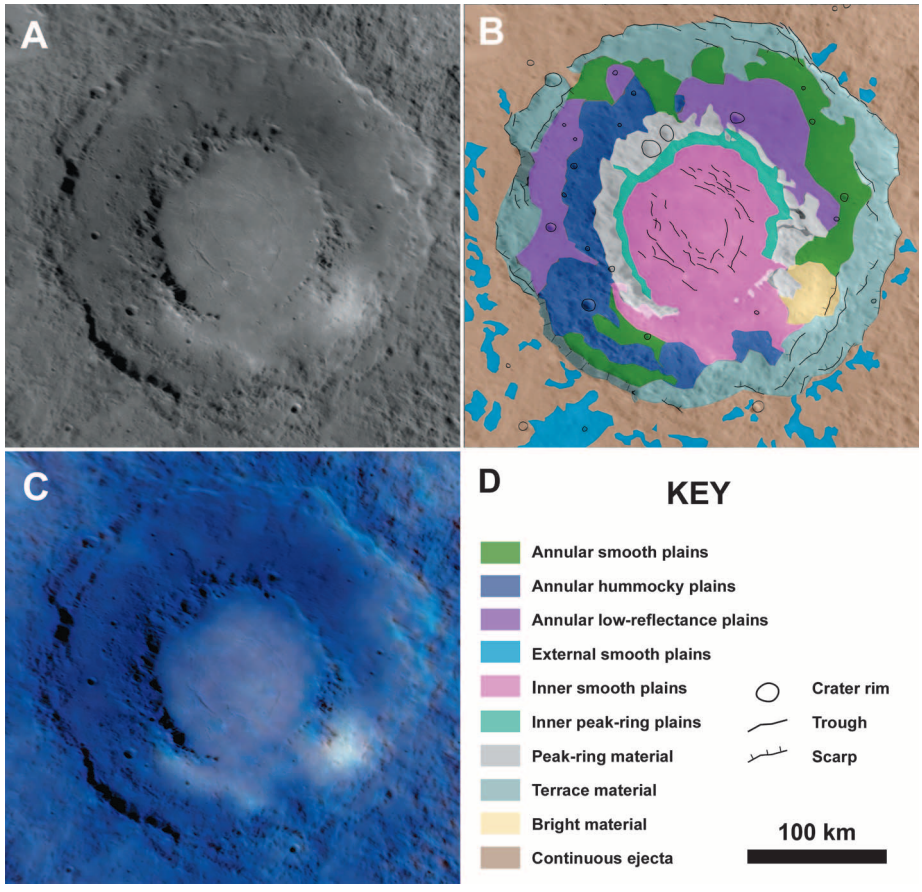

Fig. 1. Rachmaninoff peak-ring basin. (**A**) MDIS narrow-angle camera (NAC) mosaic (images 0162744128 and 0162744150); orthographic projection centered at 27.6°N, 57.6°E. (**B**) Geological sketch map of Rachmaninoff overlaid on (A), showing the variety of plains units in and around the basin. North is up. (**C**) Enhanced-color view (second and first principal components and 430-nm/1000-nm ratio in red, green, and blue, respectively) of Rachmaninoff basin imaged with the MDIS wide-angle camera (WAC) during MESSENGER's third flyby of Mercury (WAC images 162741039 to 162741083). Lower-resolution WAC observations (5 km per pixel) were merged with the higher-resolution NAC mosaic (~440 m per pixel) to display color variations with geologic terrain. (**D**) Map legend.

Downloaded from www.sciencemag.org on August 5, 2010

early modification stage of the cratering event that forms such structures, impact melt lines the interior of the crater cavity, drapes over the ejecta blocks, drains into lows, ponds to form smooth plains, and solidifies. In lunar basins, the color of the melt unit is commonly similar to that of the ejecta (*13*). Similar characteristics are seen in Rachmaninoff peak-ring basin (Fig. 1B), where annular hummocky deposits (dark blue unit; Fig. 1B) are concentrated outside of the uplifted peaks of the peak ring, and annular smooth and low-reflectance plains (green and purple units; Fig. 1B) are concentrated in the low topography along the base of the terraced wall. On the basis of these observations, we interpret Rachmaninoff annular plains to be derived from impact melt.

In many fresh peak-ring and multiring basins on the Moon and Mercury, the plains interior to the peak ring are similar in reflectance, morphology, and color properties to smooth plains in the annulus and are thus also thought to be solidified impact melt (*7*, *12*–*14*). An impact-melt origin has been proposed for the plains found within Raditladi, which appear to be similar in age to the basin (*5*).

The inner smooth plains of Rachmaninoff basin, however, differ from surrounding units in their reflectance, color properties, embayment relations, structural characteristics, and density of superposed craters. The inner smooth plains have embayed the foot of the peak ring and have obscured its southern part (Fig. 1). On the basis of these associations, we interpret the plains to have formed from fluid material that flowed across the peak ring to partly flood the units in the surrounding annulus in the southern part of the crater. These characteristics imply that the smooth plains within the peak ring formed from volcanic activity subsequent to the formation of Rachmaninoff basin. A narrow (10 to 20 km wide) region of low-reflectance smooth material (inner peak-ring plains, turquoise unit; Fig. 1B) just inside the peak ring at the outer edge of the inner smooth plains is reminiscent of geometrical arrangements in lunar impact basins that have subsided as a combined result of subsurface cooling (*15*), volcanic flooding, and embayment of the topographic low (*13*, *16*), and lithospheric flexure in response to the volcanic load (*16*). This unit could also have resulted from mass wasting of the peak ring onto the inner smooth plains.

Further evidence for volcanism in this region comes from the presence of a bright, high-reflectance patch located along the southeastern margin of the plains in the annulus between Rachmaninoff's peak ring and outer rim (bright material, yellow; Fig. 1B). The bright patch appears to be associated with rough-textured, hummocky material, which may be part of the deposit or may reflect underlying terrain over which the material is draped. The bright material is char-

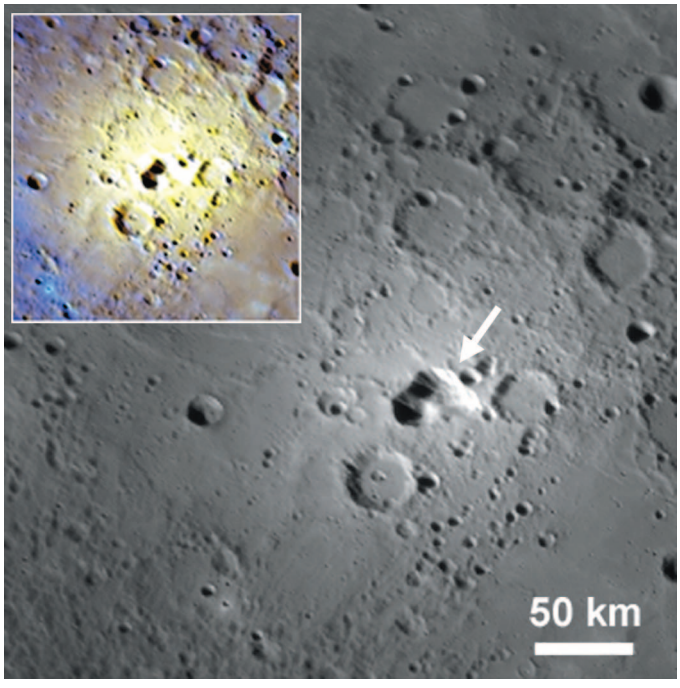

Fig. 2. MDIS NAC image of a diffuse, high-reflectance halo over 200 km in extent surrounding a ~30-km-diameter, irregularly shaped, rimless, steep-walled depression (arrow) (image 162744128). (**Inset**) Enhanced-color view (as in Fig. 1C) showing the bright halo overlying a high-reflectance smooth plains unit that embays Rachmaninoff to the north and east. Equirectangular projection centered at 27°N, 57°E (WAC images 162741039 to 162741083); north is up.

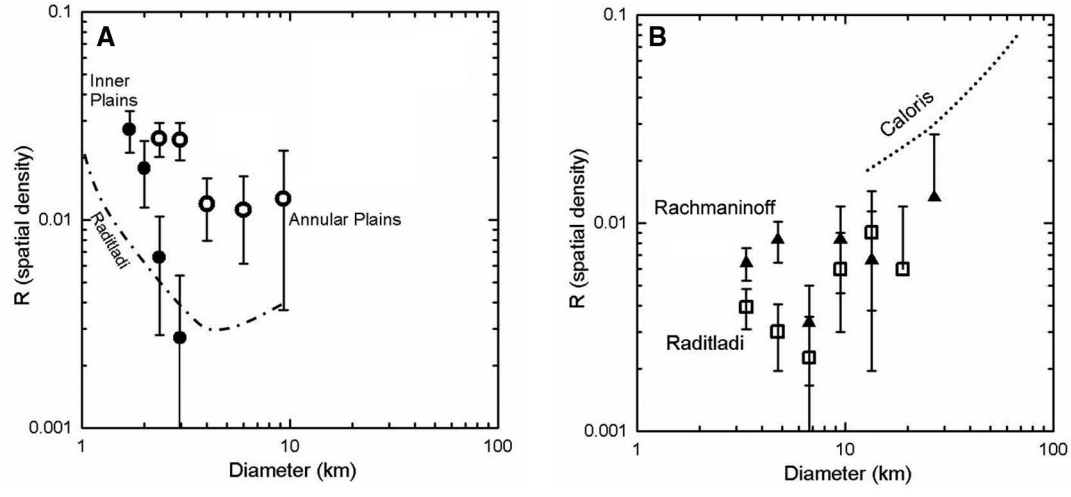

Fig. 3. Size-frequency distributions of impact craters superimposed on the Rachmaninoff and Raditladi peak-ring basins and on the plains inside Rachmaninoff [supporting online material (SOM)]. Error bars are proportional to $\sqrt{N}/N$, where N is the number of craters per given area within an increment in diameter D. (**A**) R plot of the spatial density of craters within the inner peak ring of Rachmaninoff (solid symbols, excluding probable endogenic crater-form depressions associated with the graben) compared with that for the annular plains between the peak ring and the main basin rim of Rachmaninoff (open symbols) (*25*). Shown for comparison is a curve approximately fitting the size distribution for craters on the younger smooth plains within Raditladi basin (dash-dot curve) [figure 3 of (*6*)]. The data for Raditladi are described in more detail in the SOM. (**B**) R plot of the spatial density of craters on Rachmaninoff basin and its immediate ejecta (triangles), excluding the inner plains unit; these data are interpreted to represent the stratigraphic age of the Rachmaninoff impact. Similar measurements on Raditladi basin and its immediate ejecta (open squares) reveal that Rachmaninoff is resolvably older than Raditladi. The dotted line shows the approximate size-frequency distribution for the rim of Caloris basin (*26*).

Downloaded from www.sciencemag.org on August 5, 2010

acterized by a diffuse distribution, a steep slope of the reflectance spectrum from visible to near-infrared wavelengths, and a reflectance 20% higher than that of high-reflectance plains to the north of the basin. About 480 km to the northeast of Rachmaninoff, a similar high-reflectance, diffuse halo over 200 km in extent surrounds an ~30-km-diameter, irregularly shaped, rimless, steep-walled depression (Fig. 2). The material within this halo deposit is nearly 70% higher in reflectance than the high-reflectance plains to the north, placing it among the highest-reflectance features observed on the planet, including the fresh ejecta of Kuiperian craters (*17*). Although the distinctive color of the deposit could be interpreted as the result of more space weathering than has affected fresh crater ejecta, the combination of an especially steep spectral slope and very high reflectance implies that the deposit has a different composition or physical properties and that its color is not due to space weathering.

The reflectance properties of these halo deposits are similar to those of spectrally distinct deposits observed elsewhere on Mercury in association with crater and basin interiors and interpreted to be products of pyroclastic volcanism (*18*). Scalloped depressions similar to the one northeast of Rachmaninoff basin have been identified elsewhere on Mercury, notably just inside the rim of Caloris basin (e.g., at 22.4°N, 146.3°E), and have been interpreted as sites of explosive volcanic activity (*18*–*21*) where bright material was emplaced ballistically around a central source vent. The scalloped depression northeast of Rachmaninoff is remarkable in that it is not only larger than the largest previously identified candidate vent around the rim of Caloris, but its surrounding halo of bright material extends twice as far as the deposit around that vent (*18*). We do not find any scalloped depression that could be interpreted as a candidate source vent for the bright patch within the Rachmaninoff annulus, however.

Deformation postdated volcanism within Rachmaninoff basin. Lying within the inner smooth plains unit is a set of narrow extensional troughs or graben (Fig. 1B). Extensional faulting on Mercury is rare and generally confined to impact basins (*22*, *23*). The pattern of graben in Rachmaninoff is similar to that in Raditladi, where the graben are dominantly basin-concentric and form an incomplete ring that is offset from the center of the basin (*5*). The cumulative length of imaged graben in Rachmaninoff (~460 km) is larger than in Raditladi (~180 km), indicating that the floor of Rachmaninoff experienced greater extensional strain. The extension within Rachmaninoff and Raditladi basins likely accompanied uplift of the basin floors, as is thought to be the case for the larger Caloris and Rembrandt basins (*22*, *23*). The observation that the extensional troughs in Rachmaninoff are confined to the volcanic inner plains suggests that the volcanism and uplift may have been related.

The very small number of superposed craters indicates that the inner smooth plains within Rachmaninoff basin may be among the youngest volcanic deposits on Mercury. The volcanism must postdate the cratering event because the inner plains embay or overlie units related to basin formation. To assess the time interval between basin formation and volcanism, we measured the size-frequency distribution of impact craters superposed on the inner and annular plains. The inner plains of Rachmaninoff are less cratered than the annular plains and hence younger, a difference that is particularly noticeable for craters greater than ~2 to 3 km in diameter (which are unambiguously resolvable and difficult to remove by later geological activity). This result is consistent with a volcanic origin for the inner plains. The differences in the trends of the size-frequency distributions at crater diameters of 2 to 3 km between the two areas may reflect that craters of these sizes are most likely secondary craters with uneven population statistics (*6*). Comparison of crater counts in areas associated with formation of Rachmaninoff basin (the annular plains, rim deposits, and inner ejecta blanket) with similar measurements for Raditladi basin (Fig. 3B) suggest that Rachmaninoff basin formed somewhat earlier than Raditladi basin. Although the crater size-frequency distributions for Raditladi and the two units within Rachmaninoff do not follow precisely the same trends, the inner plains of Rachmaninoff are older than the floor of Raditladi but substantially younger than the Rachmaninoff annular plains.

In principle, we may estimate absolute ages for Rachmaninoff basin and its related units by comparing these size-frequency distributions with models for the rate of production of craters on Mercury (*9*, *24*). Such models depend on differences in flux and impactor energies between the Moon and Mercury, and assumptions about the properties of the surfaces impacted, and adopted scaling relationships, and they are influenced by uncertainties in the size distribution of inner solar system asteroids. Whereas interpretations after Mariner 10 were that plains formation on Mercury ceased shortly after the end of the late heavy bombardment (~3.8 Ga), volcanism within Rachmaninoff (and formation of the plains within the younger Raditladi basin) extended well into the Mansurian and conceivably to times as recent as ~1 Ga. Models for crater retention age (*9*, *24*) involve primary cratering only, and most of the craters on the smooth plains in Fig. 3A may be secondary craters, given the pronounced steep slope of their size-frequency distribution (*6*). For this reason, the volcanism and associated deformation within Rachmaninoff could have ended even more recently.

References and Notes

1. S. C. Solomon, R. L. McNutt Jr., R. E. Gold, D. L. Domingue, *Space Sci. Rev.* **131**, 3 (2007).
2. J. W. Head *et al.*, *Space Sci. Rev.* **131**, 41 (2007).
3. P. D. Spudis, J. E. Guest, in *Mercury*, F. Vilas, C. R. Chapman, M. S. Matthews, Eds. (Univ. of Arizona Press, Tucson, 1988), pp. 118–164.
4. Rachmaninoff and its surroundings were imaged at ~440 m per pixel with MESSENGER's Mercury Dual Imaging System (MDIS) monochrome narrow-angle camera and at 5 km per pixel with the 11 filters of the MDIS wide-angle camera, which span wavelengths from 400 to 1040 nm (*27*).
5. L. M. Prockter *et al.*, *Lunar Planet. Sci.* **40**, abstr. 1758 (2009).
6. R. G. Strom, C. R. Chapman, W. J. Merline, S. C. Solomon, J. W. Head III, *Science* **321**, 79 (2008).
7. R. J. Pike, in *Mercury*, F. Vilas, C. R. Chapman, M. S. Matthews, Eds. (Univ. of Arizona Press, Tucson, 1988), pp. 165–273.
8. C. A. Wood, J. W. Head, *Proc. Lunar Sci. Conf.* **7**, 3629 (1976).
9. M. Massironi *et al.*, *Geophys. Res. Lett.* **36**, L21204 (2009).
10. B. W. Denevi *et al.*, *Science* **324**, 613 (2009).
11. M. S. Robinson *et al.*, *Science* **321**, 66 (2008).
12. M. J. Cintala, R. A. F. Grieve, *Meteorit. Planet. Sci.* **33**, 889 (1998).
13. J. W. Head *et al.*, *J. Geophys. Res.* **98**, 17149 (1993).
14. P. D. Spudis, *The Geology of Multi-Ring Basins* (Cambridge Univ. Press, New York, 1993).
15. S. R. Bratt, S. C. Solomon, J. W. Head, *J. Geophys. Res.* **90**, 12415 (1985).
16. S. C. Solomon, J. W. Head, *Rev. Geophys. Space Phys.* **18**, 107 (1980).
17. C. R. Chapman, in *Mercury*, F. Vilas, C. R. Chapman, M. S. Matthews, Eds. (Univ. of Arizona Press, Tucson, 1988), pp. 1–23.
18. L. Kerber *et al.*, *Earth Planet. Sci. Lett.* **285**, 263 (2009).
19. J. W. Head *et al.*, *Science* **321**, 69 (2008).
20. S. L. Murchie *et al.*, *Science* **321**, 73 (2008).
21. J. W. Head *et al.*, *Earth Planet. Sci. Lett.* **285**, 227 (2009).
22. T. R. Watters *et al.*, *Earth Planet. Sci. Lett.* **285**, 309 (2009).
23. T. R. Watters *et al.*, *Science* **324**, 618 (2009).
24. S. Marchi, S. Mottola, G. Cremonese, M. Massironi, E. Martellato, *Astron. J.* **137**, 4936 (2009).
25. In an R plot, the differential crater size-frequency distribution $N(D)$ is divided by the power law $dN(D) \sim D^{-3}dD$, where N is the number of craters within an increment of crater diameter D per given area.
26. C. I. Fassett *et al.*, *Earth Planet. Sci. Lett.* **285**, 297 (2009).
27. S. E. Hawkins III *et al.*, *Space Sci. Rev.* **131**, 247 (2007).

28. We are grateful to N. Chabot, N. Laslo, and H. Kang, who designed the imaging sequences that made this contribution possible, and to the tireless efforts of the engineers and technical support personnel on the MESSENGER team. The MESSENGER project is supported by the NASA Discovery Program under contracts NASW-00002 to the Carnegie Institution of Washington and NAS5-97271 to the Johns Hopkins University Applied Physics Laboratory.

Supporting Online Material

www.sciencemag.org/cgi/content/full/science.1188186/DC1
SOM Text
Fig. S1
Table S1

10 February 2010; accepted 7 July 2010
Published online 15 July 2010;
10.1126/science.1188186
Include this information when citing this paper.

Downloaded from www.sciencemag.org on August 5, 2010

Mercury's Complex Exosphere: Results from MESSENGER's Third Flyby

Ronald J. Vervack Jr.,[1]* William E. McClintock,[2] Rosemary M. Killen,[3] Ann L. Sprague,[4] Brian J. Anderson,[1] Matthew H. Burger,[3] E. Todd Bradley,[5] Nelly Mouawad,[6] Sean C. Solomon,[7] Noam R. Izenberg[1]

During MESSENGER's third flyby of Mercury, the Mercury Atmospheric and Surface Composition Spectrometer detected emission from ionized calcium concentrated 1 to 2 Mercury radii tailward of the planet. This measurement provides evidence for tailward magnetospheric convection of photoions produced inside the magnetosphere. Observations of neutral sodium, calcium, and magnesium above the planet's north and south poles reveal altitude distributions that are distinct for each species. A two-component sodium distribution and markedly different magnesium distributions above the two poles are direct indications that multiple processes control the distribution of even single species in Mercury's exosphere.

Mercury lacks the familiar collision-dominated atmosphere of the other terrestrial planets. It is instead surrounded by a tenuous surface-bounded exosphere composed primarily of atoms and molecules released from the planet's surface. Understanding the processes that generate and maintain the exosphere provides insight into the composition of Mercury's surface and the transport of material about the planet. Moreover, quantifying how these processes have modified the optical properties of the surface over Mercury's lifetime is important in understanding the planet's geologic history. Observations made by the Ultraviolet and Visible Spectrometer (UVVS) (*1*) on the MErcury Surface, Space ENvironment, GEochemistry, and Ranging (MESSENGER) spacecraft (*2*) during the first two flybys of the planet (M1 on 14 January 2008 and M2 on 6 October 2008) revealed different spatial distributions for three exospheric species: sodium (Na), calcium (Ca), and magnesium (Mg) (*3*, *4*). Here, we report results from MESSENGER's third flyby (M3 on 29 September 2009).

As during M1 and M2, most of the M3 exospheric observations were made as MESSENGER approached Mercury, enabling the UVVS to map the tail region that extends anti-sunward from the planet. The M3 trajectory also allowed the UVVS to obtain altitude scans above Mercury's north and south poles, which had not been possible during the earlier flybys because of spacecraft-pointing constraints. Near closest approach, a roll maneuver as MESSENGER entered Mercury's shadow carried the UVVS field of view in an arc perpendicular to the Sun-Mercury line. The instrument view during these "fantail" observations began southward and rolled through the dawn direction to northward, at which point measurements were interrupted by a spacecraft safe-hold event. Throughout M3, the UVVS scanned for emission lines from four species (vacuum wavelengths): Na at 589.2 and 589.8 nm, Mg at 285.3 nm, Ca at 422.8 nm, and Ca^+ at 393.5 nm (*5*).

Ionized calcium (Ca^+) emission was observed above noise levels only in a relatively small region (Fig. 1A) approximately 1 to 2 R_M (where R_M is Mercury's radius, 2440 km) tailward of the planet, with most of the emission close to the equatorial plane. In contrast, neutral Ca emission was more uniformly distributed (Fig. 2B). Line-of-sight column density estimates for Ca^+ and Ca 1 to 2 R_M downtail were of the same order of magnitude (Table 1). Because Ca^+ velocities—up to hundreds of km s^{-1}, which is consistent with the signatures of strong magnetospheric convection observed by the MESSENGER Magnetometer during M3 (*6*–*9*)—are generally much larger than the several km s^{-1} velocities expected for Ca (*10*), local production of Ca^+ from Ca is unlikely to yield either comparable column densities or the apparent localized nature of the Ca^+ emission.

The observed Ca^+ distribution can probably be explained by a combination of magnetospheric convection and centrifugal acceleration. The lifetime of Ca against photoionization is short, ~1500 s (*11*), so exospheric Ca^+ ions are formed close to the planet (within 2.5 R_M), where much of the Ca^+ pick-up process occurs (*12*). Magnetospheric convection was particularly intense during M3 (*9*), implying that planetary ions created over the poles would be swept by anti-sunward convection into the magnetotail and down into

[1]Johns Hopkins University Applied Physics Laboratory, Laurel, MD 20723, USA. [2]Laboratory for Atmospheric and Space Physics, University of Colorado, Boulder, CO 80303, USA. [3]NASA Goddard Space Flight Center, Greenbelt, MD 20771, USA. [4]Lunar and Planetary Laboratory, University of Arizona, Tucson, AZ 85721, USA. [5]Department of Physics, University of Central Florida, Orlando, FL 32816, USA. [6]Department of Astronomy, University of Maryland, College Park, MD 20742, USA. [7]Department of Terrestrial Magnetism, Carnegie Institution of Washington, Washington, DC 20015, USA.

*To whom correspondence should be addressed. E-mail: Ron.Vervack@jhuapl.edu

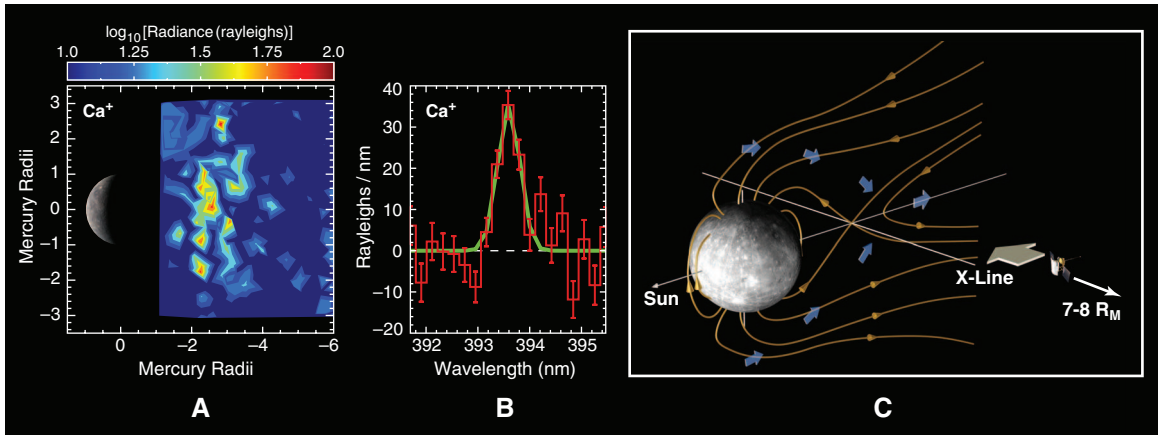

Fig. 1. Observations of Ca^+ emission in Mercury's tail region. (**A**) The image shows observed column emissions projected onto the plane containing the Sun-Mercury line and Mercury's spin axis, interpolating to fill in unobserved regions. To clearly show the full region scanned, all observations below 10 R (1 on the color scale) have been set equal to 10 R, leading to the blue background. Beyond 6 R_M downtail, no observations are above the noise level. (**B**) The red spectrum is an average of the Ca^+ emission-line observations between 1.5 and 3.5 R_M (uncertainties are 1 SD); the green line is a Gaussian fit to the average Ca^+ line. (**C**) Schematic illustration of the magnetospheric convection pattern (blue arrows) that concentrates Ca^+ in the observed narrow region before the ions are ejected down the tail. The large arrow indicates the approximate position of the observed Ca^+ emission tailward of the magnetospheric X-line.

Downloaded from www.sciencemag.org on August 5, 2010

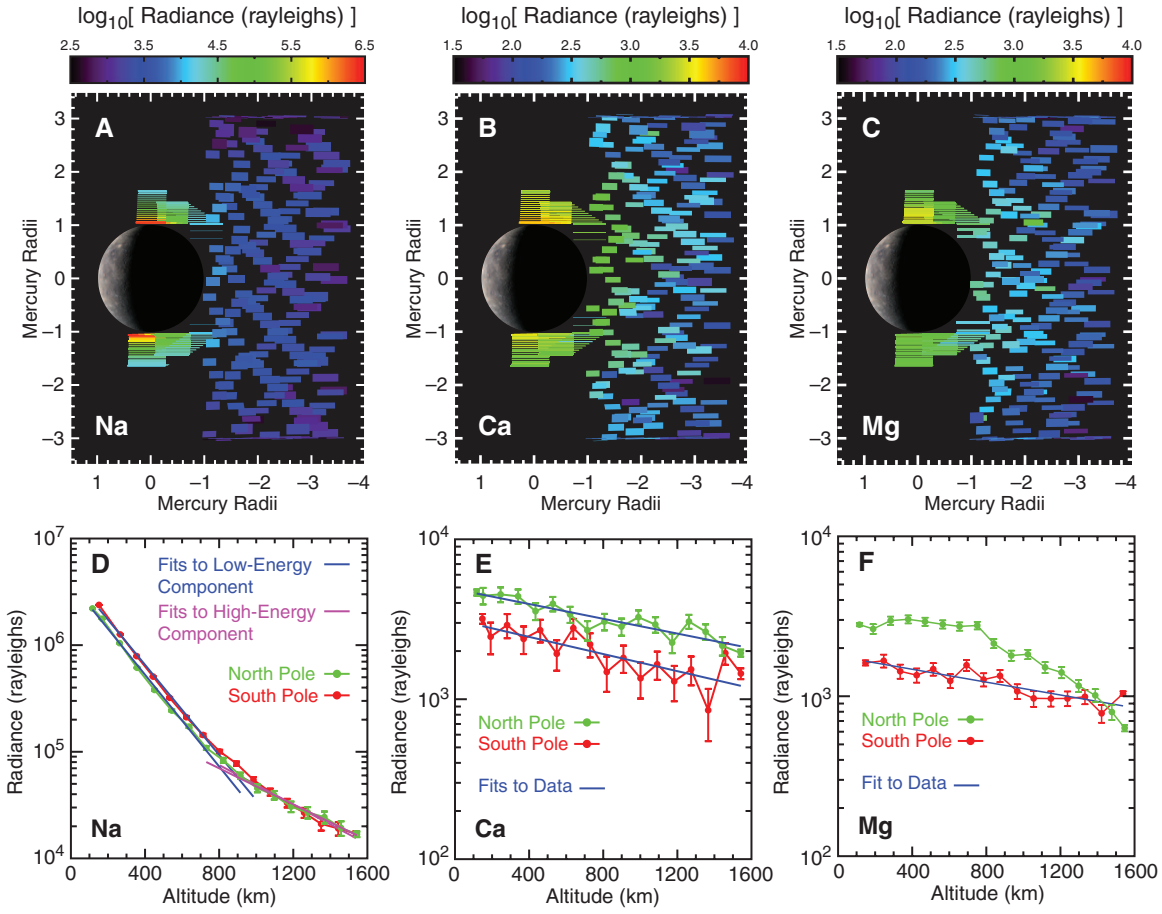

Fig. 2. (**A** to **C**) Na, Ca, and Mg emission observed in the polar, nightside, and tail regions of Mercury during MESSENGER's third flyby. Each observation is an average over the indicated region, which is the projection of the UVVS rectangular field of view onto the plane defined by the Sun-Mercury line and the spin axis of Mercury. The horizontal dimension indicates the projected slit length and becomes smaller as MESSENGER approaches Mercury. The vertical dimension indicates the range the UVVS slit moved through during the integration time (~2 s); shorter distances correspond to slower spacecraft slew rates. Owing to the spacecraft location while inbound, the lines of sight are not perpendicular to the plane but are directed sunward by 5 to 10°. (**D** to **F**) Na, Ca, and Mg emission profiles over Mercury's north and south poles (shown with 1 SD uncertainties). Exponential fits to the data indicate the general behavior of each species. The lone exception is Mg over the north pole, which cannot be fit with such a simple model as discussed in the text.

Table 1. Relevant parameters during the three MESSENGER flybys. As atoms accelerate anti-sunward, the presence of deep absorption lines in the solar spectrum causes first a decrease in *g* values followed by an increase. Without detailed modeling, only approximate (order-of-magnitude) column densities can be inferred from the observed radiances because *g* values will be different for atoms and ions at different velocities along the line of sight.

		Flyby		
		M1	**M2**	**M3**
True anomaly angle (degrees)		285	293	331
Heliocentric distance *r* (AU)		0.35	0.34	0.31
Heliocentric radial velocity *dr*/*dt* (km/s)		–9.7	–9.2	–4.9
Radiation acceleration* (cm s^{-2})	Na	176.4	179.2	89.1
	Ca	52.4	53.6	38.0
	Mg	1.8	1.8	2.0
g value† (photons s^{-1} $atom^{-1}$) (λ in vacuum)	Na (589.8 nm)	22.89	23.30	12.64
	Na (589.2 nm)	37.44	38.04	17.71
	Mg (285.3 nm)	0.315	0.318	0.339
	Ca (422.8 nm)	21.54	22.07	16.19
	Ca^+(393.5 nm)	2.85	2.95	2.87

*Radiation acceleration for atoms at rest with respect to Mercury. †*g* values, or emission probabilities, for atoms at rest with respect to Mercury (*16*).

the plasma sheet (*6*, *7*). Pick-up Ca^+ would also experience centrifugal acceleration as the magnetic field convects over the poles (*13*). This combination of convection and acceleration acts to transport Ca^+ to the region tailward of the near-planet reconnection line (the so-called X-line), which was located ~0.6 R_M anti-sunward from Mercury during M3 (*9*), concentrating Ca^+ that is produced over a relatively large volume into the near-equatorial region at higher altitudes than it originates (Fig. 1C). Consistent with the observations (Fig. 1A), the transported Ca^+ ions would be expected to have their highest densities near the equator tailward of the X-line and would fill the entire width of the magnetotail, approximately 5 to 6 R_M at the region of Ca^+ emission. In this scenario, most of the Ca^+ (~65%) is in sunlight and thus observable by the UVVS. This mechanism has been studied in detail for Na^+ ions (*14*). Because pick-up velocity is independent of mass and centrifugal acceleration depends only on the magnetic field convection, Ca^+ would participate in the same process. Moreover, the convection/acceleration mechanism is most effective for ions picked up at low altitudes over the poles (*13*), where Ca emissions during M3 were observed to be intense (Fig. 2B).

Observations of the volatile Na showed relatively high abundances over the north and south poles (Fig. 2A), but these abundances decreased by a factor of 1000 only ~1 R_M anti-sunward from the polar regions. Because radiation pressure effects on Na were relatively small during M3 (Table 1) (*15*), the observations suggest that most of the Na atoms near the poles were produced at low energy and that Na in the tail originated

Downloaded from www.sciencemag.org on August 5, 2010

from a high-energy source. In contrast, the refractory species Ca and Mg showed more gradual declines in emission from the poles to the tail region (Fig. 2, B and C). This fall-off, coupled with the much smaller response of Ca and virtually negligible response of Mg to radiation pressure in general (*16*) (Table 1), requires that these species derive from higher-energy sources sufficient to eject Ca and Mg directly to the observed radial distances, particularly in the tail region. These UVVS observations are approximately comparable with previous ground-based observations of both Na (*17*) and Ca (*10*, *18*), whereas Mg has been observed only by UVVS. However, more detailed comparisons of ground-based and spacecraft data sets require that the observations be made nearly simultaneously and along similar lines of sight owing to the high degree of spatial and temporal variability exhibited by Mercury's exosphere.

Atoms of Na are particularly sensitive to radiation pressure (*17*), which varies with Mercury's position in its elliptical orbit (*19*). The control that radiation pressure exerts over the Na distribution is illustrated through a comparison of M2 and M3 observations (Fig. 3). During M2, radiation-pressure effects on Na were stronger, producing a substantially more populated tail, with emission as much as 20 times more intense at similar downtail distances during M2 than M3. Although a change in the Na release rate between M2 and M3 cannot be completely ruled out, previous studies have shown that the Na tail effectively vanishes for radiation pressure effects less than about 112 ± 24 cm s^{-2} (*15*). The radiation pressure during M3 (Table 1) and our observations of a greatly diminished tail are consistent with that conclusion. This large change is an example of seasonal-style exospheric variability that can occur throughout Mercury's orbit.

Over the polar regions, Na exhibited a two-component structure during M3 (Fig. 2D). Exponential fits yield *e*-folding distances (the

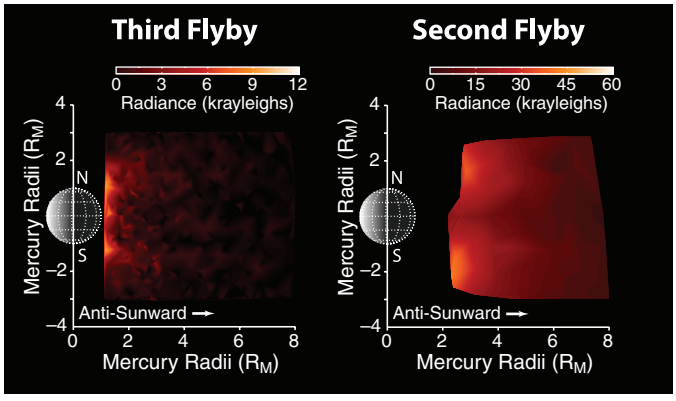

Fig. 3. Comparison of observations from the third (left) and second (right) MESSENGER flybys illustrating the markedly lower Na tail emission during M3. The images show observed column emissions projected onto the plane containing the Sun-Mercury line and Mercury's spin axis, interpolating to fill in unobserved regions. The greater degree of point-to-point variation during M3 results from there being approximately six times as many observations as during M2, leading to a lesser degree of smoothing by the interpolation. The region 1 to 2 R_M anti-sunward from the planet was not sampled during M2.

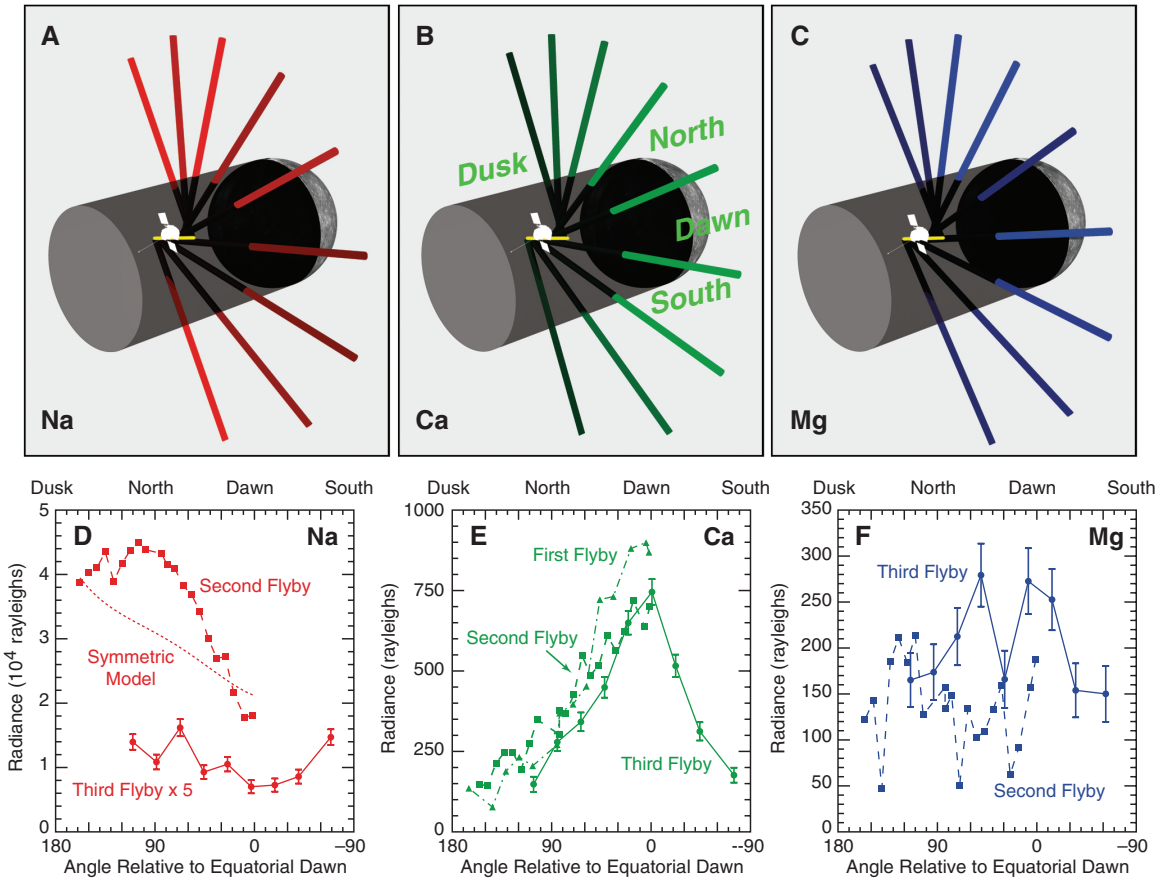

Fig. 4. (**A** to **C**) Illustrations of the geometry during the "fantail" observations of Na, Ca, and Mg tailward of Mercury during MESSENGER's third flyby. The UVVS line of sight started in the southward-pointing direction and rolled through dawn toward northern look directions. Colored lines represent the line-of-sight vector for each observation, with the brightness indicating the relative intensity. Lines are black within Mercury's shadow so as to emphasize that atoms not excited by sunlight do not emit and cannot be observed by UVVS. The yellow line indicates the spacecraft trajectory. (**D** to **F**) Observed Na, Ca, and Mg emission corresponding to the geometry in (A) to (C). Data from M3 are shown with 1 SD uncertainties; data from the first (Ca only) and second flybys are also shown for comparison (uncertainties in these data are slightly smaller owing to longer integration times but are omitted for clarity).

Downloaded from www.sciencemag.org on August 5, 2010

altitude change required for intensities to drop by a factor of *e*) of 202 km (north) and 205 km (south) for altitudes less than 800 km, and 514 km (north) and 468 km (south) for altitudes greater than 900 km. These two components are consistent with a mix of low-energy processes (such as photon-stimulated desorption) and high-energy processes (such as ion-sputtering and meteoroid impact vaporization). No previous observations of Mercury's Na exosphere have explicitly shown this structure, although ground-based observations have implied multiple source processes for Na (*15*, *20*), and a two-component distribution has been observed at the Moon (*21*).

The polar profiles for Ca and Mg (Fig. 2, E and F) are characterized by much larger scale heights than for Na, implying much higher energies for the source processes of these two species. In the south, *e*-folding distances of 1621 km and 2160 km for Ca and Mg, respectively, suggest that similar processes act on the two species. In the north, both species exhibited higher radiances, indicating larger release rates. However, whereas the Ca profile has an *e*-folding distance (1878 km) consistent with the processes acting in the south, the Mg profile is strikingly different and indicates that there may have been an additional source process at work. One possibility is that the northern Mg profile represents the combination of Mg derived directly from the surface [for instance, by heavy ion sputtering or electron-stimulated desorption (ESD)] and dissociation of MgO at higher altitudes [dissociation of CaO has been suggested as a source of high-energy Ca (*10*)]. A resonance effect related to sputtering or ESD would also affect individual species differently. Alternatively, the north-south differences in the Mg profile may reflect variations in the spatial distribution of Mg-bearing minerals on the surface. Smooth plains units are more common in the north (*22*), and volcanic deposits associated with Caloris basin (*23*) and Rachmaninoff basin (*24*) are also located at northern latitudes and could represent a source of Mg-rich materials.

Unlike the Ca and Mg profiles, the Na polar profiles exhibited no substantial north-south asymmetry in the release rates, even though some of the released Na should also derive from the high-energy processes that release Ca and Mg. The lack of a north-south Na source-rate asymmetry could result from differences in the ways various processes affect volatile and refractory species. It could also reflect spatial variations in the distribution of Na-, Ca-, and Mg-bearing minerals on the surface.

The Na, Ca, and Mg distributions in the tailward near-planet region (Fig. 4) are markedly distinct from one another. The Na fantail observations (Fig. 4, A and D) showed weak emission peaks in the south and north that are consistent with a symmetric source plus polar enhancements. However, in line with the reduced radiation pressure for Na during M3, these enhancements were less pronounced than the larger peak observed in the north during M2. An equatorial, dawnside peak in the nightside near-planet Ca distribution, suggested by M1 and M2 observations, is firmly established by the M3 fantail observations (Fig. 4, B and E), which probed the southern latitudes not sampled in the earlier flybys. The Ca distribution is remarkably consistent in both intensity and location during all three flybys, and a high-energy process is required to release Ca with sufficient energy to produce the dawnside peak at the observed distances tailward of the planet. The Mg distribution observed in the fantail region (Fig. 4, C and F) shows a weak, double-peaked concentration, with one peak near the equator and the second near 50°N. The apparent variations in the Mg distribution from M2 to M3, in contrast to the more steady Ca distribution, support the hypothesis that the dominant release processes act differently upon Mg and Ca.

The persistent location and intensity of the Ca dawnside peak in the near-planet tail region during all three flybys, which spanned highly variable magnetospheric conditions, argues against ion sputtering as the dominant process. Meteoroid-impact vaporization is also an unlikely cause unless a systematic, and perhaps large, dawn-dusk asymmetry is shown to exist in the meteoroid flux. It also is difficult to understand why the above processes would not affect Na and Mg in a similar manner. Ca may be preferentially deposited on the nightside because Ca^+ ions in the magnetosphere impact the midnight sector on Mercury's surface. Such a mechanism was suggested to explain an observed strong dawn enhancement in potassium (K) (*25*), but the high-energy release process necessary to produce the observed Ca distribution is currently unknown. Transport and loss are also factors that shape the distributions. In particular, the photoionization lifetime for Mg is approximately 10 times longer than that for Na and 100 times longer than for Ca (*11*). Photoionization losses undoubtedly play a role, but they are not likely to dominate over release in producing the distributions observed close to the planet.

Observations obtained during the MESSENGER flybys, particularly during M3, demonstrate that our knowledge of the source, transport, and loss processes controlling Mercury's exosphere is incomplete. The concentrated nature of Ca^+ in the near-planet tail region, the two-component polar profiles for the volatile species Na, and the striking differences in the polar and fantail observations for the two refractory species Ca and Mg indicate that Mercury's exosphere is both more varied and more intertwined with the magnetospheric environment than previously thought and that multiple, possibly complex, source processes may be important for the ejection of both volatile and refractory material into the exosphere. The Ca^+ observations provide evidence of magnetospheric convection effects on planetary ions, and the observed differences among the Na, Ca, and Mg distributions argue that the mix of processes at work in the exosphere not only affects volatile and refractory species differently but may be distinct for a given element or mineral. The MESSENGER flyby observations have revealed a complex exospheric system in which the observed spatial distributions suggest that multiple processes are at work in ways not yet understood.

References and Notes

1. W. E. McClintock, M. R. Lankton, *Space Sci. Rev.* **131**, 481 (2007).
2. S. C. Solomon, R. L. McNutt Jr., R. E. Gold, D. L. Domingue, *Space Sci. Rev.* **131**, 3 (2007).
3. W. E. McClintock *et al*., *Science* **321**, 92 (2008).
4. W. E. McClintock *et al*., *Science* **324**, 610 (2009).
5. Detected photon counts were converted to column emission, expressed in rayleighs (R; 1 R = 10^6 photons cm^{-2} s^{-1} emitted into a solid angle of 4π steradians), using instrument calibration coefficients determined during ground tests (*1*).
6. W.-H. Ip, A. Kopp, *J. Geophys. Res.* **107**, 1348 (2002).
7. M. Fujimoto *et al*., *Space Sci. Rev.* **132**, 529 (2007).
8. J. A. Slavin *et al*., *Science* **324**, 606 (2009).
9. J. A. Slavin *et al*., *Science* **329**, 665 (2010).
10. R. M. Killen, T. A. Bida, T. H. Morgan, *Icarus* **173**, 300 (2005).
11. M. Fulle *et al*., *Astrophys. J.* **661**, L93 (2007).
12. F. Leblanc *et al*., *Planet. Space Sci.* **55**, 1069 (2007).
13. D. C. Delcourt, T. E. Moore, S. Orsini, A. Millilo, J.-A. Sauvaud, *Geophys. Res. Lett.* **29**, 1591 (2002).
14. D. C. Delcourt *et al*., *Ann. Geophys.* **21**, 1723 (2003).
15. A. E. Potter, R. M. Killen, *Icarus* **194**, 1 (2008).
16. R. Killen, D. Shemansky, N. Mouawad, *Astrophys. J.* **181** (suppl.), 351 (2009).
17. A. E. Potter, R. M. Killen, T. H. Morgan, *Icarus* **186**, 571 (2007).
18. T. A. Bida, R. M. Killen, T. H. Morgan, *Nature* **404**, 159 (2000).
19. W. H. Smyth, M. L. Marconi, *Astrophys. J.* **441**, 839 (1995).
20. R. M. Killen *et al*., *Space Sci. Rev.* **132**, 433 (2007).
21. A. L. Sprague, R. W. H. Kozlowski, D. M. Hunten, W. K. Wells, F. A. Grosse, *Icarus* **96**, 27 (1992).
22. B. W. Denevi *et al*., *Science* **324**, 613 (2009).
23. S. L. Murchie *et al*., *Science* **321**, 73 (2008).
24. L. M. Prockter *et al*., *Science* **329**, 668 (2010).
25. A. L. Sprague, *J. Geophys. Res.* **97**, 18257 (1992).

26. We thank M. Lankton and M. Kochte for their contributions to the acquisition and analysis of the data reported here and J. Slavin and D. Blewett for insightful comments. The MESSENGER project is supported by the NASA Discovery Program under contracts NAS5-97271 to the Johns Hopkins University Applied Physics Laboratory and NASW-00002 to the Carnegie Institution of Washington. R.J.V., R.M.K., and A.L.S. are supported by the MESSENGER Participating Scientist Program.

19 February 2010; accepted 24 May 2010
Published online 8 July 2010;
10.1126/science.1188572
Include this information when citing this paper.

Downloaded from www.sciencemag.org on August 5, 2010

Host Phylogeny Constrains Cross-Species Emergence and Establishment of Rabies Virus in Bats

Daniel G. Streicker,[1,2]* Amy S. Turmelle,[1,3] Maarten J. Vonhof,[4] Ivan V. Kuzmin,[1] Gary F. McCracken,[3] Charles E. Rupprecht[1]

For RNA viruses, rapid viral evolution and the biological similarity of closely related host species have been proposed as key determinants of the occurrence and long-term outcome of cross-species transmission. Using a data set of hundreds of rabies viruses sampled from 23 North American bat species, we present a general framework to quantify per capita rates of cross-species transmission and reconstruct historical patterns of viral establishment in new host species using molecular sequence data. These estimates demonstrate diminishing frequencies of both cross-species transmission and host shifts with increasing phylogenetic distance between bat species. Evolutionary constraints on viral host range indicate that host species barriers may trump the intrinsic mutability of RNA viruses in determining the fate of emerging host-virus interactions.

In recent decades, cross-species transmission (CST) of RNA viruses has resulted in a range of disease emergence outcomes (*1*), from single infection "spillover" events such as rabies virus infections in humans (*2*), to transient outbreaks bound for extinction such as Nipah virus (*3*), to sustained epidemics with the potential for endemic establishment such as the SARS coronavirus (*4*). Although they are critical to anticipating the impact of viral emergence on human and animal health, the factors that determine the frequency and outcome of CST remain obscure. In RNA viruses, evidence for high mutation rates and occasional human epidemics originating from distantly related species have popularized the view that rapid evolution allows these viruses to overcome host-specific barriers in cellular, molecular, or immunological defenses (*5*). Consequently, it has been argued that RNA viruses emerge primarily between species with high contact rates (*6*–*8*). An alternative explanation posits that innate similarity in the defenses of closely related species may favor virus exchange by flattening the fitness valley that viruses traverse during adaptation to new hosts (*9*).

Identifying the most important determinants of viral emergence requires considering how the ecological dynamics of CST interact with evolutionary factors to shape replicated patterns of viral establishment in natural communities. Rabies, a ubiquitous, multihost viral zoonosis, provides this opportunity. In the United States, bats (*Chiroptera*) are the most common source of indigenously acquired human rabies infections, and approximately 2000 rabies-positive bats are collected annually after humans or domesticated animals have been exposed to them (*10*). Transmission occurs mainly by bat bite, and infection causes encephalitis with behavioral and motor abnormalities before death (*11*). The phylogeny of rabies virus in North American bats is structured by host species, reflecting an evolutionary history of host shifts followed by predominately within-species transmission (*12*, *13*). This species association of viral lineages enables identification of the species origins of relatively rare CST events from bats to humans or domesticated animals or within the bat community (*10*). Because North American bats span evolutionary divergences of approximately 3 million to 60 million years, a substantial range of ecological and physiological differences exists among species that might influence viral emergence (*14*).

We sequenced the nucleoprotein gene of 372 rabies viruses from 23 bat species collected across the continental United States over a 10-year period (Fig. 1A and table S1). Bayesian and maximum likelihood (ML) analyses (*15*) revealed 18 phylogenetic lineages of rabies virus that were statistically compartmentalized to particular bat taxa (Fig. 1B and table S2). New viral lineages were discovered in *Lasiurus intermedius floridanus* (LiV), *L. seminolus* (LsV), and *Myotis yumanensis* (MyV), establishing each as an independent rabies virus reservoir. The host-specificity of most viral lineages allowed us to infer the species origin of 360 infections in the data set after confirming the taxonomic identities of bats with mitochondrial DNA sequencing (table S3). Forty-three unambiguous CST events were observed, involving 15 bat species and 26 different species pairs. Nearly all viruses from cross-species infections were tightly nested within source clades and were no more genetically divergent than donor-lineage viruses (table S4), suggesting that they were more likely to be dead-end infections than infections occurring within stuttering chains of transmission in the recipient species (*15*).

We applied Markov chain Monte Carlo (MCMC) simulation to viral genetic data to compare four models of the strength and direction of CST between species pairs: symmetrical bidirectional transmission, asymmetrical bidirectional transmission, and each case of unidirectional transmission (*15*). Models selected by Akaike's information criterion were exclusively asymmetrical and predominately unidirectional (21 out of 26), suggesting unequal probability of infection for a given interspecific contact rate. Using parameters estimated from MCMC simulations (table S5), we quantified the expected number of infections in species i resulting from a single infected individual of species j (the per capita CST rate, R_{ij}) and visualized these in a "transmission web" (Fig. 2). Depending on species, a single rabid bat may infect between 0 and 1.9 heterospecifics, and on average, CST occurs once for every 72.8 within-species transmission events.

We next explored the intensity of CST between bat species pairs as a function of their ecological overlap (i.e., similarity in foraging behavior, roosting strategy, and body length), geographic range overlap, and phylogenetic relatedness, using host trait values estimated from our data and the literature (table S6). The intensity of R_{ij} declined continuously with the genetic distance between donor and recipient species and increased to a lesser extent with the amount of geographic overlap between species (Fig. 3A); however, our ecological proxies of interspecies contact failed to predict CST (tables S7 and S8). Results were robust to exclusion of several viruses for which the taxonomic identity of the host was based on morphology alone ($F_{2,25}$ = 9.38, $P < 0.001$; table S4 lists exclusions). Finally, a reanalysis of the transmission web using a novel metric (*15*) of connectance from food web theory (the proportion of realized interspecific connections in a food web) illustrated that rates of CST were highest to and from bat species that are sympatric with many closely related species but independent of the viral genetic diversity within the donor clade and the sampling effort for each bat species [supporting online text; $F_{2,13}$ = 12.24, coefficient of determination (r^2) = 0.67, P = 0.001]. These results suggest that initial infection of a new species is facilitated by evolutionary conservation of the cellular, immunological, or metabolic traits of hosts, with secondary effects of probabilistic factors, perhaps including exposures involving high viral load, that increase with species' range overlap.

In light of the host specificity implied by compartmentalization tests and phylogenetic analyses (table S2 and Fig. 1B), the high rates of CST shown here indicate that the vast majority of cross-species infections are evolutionary dead ends. Nevertheless, it is clear that rabies virus has successfully established itself repeatedly in North American bat species (*13*). This observation prompts the critical question of what determines whether CST causes a dead-end infection or sustained transmission in recipient species. We tested

[1]Rabies Team, Centers for Disease Control and Prevention, Atlanta, GA 30333, USA. [2]Odum School of Ecology, University of Georgia, Athens, GA 30602, USA. [3]Department of Ecology and Evolutionary Biology, University of Tennessee, Knoxville, TN 37996, USA. [4]Department of Biological Sciences and Environmental Studies Program, Western Michigan University, Kalamazoo, MI 49008, USA.

*To whom correspondence should be addressed. E-mail: dstrike@uga.edu

Downloaded from www.sciencemag.org on August 5, 2010

whether historical host shifts share a common phylogenetic constraint to present-day CST, using Bayesian ancestral state estimation of the host species origin of viral lineages (*15*). Nearly all (22 of 23) host shifts occurred between bat species that were more closely related than the median pair, and 66% of host shifts occurred within the top 25% of the most closely related North American bats, which is consistent with a lack of sustained transmission in distantly related species (Fig. 3B).

Phylogenetic signal in pathogen host range has been observed in fungal infections of heterospecific plants (*16*, *17*) and in a database study of parasite community similarity in wild primates (*18*). Although the consistency of host phylogeny as a predictor of emergence has been questioned for RNA viruses because of their potential for rapid within-host adaptation (*8*), sufficient data to test this hypothesis have been unavailable until now. Our study demonstrates that rapid evolution can be insufficient to overcome phylogenetic barriers at two crucial stages of viral emergence: initial infection and sustained transmission.

The decline in CST that we observed among more distantly related bat species might result from lower interspecific contact rates or a reduced probability of infection upon exposure. Although we could examine only a small number of species traits for which data were available, we found no effect of ecological proxies of interspecific contact on CST. This result is surprising given the infectiousness of rabies virus across mammals and abundant opportunities for CST among bats that share roosting and foraging sites. One explanation is that the disorientation and indiscriminate aggression caused by rabies infection (*11*) could limit the selectivity of interspecific contacts, causing their occurrence to depend on the frequency of host species sympatry. Our analysis supported both geographic overlap and host phylogenetic distance as strong predictors of CST. These two factors probably determine the frequency of exposure and the likelihood of infection after exposure, respectively.

Two explanations could account for the elevated frequency of host shifts among closely related bats. First, similarity in the biological barriers and social structure of closely related species could minimize the amount of evolution required to achieve an optimal balance of within-

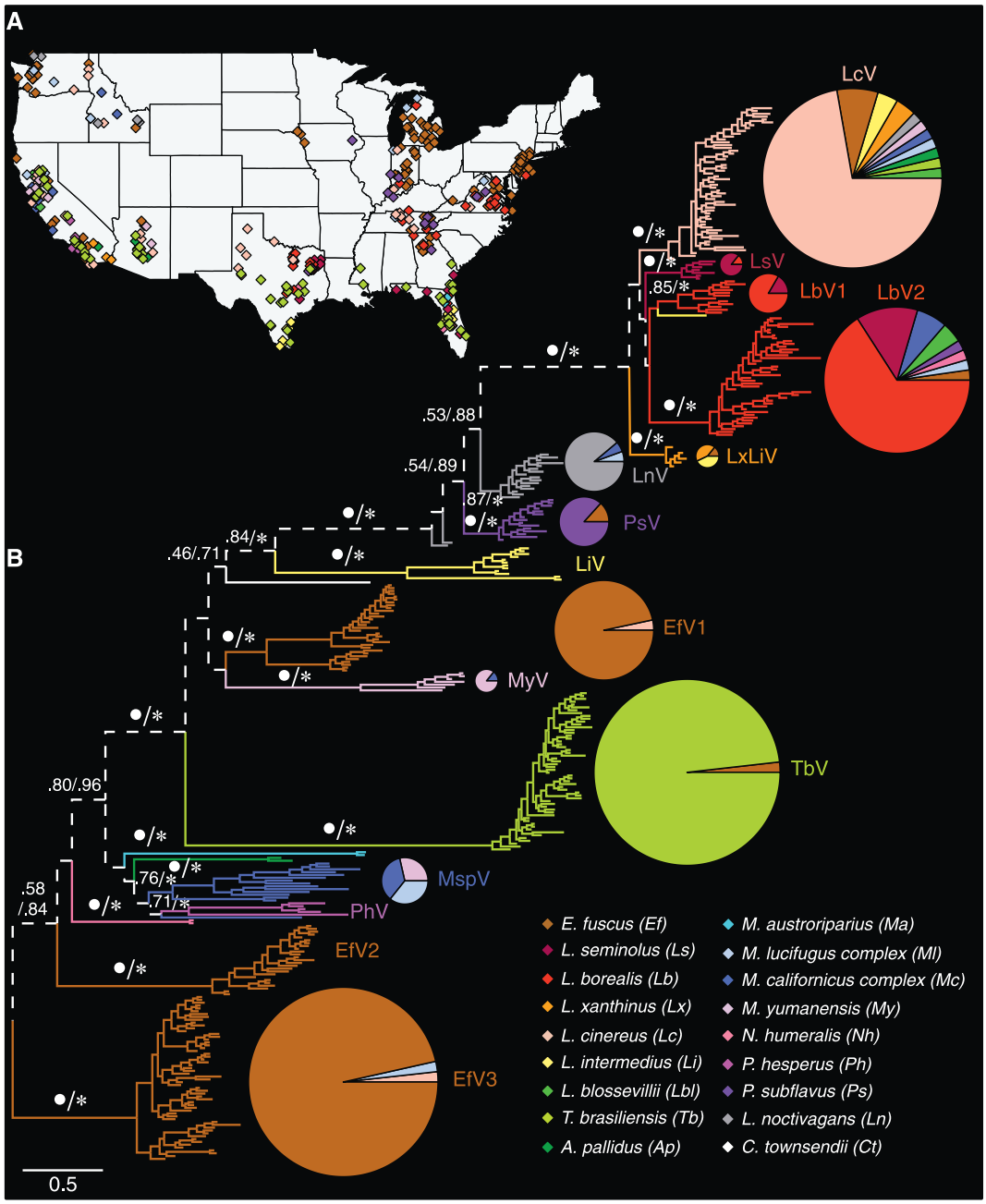

Fig. 1. Geographic origins, phylogenetic relationships, and host range of viral lineages. (**A**) Collection localities for 347 of 372 rabies virus samples; diamonds are jittered randomly to minimize overlap. (**B**) Bayesian phylogenetic tree with viral lineages labeled by donor host (table S3 contains full species names). MspV was associated with various *Myotis* species in the northwestern United States; LxLiV was associated with the western yellow bat (*L. xanthinus*) and the northern yellow bat (*L. i. intermedius*). Pie charts show the host species composition of lineages found in multiple species; the pie diameter is proportional to the number of bats sampled. ML bootstrap values (BVs) > 0.50 and Bayesian posterior probability (PP) values > 0.70 are shown to the lineage level (BV/PP). White circles are BV ≥ 0.90; asterisks are PP ≥ 0.98. The root branch has been removed for clarity; the dashed line indicates the trunk.

Downloaded from www.sciencemag.org on August 5, 2010

host replication and viral shedding (*9*). Although rabies virus uses evolutionarily conserved receptors for cell entry, receptor density on susceptible cells varies among species, leading to variable resistance to infection that maladapted viruses must overcome (*19*). Evolution of optimal virulence through modulation of transcription, gene expression, and replication might also be needed to balance entry into the central nervous system (ultimately leading to host death) with the timing and intensity of viral excretion from the salivary glands (necessary for transmission) to ensure sustained transmission within new host species (*20*). As a second limiting factor, even if the likelihood of viral establishment is independent of host phylogeny, viruses might still shift disproportionately between close relatives because of the greater frequency of CST. Although our results imply that rabies virus host shifts followed common rather than rare CST, the overwhelming support for host phylogenetic distance as the principal predictor of initial infection argues more strongly for intrinsic features of the host-virus interaction as the primary barrier to emergence.

The repeated failure of a notoriously generalist virus to colonize bat species that are capable of enzootic maintenance highlights the limitation of viral evolution to overcome host species barriers within a mammalian order. Similar effects could be critical determinants of the host range of other infections of public health or veterinary concern, such as lentiviruses in primates or morbilliviruses in carnivores. Nonetheless, the ultimate goal for predicting viral emergence is to understand drivers across varying taxonomic scales. Future studies of viral host range could examine whether the phylogenetic barriers that are evident at relatively shallow evolutionary distances dissipate for more distantly related taxa, where all emergence events might be equally improbable and driven by the frequency of interspecific contact.

Finally, we outlined a general framework to identify the origins of host shifts and quantify CST in complex multihost communities. A similar approach could be applied to any host-associated pathogen for which molecular sequence data are attainable. Quantification of per capita rates of pathogen transmission between species will be particularly useful to parameterize predictive models of viral emergence, which have traditionally ignored the process of CST despite its importance as the defining feature of zoonoses (*1*). Models incorporating such information will be

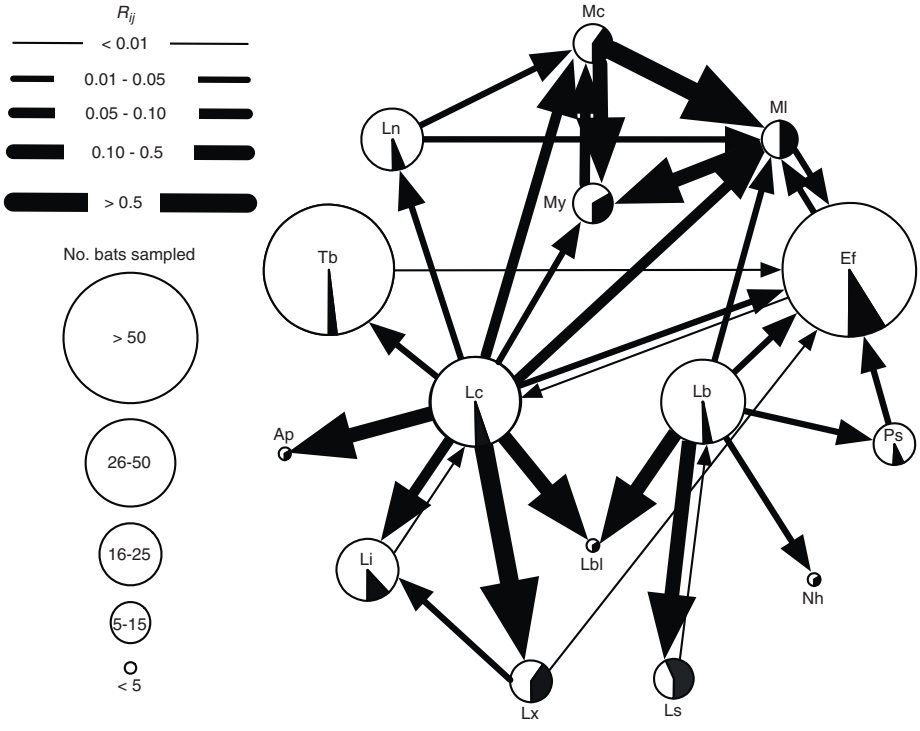

Fig. 2. Transmission web for 15 bat species. Pie charts describe the observed proportion of each species infected by CST. Arrows show the direction of transmission between species; the arrow width indicates per capita transmission rate (R_{ij}). Abbreviations for bat species names follow Fig. 1.

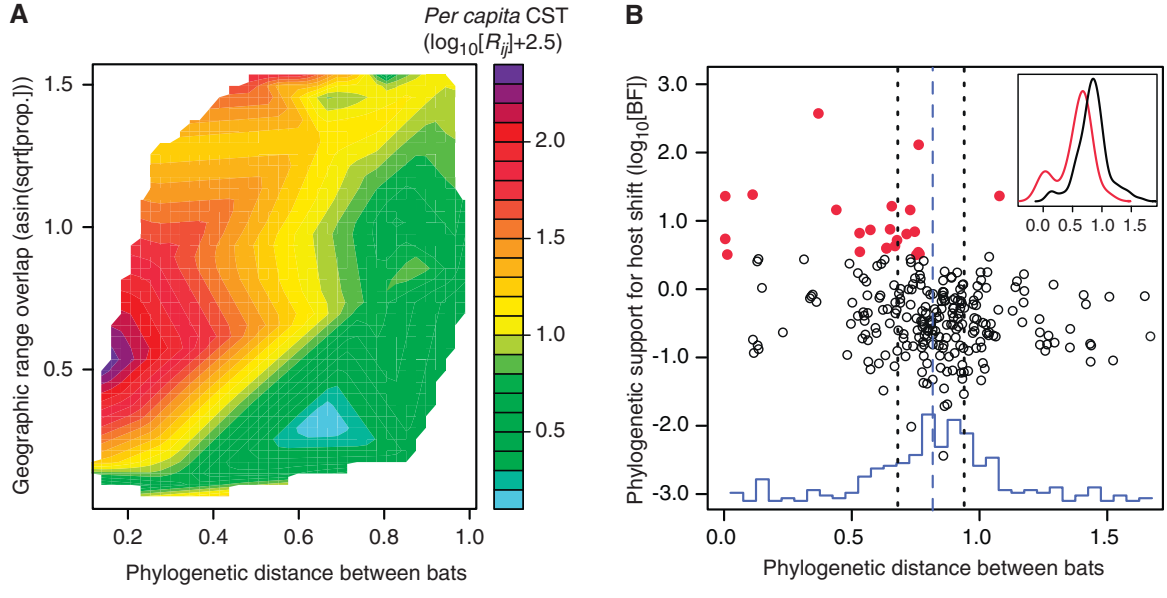

Fig. 3. Predictors of two stages of viral emergence. (**A**) Per capita CST declines with the genetic distance (substitutions per site) between bat species (slope = −3.93, $F_{1,28}$ = 21.89, P < 0.001) and increases with the proportion of their shared geographic range (slope = 1.21, $F_{1,28}$ = 8.22, P = 0.008; Full model: n = 31 bat species pairs, r^2 = 0.44; P < 0.001). Values for the contour plot were generated by bivariate interpolation. (**B**) The Bayes factor (BF) statistic describes the relative support for models containing versus lacking epidemiological linkages (i.e., historical host shifts) between each pair of viral lineages. Red circles indicate host shifts supported by ancestral state estimations (BF > 3), and open circles indicate host shifts that were inconsistent with phylogenetic data (BF < 3). Vertical lines show the median (blue) and lower and upper 25% limits (black) of the distribution of pairwise genetic distances between bats (blue histogram). Inset densities show the distributions of pairwise genetic distances for bat species implicated (red) or not implicated (black) in host shifts (*t* test for difference of means: t = 4.57, P < 0.0001).

Downloaded from www.sciencemag.org on August 5, 2010

critical to test the efficacy of specific disease prevention strategies applied not only within donor and recipient communities, but also in the realm where they intersect.

References and Notes

1. J. O. Lloyd-Smith *et al.*, *Science* **326**, 1362 (2009).
2. C. E. Rupprecht, C. A. Hanlon, T. Hemachudha, *Lancet Infect. Dis.* **2**, 327 (2002).
3. V. P. Hsu *et al.*, *Emerg. Infect. Dis.* **10**, 2082 (2004).
4. S. Riley *et al.*, *Science* **300**, 1961 (2003).
5. A. Moya, E. C. Holmes, F. González-Candelas, *Nat. Rev. Microbiol.* **2**, 279 (2004).
6. M. Anishchenko *et al.*, *Proc. Natl. Acad. Sci. U.S.A.* **103**, 4994 (2006).
7. H. D. Song *et al.*, *Proc. Natl. Acad. Sci. U.S.A.* **102**, 2430 (2005).
8. C. R. Parrish *et al.*, *Microbiol. Mol. Biol. Rev.* **72**, 457 (2008).
9. T. Kuiken *et al.*, *Science* **312**, 394 (2006).
10. J. D. Blanton, K. Robertson, D. Palmer, C. E. Rupprecht, *J. Am. Vet. Med. Assoc.* **235**, 676 (2009).
11. D. A. Brass, in *Rabies in Bats: Natural History and Public Health Implications*, D. A. Brass, Ed. (Livia Press, Ridgefield, CT, 1994), pp. 151–162.
12. J. S. Smith, L. A. Orciari, P. A. Yager, *Semin. Virol.* **6**, 387 (1995).
13. G. J. Hughes, L. A. Orciari, C. E. Rupprecht, *J. Gen. Virol.* **86**, 1467 (2005).
14. O. R. P. Bininda-Emonds *et al.*, *Nature* **446**, 507 (2007).
15. Materials and methods are available as supporting material on *Science* Online.
16. D. M. de Vienne, M. E. Hood, T. Giraud, *J. Evol. Biol.* **22**, 2532 (2009).
17. G. S. Gilbert, C. O. Webb, *Proc. Natl. Acad. Sci. U.S.A.* **104**, 4979 (2007).
18. T. J. Davies, A. B. Pedersen, *Proc. Biol. Sci.* **275**, 1695 (2008).
19. G. M. Baer, J. H. Shaddock, R. Quirion, T. V. Dam, T. L. Lentz, *Lancet* **335**, 664 (1990).
20. S. Finke, K. K. Conzelmann, *Virus Res.* **111**, 120 (2005).

21. For helpful discussion and comments, we thank P. Beerli, J. Davies, S. Altizer, A. Park, P. Rohani, J. Allgeier, B. Han, P. Stephens, and three anonymous reviewers. For contributing rabid bats, we thank the Arizona State Public Health Laboratory, the California Department of Public Health, the Georgia Department of Community Health, the Florida Department of Health, the Idaho Department of Health and Welfare, the Indiana State Department of Health, the University of Iowa's University Hygienic Laboratory, the Mississippi State Department of Health, the New Jersey Department of Health and Senior Services, the Tennessee Department of Health, the Texas Department of State Health Services, the Virginia Consolidated Laboratory, and the Washington State Department of Health. For providing museum-vouchered bat tissues, we thank the Angelo State Natural History Collection, the Carnegie Museum of Natural History, the Centro de Investigaciones Biológicas del Noroeste, the Louisiana State University Museum of Natural Science, the Museum of Vertebrate Zoology, the U.S. National Museum of Natural History, the Royal Ontario Museum, and the University of Alaska Museum. The sequences generated in this study can be found at GenBank under accession numbers GU644641 to GU645012 and GU722925 to GU723257 (table S1). This work was supported by Association of Public Health Laboratories/Centers for Disease Control Emerging Infectious Diseases and NSF Graduate Research Fellowships to D.G.S., NSF-NIH Ecology of Infectious Disease grant 0430418 to G.F.M., and funding from the U.S. Army Engineer Research Development Center–Construction Engineering Research Laboratory and Western Michigan University to M.J.V.

Supporting Online Material

www.sciencemag.org/cgi/content/full/329/5992/676/DC1
Materials and Methods
SOM Text
Fig. S1
Tables S1 to S9
References

26 February 2010; accepted 10 June 2010
10.1126/science.1188836

An Emerging Disease Causes Regional Population Collapse of a Common North American Bat Species

Winifred F. Frick,[1,2]* Jacob F. Pollock,[3] Alan C. Hicks,[4] Kate E. Langwig,[4,1] D. Scott Reynolds,[5,1] Gregory G. Turner,[6] Calvin M. Butchkoski,[6] Thomas H. Kunz[1]

White-nose syndrome (WNS) is an emerging disease affecting hibernating bats in eastern North America that causes mass mortality and precipitous population declines in winter hibernacula. First discovered in 2006 in New York State, WNS is spreading rapidly across eastern North America and currently affects seven species. Mortality associated with WNS is causing a regional population collapse and is predicted to lead to regional extinction of the little brown myotis (*Myotis lucifugus*), previously one of the most common bat species in North America. Novel diseases can have serious impacts on naïve wildlife populations, which in turn can have substantial impacts on ecosystem integrity.

Emerging infectious diseases are increasingly recognized as direct and indirect agents of extinction of free-ranging wildlife (*1*–*4*). Introductions of disease into naïve wildlife populations have led to serious declines or local extinctions of different species in the past few decades, including amphibians from chytridiomycosis (*5*, *6*), rabbits from myxomatosis in the United Kingdom (*7*), Tasmanian devils from infectious cancer (*3*), and birds in North America from West Nile virus (*8*). Here we demonstrate that white-nose syndrome (WNS), an emerging infectious disease, is causing unprecedented mortality among hibernating bats in eastern North America and has caused a population collapse that is threatening regional extinction of the little brown myotis (*Myotis lucifugus*), a once widespread and common bat species.

WNS is associated with a newly described psychrophilic fungus (*Geomyces destructans*) that grows on exposed tissues of hibernating bats, apparently causing premature arousals, aberrant behavior, and premature loss of critical fat reserves (*9*, *10*) (Fig. 1). The origin of WNS and its putative pathogen, *G. destructans*, is uncertain (*9*). A plausible hypothesis for the origin of this disease in North America is introduction via human trade or travel from Europe, based on recent evidence that *G. destructans* has been observed on at least one hibernating bat species in Europe (*11*). Anthropogenic spread of invasive pathogens in wildlife and domestic animal populations, so-called pathogen pollution, poses substantial threats to biodiversity and ecosystem integrity and is of major concern in conservation efforts (*1*, *2*).

WNS has spread rapidly and now occurs throughout the northeastern and mid-Atlantic regions in the United States and in Ontario and Québec provinces in Canada and currently affects at least seven species of hibernating bats (Fig. 2). Many species of bats in temperate North America hibernate in caves and mines (*12*) in aggregations of up to half a million individuals in a single cave (*13*). In late spring, these winter aggregations typically disperse into smaller sex-segregated groups of conspecifics, when adult females form maternity colonies and adult males mostly roost alone (*14*, *15*). From August to October, females and males assemble at hibernacula or swarming sites to mate before hibernating (*16*, *17*). The mechanisms for the persistence and transmission of *G. destructans* during summer and fall months are unknown, but spread of the fungus to new geographic regions and to other species may result from social and spatial mixing of individuals across space and time.

During the past 4 years, WNS has been confirmed in at least 115 bat hibernacula in the United States and Canada and has spread over 1200 km from Howe Cave near Albany, New York, where it was first observed in February

[1]Center for Ecology and Conservation Biology (CECB), Department of Biology, Boston University, 5 Cummington Street, Boston, MA 02215, USA. [2]Department of Environmental Studies, University of California Santa Cruz, 1156 High Street, Santa Cruz, CA 95064, USA. [3]Department of Ecology and Evolutionary Biology, University of California Santa Cruz, 1156 High Street, Santa Cruz, CA 95064, USA. [4]Endangered Species Unit, New York State Department of Environmental Conservation, 625 Broadway, Albany, NY 12233, USA. [5]St. Paul's School, Concord, NH 03301, USA. [6]Wildlife Diversity Division, Pennsylvania Game Commission, 2001 Emerton Avenue, Harrisburg, PA 16669, USA.

*To whom correspondence should be addressed. E-mail: wfrick@batresearch.org

Downloaded from www.sciencemag.org on August 5, 2010

2006 (*9*) (Fig. 2). Decreases in bats at infected hibernacula range from 30 to 99% annually, with a regional mean of 73%, and all surveyed sites have become infected within 2 years of the disease arriving in their region (Fig. 3, A to C). Such sharp declines and rapid spread raise serious concerns about the impact of WNS on the population viability of affected bat species.

We investigated the impacts of disease-associated mortality on the regional population of little brown myotis in the northeastern United States by comparing trends in pre- and post-WNS populations and simulating 100 years of post-WNS population dynamics to assess the consequences of the introduction of the disease for bat population viability (*18*). We used a population matrix model parameterized with survival and breeding probabilities estimated from 16 years (1993–2008) of mark and recapture data at a maternity site of little brown myotis (*19*) to estimate population growth before WNS (table S1). We also calculated geometric mean growth rates from winter count surveys of this species conducted over the past 30 years at 22 hibernacula ranging across five states in the northeastern United States to determine regional population trends before the emergence of WNS (table S2).

Deterministic population growth calculated from the population matrix model of mean vital rates was positive [yearly population growth rate (λ) = 1.008], demonstrating that population growth was stable or increasing before the emergence of WNS. Estimates of long-term growth rates over the past 30 years indicate that 86% of hibernacula (n = 19 out of 22) had stable or increasing populations (λ = >1). Regional mean growth equaled 1.07 (range: 0.98 to 1.2) (table S2), suggesting that the regional population was growing before WNS and that vital rates estimated from the maternity site represent regional patterns. The growth of hibernating populations over the past 30 years may be in response to conservation measures, such as protective gating of mines and caves (*20*), the installation of bat houses (*21*), and the potential amelioration of impacts from pesticides banned in the 1970s (*22*).

To assess the impact of disease-related mortality on population viability, we simulated population dynamics using a stochastic population model that included demographic data from both infected and susceptible (uninfected) populations (*18*). We performed 1000 simulations of 100 years of growth from a starting population of 6.5 million bats, using means, variances, and correlations from vital rates (*19*) that incorporated environmental variability (*23*). The probability of extinction for each year was defined as the proportion of 1000 runs for which the simulated population dropped below a quasi-extinction threshold during that year. Quasi-extinction was specified as 0.01% of the starting population (that is, 650 bats). Defining extinction thresholds at low population sizes accounts for processes such as demographic stochasticity and potential Allee effects (*23*–*26*).

In the simulation model, the susceptible population retained pre-WNS vital rates estimated from the 16-year mark and recapture data (*19*), and infected populations were given vital rates associated with annual declines calculated from infected hibernacula where consecutive yearly counts were available (n = 22) (*18*). The increase of prevalence of WNS was estimated as the percentage of uninfected hibernacula that became infected each year (2007, 5%; 2008, 49%; 2009, 59%) and was incorporated into the simulation as the proportion of the susceptible population that becomes infected each year.

Because of the inherent uncertainty in predicting the dynamics of a recently emergent disease, we evaluated the potential for disease fadeout and its influence on population viability. We estimated annual declines for each of 3 years after infection and constructed nine a priori models to test hypotheses regarding the influence of density and time since infection on population growth rates at infected hibernacula (table S3). From these estimates, there is little evidence of density-dependent declines, although model results suggest that the rate of decline ameliorates with the time since infection (Fig. 3D and table S3). To incorporate this time amelioration effect into the simulation model, we used predicted values of population growth from a nonlinear model [$\lambda = 1 - 1.16 \times \exp(-0.31 \times t)$, where t = years since infection] for each of 16 years after infection, when predicted population growth stabilized (λ = 1) (Fig. 3D).

We simulated population growth for five scenarios related to this time amelioration effect, including declines ameliorated according to predicted values (Fig. 3D) at each yearly time step and that persisted at 45% (3rd-year actual mean), 20% (6th-year predicted mean), 10% (8th-year predicted mean), 5% (10th-year predicted mean), and 2% (13th-year predicted mean) per year (Fig. 4). By comparing the probabilities of extinction over 100 years for these five scenarios, we evaluated the vulnerability of the regional population to extinction,

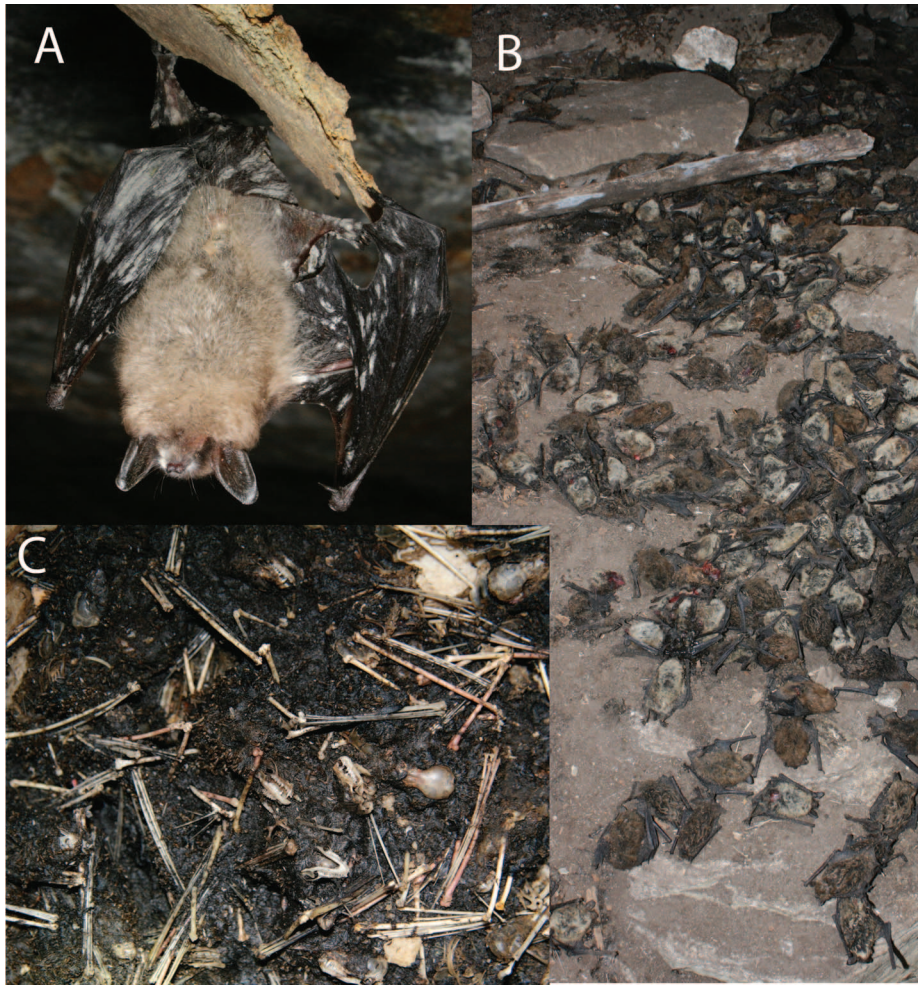

Fig. 1. (**A**) Photograph of hibernating little brown myotis infected with WNS. White fungus is visible on wings, ears, muzzle, and other exposed skin tissues. [Photo: Ryan Von Linden] (**B**) Bat carcasses piled on a cave floor, illustrating mass mortality at hibernacula infected with WNS. [Photo: Alan Hicks] (**C**) Skulls, bones, and decomposed carcasses covering the cave floor after multiple years of infection. [Photo: Marianne Moore]

Downloaded from www.sciencemag.org on August 5, 2010

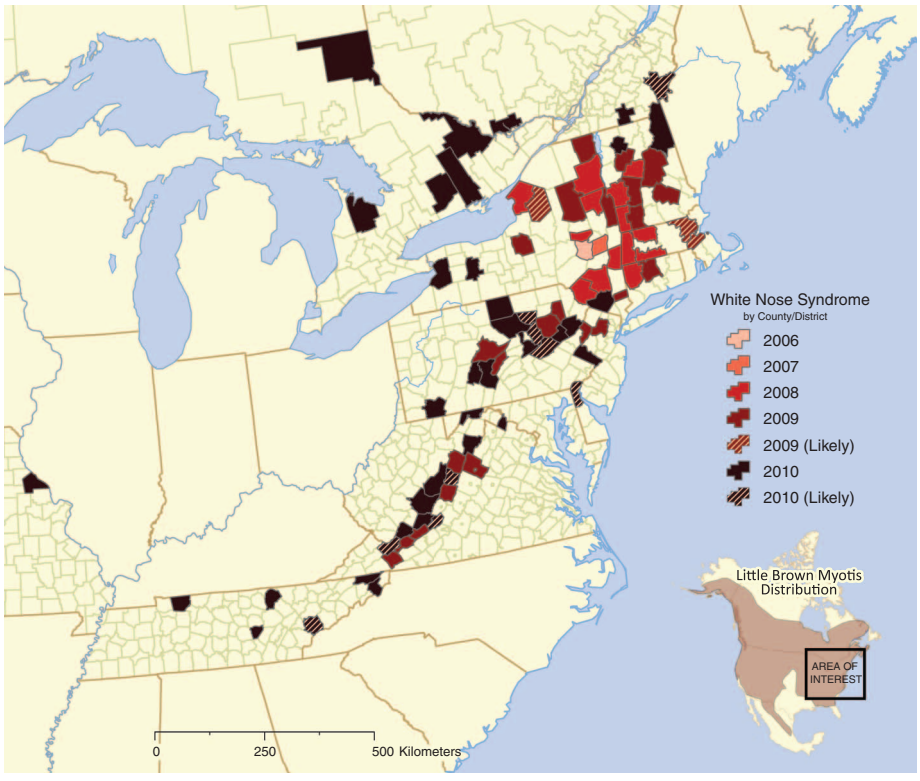

Fig. 2. Map of current distribution and spread of WNS across eastern North America.

given the uncertainty in how declines from disease mortality may persist in the future.

Using vital rates derived from mean declines in the first 3 years of infection and persisting at the observed third-year mean decline of 45% per year thereafter (Fig. 3D), we expect a 99% chance of regional extinction of little brown myotis within the next 16 years (Fig. 4A). If declines continue to ameliorate with time since infection, timelines to probable extinction lengthen but remain greater than 90% by 65 years, even if declines ameliorate and stabilize at 10% per year (Fig. 4A). Model results indicate that annual declines from WNS would have to ameliorate to less than 5% per year to significantly reduce the chance of extinction over 100 years (Fig. 4A). Even if disease mortality lessens over time, the regional population is expected to collapse from an estimated starting population of 6.5 million bats to fewer than 65,000 (1% of the pre-WNS population) in less than 20 years (Fig. 4B).

Our results paint a grim picture of a once-healthy population of an abundant and widely distributed species now experiencing unprecedented losses from WNS and facing a serious threat of regional extinction within the next 16 years (Fig. 4). Such a severe population decline, especially if the disease spreads farther south and west of its current distribution in eastern North America, may result in unpredictable changes in ecosystem

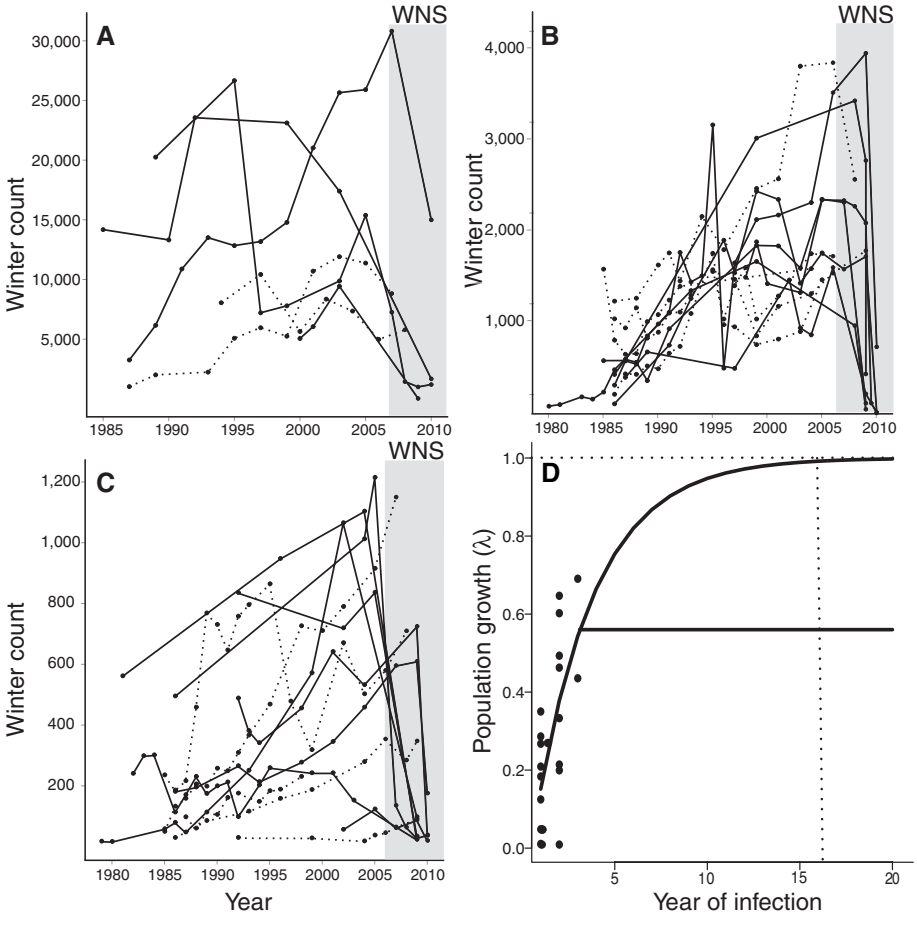

Fig. 3. (**A** to **C**) Population trends of little brown myotis over the past 30 years at (A) small (<1500 bats), (B) medium (<5000 bats), and (C) large (>5000 bats) hibernating colonies in the northeastern United States. Solid lines represent sites with bats infected with WNS; dotted lines represent uninfected sites. Hibernacula infected with WNS experienced a significant reduction in numbers as compared to the lowest available count from the past 30 years (Wilcoxon test = 190; $P < 0.002$). Large decreases in winter counts at a few hibernacula in the mid-1990s were related to winter flood events. (**D**) Population growth (λ) at hibernacula (black circles) by year since infection. The curved fitted line represents the nonlinear time-dependent model, showing amelioration of mortality from WNS until population growth reaches equilibrium at $\lambda = 1$ in 16 years since the first year of infection (vertical dotted line). The hockey-stick line represents declines from WNS persisting at the third-year mean of 45% per year, after a first-year decline of 85% and a second-year decline of 62%.

Downloaded from www.sciencemag.org on August 5, 2010

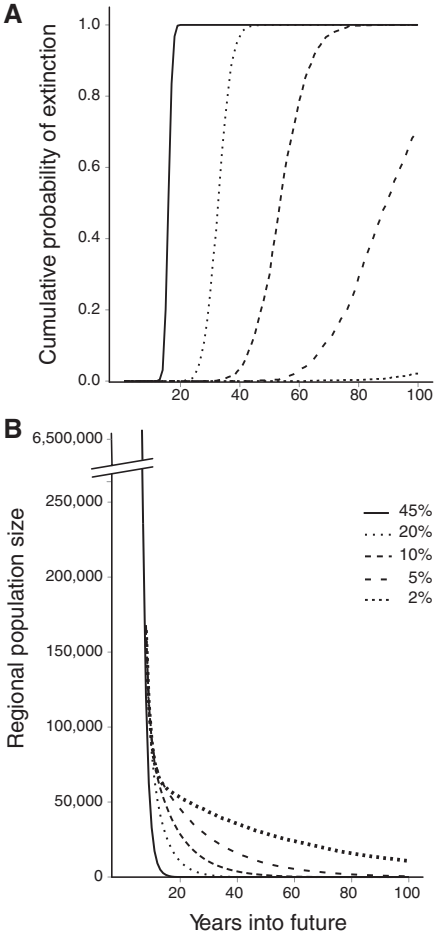

Fig. 4. (**A**) Cumulative probability of regional extinction of little brown myotis for five scenarios of time-dependent amelioration of disease mortality from WNS, based on matrix model simulation results. Each scenario represents predicted time-dependent declines for a specified number of years after infection and then holds the decline rate constant at either 45, 20, 10, 5, or 2% to demonstrate the impact of amelioration on the probability of extinction over the next 100 years. (**B**) Population size in each year averaged across 1000 simulations for each of the five scenarios of time-dependent amelioration of mortality from WNS.

structure and function (*27*, *28*). The rapid geographic spread of WNS since 2006, coupled with the severity and rapidity of population declines, support the hypothesis of introduction of a novel pathogen into a naïve population and demonstrate the seriousness of pathogen pollution as a conservation issue (*1*). Our analysis focused on little brown myotis in the northeastern United States, but several other bat species are experiencing similar mortality from WNS and may also be at significant risk of population collapse or extinction. This rapid decline of a common bat species from WNS draws attention to the need for increased research, monitoring, and management to better understand and combat this invasive wildlife disease (*1*).

References and Notes

1. P. Daszak, A. A. Cunningham, A. D. Hyatt, *Science* **287**, 443 (2000).
2. H. McCallum, A. Dobson, *Trends Ecol. Evol.* **10**, 190 (1995).
3. H. McCallum, *Trends Ecol. Evol.* **23**, 631 (2008).
4. A. M. Kilpatrick, C. J. Briggs, P. Daszak, *Trends Ecol. Evol.* **25**, 109 (2010).
5. L. Berger *et al.*, *Proc. Natl. Acad. Sci. U.S.A.* **95**, 9031 (1998).
6. K. R. Lips *et al.*, *Proc. Natl. Acad. Sci. U.S.A.* **103**, 3165 (2006).
7. F. Fenner, *FEMS Microbiol. Rev.* **24**, 123 (2000).
8. S. L. LaDeau, A. M. Kilpatrick, P. P. Marra, *Nature* **447**, 710 (2007).
9. D. S. Blehert *et al.*, *Science* **323**, 227 (2009).
10. A. Gargas, M. T. Trest, M. Christensen, T. J. Volk, D. S. Bleher, *Mycotaxon* **108**, 147 (2009).
11. S. J. Puechmaille *et al.*, *Emerg. Infect. Dis.* **16**, 290 (2010).
12. T. J. O'Shea, M. A. Bogan, *Monitoring Trends in Bat Populations of the United States and Territories: Problems and Prospects* (Biological Resources Discipline, Information and Technology Report USGS/BRD/ITR-2003-003, U.S. Geological Survey, Washington, DC, 2003).
13. R. Barbour, W. Davis, *Bats of America* (Univ. Press of Kentucky, Lexington, KY, USA, 1969).
14. T. H. Kunz, L. F. Lumsden, in *Bat Ecology,* T. H. Kunz, M. B. Fenton, Eds. (Univ. of Chicago Press, Chicago, IL, 2003), pp. 3–89.
15. T. H. Kunz, D. S. Reynolds, in (*12*), pp. 9–20.
16. W. H. Davis, H. B. Hitchcock, *J. Mammal.* **46**, 296 (1965).
17. D. W. Thomas, M. B. Fenton, R. M. R. Barclay, *Behav. Ecol. Sociobiol.* **6**, 129 (1979).
18. Information on materials and methods is available on *Science* Online.
19. W. F. Frick, D. S. Reynolds, T. H. Kunz, *J. Anim. Ecol.* **79**, 128 (2010).
20. E. T. Posluszny, C. Butchkoski, in *Proceedings of Bat Conservation and Mining: A Technical Interactive Forum* (Bat Conservation International and U.S. Department of the Interior, Office of Surface Mining, St. Louis, MO, 2000), pp. 159–168.
21. M. D. Tuttle, D. Hensley, *Bats* **11**, 3 (1993).
22. K. N. Geluso, J. S. Altenbach, D. E. Wilson, *Science* **194**, 184 (1976).
23. W. F. Morris, D. F. Doak, *Quantitative Conservation Biology: Theory and Practice of Population Viability Analysis* (Sinauer, Sunderland, MA, 2002).
24. F. Courchamp, T. Clutton-Brock, B. Grenfell, *Trends Ecol. Evol.* **14**, 405 (1999).
25. P. A. Stephens, W. J. Sutherland, *Trends Ecol. Evol.* **14**, 401 (1999).
26. F. Courchamp, B. Grenfell, T. Clutton-Brock, *Proc. Biol. Sci.* **266**, 557 (1999).
27. K. J. Gaston, *Science* **327**, 154 (2010).
28. G. W. Luck, G. C. Daily, P. R. Ehrlich, *Trends Ecol. Evol.* **18**, 331 (2003).

29. Funding was provided by grants from the U.S. Fish and Wildlife Service (USFWS) to W.F.F., J.F.P., D.S.R., T.H.K., and G.G.T. We thank three anonymous reviewers, J. P. Hayes, and D. F. Doak for helpful reviews and A. M. Kilpatrick for fruitful discussion. Funding for winter counts of bats at hibernacula was provided by USFWS Section 6 and State Wildlife Grants issued to the Pennsylvania Game Commission, and by Federal Aid in Wildlife Restoration Grant WE-173-G issued to the New York State Department of Environmental Conservation. Count data from hibernating colonies were kindly provided by the Connecticut Department of Environmental Protection; the Pennsylvania Game Commission; the New York Department of Environmental Conservation; Vermont Fish and Game; the Massachusetts Division of Fisheries and Wildlife; and K. Berner, State University of New York at Cobleskill. We are grateful to the many individuals who were involved in conducting annual counts of bats at hibernacula over the past 30 years. Data are available upon request from the authors.

Supporting Online Material

www.sciencemag.org/cgi/content/full/329/5992/679/DC1
Materials and Methods
Figs. S1 and S2
Tables S1 to S3
References

22 February 2010; accepted 24 May 2010
10.1126/science.1188594

Sex-Specific Parent-of-Origin Allelic Expression in the Mouse Brain

Christopher Gregg,[1,2] Jiangwen Zhang,[3] James E. Butler,[1,2] David Haig,[4] Catherine Dulac[1,2]*

Genomic imprinting results in preferential gene expression from paternally versus maternally inherited chromosomes. We used a genome-wide approach to uncover sex-specific parent-of-origin allelic effects in the adult mouse brain. Our study identified preferential selection of the maternally inherited X chromosome in glutamatergic neurons of the female cortex. Moreover, analysis of the cortex and hypothalamus identified 347 autosomal genes with sex-specific imprinting features. In the hypothalamus, sex-specific imprinted genes were mostly found in females, which suggests parental influence over the hypothalamic function of daughters. We show that *interleukin-18*, a gene linked to diseases with sex-specific prevalence, is subject to complex, regional, and sex-specific parental effects in the brain. Parent-of-origin effects thus provide new avenues for investigation of sexual dimorphism in brain function and disease.

Genomic imprinting is an epigenetic mode of gene regulation involving preferential expression of the paternally or maternally inherited allele (*1*). Sexual dimorphism is a central characteristic of mammalian brain function and behavior that influences major neurological diseases in humans (*2*). Here we address the potential existence of differential genomic imprinting in the brain according to the sex of individuals. Imprinting refers to gene expression differences between maternal and paternal chromosomes (*3*) and is also used more strictly to define complete allele-specific silencing (*4*). Our analysis encompasses sex differences in parent-

[1]Department of Molecular and Cellular Biology, Harvard University, Cambridge, MA 02138, USA. [2]Howard Hughes Medical Institute, Harvard University, Cambridge, MA 02138, USA. [3]FAS Research Computing, Harvard University, Cambridge, MA 02138, USA. [4]Department of Organismic and Evolutionary Biology, Harvard University, Cambridge, MA 02138, USA.

*To whom correspondence should be addressed. E-mail: dulac@fas.harvard.edu

Downloaded from www.sciencemag.org on August 5, 2010

of-origin allelic effects involving all-or-none allele-specific expression and parental biases in gene expression.

Three processes may underlie sexually dimorphic genomic imprinting (fig. S1, A to C). Nonrandom X inactivation, such as the imprinted X inactivation observed in marsupials and the mouse extra-embryonic lineages, could result in the preferential silencing of one of the parentally inherited X chromosomes in females (fig. S1A) (*5*). In addition, imprinting of individual X-linked loci in females results in gene expression from the active paternally inherited X that differs from the active maternally inherited X (fig. S1B). Studies of Turner syndrome suggested imprinting of X chromosome loci with relevance to brain function (*6*), and X-linked imprinted genes have indeed been identified in the brain (*7*, *8*). Finally, autosomal genes might be imprinted in one sex but not the other (fig. S1C). A recent study of quantitative trait loci influencing growth and body composition in mice indicates that such mechanisms may exist (*9*).

We have used Illumina transcriptome sequencing of F_1 hybrid mice generated from initial (F_1i) and reciprocal (F_1r) crosses of CAST/EiJ (CAST) and C57BL/6J (C57) mice to investigate genomic imprinting in the brain with high resolution (*10*, *11*). Here we compare parental effects in the transcriptome of the adult male versus adult female preoptic area (POA) of the hypothalamus and medial prefrontal cortex (mPFC). Detailed methods are described in (*10*) and in our companion paper (*11*).

We first assessed global levels of X-linked gene expression from the maternal X chromosome (Xm) versus the paternal X chromosome (Xp) in the adult female POA and mPFC. A significant strain-effect favoring expression from the CAST X chromosome was observed in F_1 females (Fig. 1, A and B). This difference is likely due to preferential selection of the CAST X-chromosome in the hybrids (*12*). In addition, we identified a parent-of-origin effect (Fig. 1, A and C), such that total levels of expression from the Xm were increased by 19% and 11% relative to the Xp in the mPFC and POA, respectively. The Xm bias was significantly greater in the mPFC than in the POA ($P < 0.0001$, two-tailed Fisher's exact test).

This elevated expression from the Xm versus the Xp (Fig. 1, A and C) may indicate a bias in X inactivation in the brain, a hypothesis further investigated with a transgenic mouse line expressing X-linked *egfp* under the control of the cytomegalovirus (CMV) promoter as a reporter of the active X chromosome (*13*). Control studies confirmed that the *egfp* transgene reports X inactivation (fig. S2), and egfp expression was found restricted to a subpopulation of vesicular glutamate transporter 2–positive (vGLUT2$^+$) glutamatergic neurons (~72%) (fig. S3). We compared the number of Xm- versus Xp-expressing glutamatergic neurons in adult Xm^{egfp}/Xp and Xm/Xp^{egfp} females (Fig. 2). In cortical regions, 40 to 50% more neurons expressed the Xm than the Xp in the mPFC, the sensory CTX, and the piriform CTX (Fig. 2A). We also observed a significant Xm bias in

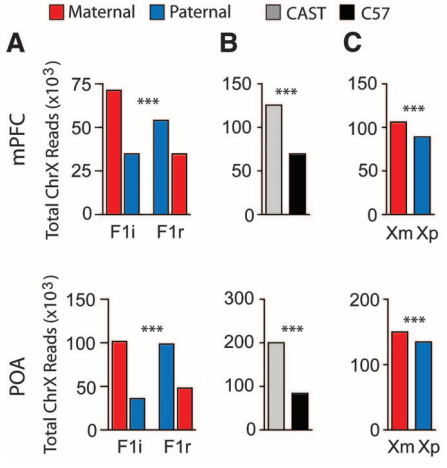

Fig. 1. Sex-specific imprinting and preferential expression of the Xm in the female brain. (**A**) Total maternal and paternal X-linked reads for the adult female mPFC and POA in F_1i and F_1r crosses reveals a highly significant association between strain and cross (mPFC, $P < 0.0001$; POA, $P < 0.0001$, two-tailed Fisher's exact test). (**B**) Identification of a significant strain effect favoring CAST X-chromosome expression (χ^2 analysis). (**C**) Preferential expression of the Xm in the mPFC and POA (χ^2 analysis). ***$P < 0.001$; *$P < 0.05$.

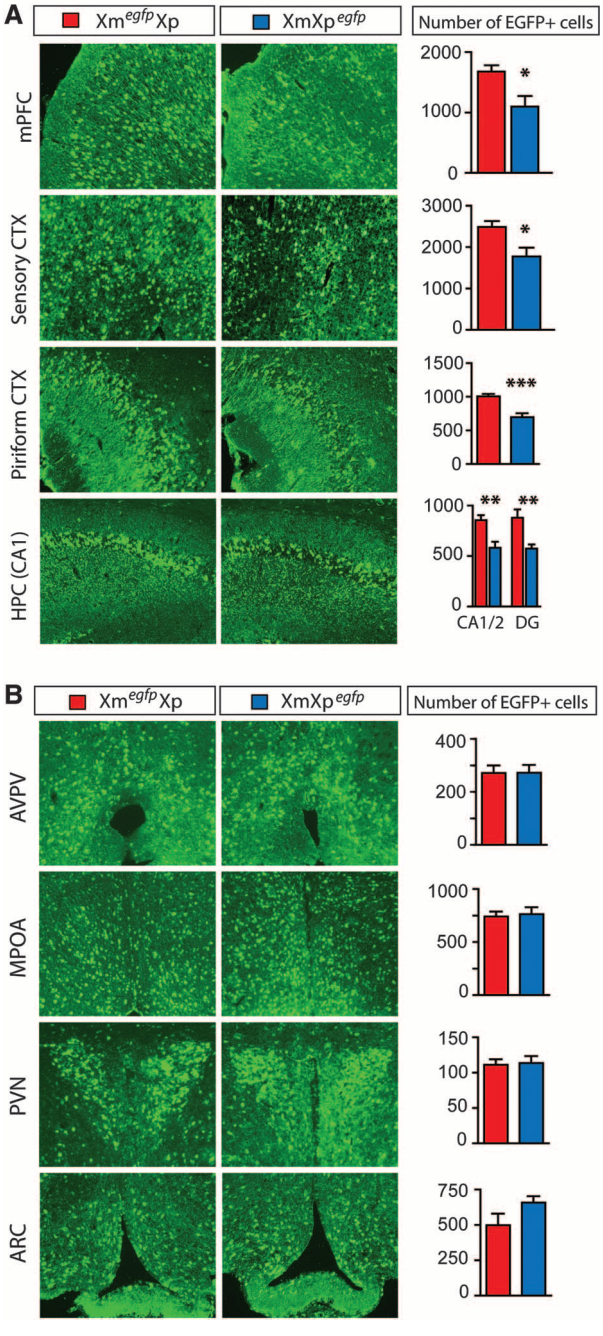

Fig. 2. Preferential expression of Xm in female cortical regions indicated by Xm^{egfp}/Xp and Xm/Xp^{egfp} transgenic mice. (**A** and **B**) The number of EGFP$^+$ cells in different cortical (A) and hypothalamic (B) brain regions of Xm^{egfp}/Xp (red) versus Xm/Xp^{egfp} (blue) 5-week-old females. Hypothalamic regions: anteroperiventricular nucleus (AVPV), medial preoptic area (MPOA), periventricular nucleus (PVN), or arcuate nucleus (ARC). Two-tailed unpaired *t* test; $n = 7$; ***$P < 0.001$; **$P < 0.01$; *$P < 0.05$. Red bars, Xm^{egfp}/Xp; blue bars, Xm/Xp^{egfp}. Scale bar, 50 μm.

Downloaded from www.sciencemag.org on August 5, 2010

the CA1/2 and dentate gyrus (DG) regions of the hippocampus (HPC) (Fig. 2A). In contrast, no difference in the number of Xm- versus Xp-expressing cells was detected in the hypothalamus (Fig. 2B). We then asked whether the bias observed in cortical versus hypothalamic glutamatergic neurons could be generalized to all or a few neuronal populations in these brain regions. We summed the Xm and Xp reads for seven well-characterized neuron-specific X-linked genes and found a significant Xm expression bias in both the mPFC (21% Xm bias; $P < 0.0001$) and POA (15% Xm bias; $P < 0.0001$, two-tailed Fisher's exact test) (fig. S4). Therefore, whereas X^{egfp}+ glutamatergic neurons in POA do not preferentially select the Xm, some other neuronal populations of the hypothalamus likely do (fig. S4).

We then assessed X-linked imprinting at the level of individual genes using a chi-square test in which the expected value was adjusted for strain and maternal X selection biases. Using the stringent cutoff of $P < 0.05$ in the F_1i and F_1r cross used in our companion study (*11*) to assess imprinting, we failed to identify X-linked imprinted loci. Using a less stringent cutoff ($P < 0.1$), the previously known maternally expressed imprinted gene (MEG) *Xrl3b* (*7*, *8*) was correctly identified, and this approach further identified nine candidate imprinted genes in the POA and three in the mPFC (table S1), such as *yipf6*, which was identified in the POA (maternal bias) and mPFC (paternal bias).

Finally, we searched for sex-specific parental allelic effects on the autosomes. As reported in our companion paper, parental expression biases in the male and female data sets were highly correlated (Fig. 3, A and B). However, single-nucleotide polymorphism (SNP) sites that exhibited a strong parental bias in one sex but not the other were also apparent in the data (Fig. 3, A and B). A chi-square test was applied in the F_1i and F_1r cross to identify SNP sites (cutoff $P < 0.05$) significantly imprinted in one sex but not the other ($P > 0.05$).

This study identified 347 candidate genes associated with sex-specific parental allelic effects in the adult brain, as defined by the presence of one or more SNP sites statistically imprinted in one sex but not the other (tables S2 and S3). The average parental expression bias exhibited by sex-specific imprinted SNP sites was 73% (POA) and 68% (mPFC), whereas the average bias for the same sites in the opposite sex was 52% (POA) and 51% (mPFC). Females had three times the total number of genes with sex-specific imprinted features (Fig. 3C) [150 genes (1.3% of 11,241 genes assessed)] as males in the POA [48 genes (0.5% of 9235 genes assessed], but no difference was observed in the mPFC. This correlates well with the facts that the POA is a highly sexually dimorphic region of the brain involved in the control of maternal and mating behaviors and that imprinting is known to influence maternal behavior (*14*). We noted a paternal bias in the number of sex-specific genes identified in all samples (Fig. 3C).

We carried out an in-depth analysis of two candidate genes subject to sex-specific parental effects: *mitochondrial ribosomal protein 48* (*Mrpl48*) and *interleukin-18* (*Il18*). Mitochondria are strictly maternally inherited, and mitochondrial ribosomal proteins regulate translation in mitochondria but are encoded in the nuclear DNA (*15*). *Mrpl48* is one of four *Mrpl* genes found in our companion studies, which indicates parental control over the bioenergetics of neural cells. In the present study, *Mrpl48* was identified as paternally expressed in the female POA but not the male POA (Fig. 4A and fig. S5A). In the female POA, eight out of nine *Mrpl48* SNP sites exhibited a paternal expression bias in the F_1i and F_1r cross, four of which achieved statistical significance ($P < 0.05$) (Fig. 4A). In contrast, none of the nine SNP sites exhibited a paternal expression bias in the male POA. The female-specific paternal expression bias was confirmed in the POA by Sequenom matrix-assisted laser desorption/ionization–time-of-flight mass spectrometry (MALDI-TOF) analysis (Fig. 4A).

Il18 encodes a cytokine expressed by neurons, astrocytes, and microglia that modulates neuroinflammation as well as homeostatic processes and behavior (*16*). *Il18* has been linked to multiple sclerosis, a highly sexually dimorphic disease that predominates in women and is associated with parent-of-origin effects through the maternal lineage (*17*). We found *Il18* to be preferentially expressed from the maternal allele in the female but not male mPFC or the POA. We identified two SNP sites (three bases apart) in one exon of *Il18* in the female mPFC that indicate that 74% of transcription from this region

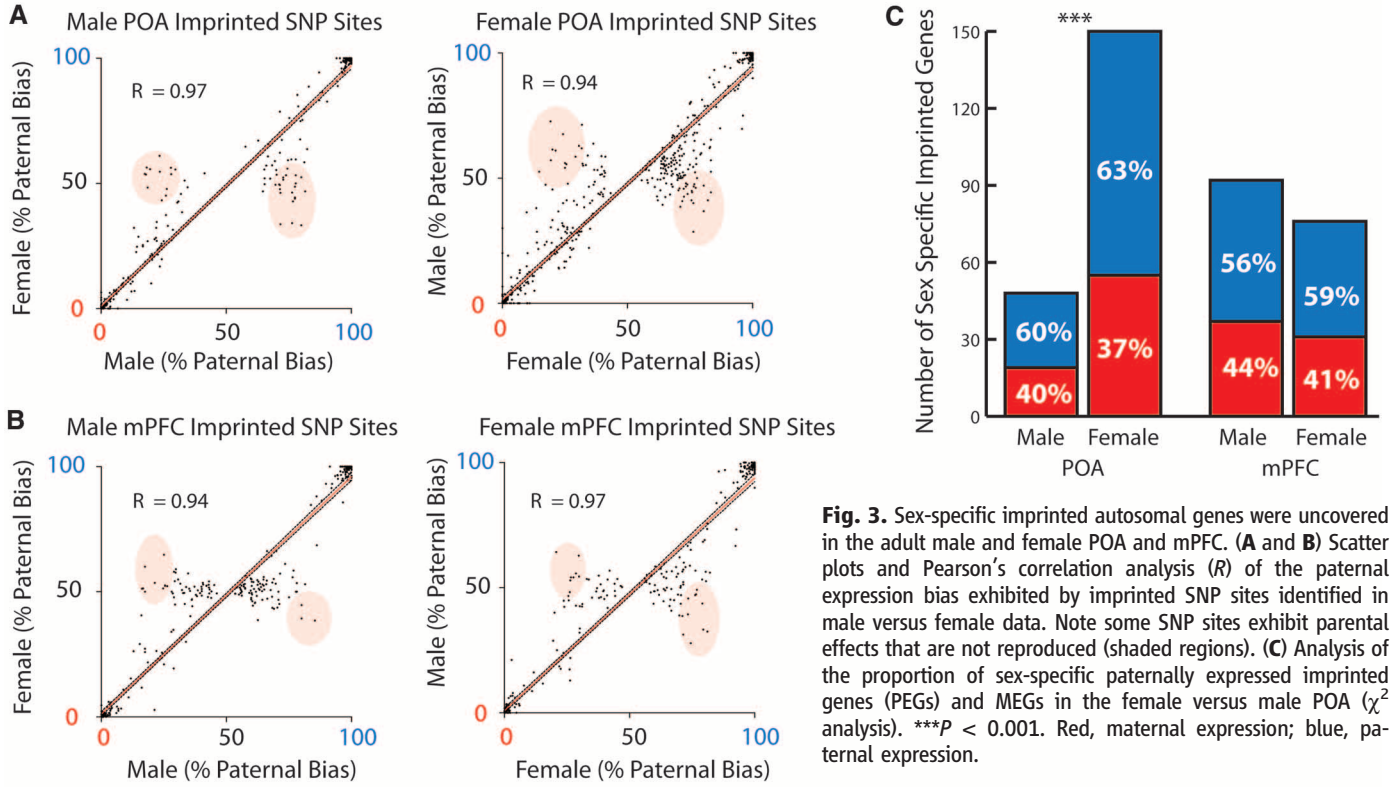

Fig. 3. Sex-specific imprinted autosomal genes were uncovered in the adult male and female POA and mPFC. (**A** and **B**) Scatter plots and Pearson's correlation analysis (*R*) of the paternal expression bias exhibited by imprinted SNP sites identified in male versus female data. Note some SNP sites exhibit parental effects that are not reproduced (shaded regions). (**C**) Analysis of the proportion of sex-specific paternally expressed imprinted genes (PEGs) and MEGs in the female versus male POA (χ^2 analysis). ***$P < 0.001$. Red, maternal expression; blue, paternal expression.

Downloaded from www.sciencemag.org on August 5, 2010

of the locus arises from the maternal allele (Fig. 4B and fig. S5B).

Il18 signaling has anorectic effects, and heterozygous *Il18* female, but not male, mice exhibit hyperphagia (*18*). We used quantitative polymerase chain reaction (QPCR) to assess *Il18* levels in the mPFC and the hypothalamus of *Il18* heterozygous mice on a C57 background (Fig. 4C and fig. S5B). Loss of the maternal allele in the mPFC of $Il18^{-/+}$ females, but not males, resulted in a reduction by a factor of 2.3 in the level of *Il18* expression relative to animals in which the paternal allele was deleted (Fig. 4C). No significant parent-of-origin effects were observed in the hypothalamus in males or females (Fig. 4C). These results are consistent with the preferential expression of the maternal allele in the female mPFC uncovered by the Illumina RNA-sequencing (RNA-Seq) analysis.

Il18 is adjacent to *SDHD* (*succinate dehydrogenase complex, subunit D*) and *Bcdo2* (*beta, beta-carotene 9',10'-dioxygenase variant 2*) in mouse and human. Mutations in *SDHD* lead to head and neck paragangliomas in humans only when paternally inherited, yet previous studies have failed to detect imprinting at this locus (*19*). We found evidence for sex-specific parent-of-origin effects in the mPFC, but not the POA, for both *SDHD* (male maternal bias) and *Bcdo2* (female paternal bias) (fig. S6), which suggested a putative gene cluster with highly complex, region-specific and sex-specific parent-of-origin effects. Future studies will be required to determine the existence of an imprinting control region or other defining features of bona fide imprinted gene clusters.

Our data present evidence for epigenetic mechanisms by which parents may differentially influence gene expression in the brain of daughters versus sons and provide insights into sexually dimorphic epigenetic pathways recently uncovered in the brain (*20*). Some of the genes identified have known relevance to behavior and disease, although the mechanisms and functions of these parental effects are unclear. Previous analysis of X inactivation in the brain focused on very early stages of neural development and failed to observe any parental bias (*21*). The Xm bias may emerge during development through differential cell proliferation or survival, although a few studies have suggested that X inactivation in female somatic lineages favors selection of the Xm (*22*–*24*). The Xm enrichment contrasts with the paternal bias found among autosomal genes subject to sex-specific imprinting and the 70% paternal bias of autosomal genes identified in our companion study (*11*). The X chromosome is enriched for genes involved in brain function (*25*, *26*), and theoretical work has postulated that the maternally biased inheritance of the X selects for maternal interests (*27*, *28*). Investigating the potential relations between maternal and paternal gene expression programs may shed light on brain function, evolution, and disease.

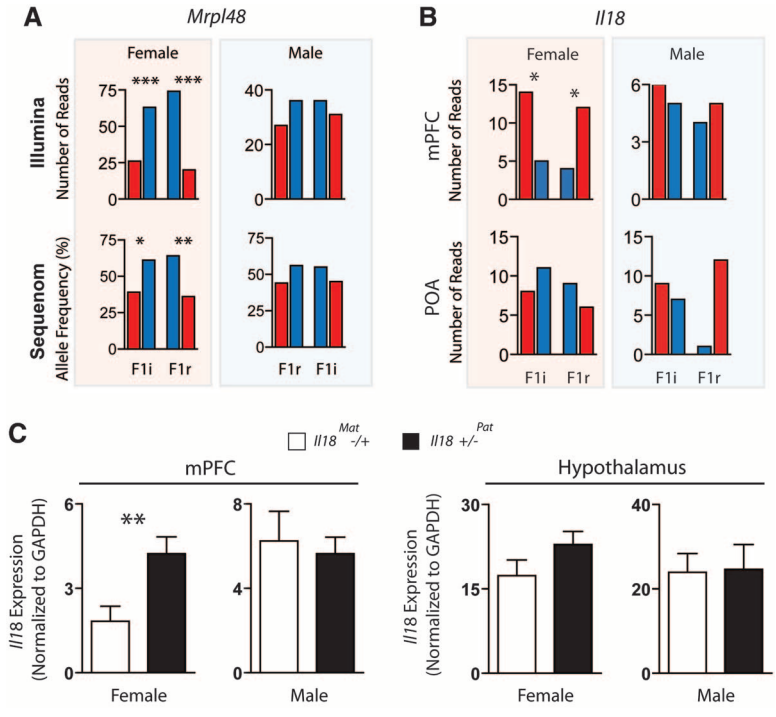

Fig. 4. Sex-specific imprinted expression of *Mrpl48* and *Il18* in the female brain. (**A**) Illumina read data for an imprinted SNP in the 3′ untranslated region (3′ UTR) of *Mrpl48* [highlighted in blue in (A); SNP_ID: uc009inh.1_801] indicate preferential expression of the paternal allele in the female but not male POA (χ^2 analysis). Sequenom analysis confirmed the result (average allele frequency from three biological and three technical replicates). (**B**) Illumina read data for the imprinted SNP in *Il18* (SNP_ID: uc009inh.1_801) indicate preferential expression of the maternal allele in the female mPFC, but not the male mPFC or the POA (χ^2 analysis). (**C**) QPCR analysis of *Il18* expression in maternal- versus paternal-deletion *Il18* heterozygous mice on C57 background reveals reduced expression in the mPFC of female maternal-deletion mice relative to paternal-deletion mice (n = 10, two-tailed, unpaired t test, P = 0.0086). No difference was observed in the male mPFC (n = 5) or the hypothalamus (females: n = 5, males: n = 6). ***P < 0.001; **P < 0.01; *P < 0.05. Red, maternal expression; blue, paternal expression. GAPDH, glyceraldehyde-3-phosphate dehydrogenase.

References and Notes

1. W. Reik, J. Walter, *Nat. Rev. Genet.* **2**, 21 (2001).
2. J. B. Becker *et al.*, Eds., *Sex Differences in the Brain: From Genes to Behavior* (Oxford Univ. Press, New York, 2008).
3. J. G. Hall, *Am. J. Hum. Genet.* **46**, 857 (1990).
4. M. S. Bartolomei, S. M. Tilghman, *Annu. Rev. Genet.* **31**, 493 (1997).
5. B. Payer, J. T. Lee, *Annu. Rev. Genet.* **42**, 733 (2008).
6. D. H. Skuse *et al.*, *Nature* **387**, 705 (1997).
7. A. S. Raefski, M. J. O'Neill, *Nat. Genet.* **37**, 620 (2005).
8. W. Davies *et al.*, *Nat. Genet.* **37**, 625 (2005).
9. R. Hager, J. M. Cheverud, L. J. Leamy, J. B. Wolf, *BMC Evol. Biol.* **8**, 303 (2008).
10. Materials and methods are available as supporting material on *Science* Online.
11. C. Gregg *et al.*, *Science* **329**, 643 (2010); published online 8 July 2010 (10.1126/science.1190830).
12. E. Heard, P. Clerc, P. Avner, *Annu. Rev. Genet.* **31**, 571 (1997).
13. J. Wang *et al.*, *Nat. Genet.* **28**, 371 (2001).
14. E. B. Keverne, *Adv. Genet.* **59**, 217 (2007).
15. E. C. Koc *et al.*, *J. Biol. Chem.* **276**, 43958 (2001).
16. S. Alboni, D. Cervia, S. Sugama, B. Conti, *J. Neuroinflammation* **7**, 9 (2010).
17. B. M. Herrera *et al.*, *Neurology* **71**, 799 (2008).
18. E. P. Zorrilla *et al.*, *Proc. Natl. Acad. Sci. U.S.A.* **104**, 11097 (2007).
19. B. E. Baysal, *Am. J. Med. Genet. C. Semin. Med. Genet.* **129C**, 85 (2004).
20. M. M. McCarthy *et al.*, *J. Neurosci.* **29**, 12815 (2009).
21. S. S. Tan, E. A. Williams, P. P. Tam, *Nat. Genet.* **3**, 170 (1993).
22. L. H. Chadwick, H. F. Willard, *Mamm. Genome* **16**, 691 (2005).
23. D. J. Fowlis, J. D. Ansell, H. S. Micklem, *Genet. Res.* **58**, 63 (1991).
24. D. S. Falconer, J. H. Isaacson, I. K. Gauld, *Genet. Res.* **39**, 237 (1982).
25. D. K. Nguyen, C. M. Disteche, *Nat. Genet.* **38**, 47 (2006).
26. U. Zechner *et al.*, *Trends Genet.* **17**, 697 (2001).
27. D. Haig, *Evolution* **60**, 440 (2006).
28. D. Haig, *Cytogenet. Genome Res.* **113**, 68 (2006).

29. We thank L. Luo, T. Maniatis, R. Losick, S. Hippenmeyer, and members of the Maniatis and Dulac labs for critical comments on the manuscript. We thank R. Hellmiss for help with figures and R. Jaenisch for X^{egfp} mice. This work was supported by the Klarman Foundation for Eating Disorders and the Howard Hughes Medical Institute (HHMI). C.G. is supported by a Human Frontiers long-term fellowship and Alberta Heritage Foundation for Medical Research Incentive Award. C.D. is an HHMI investigator. All data can be found in GEO: GSE22131.

Supporting Online Material

www.sciencemag.org/cgi/content/full/science.1190831/DC1
Materials and Methods
Figs. S1 to S6
Table S1 to S3
References

13 April 2010; accepted 24 June 2010
Published online 8 July 2010;
10.1126/science.1190831
Include this information when citing this paper.

Downloaded from www.sciencemag.org on August 5, 2010

Nonlinear Elasticity and an 8-nm Working Stroke of Single Myosin Molecules in Myofilaments

Motoshi Kaya and Hideo Higuchi*

Using optical trapping and fluorescence imaging techniques, we measured the step size and stiffness of single skeletal myosins interacting with actin filaments and arranged on myosin-rod cofilaments that approximate myosin mechanics during muscle contraction. Stiffness is dramatically lower for negatively compared to positively strained myosins, consistent with buckling of myosin's subfragment 2 rod domain. Low stiffness minimizes drag of negatively strained myosins during contraction at loaded conditions. Myosin's elastic portion is stretched during active force generation, reducing apparent step size with increasing load, even though the working stroke is approximately constant at about 8 nanometers. Taking account of the nonlinear nature of myosin elasticity is essential to relate myosin's internal structural changes to physiological force generation and filament sliding.

Molecular motors, such as muscle myosins, axonemal dyneins, and mitotic spindle kinesins, function as assemblies of motors (*1*). To achieve their motile activities efficiently, it is crucial for these motors to generate force collectively and to minimize the interference between motors (*2*, *3*). In Huxley's model of muscle contraction (*4*), it is postulated that an attached myosin generates the sliding movement of an actin filament and is subsequently pulled into a drag region, resulting in drag (negative) forces. Because the contribution of individual myosin giving negative force cannot be separated from the integrated forces of all attached myosins in muscle fiber measurements (*4*–*6*), the molecular mechanism of how dragged myosins affect the dynamics of muscle contraction remains unclear. To elucidate this mechanism, we focus on the changes in elasticity of single myosins for both the positive and negative strain directions, because it directly affects both the active and drag force generation when myosins are stretched or shortened (*2*, *4*).

Streptavidin-coated quantum dots (QDs) were attached to biotinylated actin filaments to minimize the uncertainty in the bead-actin linkage stiffness (*7*, *8*). The stiffness of actin filaments between myosin binding and QDs positions was ~20 pN/nm [supporting online material (SOM) text 1] (*9*), which was much greater than observed for single myosins. An actin filament bound to QDs was suspended between two streptavidin-coated beads held in two optical traps (Fig. 1A). For no nucleotide or 1 mM adenosine diphosphate (ADP) conditions, single myosins embedded in myosin-rod cofilaments were tightly bound to the actin filaments. The positions of the two trapped beads were then triangularly moved along the longitudinal axis of the cofilament (Fig. 1B). The total force exerted by a single myosin was then calculated as the sum of the forces exerted on the two trapped beads (fig. S5). By taking the ensemble average on 50 tracking traces, the precision was greatly improved, up to 0.3 nm for QDs bound to actin filaments at 2-ms exposure during the stiffness measurements (fig. S6).

The force-displacement curve for a single myosin showed the nonlinear elasticity for both no nucleotide and 1 mM ADP conditions (Fig. 1C). Myosin-rod cofilaments attached to the glass surface were slightly displaced relative to the surface during the stretching and shortening of the single myosins (fig. S7). The stiffness of the myosin-rod cofilaments was 9.2 pN/nm (Fig. 1C). The displacements of the myosins were obtained by subtracting the displacements of the myosin-rod cofilaments and the estimated elongation of the actin filament from those of the QDs (SOM text 1). The stiffness of a single myosin was greater (>2.5 pN/nm) when stretched by a force >~2 pN compared with (0.02 to 0.5 pN/nm) when it is compressed (fig. S1). The biphasic force response between the positive and negative strain regions was consistent for both no nucleotide and 1 mM ADP conditions (Fig. 1C). In contrast to the linear elasticity, the nonlinear elasticity allows for large active force when myosins are actively stretched but reduces negative force when myosins are compressed (SOM text 2).

What part of the myosin head is responsible for the biphasic elastic response? The low stiffness region was observed for displacements from 0 to –80 nm. Eighty nanometers is approximately double the length of a myosin subfragment 2 (S2) (*10*), implying that the low stiffness characterizes the elastic response of the myosin S2. The stiffness value of 0.02 pN/nm (fig. S1) is consistent with the theoretically calculated bending stiffness of myosin S2 (~0.01 pN/nm) (*11*). The large stiffness observed in the positive dis-

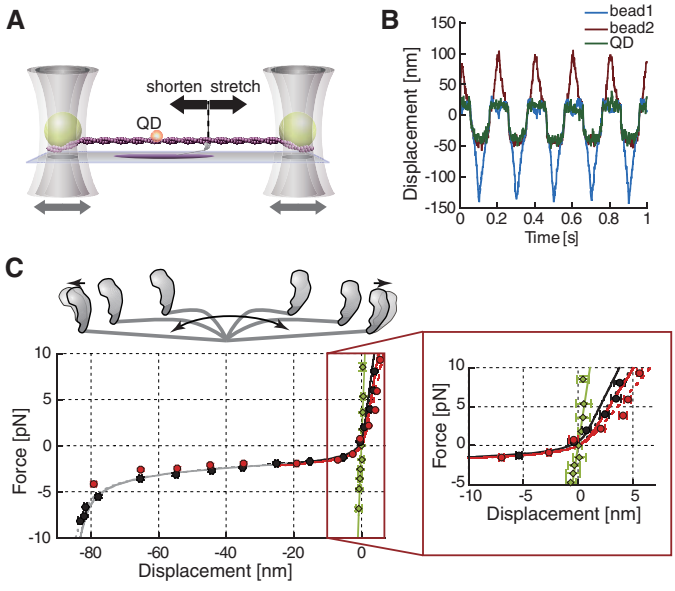

Fig. 1. Measurement of single-myosin stiffness. (**A**) Schematic diagram of the optical trap system for a single-myosin stiffness measurement. (**B**) Time course of displacement of beads and a quantum dot on an actin filament bound to a single myosin during oscillation of the optical trap. (**C**) Force-displacement curve of single myosins in no nucleotide (black) and the presence of 1 mM ADP (red). Data points (black and red circles, mean ± SE) were combined from the force-displacement curves of individual myosins (n = 8 for no nucleotide, and n = 7 for ADP) based on the ensemble-averaged data (fig. S5). Green diamonds show the linear force-displacement relationship for myosin-rod cofilaments (n = 10) (fig. S7). The dotted lines are the fitting curves on the original data for displacements above –10 nm, and the solid lines are the fitting curves adjusted by accounting for the compliance of myosin-rod cofilaments and actin filaments (SOM text 1). The gray dotted and solid lines for no nucleotide are the corresponding fitting curves for displacements below –10 nm. As shown by the black arrows in the illustration of myosins on the top, plots with displacements either positive or below –80 nm characterize the stiffness of myosin S1, whereas those with displacements between 0 and –80 nm characterize the stiffness of myosin S2. The right panel shows the force-displacement curve in a zoomed range of strain.

Department of Physics, Graduate School of Science, University of Tokyo, 7-3-1 Hongo Bunkyou-ku Tokyo, 113-0033 Japan.

*To whom correspondence should be addressed. E-mail: higuchi@phys.s.u-tokyo.ac.jp

placement region and for displacements of lower than –80 nm characterizes the elasticity of myosin S1 when the myosin S2 portion is fully stretched in either direction. The maximum stiffness of 2.6 (ADP) to 2.9 pN/nm (fig. S1) (no nucleotide) is consistent with both the stretching and bending stiffness of myosin S1 (2 pN/nm) (*8*, *12*) but not with the bending (~0.01 pN/nm) or stretching (60 to 80 pN/nm) stiffness of myosin S2 (*11*).

The stiffness of 2.6 to 2.9 pN/nm obtained here is higher than most previously reported values (table S1). We may have obtained higher stiffness values in this study for three reasons: First, the uncertainties of the bead-linkage stiffness and myofilament compliance were reduced by the direct measurement of the actin and the myosin-rod displacements; second, the stiffness of two-headed myosins here might be higher than that of single-headed myosins; third, the cooperative behavior of the two heads may have led to an optimal orientation of one head for stiffness production (*13*, *14*) (SOM text 3).

Next, we investigated how the observed elasticity of single myosins affects the displacement of single myosins during actomyosin interaction. The values of unitary displacement of single myosins have varied from 3 to 17 nm (table S1), probably because of the nonprocessivity of the myosin II motor, different myosin preparations, and the random orientations of myosin heads relative to an actin filament. Here, displacements and forces of single skeletal myosins during processive movement were generated by a few myosin molecules synthesized into myosin-rod cofilaments (fig. S8) so that myosins could interact processively with actin filaments in a more natural environment. Myosin molecules were allowed to interact with biotinylated actin filaments attached to single streptavidin beads (Fig. 2A). The displacements and forces generated by myosins were measured by an optical trap (*15*) (Fig. 2A). Similar to the stiffness measurements, we assumed cooperativity between the two heads (SOM text 3).

To estimate the maximum number of myosin molecules interacting with an actin filament, the number of interacting molecules as a function of the half-length of the myosin-rod cofilament was

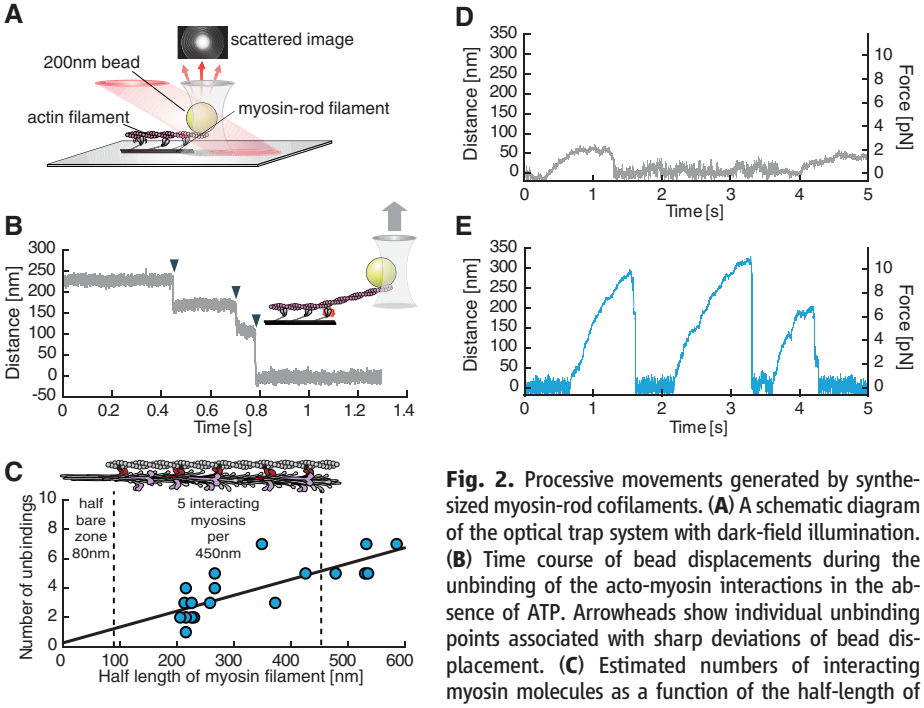

Fig. 2. Processive movements generated by synthesized myosin-rod cofilaments. (**A**) A schematic diagram of the optical trap system with dark-field illumination. (**B**) Time course of bead displacements during the unbinding of the acto-myosin interactions in the absence of ATP. Arrowheads show individual unbinding points associated with sharp deviations of bead displacement. (**C**) Estimated numbers of interacting myosin molecules as a function of the half-length of myosin-rod cofilaments. The lengths were estimated from fluorescent images (fig. S8). The linear regression indicates ~5 interacting molecules per half-length of 450 nm (r^2 = 0.63), as illustrated by the myosin heads in red on the top. Myosins in pink illustrate existing myosins that cannot interact with an actin. (**D** and **E**) Time courses of bead displacements generated by short (415 nm, gray) and long (900 nm, blue) myosin-rod cofilaments, respectively, in an ATP concentration of 20 μM.

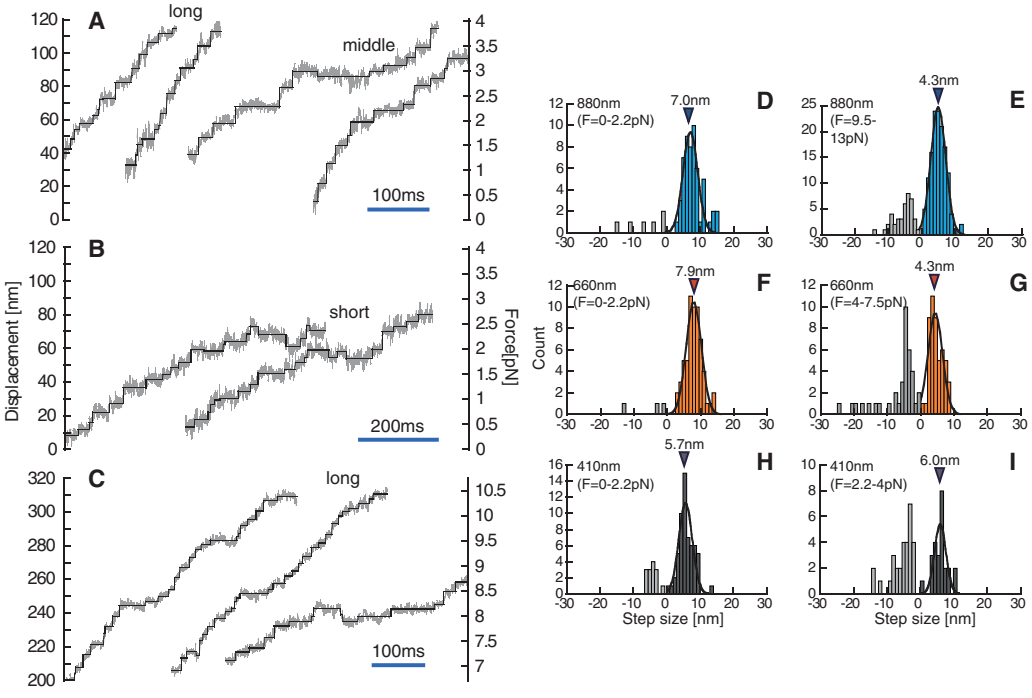

Fig. 3. Stepwise displacements generated by myosin-rod cofilaments. (**A** to **C**) Raw bead displacement data (gray line) generated by short, middle, and long myosin-rod cofilaments at low [(A) and (B)] and high (C) loads. The individual steps (black line) were detected by the step-finding algorithm. (**D** to **I**) Histograms of step sizes for long (880 ± 18 nm, n = 3), middle (660 nm, n = 1), and short (410 ± 7 nm, n = 2) myosin-rod cofilaments at different loads. The mean step sizes were determined by the values at the central positions of single Gaussian curves.

obtained from the measurement of unbinding events of rigor bonds (*16*) (Fig. 2B). Five myosins per half cofilament length of 450 nm, on average, were able to interact with an actin (Fig. 2C), which corresponds to approximately 1.5 interacting molecules for each 43-nm pitch in a native thick filament, consistent with the structural configuration of native thick and thin filaments (SOM text 4).

The time course of bead displacements for short and long cofilaments showed stepwise movements of actin filaments over 100 to 300 nm, corresponding to 3 to 11 pN of loads in 20 μM ATP (Fig. 2, D and E, and Fig. 3, A to C). A histogram of the step sizes, detected by a step-finding algorithm (*17*, *18*), was well approximated by a Gaussian curve, with a peak at 4 to 7 nm (Fig. 3, D to I), depending on the applied load. For three cofilament lengths, the elementary step size consistently decreased from 7 to 4 nm with increasing load (Fig. 4A). The similarity of the step sizes at low and high loads was confirmed using a pair-wise distance analysis procedure (fig. S9). The forward steps are presumably generated by the attachment of active myosins, because the detachment of drag motors associated with low stiffness should not be evident in the forward-step generation, while the backward steps (e.g., Fig. 3, D to I) are the consequence of the detachment of active motors.

How many myosins contribute to step generation? Dwell times for adjacent steps and no load for three cofilament lengths were estimated by extrapolating curves fitted to the relationship between dwell times and loads (fig. S10). The turnover time of a single myosin in 20 μM ATP was calculated as the sum of the measured lifetime of attachment (τ_{on} = 33 ms) and the estimated lifetime of detachment (τ_{off} = 25 ms) (SOM text 5). These estimated values were combined and plotted against the number of interacting heads (*N*) (Fig. 4B). The relationships fit well to an inverse function of *N*, suggesting that individual steps were generated by the turnover of one myosin head, which randomly bound with an actin within the turnover time of single myosin heads (SOM text 6 and fig. S3). Thus, the observed step sizes characterize the mechanical properties of single myosin heads, suggesting that the step sizes of single myosin heads vary from 7 to 4 nm in a load-dependent manner (Fig. 4A). Load-dependent step size has also been shown in experiments using stepwise length releases in single muscle fibers (*19*–*22*). Thus, the load-dependent changes in the step size are an essential property of skeletal myosin.

The load-dependent step size can be interpreted in the following manner (fig. S11). First, the detached myosin reattaches to an actin filament and then performs the working stroke (d_w), which is generated by the conformational changes of the myosin head (*23*). When no load is applied, the size of the working stroke is directly translated into the sliding movement of the actin filament, that is, the observed step size (d_s). However, when a load is applied, the working stroke is limited by the stretch of the elastic portion of myosin head (d_e). Consequently, the observed step size ($d_s = d_w - d_e$) decreases. Thus, the working stroke size, calculated as the sum of the observed step sizes and the corresponding stretch of the elastic portion of the myosin head estimated from the force-displacement curve (Fig. 1C), appears to be load-independent and is approximately 8 nm (Fig. 4A). A working stroke of 8 nm is slightly larger than the typical size of 5 nm for S1 (*24*, *25*) and smaller than the values of 10 to 12 nm estimated in structural studies on single myosins (*23*), but is more consistent with the 7 to 10 nm observed in studies on two-headed myosins (*14*) and muscle fibers (*21*). Thus, the discrepancy of working stroke size between the present study and the S1 measurement might be attributed to the difference in the number of myosin heads interacting with actin (or in structure) (*14*).

Similar step sizes were observed for myosin-rod cofilaments of three different lengths, which consist of different numbers of interacting molecules (Fig. 4A). This result can be explained by the nonlinear elasticity of single myosins. Because the duty ratio [$\tau_{on} / (\tau_{on} + \tau_{off})$] is 0.57 for no load or higher for loaded conditions (fig. S10), more than half of the interacting myosin molecules are in the strongly bound state. If the elasticity of myosins were linear even in the negative strain region (*2*, *4*), the drag forces would become substantially higher with an increasing population of the strongly bound myosins for longer cofilament (SOM text 2 and fig. S2), resulting in smaller step sizes. In contrast, the nonlinear elasticity obtained here ensures small drag forces even for long cofilaments with more drag motors. Thus, the similar step sizes observed for different cofilament lengths are well explained by the concept of nonlinear elasticity (SOM text 2 and fig. S2).

By measuring the step sizes of single myosins detected from the processive movements of the synthetic myosin-rod cofilaments, we found that step size is load-dependent and working size is load-independent on the single-molecule level. We also found a nonlinear elasticity of skeletal myosins by measuring the elastic property of "full-length" myosins for a wide range of positive and negative strains. The nonlinear elasticity implies that the attachment and working stroke of active myosins with high stiffness is primarily responsible for the forward step generation, whereas the detachment of drag myosins with low force due to low stiffness does not primarily contribute to the forward steps. Based on these findings, we propose a model for the molecular mechanism of muscle contraction (fig. S2 and fig. S11). During force generation, individual myosins repeatedly perform the working distance of 8 nm. After completion of force generation, myosins become much softer as they shorten and possibly buckle, resulting in a reduction of the drag force against the subsequent force generation performed by other neighboring myosins. Such molecular properties may be inherent in the assembly of molecular motors and may reduce molecular interference, leading to the high mechanical efficiency of muscle contraction (*26*).

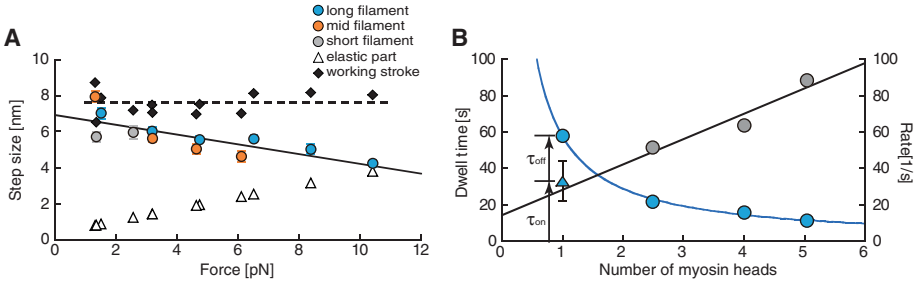

Fig. 4. (**A**) Mean step sizes, working stroke sizes, and the amounts of stretch in the elastic portion of single myosins as functions of the loads. The amount of stretch for no nucleotide condition (triangles) is estimated from the nonlinear fitting curve with forces on the force-displacement curve depicted in Fig. 1C. The working stroke sizes (diamonds) were given as sums of the observed step sizes (circles, mean ± SE) and the corresponding amounts of stretch in the elastic portion. The horizontal dashed line indicates a mean working stroke size of 7.6 nm, independent of loads. The black linear regression line on the step size represents the trend of the load-dependent step size. (**B**) Dwell times between steps at no load as a function of the number of interacting heads. The number of interacting myosin heads (*N*) is estimated from Fig. 2C by assuming the cooperativity between the two heads (SOM text 3). Dwell times for the *n* = 2.5, 4, and 5 myosins at no load were estimated from the dwell time-force relationships (fig. S10). The dwell time for a single myosin head (*n* = 1) corresponds to the turnover time in 20 μM ATP, which is calculated as the sum of the measured attachment lifetime (τ_{on} = 33 ms) and the estimated detachment lifetime (τ_{off} = 25 ms) (SOM text 5). Dwell times (blue circles) fit well with an inverse function of *N* (blue line). The rate constants (gray circles), given as inverse dwell times, also fit well with a linear function of *N* (black line) (SOM text 6).

References and Notes

1. J. Howard, in *Mechanics of Motor Proteins and the Cytoskeleton* (Sinauer, Sunderland, MA, 2001), pp. 213–227.
2. E. Pate, H. White, R. Cooke, *Proc. Natl. Acad. Sci. U.S.A.* **90**, 2451 (1993).
3. P. Bieling, I. A. Telley, J. Piehler, T. Surrey, *EMBO Rep.* **9**, 1121 (2008).
4. A. F. Huxley, *Prog. Biophys. Biophys. Chem.* **7**, 255 (1957).
5. L. E. Ford, A. F. Huxley, R. M. Simmons, *J. Physiol.* **269**, 441 (1977).
6. Y. E. Goldman, J. A. MacCray, D. P. Vallette, *J. Physiol.* **398**, 72 (1988).
7. C. Veigel, M. L. Bartoo, D. C. White, J. C. Sparrow, J. E. Molloy, *Biophys. J.* **75**, 1424 (1998).
8. A. Lewalle, W. Steffen, O. Stevenson, Z. Ouyang, J. Sleep, *Biophys. J.* **94**, 2160 (2008).
9. H. Higuchi, T. Yanagida, Y. E. Goldman, *Biophys. J.* **69**, 1000 (1995).
10. D. A. Winkelmann, L. Bourdieu, A. Ott, F. Kinose, A. Libchaber, *Biophys. J.* **68**, 2444 (1995).
11. I. Adamovic, S. M. Mijailovich, M. Karplus, *Biophys. J.* **94**, 3779 (2008).
12. J. Howard, J. A. Spudich, *Proc. Natl. Acad. Sci. U.S.A.* **93**, 4462 (1996).
13. S. C. Hopkins *et al.*, *J. Mol. Biol.* **318**, 1275 (2002).
14. M. J. Tyska *et al.*, *Proc. Natl. Acad. Sci. U.S.A.* **96**, 4402 (1999).
15. M. Nishiyama, E. Muto, Y. Inoue, T. Yanagida, H. Higuchi, *Nat. Cell Biol.* **3**, 425 (2001).
16. T. Nishizaka, R. Seo, H. Tadakuma, K. Kinosita Jr., S. Ishiwata, *Biophys. J.* **79**, 962 (2000).
17. J. W. Kerssemakers *et al.*, *Nature* **442**, 709 (2006).
18. A. Gennerich, A. P. Carter, S. L. Reck-Peterson, R. D. Vale, *Cell* **131**, 952 (2007).
19. A. F. Huxley, R. M. Simmons, *J. Physiol.* **218**, 59P (1971).
20. G. Piazzesi, L. Lucii, V. Lombardi, *J. Physiol.* **545**, 145 (2002).
21. G. Piazzesi *et al.*, *Cell* **131**, 784 (2007).
22. M. Reconditi *et al.*, *Nature* **428**, 578 (2004).
23. M. A. Geeves, K. C. Holmes, *Adv. Protein Chem.* **71**, 161 (2005).
24. W. Steffen, D. Smith, J. Sleep, *Proc. Natl. Acad. Sci. U.S.A.* **100**, 6434 (2003).
25. M. Capitanio *et al.*, *Proc. Natl. Acad. Sci. U.S.A.* **103**, 87 (2006).
26. C. J. Barclay, *J. Physiol.* **497**, 781 (1996).

27. We are grateful to J. Kerssemakers and M. Dogterom for generously providing their step-finding algorithm, W. Herzog and Y. Goldman for valuable discussion and critical reading of this manuscript, and T. Kambara for comments. This work has been supported by Grants-in-Aid for Scientific Research in Priority Areas from the Japan Ministry of Education, Culture, Sports, Science, and Technology (H.H.), Core Research for Evolutional Science and Technology of the Japan Science and Technology Agency (H.H.), and Young Scientists from the Japan Society for the Promotion of Science (M.K.).

Supporting Online Material

www.sciencemag.org/cgi/content/full/329/5992/686/DC1
Materials and Methods
SOM Text
Figs. S1 to S11
Table S1
References

27 April 2010; accepted 25 June 2010
10.1126/science.1191484

Long Noncoding RNA as Modular Scaffold of Histone Modification Complexes

Miao-Chih Tsai,[1] Ohad Manor,[2] Yue Wan,[1] Nima Mosammaparast,[3] Jordon K. Wang,[1] Fei Lan,[3,4] Yang Shi,[3] Eran Segal,[2] Howard Y. Chang[1]*

Long intergenic noncoding RNAs (lincRNAs) regulate chromatin states and epigenetic inheritance. Here, we show that the lincRNA HOTAIR serves as a scaffold for at least two distinct histone modification complexes. A 5′ domain of HOTAIR binds polycomb repressive complex 2 (PRC2), whereas a 3′ domain of HOTAIR binds the LSD1/CoREST/REST complex. The ability to tether two distinct complexes enables RNA-mediated assembly of PRC2 and LSD1 and coordinates targeting of PRC2 and LSD1 to chromatin for coupled histone H3 lysine 27 methylation and lysine 4 demethylation. Our results suggest that lincRNAs may serve as scaffolds by providing binding surfaces to assemble select histone modification enzymes, thereby specifying the pattern of histone modifications on target genes.

Long intergenic noncoding RNAs (lincRNAs) regulate dosage compensation, imprinting, and developmental gene expression by establishing chromatin domains in an allele- and cell-type specific manner (*1*, *2*). LincRNAs are intimately associated with chromatin-remodeling complexes (*3*–*7*), but molecular mechanisms of their functions are still lacking. Posttranslational modifications of histones recruit DNA-binding proteins and chromatin-remodeling machinery and are often coupled for combinatorial control (*8*). For instance, in embryonic stem cells many genes, such as the *HOX*, that encode developmental regulators are transcriptionally silent but possess bivalent histone H3 lysine 4 (H3K4) and lysine 27 (H3K27) methylation, which are resolved into univalent H3K4 or H3K27 methylation domains upon differentiation (*9*, *10*). Here, we show that a lincRNA can coordinate histone modifications by binding to multiple histone modification enzymes.

The lincRNA HOTAIR is transcribed from the *HOXC* locus and targets polycomb repressive complex 2 (PRC2, which comprises H3K27 methylase EZH2, SUZ12, and EED) to silence *HOXD* and select genes on other chromosomes (*7*, *11*). The genomic regions flanking *HOXD* are also bound by CoREST/REST repressor complexes (*12*), which contain LSD1 (KDM1/BHC110), a demethylase that mediates enzymatic demethylation of H3K4me2 (*13*) and that is required for proper repression of *Hox* genes in *Drosophila* (*14*). We therefore hypothesized that HOTAIR may coordinately interact with both PRC2 and LSD1. Immunoprecipitation (IP) of either endogenous LSD1 or FLAG-tagged LSD1 from primary foreskin fibroblasts or HeLa cells specifically retrieved endogenous HOTAIR RNA with enrichment comparable with that of EZH2 IP, the positive control (Fig. 1A and fig. S1A) (*15*). IP of three other chromatin proteins did not retrieve HOTAIR (fig. S1A), and neither LSD1, EZH2, nor FLAG-LSD1 IP retrieved U1 RNA, a nuclear ncRNA that served as a negative control. Purified biotinylated HOTAIR RNA, but not green fluorescent protein (GFP) RNA or an antisense HOTAIR fragment, specifically retrieved EZH2, SUZ12, and LSD1 from HeLa cell nuclear extract (Fig. 1B and fig. S1B). LSD1 forms a complex with CoREST (*16*), which can bridge LSD1 to the neuronal gene silencer REST (*17*). REST is believed to mediate silencing through two distinct effector arms: one via LSD1-CoREST, and separately via the adaptor protein CDYL and the H3K9 KMT G9a (*18*). HOTAIR specifically bound to CoREST and REST but not CDYL or G9a, nor to the putative PRC1 subunit YY1 (Fig. 1B). Further, biotinylated HOTAIR bound to purified PRC2 and LSD1 complexes in vitro (Fig. 1C and fig. S1C). These results suggest that HOTAIR directly interacts with PRC2 and LSD1 complexes.

Using a series of HOTAIR deletion mutants, the PRC2-binding activity mapped to nucleotides 1 to 300 of HOTAIR, whereas the LSD1 complex–binding activity mapped to nucleotides 1500 to 2146 (Fig. 1D). Deletion mutants that retained nucleotides 1 to 300 bound EZH2 or SUZ12 with equal efficiency as full-length HOTAIR, and deletion mutants that retained nucleotides 1500 to 2146 retained LSD1-binding activity. Thus, HOTAIR is a modular bifunctional RNA that has distinct binding domains for PRC2 and LSD1 complexes. Computational analysis and RNA footprinting showed that

[1]Howard Hughes Medical Institute and Program in Epithelial Biology, Stanford University School of Medicine, Stanford, CA 94305, USA. [2]Department of Computer Science and Applied Mathematics, Weizmann Institute of Science, Rehovot 76100, Israel. [3]Department of Pathology, Harvard Medical School, and Division of New Born Medicine, Department of Medicine, Children's Hospital Boston, Boston, MA 02138, USA. [4]Constellation Pharmaceuticals, 215 First Street, Suite 200, Cambridge, MA 02142, USA.

*To whom correspondence should be addressed. E-mail: howchang@stanford.edu

Downloaded from www.sciencemag.org on August 5, 2010

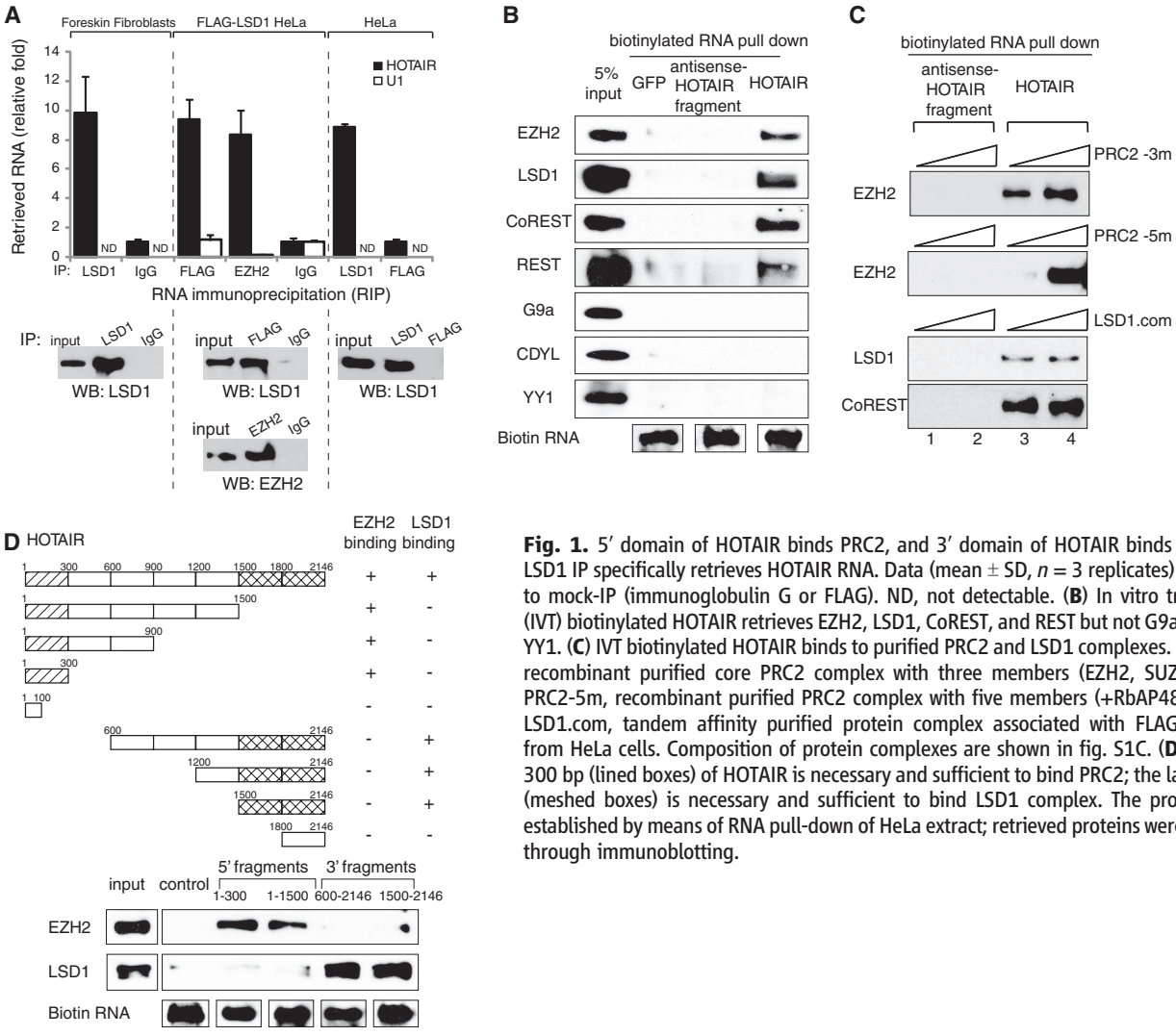

Fig. 1. 5′ domain of HOTAIR binds PRC2, and 3′ domain of HOTAIR binds LSD1. (**A**) LSD1 IP specifically retrieves HOTAIR RNA. Data (mean ± SD, $n = 3$ replicates) is relative to mock-IP (immunoglobulin G or FLAG). ND, not detectable. (**B**) In vitro transcribed (IVT) biotinylated HOTAIR retrieves EZH2, LSD1, CoREST, and REST but not G9a, CDYL, or YY1. (**C**) IVT biotinylated HOTAIR binds to purified PRC2 and LSD1 complexes. PRC2-3m, recombinant purified core PRC2 complex with three members (EZH2, SUZ12, EED); PRC2-5m, recombinant purified PRC2 complex with five members (+RbAP48, AEBP2); LSD1.com, tandem affinity purified protein complex associated with FLAG-HA-LSD1 from HeLa cells. Composition of protein complexes are shown in fig. S1C. (**D**) The first 300 bp (lined boxes) of HOTAIR is necessary and sufficient to bind PRC2; the last 646 bp (meshed boxes) is necessary and sufficient to bind LSD1 complex. The profiles were established by means of RNA pull-down of HeLa extract; retrieved proteins were detected through immunoblotting.

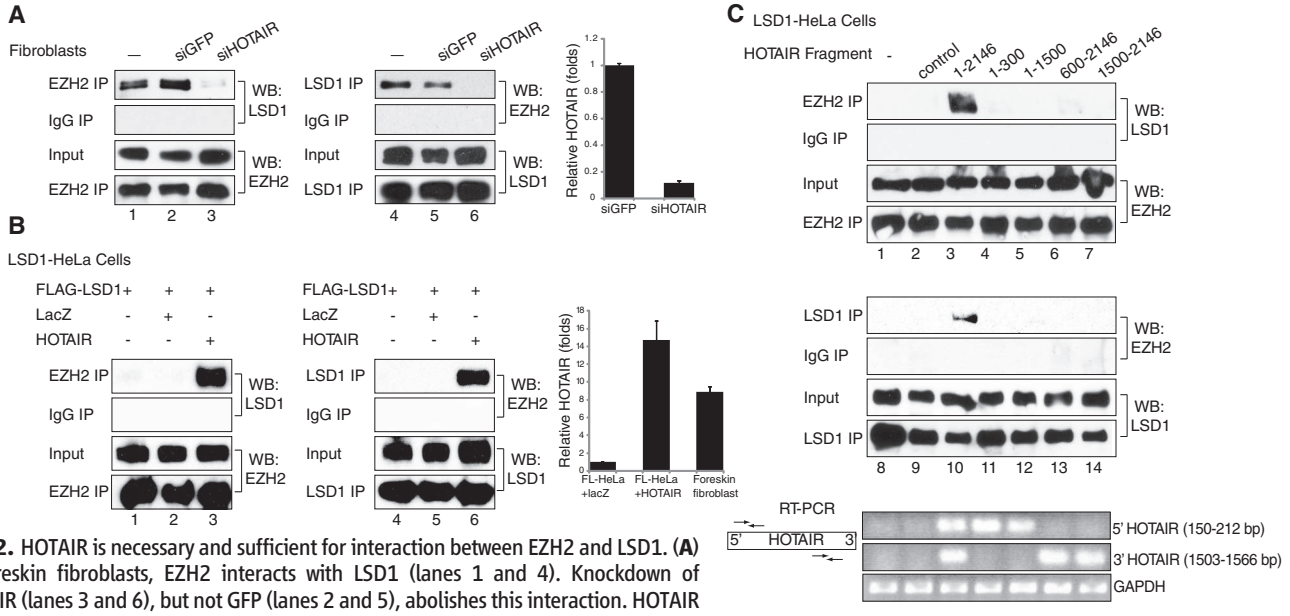

Fig. 2. HOTAIR is necessary and sufficient for interaction between EZH2 and LSD1. (**A**) In foreskin fibroblasts, EZH2 interacts with LSD1 (lanes 1 and 4). Knockdown of HOTAIR (lanes 3 and 6), but not GFP (lanes 2 and 5), abolishes this interaction. HOTAIR levels (mean ± SD) are shown on the right. (**B**) HOTAIR expression in FLAG-LSD1 HeLa cells induces EZH2 and LSD1 interaction (lanes 3 and 6). (**C**) Full-length HOTAIR induces EZH2 and LSD1 interaction (lanes 3 and 10) but not HOTAIR mutants lacking either 5′ or 3′ domain (lanes 4 to 7 and 11 to 14). Presence of indicated RNA domains was confirmed by means of RT-PCR (bottom).

Downloaded from www.sciencemag.org on August 5, 2010

the PRC2- and LSD1-binding domains of HOTAIR are likely to possess extensive but distinct secondary structures (fig. S2).

The presence of independent binding sites for PRC2 and LSD1 on HOTAIR suggests that HOTAIR may bridge PRC2 and LSD1 complexes. EZH2 IP retrieved LSD1, and conversely LSD1 IP retrieved EZH2 from foreskin fibroblasts (Fig. 2A). We estimate that less than 5% of the two complexes physically interact with each other, which is consistent with prior purification results that isolated PRC2 and CoREST-LSD1 as separate complexes (*19*, *20*). RNA interference (RNAi) of HOTAIR or ribonuclease treatment of the IP abrogated the interaction between EZH2 and LSD1, suggesting that HOTAIR is required to bridge this interaction (Fig. 2A and fig. S3). Wild-type HeLa cells or HeLa cells stably expressing FLAG-LSD1 (FL-HeLa) expressed ~10-fold less HOTAIR than foreskin fibroblasts and showed undetectable endogenous interaction between PRC2 and LSD1. Enforced expression of HOTAIR in FL-HeLa cells to a level comparable with foreskin

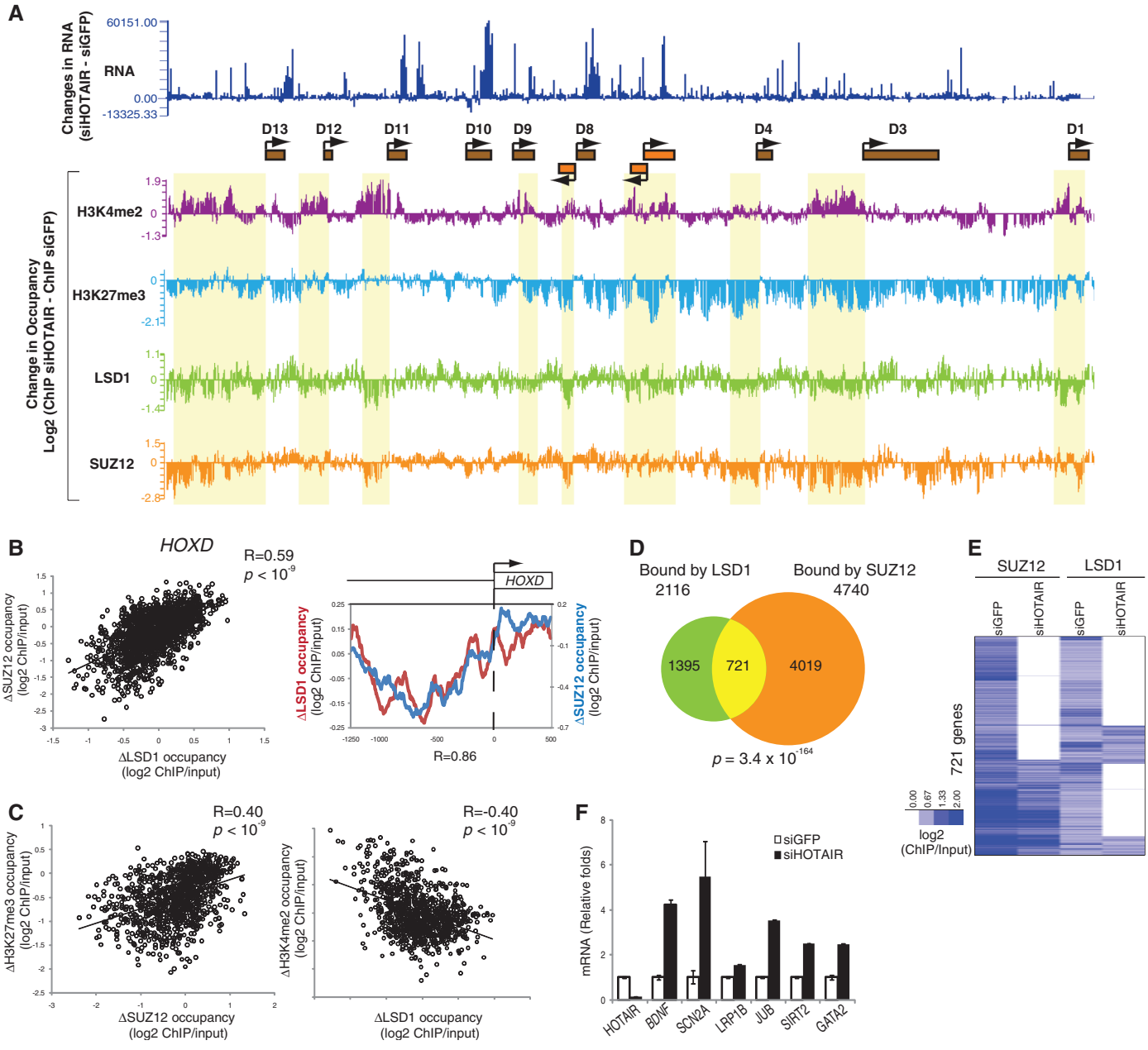

Fig. 3. HOTAIR coordinates localization of PRC2 and LSD1 genome-wide. (**A**) Changes in mRNA and occupancy of H3K4me2, H3K27me3, LSD1, and SUZ12 across *HOXD* locus after RNAi of HOTAIR in foreskin fibroblasts. Yellow boxes indicate regions of notable correlation between gain of H3K4me2 and concordant loss of LSD1, H3K27me3, and SUZ12. (**B**) The patterns of change in LSD1 (*x* axis) and SUZ12 occupancy (*y* axis) upon HOTAIR knockdown across the *HOXD* locus are significantly correlated (Pearson correlation, $R = 0.59$, $P < 10^{-9}$, Student's *t* test). This correlation is concentrated in proximal promoters of *HOXD* genes ($R = 0.86$). (**C**) Positive correlation of changes in SUZ12 (*x* axis) and H3K27me3 occupancy (*y* axis) and negative correlation of LSD1 (*x* axis) and H3K4me2 occupancy (*y* axis). (**D**) Venn diagram shows the genes occupied by SUZ12 (4740 genes), LSD1 (2116 genes), or both (721 genes). (**E**) Heat map of SUZ12 and LSD1 co-occupied genes (721 genes). Each column is an experiment; each row is a gene. HOTAIR knockdown led to concordant loss of SUZ12 and LSD1 occupancy. Chromatin occupancy is indicated in blue per the scale bar. (**F**) HOTAIR knockdown leads to transcription derepression of target genes. Mean ± SD of quantitative RT-PCR data are shown.

Downloaded from www.sciencemag.org on August 5, 2010

fibroblasts allowed robust interaction between PRC2 and LSD1 (Fig. 2B). Gel filtration chromatography confirmed that HOTAIR expression shifts PRC2 subunits into a higher molecular weight complex coincident with the LSD1 complex, suggesting the formation of a higher ordered complex composed of HOTAIR, PRC2, and LSD1 complexes in HOTAIR-overexpressing cells (fig. S4). Moreover, expression of each HOTAIR mutant that lacked the ability to bind either PRC2 or LSD1 in vitro failed to induce PRC2-LSD1 interaction in cells (Fig. 2C and fig. S3C).

HOTAIR-mediated bridging of PRC2 and LSD1 complexes also enables their coordinate binding to target genes on chromatin. HOTAIR is required for H3K27 methylation and transcriptional silencing across the *HOXD* locus (*7*). Therefore, we mapped PRC2 (as indicated by SUZ12) and LSD1 occupancy across the *HOX* loci and on promoters genome-wide by means of chromatin IP followed by microarray analysis (ChIP-chip) in primary foreskin fibroblasts after control RNAi or HOTAIR knockdown (Fig. 3 and figs. S5 to S7). HOTAIR knockdown decreased SUZ12 and LSD1 occupancy in a similar pattern across *HOXD* [Pearson's correlation coefficient (R) = 0.59, $P < 10^{-9}$, Student's t test] (Fig. 3, A and B, and fig. S6). Coordinate loss of SUZ12 and LSD1 occupancy caused by HOTAIR knockdown were concentrated in proximal promoters of *HOXD* genes (Fig. 3B). These regions correspondingly lost H3K27me3 and gained H3K4me2, the respective histone methylation products of PRC2 and LSD1 complexes ($R = 0.40$, $P < 10^{-9}$, Student's t test) (Fig. 3, A and C, and figs. S6 and S7). The loss of H3K27me3 occurred across broad domains encompassing multiple *HOXD* genes and intergenic regions, whereas the gain of H3K4me2 was concentrated near the transcriptional start sites of *HOXD* genes (*8*). Multiple independent small interfering RNAs targeting HOTAIR gave the same results.

Examining human promoters genome-wide, ChIP-chip analysis showed that PRC2 and LSD1 occupied 4740 and 2116 gene promoters, respectively (Fig. 3D). Nearly one third of LSD1-occupied promoters, comprising 721 genes, were also occupied by SUZ12, revealing a significant overlap (257 overlap expected by chance alone; $P = 3.4 \times 10^{-164}$, hypergeometric distribution). Among these 721 genes co-occupied by SUZ12 and LSD1, the distances between the binding sites of SUZ12 and LSD1 were predominantly less than 500 base pairs (bp), which is the fragmentation size of chromatin in our ChIP assay and the limit of resolution (fig. S8A).

HOTAIR knockdown led to concordant loss of SUZ12 and LSD1 occupancy in 289 of the 721 genes normally co-occupied by SUZ12 and LSD1 (almost 40%) (Fig. 3E and table S1). Additional genes showed more exclusive loss of LSD1 occupancy (33%) or SUZ12 occupancy (16%), suggesting that HOTAIR may be involved in other LSD1- or SUZ12-dependent pathways. ChIP followed by quantitative polymerase chain reaction (PCR) confirmed the requirement of HOTAIR for PRC2 and LSD1 localization for all six genes tested (fig. S8C). HOTAIR knockdown did not change the chromatin occupancy by PRC2 and LSD1 at hundreds of other genes, nor did it affect the protein or mRNA level of the subunits of PRC2 or LSD1 complexes (Fig. 2A and fig. S9, A to C). The functional consequence of coordinate targeting of PRC2 and LSD1 by HOTAIR is gene repression: Genes co-occupied by SUZ12-LSD1 in a HOTAIR-dependent manner are also significantly induced upon HOTAIR knockdown as measured with microarray or quantitative reverse transcription PCR (RT-PCR) [$P < 0.05$, Gene Set Enrichment Analysis (*21*)] (Fig. 3F and fig. S8D). These results suggest that a single lincRNA—HOTAIR—may be required to target both PRC2 and LSD1 to hundreds of genes across the genome in order to coordinate histone modifications for gene silencing.

Both PRC2 and LSD1 can bind multiple proteins that are thought to provide DNA target specificity (*17*, *22*). A possible consequence of the HOTAIR-mediated bridging is that PRC2 may be recruited to LSD1-CoREST-REST–binding sites, and conversely LSD1 may be recruited to PRC2-binding sites. Previous genome-scale mapping studies of PRC2 already identified the REST motif as one of the most enriched DNA sequence motifs within PRC2-binding sites but with no mechanistic explanation (*23*). We searched for enriched sequence motifs in SUZ12-binding sites lost upon HOTAIR knockdown ("HOT-S sites") and identified several enriched motifs (*24*), including a motif that corresponds to the right half of the canonical REST motif ($P = 1.05 \times 10^{-12}$) (Fig. 4A and fig. S10). REST is able to bind only one half-site of the canonical REST motif (*25*), and genes containing HOT-S sites are enriched for experimentally measured REST occupancy ($P < 1.27 \times 10^{-16}$, hypergeometric distribution) (fig. S9D and table S2) (*25*). The most significantly enriched motif in LSD1-binding sites that are lost upon HOTAIR knockdown ("HOT-L sites") is a CG-rich motif ($P = 3.66 \times 10^{-10}$) (Fig. 4B and fig. S10), which is important for PRC2 binding (*23*, *26*, *27*). Thus, the enrichment of the CG-rich motif may reflect the HOTAIR-dependent recruitment of LSD1 complexes to PRC2-bound sites, which are often in CpG islands. We examined the gain of SUZ12 and LSD1 occupancy on chromatin when HOTAIR is overexpressed in primary lung fibroblasts, which do not express endogenous HOTAIR. HOTAIR overexpression caused ectopic occupancy of LSD1 and SUZ12 that significantly overlapped ($P < 7.31 \times 10^{-95}$). Further, motif analysis of the ectopically gained binding sites recovered an almost identical CG-rich motif ($P = 7.9 \times 10^{-37}$) (Fig. 4C), suggesting that this motif is involved in HOTAIR target selection. Nonetheless, the REST half-site and the CG-rich motif are currently not sufficient for de novo prediction of all HOTAIR-dependent genes, suggesting that additional motifs, binding partners, and/or motif arrangements may be important.

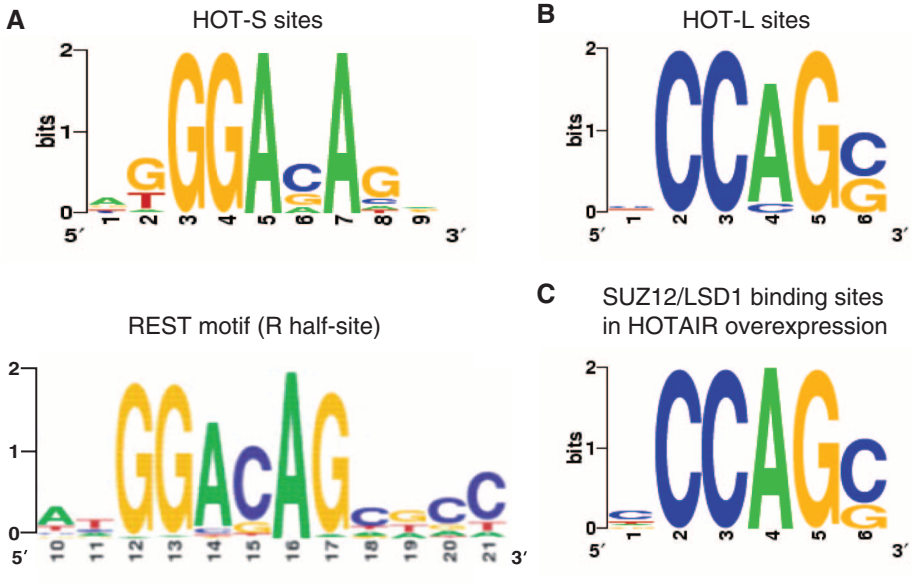

Fig. 4. HOTAIR-dependent SUZ12- and LSD1-binding motifs. (**A**) SUZ12 occupancy sites lost upon HOTAIR knockdown (HOT-S sites) are enriched for a DNA motif very similar to the right half of canonical REST motif. (**B**) LSD1 occupancy sites lost upon HOTAIR knockdown (HOT-L sites) are enriched for a CG-rich motif. (**C**) A nearly identical CG-rich motif is enriched in LSD1/SUZ12–binding sites gained upon HOTAIR overexpression, suggesting that this motif is involved in HOTAIR target selection.

Downloaded from www.sciencemag.org on August 5, 2010

In this report, we demonstrate that the lincRNA HOTAIR can link a histone methylase and a demethylase by acting as a modular scaffold (fig. S11). Other lincRNAs may also contain multiple binding sites for distinct protein complexes that direct specific combinations of histone modifications on target gene chromatin. Some lincRNAs may be "tethers" that recruit several chromatin modifications to their sites of synthesis (*2*) while other lincRNAs can act on distantly located genes as "guides" to affect their chromatin states (*2*). On the basis of their dynamic patterns of expression (*28*), specific lincRNAs can potentially direct complex patterns of chromatin states at specific genes in a spatially and temporally organized manner during development and disease states.

References and Notes

1. C. P. Ponting, P. L. Oliver, W. Reik, *Cell* **136**, 629 (2009).
2. J. T. Lee, *Genes Dev.* **23**, 1831 (2009).
3. A. M. Khalil *et al.*, *Proc. Natl. Acad. Sci. U.S.A.* **106**, 11667 (2009).
4. R. R. Pandey *et al.*, *Mol. Cell* **32**, 232 (2008).
5. T. Nagano *et al.*, *Science* **322**, 1717 (2008).
6. J. Zhao, B. K. Sun, J. A. Erwin, J. J. Song, J. T. Lee, *Science* **322**, 750 (2008).
7. J. L. Rinn *et al.*, *Cell* **129**, 1311 (2007).
8. O. J. Rando, H. Y. Chang, *Annu. Rev. Biochem.* **78**, 245 (2009).
9. B. E. Bernstein *et al.*, *Cell* **125**, 315 (2006).
10. T. S. Mikkelsen *et al.*, *Nature* **448**, 553 (2007).
11. R. A. Gupta *et al.*, *Nature* **464**, 1071 (2010).
12. V. V. Lunyak *et al.*, *Science* **298**, 1747 (2002).
13. Y. Shi *et al.*, *Cell* **119**, 941 (2004).
14. L. Di Stefano, J. Y. Ji, N. S. Moon, A. Herr, N. Dyson, *Curr. Biol.* **17**, 808 (2007).
15. Materials and methods are available as supporting material on *Science* Online.
16. M. G. Lee, C. Wynder, N. Cooch, R. Shiekhattar, *Nature* **437**, 432 (2005).
17. L. Ooi, I. C. Wood, *Nat. Rev. Genet.* **8**, 544 (2007).
18. P. Mulligan *et al.*, *Mol. Cell* **32**, 718 (2008).
19. Y. J. Shi *et al.*, *Mol. Cell* **19**, 857 (2005).
20. A. Kuzmichev, K. Nishioka, H. Erdjument-Bromage, P. Tempst, D. Reinberg, *Genes Dev.* **16**, 2893 (2002).
21. A. Subramanian *et al.*, *Proc. Natl. Acad. Sci. U.S.A.* **102**, 15545 (2005).
22. T. K. Kerppola, *Trends Cell Biol.* **19**, 692 (2009).
23. M. Ku *et al.*, *PLoS Genet.* **4**, e1000242 (2008).
24. E. Sharon, S. Lubliner, E. Segal, G. Stormo, *PLOS Comput. Biol.* **4**, e1000154 (2008).
25. D. S. Johnson, A. Mortazavi, R. M. Myers, B. Wold, *Science* **316**, 1497 (2007).
26. J. C. Peng *et al.*, *Cell* **139**, 1290 (2009).
27. G. Li *et al.*, *Genes Dev.* **24**, 368 (2010).
28. M. Guttman *et al.*, *Nature* **458**, 223 (2009).

29. Microarray data are deposited in Gene Expression Omnibus (www.ncbi.nlm.nih.gov/geo/) under accession number GSE22345. We thank members of the D. Herschlag lab for assistance with RNA footprinting and X. Tan, P. Khavari, and J. Wysocka for critical reading of the manuscript. This work was supported by the California Institute for Regenerative Medicine (RN1-00529-1 to H.Y.C.), NIH (R01-HG004361 to H.Y.C. and E.S and R01-CA118487 to Y.S), the Susan G. Komen Foundation (M.-C.T.), the Azrieli Foundation (O.M.), NSF (J.K.W.), and the Agency for Science, Technology, and Research (Y.W.). E.S. is the incumbent of the Soretta and Henry Shapiro career development chair. Y.S. is co-founder and on the scientific advisory board of Constellation Pharmaceuticals. H.Y.C. is an Early Career Scientist of the Howard Hughes Medical Institute.

Supporting Online Material

www.sciencemag.org/cgi/content/full/science.1192002/DC1
Materials and Methods
Figs. S1 to S11
Tables S1 and S2
References and Notes

7 May 2010; accepted 28 June 2010
Published online 8 July 2010;
10.1126/science.1192002
Include this information when citing this paper.

FAN1 Acts with FANCI-FANCD2 to Promote DNA Interstrand Cross-Link Repair

Ting Liu,[1]* Gargi Ghosal,[2]* Jingsong Yuan,[2] Junjie Chen,[2]† Jun Huang[1]†

Fanconi anemia (FA) is caused by mutations in 13 *Fanc* genes and renders cells hypersensitive to DNA interstrand cross-linking (ICL) agents. A central event in the FA pathway is mono-ubiquitylation of the FANCI-FANCD2 (ID) protein complex. Here, we characterize a previously unrecognized nuclease, Fanconi anemia–associated nuclease 1 (FAN1), that promotes ICL repair in a manner strictly dependent on its ability to accumulate at or near sites of DNA damage and that relies on mono-ubiquitylation of the ID complex. Thus, the mono-ubiquitylated ID complex recruits the downstream repair protein FAN1 and facilitates the repair of DNA interstrand cross-links.

Fanconi anemia (FA) is characterized by congenital malformations, bone marrow failure, cancer, and hypersensitivity to DNA interstrand cross-linking (ICL) agents (*1*–*3*). Resistance to DNA ICL agents probably requires all FA proteins (*4*, *5*). Eight FA proteins (A, B, C, E, F, G, L, and M) are assembled into the nuclear FA core complex that mono-ubiquitylates its two substrates, FANCI and FANCD2 (*4*–*10*), which, in turn, form DNA damage–induced nuclear foci together with other key DNA damage–response proteins (*1*, *4*). Failure to mono-ubiquitylate FANCI and FANCD2 results in highly decreased efficiency of DNA cross-link repair (*4*). The mono-ubiquitylated FANCI-FANCD2 (ID) complex might promote the recognition and subsequent removal of DNA lesions through nucleolytic cleavage of DNA strands by recruitment of ubiquitin-binding proteins that are important for this repair process (*11*–*16*). DNA damage–response and –repair proteins can be recruited to sites of DNA damage via their ubiquitin-binding domains (*17*–*20*). We identified a protein, KIAA1018, that contains a single ubiquitin-binding zinc finger (ZNF) domain at its N terminus and a virus-type replication-repair (VRR)–nuclease domain (or DUF994 domain) (*21*, *22*) at its C terminus (fig. S1, A and B). KIAA1018 relocalized to damage-induced foci after mitomycin C (MMC) treatment (fig. S1, C to F), suggesting that this protein is involved in DNA damage response. Because of the functional analyses performed below, we designated this protein as Fanconi anemia–associated nuclease 1 (FAN1).

Proteins associated with FAN1 were identified by mass spectrometry in a human embryonic kidney 293T–derivative cell line stably expressing a triple-tagged FAN1 (*23*). We repeatedly found the ID complex as major FAN1-associated proteins (fig. S2A). Mass spectrometry analyses of triple-tagged FANCD2-associated protein complexes revealed peptides that corresponded to FAN1 (fig. S2B), indicating that these proteins probably form a complex in vivo. Immunoprecipitation (IP) confirmed the interaction of FAN1 with FANCD2 and weakly with FANCI (Fig. 1A). Although FAN1 could interact with the unmodified ID complex, its association with the ID complex was greatly enhanced after MMC treatment (Fig. 1B), which coincides with FANCI-FANCD2 mono-ubiquitylation (*6*–*8*). Their association was further confirmed by in vivo colocalization experiments (fig. S2, C and D).

Upon reduction of endogenous FAN1 expression, we still detected MMC-induced mono-ubiquitylation and foci formation of FANCI-FANCD2 (Fig. 1C and fig. S3, A and B). Upon depletion of FANCD2 or FANCI, we failed to observe FAN1 foci after MMC treatment and saw a substantially reduced chromatin accumulation of FAN1 after MMC treatment (Fig. 1, D and E, and fig. S3C). Knockdown of FAN1 caused a significant increase in MMC but not camptothecin sensitivity (Fig. 1, F and G, and fig. S3D), increased levels of MMC-induced chromosome instability (fig. S4, A and B), and profound G_2/M-phase arrest (fig. S4C), all typical of FA cells (*1*–*5*). Double knockdown of FAN1 with FANCD2 or FANCA did not lead to any further increase in these phenotypes (Fig. 1F and

[1]Life Sciences Institute, Zhejiang University, Hangzhou, Zhejiang 310058, China. [2]Department of Experimental Radiation Oncology, University of Texas M.D. Anderson Cancer Center, 1515 Holcombe Boulevard, Houston, TX 77030, USA.

*These authors contributed equally to this work.
†To whom correspondence should be addressed. E-mail: jchen8@mdanderson.org (J.C.), jhuang@zju.edu.cn (J.H.)

Downloaded from www.sciencemag.org on August 5, 2010

fig. S4). Altogether, FAN1 promotes ICL repair downstream of the ID complex and does so through a common pathway.

The ZNF domain deletion mutant (ΔZNF) of FAN1 lost its foci-formation ability, whereas the nuclease domain mutant (ΔNUC) still localized to nuclear foci after MMC treatment (fig. S5, A to C). An N-terminal fragment, which contains the intact ZNF domain, but not a ZNF domain–disrupting point mutant (ZNF-C44F), is sufficient for foci formation after MMC treatment (fig. S5, A to C). Wild-type (WT) or the ΔNUC mutant of FAN1, but not the FAN1 mutant that lacks its ZNF domain (ΔZNF), specifically interacted with a ubiquitin-glutathione S-transferase fusion protein (Ubi-GST) in vitro (Fig. 2A). In addition, Ubi-GST pulled down the N-terminal fragment of FAN1 containing the ZNF domain, but not the ZNF-C44F mutant (Fig. 2A). WT FAN1, but not FAN1 mutant that lacks its ZNF domain (ΔZNF), interacts with the ID complex, and this interaction is greatly enhanced after MMC treatment (Fig. 2B). WT FANCD2/FANCI interacted strongly with FAN1, whereas the ubiquitylation-deficient point mutants showed only moderate or residual binding (Fig. 2C). Moreover, the N-terminal fragment of FAN1 containing the intact ZNF domain, but not its corresponding ZNF-C44F mutant or the ZNF domain of RAD18 (RAD18-ZNF), interacted with FANCD2 (Fig. 2D). WT FANCD2 could restore FAN1 foci formation in FANCD2-deficient PD20 cells, but the mono-ubiquitylation mutant Lys^{561} → Arg^{561} (K561R) (*24*) of FANCD2 did not (Fig. 2E and fig. S5D). Foci formation of the FAN1 ZNF domain alone also depends on FANCD2 mono-ubiquitylation (Fig. 2F and fig. S5E). The mono-ubiquitylation mutant (K523R) of FANCI partially complemented FAN1 foci formation in FANCI-depleted cells (Fig. 2G and fig. S5F), as mono-ubiquitylation of FANCI is not critical for the function of the FA pathway (*8*, *25*). Thus, mono-ubiquitylated FANCD2 (and FANCI) acts to facilitate FAN1 accumulation at sites of DNA damage.

ICL repair involves nucleolytic cleavage at or near the site of ICL to produce a suitable substrate that can subsequently be repaired by homologous recombination (HR) (*1*–*4*). Purified

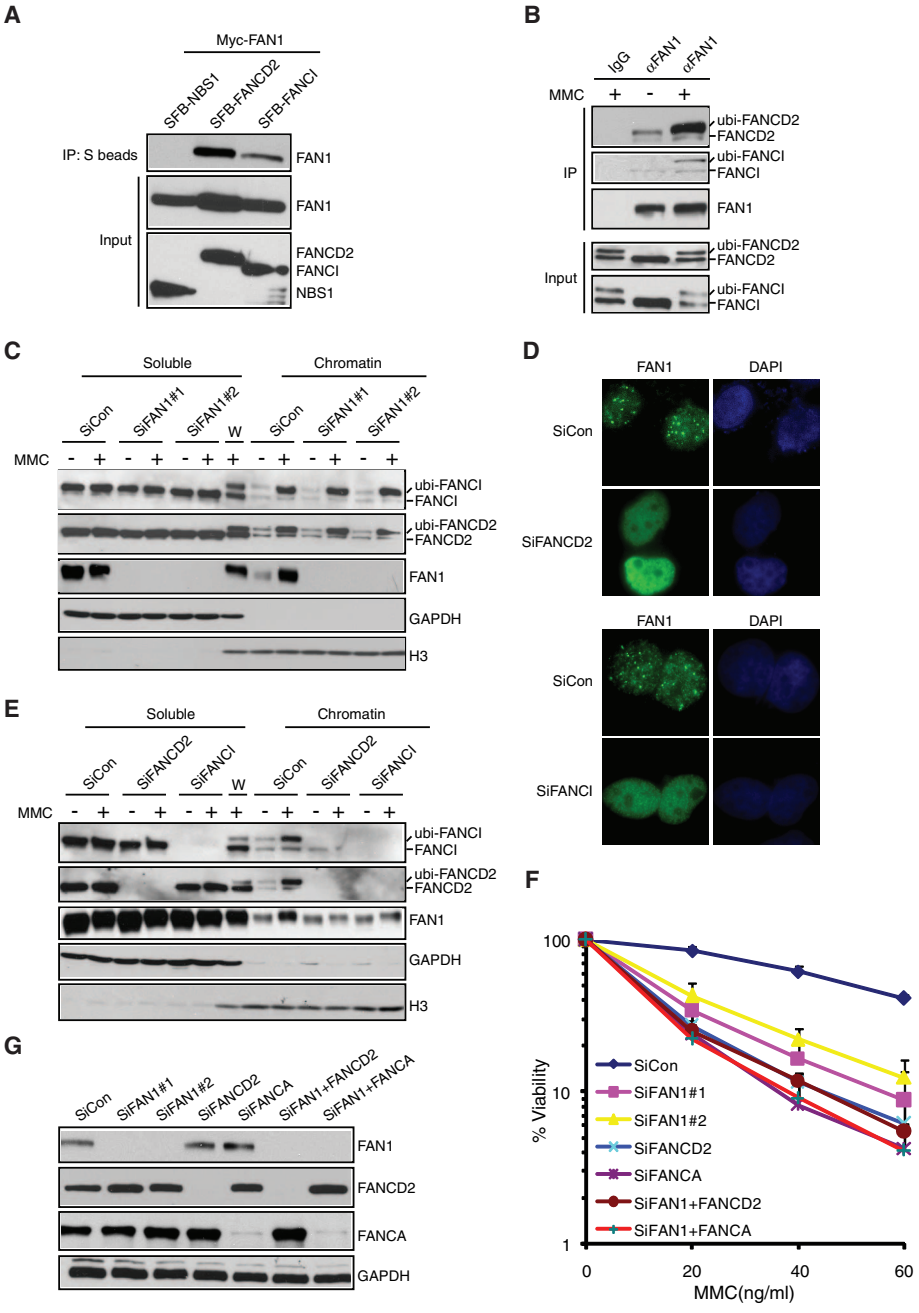

Fig. 1. FAN1 acts in ICL repair downstream of FANCD2/I. (**A**) Ectopically expressed FAN1 interacts with FANCD2/FANCI. 293T cells were cotransfected with plasmids encoding Myc-tagged FAN1 and S, FLAG, and, streptavidin-binding peptide tag (SFB)–tagged FANCD2 or FANCI. IP reactions were done using the antibodies as indicated. (**B**) Interaction between FAN1 and FANCD2/I before and after MMC treatment was monitored by IP with an antibody to FAN1 (anti-FAN1) and detected on SDS–polyacrylamide gel electrophoresis (PAGE) gels with the indicated antibodies (top three panels). IgG, immunoglobulin G. (**C**) FAN1 is not required for FANCD2/I mono-ubiquitylation. Soluble and chromatin fractions prepared from mock-treated or MMC-treated HeLa cells and immunoblotting experiments were performed using the indicated antibodies. W, whole-cell extracts; SiCon, control siRNA; GAPDH, glyceraldehyde-3-phosphate dehydrogenase; H3, histone H3. (**D**) FANCD2/I is required for FAN1 foci formation. HeLa cells were transfected with either FANCD2/I siRNAs or control siRNA and then treated with 1 μM MMC for 24 hours before immunostaining experiments were performed. DAPI, 4′,6′-diamidino-2-phenylindole. (**E**) FANCD2/I is required for FAN1 chromatin recruitment. Chromatin fractions were isolated, and immunoblotting experiments were performed using the indicated antibodies. (**F** and **G**) FAN1-depleted cells display increased MMC sensitivity. These experiments were performed in triplicate, and the results were the average of three independent experiments. The SD is shown for different doses of MMC or irradiation.

Downloaded from www.sciencemag.org on August 5, 2010

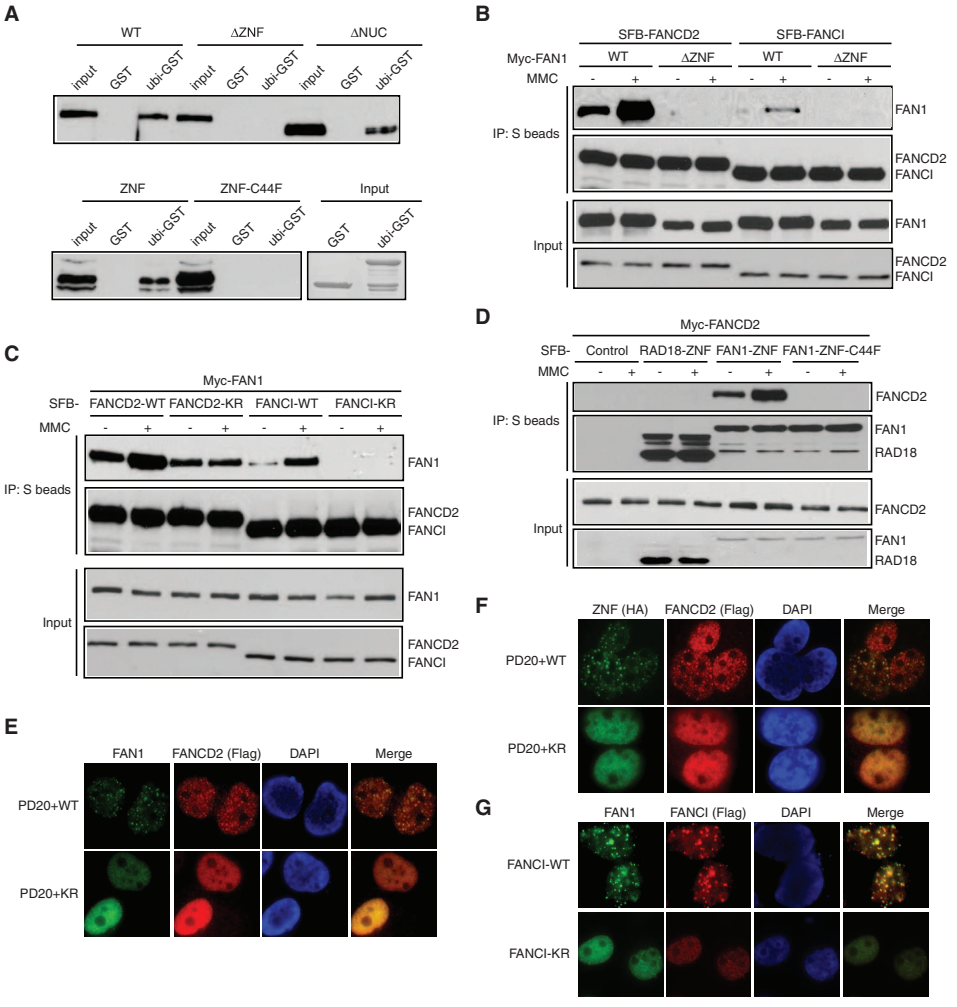

Fig. 2. Focus-localization of FAN1 depends on its ZNF domain and mono-ubiquitylation of the ID complex. (**A**) The ZNF domain of FAN1 is essential and sufficient for binding to ubiquitin in vitro. (**B**) The ZNF domain of FAN1 is required for binding to FANCD2/I. 293T cells stably expressing SFB-tagged FANCD2 or FANCI were transfected with plasmids encoding Myc-tagged WT or ZNF domain–deletion mutant of FAN1. Cells were mock treated or treated with MMC before IP reactions were performed. (**C**) Mono-ubiquitylation of FANCD2/FANCI is required for binding to FAN1. (**D**) The ability to bind the mono-ubiquitylated form of FANCD2 is specific to the ZNF domain of FAN1. IP reactions were performed as described in (B). (**E** and **F**) Dependence of DNA damage–induced FAN1 foci formation on mono-ubiquitylation of FANCD2. PD20 cells, expressing SFB-tagged WT FANCD2 or the K561R mutant (FANCD2-KR), were treated with MMC (E) or transfected with plasmids encoding hemagglutinin (HA)–tagged FAN1 ZNF domain before MMC treatment (F). Immunostaining experiments were performed as indicated. (**G**) Partial dependence of damage-induced FAN1 foci formation on mono-ubiquitylation of FANCI. HeLa cells depleted of endogenous FANCI were infected with viruses encoding siRNA-resistant HA-Flag–tagged WT or K523R mutant of FANCI (FANCI-KR). Cells were treated with MMC and immunostained as indicated.

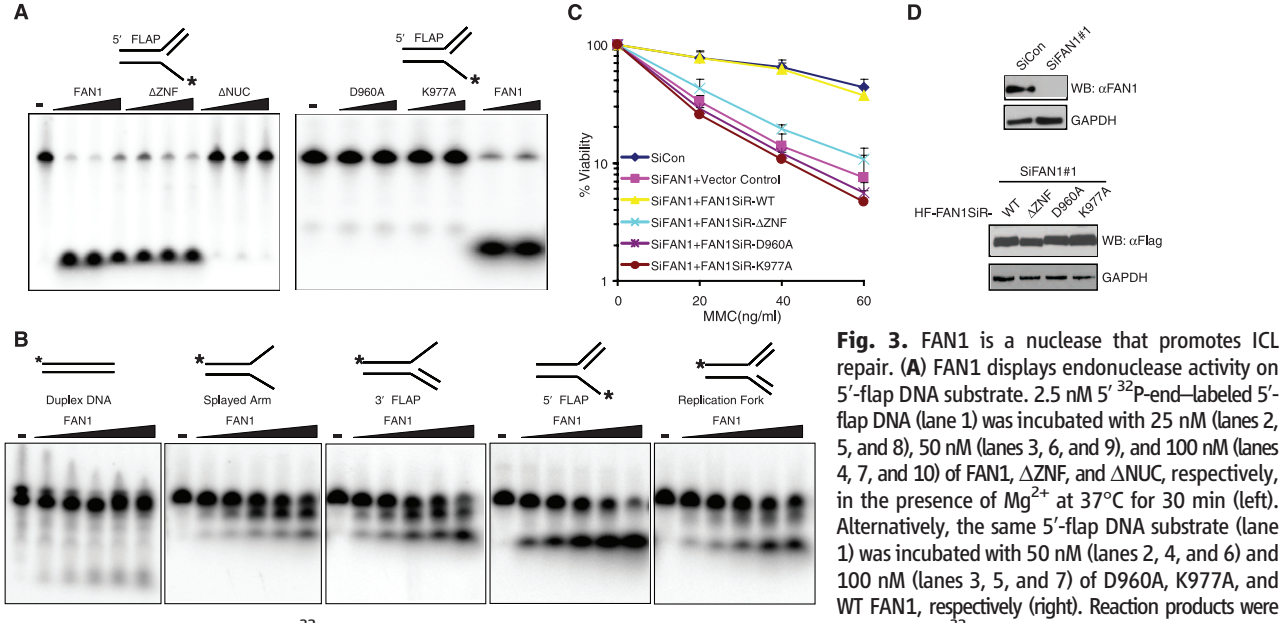

Fig. 3. FAN1 is a nuclease that promotes ICL repair. (**A**) FAN1 displays endonuclease activity on 5′-flap DNA substrate. 2.5 nM 5′ ^{32}P-end–labeled 5′-flap DNA (lane 1) was incubated with 25 nM (lanes 2, 5, and 8), 50 nM (lanes 3, 6, and 9), and 100 nM (lanes 4, 7, and 10) of FAN1, ΔZNF, and ΔNUC, respectively, in the presence of Mg^{2+} at 37°C for 30 min (left). Alternatively, the same 5′-flap DNA substrate (lane 1) was incubated with 50 nM (lanes 2, 4, and 6) and 100 nM (lanes 3, 5, and 7) of D960A, K977A, and WT FAN1, respectively (right). Reaction products were analyzed on denaturing PAGE. Asterisks indicate 5′ ^{32}P-end label. (**B**) FAN1 is a structure-specific endonuclease. Indicated 2.5 nM 5′ ^{32}P-end–labeled DNA substrates (lane 1) were incubated with 1, 5, 10, 25, and 50 nM FAN1 (lanes 2 to 6) in the presence of Mg^{2+} for 30 min at 37°C. Reaction products were analyzed on denaturing PAGE. (**C** and **D**) The ZNF domain and nuclease activity of FAN1 are required for restoring cellular resistance to MMC. HeLa-derivative cell lines stably expressing siRNA-resistant HA-Flag–tagged WT (FAN1SiR-WT), ΔZNF mutant (FAN1SiR-ΔZNF), D960A mutant (FAN1SiR-D960A), and K977A mutant (FAN1SiR-K977A) of FAN1 were generated. FAN1 expression was confirmed by immunoblotting with the use of Flag antibody, and extracts were prepared from cells transfected with FAN1 siRNA#1 (D). These experiments were performed in triplicate, and the results were the average of three independent experiments (C). The SD is shown for different doses of MMC.

Downloaded from www.sciencemag.org on August 5, 2010

FAN1 (fig. S6, A and B) was incubated with 5′-flap DNA substrate and displayed nuclease domain-dependent endonuclease activity (Fig. 3A). FAN1 could also cleave branched DNA structures (such as splayed-arm, 3′-flap, 5′-flap, or replication-fork structures), but not duplex DNA (Fig. 3B), indicating that FAN1 is a structure-specific endonuclease. To confirm that the nuclease activity we observed is intrinsic to FAN1, we generated FAN1 mutations at two highly conserved residues within its nuclease domain (D960A and K977A). Both of these mutants abolished the endonuclease activity of FAN1 on 5′-flap DNA substrate or other branched DNA substrates (Fig. 3A and fig. S6C).

To explore the physiological relevance of this highly conserved nuclease domain and the ZNF domain of FAN1 in ICL repair, we knocked down FAN1 in HeLa cells using siFAN1#1 [FAN1-specific small interfering RNA (siRNA) 1] and reintroduced siRNA-resistant full-length FAN1, ΔZNF, or the nuclease-inactivating mutants (D960A and K977A) of FAN1. Clonogenic assays indicated that reconstitution with WT FAN1, but not its ZNF deletion (D960A or K977A mutant), restored cell survival after MMC treatment (Fig. 3, C and D), suggesting that both the nuclease activity and the ZNF domain of FAN1 are important for FAN1 function in promoting cell survival after MMC treatment.

FAN1 is a nuclease that associates with mono-ubiquitylated FANCI-FANCD2, mutations that may be responsible for FA in a subset of human patients. FAN1 is a structure-specific endonuclease that may act together with other repair proteins to mediate endonucleolytic digestion of cross-linked DNA structures and, thus, generate ends that can serve as substrates for HR repair.

References and Notes

1. W. Wang, *Nat. Rev. Genet.* **8**, 735 (2007).
2. G. L. Moldovan, A. D. D'Andrea, *Cell* **139**, 1222 (2009).
3. A. D. D'Andrea, M. Grompe, *Nat. Rev. Cancer* **3**, 23 (2003).
4. G.-L. Moldovan, A. D. D'Andrea, *Annu. Rev. Genet.* **43**, 223 (2009).
5. L. J. Niedernhofer, A. S. Lalai, J. H. Hoeijmakers, *Cell* **123**, 1191 (2005).
6. A. F. Alpi, P. E. Pace, M. M. Babu, K. J. Patel, *Mol. Cell* **32**, 767 (2008).
7. A. E. Sims *et al.*, *Nat. Struct. Mol. Biol.* **14**, 564 (2007).
8. A. Smogorzewska *et al.*, *Cell* **129**, 289 (2007).
9. A. F. Alpi, K. J. Patel, *DNA Repair (Amst.)* **8**, 430 (2009).
10. N. Matsushita *et al.*, *Mol. Cell* **19**, 841 (2005).
11. P. Knipscheer *et al.*, *Science* **326**, 1698 (2009); published online 12 November 2009 (10.1126/science.1182372).
12. A. Ciccia *et al.*, *Mol. Cell* **25**, 331 (2007).
13. N. Bhagwat *et al.*, *Mol. Cell. Biol.* **29**, 6427 (2009).
14. K. Hanada *et al.*, *EMBO J.* **25**, 4921 (2006).
15. M. Räschle *et al.*, *Cell* **134**, 969 (2008).
16. L. J. Niedernhofer *et al.*, *Mol. Cell. Biol.* **24**, 5776 (2004).
17. J. Huang *et al.*, *Nat. Cell Biol.* **11**, 592 (2009).
18. B. Wang *et al.*, *Science* **316**, 1194 (2007).
19. B. Sobhian *et al.*, *Science* **316**, 1198 (2007).
20. H. Kim, J. Chen, X. Yu, *Science* **316**, 1202 (2007).
21. L. M. Iyer, M. M. Babu, L. Aravind, *Cell Cycle* **5**, 775 (2006).
22. L. N. Kinch, K. Ginalski, L. Rychlewski, N. V. Grishin, *Nucleic Acids Res.* **33**, 3598 (2005).
23. Materials and methods are available as supportnig material on *Science* Online.
24. Single-letter abbreviations for the amino acid residues are as follows: A, Ala; C, Cys; D, Asp; E, Glu; F, Phe; G, Gly; H, His; I, Ile; K, Lys; L, Leu; M, Met; N, Asn; P, Pro; Q, Gln; R, Arg; S, Ser; T, Thr; V, Val; W, Trp; and Y, Tyr.
25. M. Ishiai *et al.*, *Nat. Struct. Mol. Biol.* **15**, 1138 (2008).

26. This work was supported in part by grants from Startup Fund (Life Sciences Institute, Zhejiang University to J.H.), the Fundamental Research Funds for the Central Universities, China (to J.H.), and the NIH (to J.C.). We thank L. Li, X. Shen, and Y. Zhang for reagents. J.H. would like to thank J.C. for his continuous support and mentoring. J.C. is a recipient of an Era of Hope Scholar award from the U.S. Department of Defense and is a member of M.D. Anderson Cancer Center.

Supporting Online Material

www.sciencemag.org/cgi/content/full/science.1192656/DC1
Materials and Methods
SOM Text
Figs. S1 to S8
References

21 May 2010; accepted 23 June 2010
Published online 29 July 2010;
10.1126/science.1192656
Include this information when citing this paper.

Downloaded from www.sciencemag.org on August 5, 2010

NEW PRODUCTS

AMINO ACID ANALYZERS

The Biochrom 30+ Series of amino acid analyzers are based on ion-exchange chromatography with postcolumn derivatization of samples using ninhydrin. These instruments accurately identify and quantify free amino acids, as well as the amino acid composition of proteins and peptides. The new Biochrom 30+ Series offer rapid protocols that increase sample throughput by cutting analysis time compared with standard protocols. The instrument is PC-operated, with the user-friendly software controlling all functions, from the autosampler to the analysis and export of data. Advanced fluidics and robust hardware mean easy maintenance for users, backed by the reassurance of Biochrom's dedicated service and support team. A unique feature of all Biochrom amino acid analyzers is the column cleaning and repacking service, giving columns an almost indefinite life and cutting the cost of ownership.

Biochrom

For info: +44-(0)-1223-427806 | www.biochrom.co.uk

TIME-OF-FLIGHT MASS SPECTROMETRY

The JMS-S3000 SpiralTOF is a matrix-assisted laser desorption/ionization time-of-flight (MALDI-TOF) mass spectrometer. It features innovative ion optics with an extended flight length in a compact footprint, delivering a resolving power of greater than 60,000 (FWHM) over a mass range of 10,000 m/z to 30,000 m/z. The system features patented technology consisting of a staggered figure-eight ion trajectory of 17 meters. Because the ion packets are refocused during each turn, the divergence of the ions is reduced over the flight distance. The SpiralTOF ion optical system is engineered to overcome the limits of delayed extraction with kinetic energy convergence resulting in high sensitivity, resolving power, and mass accuracy over a wide mass range.

JEOL USA

For info 978-535-5900 | www.jeol.com

BASIC COMPOUND EXTRACTION

The Evolute WCX is a mixed-mode weak cation exchanger developed for extraction of strongly basic analytes and quaternary amines from aqueous samples. These analytes are typically found in pesticides and provide analytical scientists the ability to extract pesticides from diverse matrices, ranging from groundwater to blood samples. The resin-based sorbent is surface modified with well-defined hydroxyl-functional oligomers, imparting excellent water wettability. An optimized combination of nonpolar (hydrophobic), polar (hydrophilic), and cation exchange interactions allows efficient extraction of strongly basic analytes of wide-ranging polarities and quaternary amines, allowing for up to 50 percent more efficient recoveries of pesticide residues.

Biotage

For info: 1800-446-4752 | www.biotage.com

WATER INFORMATION MANAGEMENT

Millitrack is a web graphical user interface software tool for Millipore water purification system users. The new software enables long-term electronic archiving of water quality records, as well as remote access to a water purification system for real-time remote monitoring. Millitrack software allows users to save monitoring data from their water purification system on a long-term basis, including resistivity/conductivity measurements, total oxidizable carbon levels, and system parameters. The records archived and indexed using Millitrack software can be exported to any database file that has a data management tool.

Millipore

For info: 800-548-7853 | www.millipore.com/millitrack2

HIGH CONTENT SCREENING MICROSCOPY

The High Content Screening Automation (HCS A) package for confocal research microscopes combines the strength of high-resolution point scanners with the new, ingenious LAS AF MATRIX M3 software platform to deliver a highly flexible tool for automated imaging in multiple dimensions. Basic automation like mosaicking of tissue slides or multiwell plate screening in 2D and 3D are part of the starting packages. Five new autofoci, single object tracking, and automated control of water objectives ensure excellent results. Users have the choice among three platforms for the Leica HCS A: the Leica TCS SP5 broadband confocal, the Leica TCS LSI to visualize specimen from micro- to macroscale, and the Leica TCS SPE, known for ease of use and robustness.

Leica Microsystems

For info: 800-248-0123 | www.leica-microsystems.com

SIRNA GENERATION KITS

The Turbo Dicer small interfering RNA (siRNA) Generation Kit enables easy and cost-effective generation of a large number of siRNAs from full-length target genes. The kit allows researchers to quickly produce multiple siRNA species against a target mRNA and achieve effective gene silencing with minimal guesswork. Because the Turbo Dicer Enzyme generates minimal concentration of any individual siRNA species, off-target effects are not a problem. The Turbo Dicer siRNA Generation Kit conveniently contains everything that is required for preparing double stranded RNA from your target gene(s), dsRNA cleavage, siRNA cleanup, and transfection. Both the Recombinant Turbo Dicer Enzyme and the RNA Purification Columns are available separately.

AMS Biotechnology

For info: +44-(0)1235-828200 | www.amsbio.com

Electronically submit your new product description or product literature information! Go to **www.sciencemag.org/products/newproducts.dtl** for more information.

Newly offered instrumentation, apparatus, and laboratory materials of interest to researchers in all disciplines in academic, industrial, and governmental organizations are featured in this space. Emphasis is given to purpose, chief characteristics, and availability of products and materials. Endorsement by *Science* or AAAS of any products or materials mentioned is not implied. Additional information may be obtained from the manufacturer or supplier.

Downloaded from www.sciencemag.org on August 5, 2010

Multiply The Power of Science

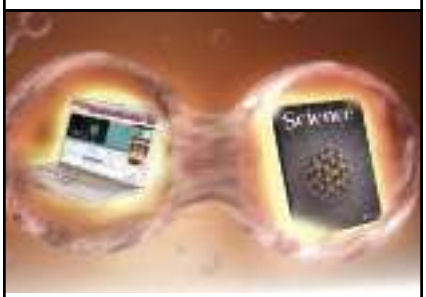

Science Careers
Classified Advertising

For full advertising details, go to ScienceCareers.org and click For Employers, or call one of our representatives.

Tracy Holmes
Worldwide Associate Director
Science Careers
Phone: +44 (0) 1223 326525

UNITED STATES & CANADA

E-mail: advertise@sciencecareers.org
Fax: 202-289-6742

Tina Burks
Midwest/West Coast/
South Central/Canada
Phone: 202-326-6577

Elizabeth Early
East Coast & Industry
Phone: 202-326-6578

Kate Panganiban
Advertising Operations Manager
Phone: 202-326-6582

Online Job Posting Questions
Phone: 202-326-6577

EUROPE & REST OF WORLD

E-mail: ads@science-int.co.uk
Fax: +44 (0) 1223 326532

Alex Palmer
Phone: +44 (0) 1223 326527

Susanne Kharraz Tavakol
Phone: +44 (0) 1223 326529

Dan Pennington
Phone: +44 (0) 1223 326517

Lisa Patterson
Phone: +44 (0) 1223 326528

JAPAN

ASCA Corporation
Jie Chin
Phone: +81-3-6802-4616
Fax: +81-3-6802-4615
E-mail: careerads@sciencemag.jp

To subscribe to *Science*:
In US call 866 434-2227
In the rest of the world call +1 202 326-6417

All ads submitted for publication must comply with applicable US and non-US laws. *Science* reserves the right to refuse any advertisement at its sole discretion for any reason, including without limitation for offensive language or inappropriate content, and all advertising is subject to publisher approval. *Science* encourages our readers to alert us to any ads that they feel may be discriminatory or offensive.

Science Careers
From the journal *Science* AAAS

NANYANG TECHNOLOGICAL UNIVERSITY

The Singapore 2010 Youth Olympic Village

The Elite NANYANG
ASSISTANT PROFESSORSHIP

Singapore's science and technology university, Nanyang Technological University (NTU), invites outstanding researchers and scholars to apply for appointments as the elite Nanyang Assistant Professors. Up to 10 appointments will be made.

Successful candidates will

- Receive start-up research grants of up to S$1 million
- Enjoy attractive remuneration package and other benefits including assistance with accommodation
- Hold tenure track appointments and play lead roles in the university's new wave of multi-disciplinary, integrative research.

Candidates should be under the age of 40 years at the date of application, within 10 years of gaining their PhD and ready for independent leadership of their own research groups.

For enquiries, please email to:
NanyangProfessorship@ntu.edu.sg

About the University

Nanyang Technological University, among the world's top 100 universities*, has made unprecedented research investments, emphasizing cutting-edge research and revolutionary technological innovations across multiple disciplines.

The University will be embarking on key global themes that will have great impact to the 21st century.

NTU has already attracted high caliber faculty and researchers to its ranks and will continue consolidating its world-level teams, especially in niches research areas like sustainability, water and environmental life science and engineering; clean energy; healthcare, neuroscience, bio-engineering; structural biology; research relevant to Asian culture and economics; cultural intelligence; and interactive digital media. However, NTU welcomes all other areas, including humanities and social sciences.

* *Time Higher Education-QS World University Rankings 2009*

Application now open for submission till
1 October 2010, 11.59 pm (UTC/GMT + 8 hours)
Kindly note that only online applications will be accepted.

http://www.ntu.edu.sg/NAP/

Department of Health and Human Services
National Institutes of Health
National Institute on Alcohol Abuse and Alcoholism

Director, Division of Treatment and Recovery Research (DTRR)

The National Institute on Alcohol Abuse and Alcoholism (NIAAA), a major research component of the National Institutes of Health (NIH) and the Department of Health and Human Services (HHS), is recruiting for a senior executive to serve as the Director of the Division of Treatment and Recovery Research (DTRR).

The Director, DTRR, provides national leadership for research on the treatment of alcohol use disorders, including setting scientific priorities through the development of long-term strategic plans and execution of funding decisions. In this capacity, the Director, DTRR leads the Division's efforts on planning, stimulating, developing, and supporting clinical research on cutting-edge therapies for alcoholism. Clinical research at the NIAAA encompasses medications development, behavioral therapies, combined medications and behavioral therapies, recovery research, health services research, and the translation of research into clinical practice. Medications development is one of the NIAAA's top research priorities. The Director, DTRR, oversees the NIAAA's work on the full continuum of research included under medications development—from human laboratory studies to clinical trials, which requires close collaboration with internal and external scientists and researchers with other Federal State and Local government agencies, and national and international research organizations. The Director, DTRR serves as the principal advisor to the Director, NIAAA on alcohol treatment and recovery issues and advises the National Advisory Council on pending grant applications and the status of programs in the federal and private sector.

The selected candidate will be expected to hold a M.D., Ph.D., or equivalent degree. Criteria for selection includes: experience in developing, implementing and/or evaluating behavioral and clinical therapies, specifically in the area of medications development, relevant to alcoholism; experience in managing/leading a complex clinical research organization, experience and expertise in communicating clinical, basic research and programmatic information to scientific and non-scientific audiences; a strong publication record in the field of clinical, behavioral, and medications development research and experience in developing, implementing and managing multidisciplinary and trans-disciplinary research programs on treatments for alcohol use disorders and determinants of post-treatment recovery.

The Director, DTRR, is an Excepted Service position (Title 42), and the successful candidate will be appointed at a salary commensurate with qualifications and experience. Full Federal benefits including leave, health and life insurance, long-term care insurance, retirement, and savings plan (401K equivalent) will be provided.

Interested candidates should submit a curriculum vitae, bibliography, and the names, addresses, contact numbers (phone and fax) and e-mail address of four references by the closing date to the following e-mail account:

E-mail: dtrrdirrecruit@mail.nih.gov

Applications will be accepted through **September 15, 2010**, or until the position is filled.

Department of Health and Human Services
National Institutes of Health
National Heart, Lung and Blood Institute
Division of Intramural Research

Human iPS Core Facility Director

An expert is sought in the area of stem cell biology to direct the new human induced pluripotent stem cell (iPS) Core Facility within the Division of Intramural Research (DIR), National Heart, Lung and Blood Institute (NHLBI), NIH in Bethesda, Maryland USA. The successful applicant will interact with multiple DIR Principal Investigators in the creation, design and interpretation of experiments involving iPS cells. He/she will oversee the iPS Core Facility personnel and be responsible for the introduction and maintenance of standard operating procedures and QA/QC measures.

The mission of the DIR is to improve the health of all Americans through basic and clinical research, research training, and translation of discoveries. The iPS Core Facility is part of a new NHLBI DIR Initiative in Molecular Medicine. The primary goal of the Core is to develop human iPS cells as cell-based models to better understand and treat a host of diseases relevant to the overall mission of the NHLBI. Although the iPS Core Facility is oriented toward providing service and conducting collaborative research, the Director will have the opportunity to devote up to 20% of his/her time to undertaking a personal research program.

We are seeking an experienced scientist (with Ph.D. or equivalent) with an outstanding track record in stem cell biology. Previous experience in generating human iPS cells and working with human ES cells is advantageous. Salary will be commensurate with qualifications and experience. More detailed information about the NHLBI Division of Intramural Research may be found at: **http://dir.nhlbi.nih.gov/ .**

A competitive salary commensurate with experience and qualifications is offered. Appointees may be US citizens, resident aliens or non-resident alien with or eligible for a valid employment visa. The review of applications will begin 30 days after the initial posting and the search will remain open until the position is filled.

Please submit a cover letter highlighting key qualifications; current curriculum vitae with complete bibliography; names and addresses of four references; and a one-page summary of the applicant's philosophy of core facility operation as well as current and future research interests in PDF or MS Word format only (no paper applications will be accepted) to:

Robert S. Balaban, Ph.D., Scientific Director, NHLBI
c/o Ariel Herman, IAMB Section Chief, NHLBI
NHLBI_recruit@mail.nih.gov

NIH Intramural Research Program is Recruiting "Earl Stadtman Investigators"

The National Institutes of Health, the nation's premier agency for biomedical and behavioral research, is pleased to announce a new call for top-tier tenure-track candidates to become "NIH Earl Stadtman Investigators." We have multiple positions to offer.

We are looking for creative and independent thinkers eager to take on high-risk, high-impact research. Regardless of your expertise — in the field or in the lab (wet or dry), within a discipline well established or on the frontiers of science — please consider the NIH for your career development. Areas of active recruitment include sensory biology and the neurosciences, symptoms research, systems biology, stem cells, infectious diseases and bioinformatics.

Who we are: Among our approximately 1,200 principal investigators and 4,000 trainees actively engaged in research are world-renowned experts in immunology, cancer, rare diseases, genetics, translational research, imaging, vaccine development, health disparities, systems biology, sensory biology, structural biology, computational biology, neurosciences, and development, to name but a few scientific areas. Our strength is our diversity in pursuit of a common goal, to alleviate human suffering.

The intramural program includes the NIH Clinical Center, the world's largest hospital entirely devoted to biomedical research, as well as the National Library of Medicine and PubMed, the Vaccine Research Center, and the International Centers for Excellence in Research working in the field in sub-Sahara Africa, South America and Asia. We constitute the world's largest training facility for the biomedical and behavioral sciences. Our researchers include numerous members of the National Academy of Sciences and the Institute of Medicine, Searle Scholars, winners of the Lasker Award, Nobel Prize, the National Medal of Science and the Presidential Early Career Awards, and recipients of many other high honors. Among us are the editors of top journals, the writers of some of the most highly cited papers in the biomedical sciences, and generators of licenses and patents yielding nearly $100 million in annual royalties. We are on the cutting edge of new discoveries and their application to the clinic. We perform work in labs, in clinics, out in the field, and on nearly every continent; and every day we advance the state of science to improve the quality of life.

What we seek: To maintain our position at the cutting edge, we seek the continued infusion of a diverse and creative staff. The Earl Stadtman Investigator recruitment is an opportunity to explore the limits of your productivity and your independence from preconceived research objectives. Please share with us your ideas for a novel research program and career aspirations and how they contribute to the NIH mission.

Qualifications/eligibility: Candidates must have an M.D., Ph.D., D.D.S./D.M.D., D.V.M, D.O., R.N./Ph.D., or equivalent doctoral degree and have an outstanding record of research accomplishments as evidenced by publications in major peer-reviewed journals. Preference will be given to applicants who are in the early stages of their research careers; only non-tenured applicants will be considered. Candidates in any area of biomedical, translational and behavioral research are invited to apply. Appointees may be U.S. citizens, resident aliens or non-resident aliens with, or eligible to obtain, a valid employment-authorization visa.

Salary: Successful candidates are offered competitive salaries commensurate with experience and qualifications, and they are assigned ample research space, supported positions and an operating budget. Our scientists focus entirely on their research with ample opportunities to mentor and train outstanding fellows at all levels.

How to apply: Complete applications must be received by October 1, 2010. Interested applicants must submit a curriculum vitae, a three-page research plan, a one-page description of their vision for their future research and its potential impact, and contact information for three professional references through our online application system at http://tenuretrack.nih.gov/apply. Letters of recommendation will be requested automatically when you submit your application. No paper applications will be accepted.

What to expect: Search committees of subject-matter experts will review and evaluate applicants based on the following criteria: publication record, potential scientific impact of current and proposed research, scientific vision, demonstrated independence, and awards. The committees will identify the most highly qualified candidates to invite to the NIH for a lecture open to the NIH scientific staff in December 2010 and for interviews with the search committees. Top candidates then will be nominated as finalists for Earl Stadtman tenure-track positions.

The Scientific Directors, who lead our 23 intramural programs, and the search committee chairs will work together to identify the finalists to be recruited as Earl Stadtman Investigators. Candidates not selected as Stadtman finalists can be considered for other open NIH research positions. The entire process from application review to job offer may take several months, depending on the volume of applications.

The inspiring story of Earl and Thressa Stadtman's research is at http://history.nih.gov/exhibits/stadtman. More information about the NIH Intramural Research Program is at http://intramural.nih.gov/search and http://sourcebook.od.nih.gov/sci-prgms/sci-prgms-toc.htm. Specific questions regarding this recruitment effort may be directed to Dr. Roland Owens, Assistant Director, NIH Office of Intramural Research at owensrol@mail.nih.gov.

The NIH Intramural Research Program, with its extensive infrastructure and critical mass of expertise well established, has a crucial role in both maintaining America's research excellence and advancing treatments and cures. Come join the team whose hallmarks are stable funding, intellectual freedom, shared resources and broad expertise.

DHHS and NIH are Equal Opportunity Employers

Nanjing University

Dean, College of Engineering

Nanjing University, China, invites applications and nominations for the position of the Dean of the College of Engineering and Applied Sciences. Nanjing University is a top ranked University in China, and is located in the beautiful ancient city of Nanjing (formal capital of six dynasties and 200 miles west of Shanghai). The newly established college aims to build a world class engineering program that will play a critical role in transforming technology in the 21st century. The college is located in a new campus of 300 acres and with a planned faculty of 120 who cover broader research and education programs including but not limited to material science and engineering, quantum electronics and optical engineering, green energy, and biomedical engineering.

The candidates should hold a full professor or equivalent position with a distinguished scholarship and track records. The candidate must demonstrate strong leadership in research and education, and have organizational, as well as interpersonal skills to build an internationally competitive engineering program at Nanjing University. Ample budget for building up the college and competitive salary package for the Dean will be provided.

In addition, the college plans to hire about 100 faculty with outstanding calibers at all ranks in next few years, especially in the area of biomedical engineering, materials science and engineering, energy science and technology, optical/information engineering.

Candidates or nominators should submit their letter of intent or recommendation letter, curriculum vitae, and 5 names of reference via e-mail to: **Prof. Yi-qiang QIN, College of Engineering and Applied Sciences, Nanjing University, Nanjing, China 210093, People's Republic of China, Phone: +86-(25)83686587, e-mail: yqqin@nju.edu.cn**. Review of applications will start immediately and continue until the position is filled.

UNIVERSITY OF DELAWARE

UNIDEL PROFESSOR OF HEALTH SCIENCES

EFFECTIVE SEPTEMBER 1, 2011

The College of Health Sciences at the University of Delaware is seeking nominations and applications for a newly created endowed chair with expertise in physiology, broadly defined. We seek a visionary senior scientist with a vigorous research program, strong record of mentoring graduate students and postdoctoral fellows, and extramural funding, to provide leadership in developing 1) an exciting new clinical research complex, and 2) new inter-institutional collaborations through the emerging Delaware Health Sciences Alliance. The Unidel Professor will also be expected to continue a productive, externally funded research program, mentor graduate students and postdoctoral fellows, and teach. For a full description of this position, visit udel.edu/udjobs

The University of Delaware is an Equal Opportunity Employer.

Explore Engage Excel™

St. Jude Children's Research Hospital
ALSAC • Danny Thomas, Founder
Finding cures. Saving children.

FACULTY POSITIONS
DEPARTMENT OF HEMATOLOGY

The Department of Hematology, at St. Jude Children's Research Hospital, is seeking to fill faculty positions at the level of ASSISTANT and/or ASSOCIATE MEMBER. We are specifically seeking applicants whose research program is or will be focused on laboratory-based research in Hematology. Candidates with interests in erythropoiesis, stem cell biology, gene therapy, iron metabolism, or other areas in molecular hematopoiesis are encouraged to apply. Research plans that are either basic or translational science will be considered. An MD, PhD, or a combined degree is required.

The Hematology Department currently consists of ten faculty members who are engaged in clinical and laboratory research in sickle cell disease, thalassemia, hemophilia disorders, stem cell biology, gene therapy for blood and immune cell disorders, and other aspects of molecular hematopoiesis.

St. Jude offers a rich academic environment for laboratory-based research in Hematology with state-of-the-art resources for genomics, molecular bioinformatics, genetic animal models, cell and animal imaging, cell sorting and flow cytometry. We also have an active GMP-manufacturing facility, and other strong clinical resources. Numerous opportunities exist for interdisciplinary academic collaborations, both within the Department of Hematology and within the institution.

Interested individuals should send their CV and a brief description of their research plans to:

Brian Sorrentino, MD – Chair, Search Committee Chair
Hematology Faculty Search Committee, Department of Hematology
St. Jude Children's Research Hospital
262 Danny Thomas Place – MS #341
Memphis, TN 38105-3678
E-mail: Brian.sorrentino@stjude.org
Ph: (901) 595-2727

St. Jude is an Equal Opportunity Employer and a Drug-Free Workplace.

www.stjude.org

Chief Scientist in Theoretical Physics
Permanent Position, RIKEN, Japan

RIKEN invites applications for the position of Chief Scientist (Laboratory Director) to lead a new laboratory working on theoretical subatomic physics that is related to ongoing research activities at RIKEN Nishina Center for Accelerator-Based Science. The present position is a permanent appointment, subject to RIKEN's mandatory retirement age of 60. The anticipated starting date is, in the earliest case, April 1, 2011.

Applicants should send a full curriculum vitae with photograph; a list of publications; one copy each of five key publications; a statement (about five pages of A4 (or letter) sized paper) explaining former research experience and future research plans. Arrangements should be made for at least two letters of reference to be sent directly to the address below.

Closing date: 1 November 2010

Applicants should address all correspondence to: Dr. Akira Furusaki, Chief Scientist Search Committee Chair, RIKEN Advanced Science Institute, 2-1 Hirosawa, Wako, Saitama 351-0198 Japan

For more information, please visit:
http://www.riken.jp/engn/r-world/info/recruit/k101101_e_rnc.html

RIKEN

Agriculture and Agri-Food Canada | Agriculture et Agroalimentaire Canada

Canada

RESEARCH SCIENTIST POSITIONS AT AGRICULTURE AND AGRI-FOOD CANADA

Agriculture and Agri-Food Canada (AAFC) is seeking qualified scientists to fill up to 34 positions in various disciplines at research centres across Canada. AAFC's Research Branch addresses issues in all aspects of agri-food science through innovative research working in close cooperation with industry and the university sector. As an AAFC research scientist, you will be part of a team of 500 researchers dedicated to the advancement of Canada's agri-food industry, to environmental quality, and to the health and prosperity of Canadians.

Research scientist positions are available in the following six streams:

ENVIRONMENTAL RESEARCH (7 POSITIONS)

- Agricultural Hydrology (Brandon, MB)
- Agrometerology (2 positions – Brandon, MB and Ottawa, ON)
- Water Quality (Fredericton, NB)
- Ecosystems Modeling (2 positions – Lethbridge, AB and Québec, QC)
- Remote Sensing (Ottawa, ON)

FOOD SAFETY AND QUALITY (4 POSITIONS)

- Chemistry (Guelph, ON)
- Food Microbiology (Guelph, ON)
- Meat Safety (Lacombe, AB)
- Clinical Nutrition (Winnipeg, MB)

BIORESOURCES RESEARCH (3 POSITIONS)

- Rumen Molecular Microbiology (Lethbridge, AB)
- Molecular Pathology/Biopesticides (London, ON)
- Metabolomics/Proteomics (London, ON)

BIODIVERSITY RESEARCH (4 POSITIONS)

- Taxonomy-Botany (2 positions – Ottawa, ON)
- Taxonomy-Biosystematics (Ottawa, ON)
- Taxonomy-Molecular Insect Taxonomy (Ottawa, ON)

CROP PRODUCTION SYSTEMS (13 POSITIONS)

- Agronomy (Charlottetown, PE)
- Cropping Systems (Charlottetown, PE)
- Entomology (Kentville, NS)
- Quantitative Genetics/Bioinformatics (Lethbridge, AB)
- Pathology (2 positions – Lethbridge, AB and Saskatoon, SK)
- Genomics (London, ON)
- Genetic Enhancement – Perennial Crops (2 positions – Lethbridge, AB and Québec, QC)
- Genetic Enhancement – Wheat (2 positions – Swift Current, SK and Ottawa, ON)
- Epigenetics (Saskatoon, SK)
- Weed Ecology (Harrow, ON)

ANIMAL PRODUCTION SYSTEMS (3 POSITIONS)

- Beef/Pork Phenomics (Lacombe, AB)
- Molecular Biology – Swine (Sherbrooke, QC)
- Molecular Biology – Beef Cattle (Lethbridge, AB)

Deadline for applications is August 29, 2010

Applications will be accepted from candidates enrolled in, but who have not yet completed a Ph.D. program. Completion of the Ph.D. defence must occur by December 31, 2010 and the granting of the Ph.D. degree no later than May 31, 2011.

Proficiency in English and/or French is essential at the time of appointment, depending on the particular position.

For more information or to apply please visit **jobs-emplois.gc.ca**

We thank all those who apply; only those selected for further consideration will be contacted. We are committed to Employment Equity. Preference will be given to Canadian Citizens. The Public Service of Canada is committed to developing inclusive, barrier-free selection processes and work environments.

STONY BROOK

Director Cancer Center

Stony Brook University's (SBU) Cancer Center is the leading academic cancer care program serving Long Island's Nassau and Suffolk Counties, population of 3 million. The SBU Cancer Center includes broad-based clinical care as well as clinical, translational, and basic research programs. Located nearby, SBU has ongoing relationships with Brookhaven National Laboratory and Cold Spring Harbor Laboratory, providing excellent opportunities for collaborative research.

Stony Brook University seeks a visionary leader as the director of the SBU Cancer Center. The successful candidate will be responsible for advancing the clinical care and research programs with the ultimate goal of becoming an NCI-designated cancer center. The director will report to the SVP Health Sciences and dean, Ken Kaushansky, M.D., and work closely with SBU leadership to develop and implement a vision that substantially increases the multidisciplinary and interdisciplinary cancer research and clinical care within SBU. Candidates must have an M.D, Ph.D., Pharm.D., or equivalent degree and must possess strong academic credentials and national prominence in cancer research. With demonstrated ability to recruit, develop, and manage faculty and staff, the successful candidate will be an outstanding and respected academic leader with a track record of building competitive programs.

Stony Brook University is being assisted by executive search consultants from Witt/Kieffer. Confidential nominations, letter of application and C.V., or requests for information should be directed to: Karen Otto or Anne Zenzer, Witt/Kieffer, 2015 Spring Road, Suite 510, Oak Brook, Illinois 60523. (630) 990-1370, *SBUCancerCenterDirector@wittkieffer.com*

Stony Brook University/SUNY is an equal opportunity/affirmative action employer.
Women, people of color, individuals with disabilities, and veterans are encouraged to apply

---

HERMAN B WELLS CENTER FOR PEDIATRIC RESEARCH
INDIANA UNIVERSITY School of Medicine

Asthma and Allergic Diseases Program
Assistant Professor

The Department of Pediatrics, Section of Pulmonology, Critical Care and Allergy and the HB Wells Center for Pediatric Research (**www.wellscenter.iupui.edu**) is recruiting for a faculty position at the Assistant Professor level. We are particularly interested in candidates working in asthma and allergic disease-related research to complement existing strengths in cytokine and T cell biology, and airway physiology in the areas of epithelial cell biology and viral infection. Candidates will have a Ph.D., M.D. or M.D./Ph.D. with a strong research background and either current, or potential for, independent funding. New faculty will be provided with generous start-up packages and join an active multi-disciplinary Immunology and Airway Disease research community and candidates with an M.D. will be given significant time for research. Interested candidates are encouraged to submit a curriculum vitae and a short description of research interests by email to:

Mark H. Kaplan, Ph.D., Director of Pediatric Pulmonary Basic Research, Wells Center for Pediatric Research, Department of Pediatrics, Indiana University School of Medicine, 1044 West Walnut St., Room 202, Indianapolis, IN 46202, airway@iupui.edu

Indiana University is an EEO/AA educator, employer and contractor (M/F/D)

HERMAN B WELLS CENTER FOR PEDIATRIC RESEARCH
INDIANA UNIVERSITY School of Medicine

Developmental Biology and Neonatal Medicine Program
Assistant/Associate Professors

The Department of Pediatrics and Section of Neonatal-Perinatal Medicine is recruiting two faculty positions at the Assistant/Associate Professor level. We are especially interested in applicants whose research focus complements and extends the Program's strengths in neural crest biology, cardiopulmonary vascular development and the use of vertebrate models to investigate congenital diseases. Successful candidates can be a Ph.D., M.D. or M.D./Ph.D. and will be expected to establish innovative, externally funded research programs. The positions come with generous start-up packages, outstanding laboratory space and protected time for research-related activities. Laboratory space will be in the Herman B Wells Center for Pediatric Research (**http://www.wellscenter.iupui.edu/**), which has ongoing collaborative programs in developmental biology, hematologic malignancies and stem cells, heart research, pediatric hematology/oncology, diabetes, pulmonary inflammation and translational medicine.

Review of applications will begin immediately, and will continue until the positions are filled. Interested candidates should submit their *curriculum vitae*, a research program summary, a statement of future plans, and the names and contact information of three references to: **Simon J Conway, Ph.D., Director, Program in Developmental Biology and Neonatal Medicine, Wells Center for Pediatric Research, Department of Pediatrics, Indiana University School of Medicine, 1044 W. Walnut Street, Room 402E, Indianapolis, IN 46202, siconway@iupui.edu.**

Indiana University is an EEO/AA educator, employer and contractor (M/F/D).

K-STATE Kansas State University

BIOSECURITY RESEARCH INSTITUTE
RESEARCH DIRECTOR
ASSOCIATE VICE PRESIDENT FOR RESEARCH

Kansas State University (K-State) is seeking to hire a senior scientist with substantial animal infectious disease experience to direct the Biosecurity Research Institute's biocontainment research and education programs in Pat Roberts Hall (PRH) at K-State. A recognized infectious disease scientist is sought to direct PRH research and serve as the Peine Professor for Biosecurity. This individual will also serve as an Associate Vice President for Research facilitating bio-preparedness research campus-wide.

The successful candidate will have a PhD or equivalent research credential, a stellar scientific publication record, and a demonstrated ability to direct multi-disciplinary scientific investigations. Moreover, the candidate must hold or be capable of holding a top secret security clearance in order to fulfill all the anticipated duties of this full-time administrative position.

In 2009, after a 3-year selection process, the Department of Homeland Security chose a site adjacent to PRH as the home for the National Bio and Agro-defense Facility. The candidate selected will be expected to exploit the public and private-sector opportunities this provides.

See **http://www.k-state.edu/research/news/jobs.html** for a complete job description. Those interested should submit a letter of application, curriculum vitae, and names of at least 3 references including contact information to:

KANSAS STATE UNIVERSITY
ATTN: BRI SEARCH COMMITTEE
108 ANDERSON HALL
MANHATTAN, KANSAS 66506-0113

Screening of applicants will begin **September 16, 2010** and continue until a suitable candidate has been identified.

Kansas State University is an Equal Opportunity Employer and actively seeks diversity among its employees.

Johnson & Johnson
Family of Companies

What type of mark will you make?

Centocor Research and Development

Biologics Research, Biotechnology Center of Excellence, Centocor Research and Development, a member of the Johnson & Johnson Family of Companies, is recruiting for several positions located in Radnor, PA and San Diego, CA as noted below.

Centocor Research and Development develops innovative biomedicines. The world leader in monoclonal antibody production and technology, Centocor has brought critical biologic therapies to patients suffering from debilitating immune disorders and is expanding to support all therapeutic areas.

We are recruiting in the following targeted research areas:

- Protein expression and purification
- Biophysical characterization of antibodies
- Antibody modeling and design
- Structural biology of proteins and peptides
- Peptide toxin engineering
- Antibody engineering
- Stem cell culture and development
- Assay development and HT automation
- Outsourcing and business strategy

The candidates will be responsible for the engineering and optimization of antibody, protein, and peptide drug candidates; establishing close coordination with the therapeutic areas; collaborating with other functional groups to assist in the effective progression of projects through the lead optimization process; and partnering with academic and industry leaders in fields relevant to the development and implementation of enabling technologies to support optimization and development of protein therapeutics.

The candidates will help identify and implement technologies to improve the design and development of biopharmaceutical candidates within the areas described above, and will be expected to participate in and eventually lead cross-functional project teams.

As these roles require a high degree of interaction with groups both internal and external to Johnson & Johnson, the successful candidates must possess strong leadership skills and organizational abilities. The candidates will be required to collaborate with team members to share concepts, strategies, techniques and tools.

For these positions, candidates with Ph.D.s or M.D.s with expertise in biochemistry, biophysics, immunology, or related fields are preferred. Candidates with postdoctoral experience and/or pertinent industrial experience are much preferred.

Please contact Gitaanjali Gidwani at ggidwani@its.jnj.com to be considered for these opportunities.

BE VITAL

Visit careers.jnj.com to learn more about opportunities to make your mark within our organization.

© Johnson & Johnson Services, Inc. 2010. Centocor Research and Development is a member of the Johnson & Johnson Family of Companies. Johnson & Johnson companies are equal opportunity employers.

INDIAN INSTITUTE OF CHEMICAL BIOLOGY
(Council of Scientific & Industrial Research)
4 Raja S. C. Mullick Road, Kolkata-700 032, India

Indian Institute of Chemical Biology (IICB) is a 75 year old premier Research Institution conducting high quality research in chemical and biomedical sciences. Applications are invited from young and enthusiastic talents willing to take up challenging modern problems in the following areas :

- **Cell biology & physiology**
- **Synthetic and natural product chemistry**
- **Chemical biology**
- **Molecular & human genetics**
- **Infectious diseases & immunology**
- **Pharmaceutical & bio-analytical sciences**
- **Structural & computational biology**
- **Synthetic biology**
- **Systems biology**

In addition, the institute is particularly eager to recruit scientists, who would work in the areas of leishmaniasis and natural product chemistry. Scientists working in other areas, but willing to develop a research program in leishmaniasis and natural product chemistry, are welcome to apply. These are independent positions and generous initial support will be given. Applicants are requested to forward their CV and list of publications along with statement of future programs, and list of references to the Director of IICB via e-mail (siddhartharoy@iicb.res.in) followed by a hard copy.

For further details please visit career@iicb in our website www.iicb.res.in

universität wien

The Rectorate of the University of Vienna invites applications for two tenure-track positions of University Assistant (*UniversitätsassistentIn*) at the Faculty of Physics in the following fields:

Computational Materials Physics

Position in any area of computational theoretical solid state physics including nanostructured materials, surfaces/interfaces, alloy modelling, semiconductor modelling or closely related fields.

Physics

Position in any area of experimental or theoretical physics along the lines of the main research areas of the Faculty of Physics (Quantum Physics and Quantum Information, Particle Physics and Gravitational Physics, Physics of Complex Nanoscale Matter, Aerosol and Cluster Physics) or closely related fields.

Further information about these positions and about the Faculty of Physics can be obtained from the website http://physics.univie.ac.at.

Detailed information on the job announcements can be found at *http://personalwesen.univie.ac.at/fuer-bewerberinnen/laufbahnstellen/fakultaet-fuer-physik*. Requests for further information may be addressed to the Dean of the Faculty of Physics at *dekanat.physik@univie.ac.at*.

Applications shall be submitted to the Job Center of the University of Vienna (*http://jobcenter.univie.ac.at*) in English no later than **September 10th, 2010**.

The University of Vienna intends to increase the number of women on its faculty, particularly in high-level positions, and therefore specifically invites applications by women. Among equally qualified applicants women will receive preferential consideration.

The University of Vienna, one of Europe's oldest universities, offers approximately 8,900 employees manifold opportunities in research, teaching and administration. As stated in its development plan, the University of Vienna aims at strengthening its position as a major research-oriented university. Key elements of this strategy include the provision of an attractive range of research-based study programmes, support for furthering the work of junior academic colleagues and high-calibre professorial appointments.

MONASH University

Three ARC Super Science Research Fellows and Three PhD students in Structural Biology, Drug Delivery, and Nanotechnology

Faculty of Medicine, Nursing and Health Sciences, Faculty of Pharmacy and Pharmaceutical Sciences, the Faculty of Engineering and Melbourne Centre for Nanofabrication

We are looking for three exceptional ARC Super Science Fellows and three PhD Scholarship students to undertake research in Pore Forming Proteins and their potential utility as machines for the intracellular delivery of proteins and nanoparticles.

Postdoctoral Fellowships
1) You'll be a scientist with a demonstrated track record in molecular biology, protein chemistry and protein crystallography. Experience in cell biology or autophagy is also desirable.

2) You'll be a scientist with a demonstrated track record in molecular biology, protein chemistry and cell biology. Broader experience in drug delivery is desirable.

3) You'll be a scientist with a demonstrated track record in nanoparticle fabrication, functionalisation, and physical and chemical characterisation, with a particular interest in the biological application of nanotechnology.

To be eligible, you must not have held your PhD more than 3 years.

PhD Scholarships
A PhD scholarship will be associated with each of the Super Science Fellows. You should have a demonstrated interest in one of the three above mentioned research areas, and must have a degree recognised as H1 equivalent in Australia.

For both fellowships and PhD scholarships please refer to the link in 'Applications' below.

The University
You will be based at Monash University in Melbourne, Australia a GO8 University in one of the World's most livable cities.

The Benefits
Remuneration package (Fellowships): AUD$80,404 - AUD$95,481 pa Level B (includes employer superannuation of 9%)
PhD Scholarship: Stipend AUD$22,500 (tax free) for three years, indexed annually

Duration
Three Fellows will be offered a full-time position, fixed term for three years from commencement date. Start dates are negotiable, but preferably will be before 31 December 2010.

Enquiries
Professor James Whisstock email **James.Whisstock@monash.edu**

Ref No
A1011092

Applications Close
Thursday, 2 September 2010

Applications
http://monash.turborecruit.com.au/job/job_details.cfm?id=503700&from=

Science Careers
is the forum that
answers questions.

Visit our ENHANCED WEBSITE!

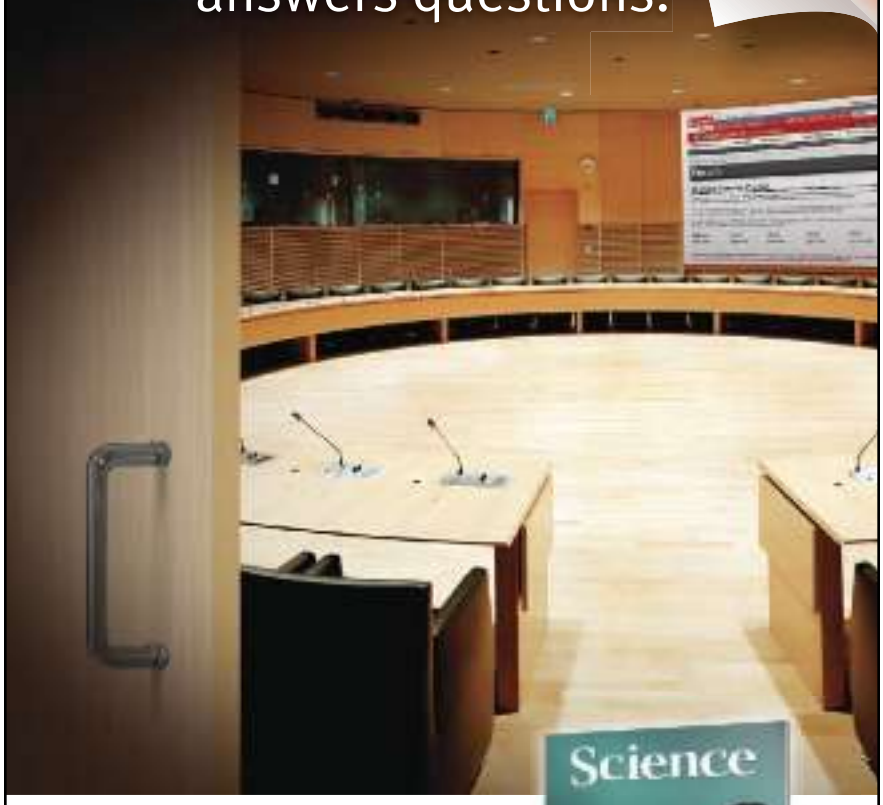

Your Future Awaits.

Science Careers is dedicated to opening new doors and answering questions on career topics that matter to you. We're the go-to career site for connecting with top employers, industry experts, and your peers. We're the source for the latest and most relevant career information across the globe.

With community feedback and a professional atmosphere, our careers forum allows you to connect with colleagues and associates to get the advice and guidance you seek.

Science Careers Forum:

» Relevant Career Topics
» Advice and Answers
» Community, Connections, and More!

Visit the forum and get your questions answered today!

Science Careers
From the journal *Science* AAAS
ScienceCareers.org

Department of Health and Human Services
National Institutes of Health
National Institute of Diabetes and Digestive and Kidney Diseases

Program Director in Pharmacogenomics

Health Scientist Administrator, GS-13/14

The Division of Diabetes, Endocrinology and Metabolic Diseases (DDEMD), National Institute of Diabetes and Digestive and Kidney Diseases (NIDDK), National Institutes of Health (NIH) is expanding its programs in diabetes and obesity research. An opportunity exists for a basic or clinical scientist to join a dedicated and dynamic group of health scientist administrators to help guide NIH funded research in pharmacogenomics.

A basic or clinical scientist with expertise in the areas of pharmacogenomics or clinical pharmacology with human genetics and genomics expertise relevant to diabetes and obesity is sought for this position. The Program Director will be responsible for oversight of research grants as well as the management and participation in team science and development of potential initiatives in these areas.

This position involves close interaction with leading researchers, scientific administration of grants and contracts, program planning and development, and the opportunity to organize and attend scientific meetings. A successful candidate will have basic research experience, with a track record of publications in research in pharmacogenomics or clinical pharmacology and human genetics/genomics, excellent interpersonal and written communications skills, the ability to identify research priorities and opportunities, and the ability to track and analyze the success of initiatives and programs. In carrying out these responsibilities, the Program Director will interact with national leaders in pharmacogenomics, diabetes and obesity research. Many DDEMD research activities are conducted through partnerships between the NIDDK and other components of NIH and DHHS, as well as voluntary organizations. The Program Director will play a leadership role in fostering these partnerships.

The position is located in Bethesda, Maryland. Salary and benefits will be commensurate with the experience of the applicant. Recruitment for this position will be through an NIH-wide job announcement for Health Scientist Administrator. For qualification requirements, evaluation criteria, and application instructions, view the vacancy announcements at **http://www.jobs.nih.gov/hsa/** . All applications must be received by **August 20th**. For additional information, please contact Chandra Mays at 301-594-8208.

DHHS and NIH are Equal Opportunity Employers

MARSHALL UNIVERSITY.

The Department of Biological Sciences at **Marshall University**, as part of the State of West Virginia's Eminent Scholars Recruitment and Enhancement (ESRE) Initiative, invites applications for a tenure-track, **Associate or Full Professor** position in **Phycology**. The successful candidate will lead an interdisciplinary team of faculty members focused on research and economic development activities associated with West Virginia's extensive water and energy resources. Duties will include establishing an extramurally funded research program, mentoring junior faculty members, and participating in courses serving the department's Watershed Resource Sciences area of emphasis. Candidates must possess a Ph.D. in biology or a closely related discipline, and show evidence of research productivity and extramural funding in freshwater phycology.

Qualified applicants should send a cover letter, current curriculum vitae, statement of research interests and goals, teaching philosophy, and up to three selected reprints. Applicants should also arrange for three letters of reference to be sent directly to the department. Application materials may be submitted electronically (preferred) to **phycologysearch@marshall.edu** or by mail to: **Dr. Charles Somerville, Dean, College of Science, re: Phycology Search, Marshall University, One John Marshall Drive, Huntington, WV 25755**. Review of applications begins on **15 September 2010**, and will continue until the position is filled.

Marshall University is the recipient of two National Science Foundation awards that seek to increase diversity through the ADVANCE and LSAMP Programs – women and minorities are encouraged to apply.

UNIVERSITY OF LIVERPOOL

Faculty of Science and Engineering
School of Physical Sciences
Department of Chemistry

2 Research Co-ordinators

£36,715 - £46,510 pa

Two 5-year Research Co-ordinator positions are available in the group of Professor M J Rosseinsky. A PhD in Chemistry, Physics or Materials Science, excellent research skills in synthetic materials chemistry (oxides, porous materials, hybrid nanomaterials) plus an excellent publication record and demonstrated ability to take responsibility in research organisation are essential; skills in at least two of diffraction methods, sorption measurements, energy materials, equipment/measurement development, bionanomaterials, molecular synthesis, thin films are desirable.

Job Ref: R-572400/S **Closing Date: 3 September 2010**

For full details, or to request an application pack, visit www.liv.ac.uk/working/job_vacancies/ or e-mail jobs@liv.ac.uk Tel 0151 794 2210 (24 hr answerphone) please quote job ref in all enquiries.

COMMITTED TO DIVERSITY AND EQUALITY OF OPPORTUNITY

Stonewall DIVERSITY CHAMPION

POSITIVE ABOUT DISABLED PEOPLE

Science Careers online @sciencecareers.org

Nontraditional Careers:
Opportunities Away From the Bench

Webinar

Want to learn more about exciting and rewarding careers outside of academic/industrial research? View a roundtable discussion that looks at the various career options open to scientists across different sectors and strategies you can use to pursue a nonresearch career.

Now Available
On Demand
www.sciencecareers.org/webinar

Participating Experts:

Dr. Lori Conlan
Director of Postdoc Services,
Office of Intramural Training and Education
National Institutes of Health

Pearl Freier
President
Cambridge BioPartners

Dr. Marion Müller
Director, DFG Office North America
Deutsche Forschungsgemeinschaft
(German Research Foundation)

Richard Weibl
Director, Center for Careers in Science and Technology
American Association for the Advancement of Science

Produced by the
Science/AAAS Business Office.

Science Careers
From the journal *Science* AAAS

Novartis is delighted to congratulate the winners of the

2010 **Novartis Immunology Prizes**

The prizes are awarded for outstanding achievements to the understanding of immunology and major immunological discoveries that lead to therapeutic applications in such fields as transplantation, haematopoiesis, cancer immunology, immunity to infectious diseases, rheumatology, dermatology and asthma.

Each Prize is worth SFr. 100 000.

Basic Immunology Prize

Prof. Michael Bevan, Howard Hughes Medical Institute, University of Washington, Seattle, for his studies on T-cell selection and regulation and memory formation of CD8+ cytotoxic T-cells in response to pathogens.

Clinical Immunology Prize

Prof. Charles Dinarello, University of Colorado, and **Prof. Jürg Tschopp**, University of Lausanne, Switzerland, for the discovery, biology and regulation of Interleukin-1 beta and the use of IL-beta antagonists for the successful treatment of certain inflammatory diseases.

The 2010 Novartis Immunology Prizes will be awarded at the XIVth International Congress of Immunology in Kobe, Japan, on 23 August 2010.

Reviews by the Novartis Prize Awardees will be published in the *European Journal of Immunology.*

Jury: Sir Andrew McMichael (Chair), Tadamitsu Kishimoto, Bernard Malissen, Philippa Marrack, Hidde Ploegh, David H. Sachs, Jan de Vries.

NOVARTIS

Visit: www.novartisimmunologyprizes.org

THE GEORGE WASHINGTON UNIVERSITY
WASHINGTON DC

Faculty Position in Developmental Neurobiology
Institute for Neuroscience and Department of Biological Sciences

The newly formed Institute of Neuroscience and the Department of Biological Sciences of the George Washington University in Washington DC are accepting applications for a tenure or tenure-track faculty member at the rank of Associate or Assistant Professor with expertise in the field of Developmental Neurobiology. This position will be one of five added to the existing community of GWU neuroscientists as part of an initiative to expand research in developmental disorders including autism. We seek an investigator whose research focuses on developmental neurobiology. This individual will teach an undergraduate course in the Department of Biological Sciences as well as participate in graduate education in the department and in the Institute for Biomedical Sciences. The successful candidate will participate in the development of multi-investigator projects for extramural funding in the Institute for Neuroscience research activities including development of multi-investigator projects for extramural funding. Salary and start up funds will be commensurate with experience. **Basic Qualifications:** a Ph.D. in an appropriate discipline, postdoctoral experience, and substantial accomplishments in biological research demonstrated by a significant number of publications in outstanding peer-reviewed journals. **Preferred Qualifications:** a growing research program focused on synapse assembly in the developing nervous system of model organisms including, but not limited to *C. elgans*, *D. melanogaster*, and *D. rerio*. Integration of genetic analysis with optical imaging and cell biological methods is encouraged.

Application Procedure: to be considered please send a complete curriculum vitae plus names and contact information for three references electronically to: **Anthony-Samuel LaMantia, Ph.D., Professor of Pharmacology and Physiology, Director, GWU Institute for Neuroscience** at **phmasl@gwumc.edu** or by mail to: **The Department of Pharmacology and Physiology, GWU Institute for Neuroscience, 2300 Eye Street NW, Room 661, Washington, DC 20035**.

Only complete applications will be considered. Review of Applications will begin on **October 15, 2010**, and will continue until the position is filled.

The George Washington University is an Equal Opportunity/Affirmative Action Employer. The University Search Committee seeks to attract an active, culturally and academically diverse faculty of the highest caliber.

THE UNIVERSITY OF HONG KONG

Founded in 1911, The University of Hong Kong is committed to the highest international standards of excellence in teaching and research, and has been at the international forefront of academic scholarship for many years. The University has a comprehensive range of study programmes and research disciplines spread across 10 faculties and about 100 sub-divisions of studies and learning. There are over 23,400 undergraduate and postgraduate students coming from 50 countries, and more than 1,200 members of academic and academic-related staff.

Tenure-Track Associate Professor/Assistant Professor in the Department of Physics (Ref.: 20100444)

Applications are invited for tenure track appointment as Associate Professor/Assistant Professor in the Department of Physics, from as soon as possible. The post will initially be made on a three-year term. Appointment with tenure will be considered during the second three-year contract.

Applicants specialising in the field of *Experimental Condensed Matter Physics* are preferred, but strong candidates working in other areas of physics will also be considered. Candidates with good qualifications and commitment to high-quality research and excellence in teaching are encouraged to apply.

Annual salaries will be in the following ranges (subject to review from time to time at the entire discretion of the University):

Associate Professor	:	HK$626,400 – 968,700
Assistant Professor	:	HK$477,360 – 737,700

(approximately US$1 = HK$7.8)

Applicants should indicate clearly the reference number and *which* level they wish to be considered for.

A highly competitive salary commensurate with qualifications and experience will be offered. The appointment will attract a contract-end gratuity and University contribution to a retirement benefits scheme, totalling up to 15% of basic salary, as well as leave, and medical/dental benefits. Housing benefits will be provided as applicable. At current rates, salaries tax does not exceed 15% of gross income.

For enquiries of the existing research activities and the specific job requirements, please write to Professor F.C. Zhang, Head of the Department of Physics (e-mail: physhead@hku.hk). Please send an application form together with a curriculum vitae, a detailed publication list, a research plan, and a statement on teaching philosophy to the Appointments Unit (Senior), Human Resources Section, Registry, The University of Hong Kong, Hong Kong. **Further particulars and application forms** (152/708) can be obtained at http://www.hku.hk/apptunit/; or from the Appointments Unit (Senior), Human Resource Section, Registry, The University of Hong Kong, Hong Kong (**fax:** (852) 2540 6735 or 2559 2058; **e-mail:** senrappt@hku.hk). **Review of applications will start from November 30, 2010 and will continue until the post is filled.** Candidates who are not contacted within 3 months from the date of their applications may consider their applications unsuccessful.

The University is an equal opportunity employer and is committed to a No-Smoking Policy

Science Careers online @sciencecareers.org

POSITIONS OPEN

SOYBEAN AGRONOMIST
Assistant/Associate Professor
Iowa State University

To apply online, visit our **website: http://www.iastatejobs.com/applicants/Central?quickFind=78734.** *Iowa State University is an Equal Opportunity/Affirmative Action Employer.*

The Harvard University Department of Psychology anticipates making a tenure-track appointment at the **ASSISTANT PROFESSOR** level, to begin July 1, 2011.

We seek candidates with exceptional promise in the social psychology of emotion. Research and teaching expertise might include topics such as social psychophysiology, nonverbal communication of emotion, social embodiment, emotion contagion, or empathy; quantitative methodological expertise is also desirable. Our interest is less in specific areas than in innovation and excellence.

Candidates should expect to have completed the requirements for the Ph.D. prior to appointment and to have demonstrated a promise of excellence in both research and teaching. Teaching duties will include offerings at both undergraduate and graduate levels.

Candidates should submit curriculum vitae and representative reprints, and have at least three letters of recommendation sent to: **Social Emotion Search Committee, Harvard University, Department of Psychology, William James Hall 230, 33 Kirkland Street, Cambridge, MA 02138.** The closing date for applying is October 1.

Applications from women and minority groups are strongly encouraged. Harvard University is an Affirmative Action/Equal Opportunity Employer.

FACULTY POSITION
in Diabetes or Obesity

The Vanderbilt Diabetes Center and the Department of Medicine in the Vanderbilt University School of Medicine, is recruiting a tenure-track or tenured scientist (M.D. or Ph.D.) at the **ASSISTANT PROFESSOR, ASSOCIATE PROFESSOR,** or **PROFESSOR** level to conduct in vivo investigation in humans on diabetes, metabolism, or obesity. Vanderbilt has outstanding resources available for diabetes and obesity research, including the Vanderbilt Diabetes Research and Training Center and the new Vanderbilt Institute for Obesity and Metabolism. The Vanderbilt Institute for Clinical and Translational Research provides outstanding infrastructure support for translational research in humans. An extensive system of core laboratories is available to all investigators. Applicants should submit curriculum vitae and a concise statement of research plans. Please send information or direct any inquiries to:

Vanderbilt Diabetes Center
Telephone: 615-322-7990
E-mail: dc.brown@vanderbilt.edu

Vanderbilt University is an Equal Opportunity Employer. Women and minorities are encouraged to apply.

GWR Instruments, Inc. is inviting applications for **RESEARCH AND DEVELOPMENT ENGINEER** to work in the field of superconducting gravimeters at its San Diego Facility. Duties include use of technologies related to superconducting gravimeters for installing, testing, and analyzing the performance of new and existing products. M.S. in physics with three years experience in related field is required. Visit **website: http://www.gwrinstruments.com/about.htm. E-mail: careers@gwrinstruments.com.**

Equal Opportunity Employer.

The University of Charleston School of Pharmacy invites applications and nominations for a 12-month full-time **PHARMACEUTICS POSITION** at the rank of **ASSISTANT** or **ASSOCIATE PROFESSOR.** Applicants should have earned a Ph.D. in pharmaceutics, and should have postdoctoral experience. Applicants should send their letter of interest, curriculum vitae, and three letters of recommendation to **Susan Jarvis** at **e-mail: susanjarvis@ucwv.edu.** *The University of Charleston is an Equal Opportunity/Affirmative Action Employer.*

POSITIONS OPEN

ENDOWED CHAIR POSITION
IN PROTEOMICS

The Medical University of South Carolina seeks to recruit an outstanding scientist in the proteomics field for appointment to a new South Carolina Center of Excellence Endowed Chair Position. The selected person will be expected to establish an outstanding individual research program in proteomics as well as lead further development of proteomics research in the institution and serve as Director of the MUSC Proteomics Center. People whose research relates to the university's priority areas of cancer, cardiovascular science, and neuroscience and with possible interests in disease/therapy biomarkers are of particular interest. Appointment level will be commensurate with experience. Candidates for appointment at the professor or associate professor level will be considered.

Extramural research funding awards to MUSC in the 2009 fiscal year exceeded $217 million, reflecting tremendous continued growth in the research enterprise, including most recently a National Cancer Institute (NCI)-designated cancer center, an NIH Clinical and Translational Science Award, and major regional and national partnerships. Two new research buildings dedicated to interdisciplinary work in drug discovery, bioengineering, and cancer genomics will open in 2011.

This is an exceptional opportunity for a talented, experienced and committed individual to exert a major impact on the next phase of development and growth of the research and translational sciences programs at MUSC.

Located on the Atlantic coast in South Carolina, Charleston boasts one of the nation's most historic downtown areas, beaches and other outdoor recreational resources, and international cultural events such as the Spoleto Festival USA.

Interested candidates should submit their curriculum vitae, a summary of future research plans, and names of three references to apply. Nominations are also welcomed. Submit materials to: **Kenneth D. Tew, Ph.D., D.Sc., John C. West Professor of Cancer Research and Chairman, Department of Cell and Molecular Pharmacology, Medical University of South Carolina, 173 Ashley Avenue, Charleston, SC 29425.**

MUSC is an Equal Opportunity Employer supporting workplace diversity M/F/V/D.

The Harvard University Department of Psychology invites applications for a tenure-track **ASSISTANT PROFESSOR POSITION** in the area of Clinical Psychology, to begin July 2011. Applicants must have an active, high-quality research program with potential for extramural funding and an ability to contribute to the undergraduate and doctoral teaching missions of the department, including the American Psychological Association-accredited doctoral program in clinical science. Those whose research uses approaches from cognitive and affective neuroscience, molecular genetics, and epigenetics to answer questions about mood disorders or other forms of psychopathology are especially encouraged to apply, although all competitive applications will be considered. Please submit your application by the October 15, 2010 deadline. Applications should be sent to: **Chair, Clinical Psychology Search Committee, Harvard University, 33 Kirkland Street, Cambridge MA 02138,** and should include curriculum vitae, selected reprints/preprints, a research and teaching statement, and three letters of recommendation. *Women and minority candidates are strongly encouraged to apply. Harvard University is an Equal Opportunity/Affirmative Action Employer.*

CAREER OPPORTUNITY. Doctor of Optometry (O.D.) degree in 27 months for Ph.D.s in science and M.D.s. Excellent career opportunities for O.D.-Ph.D.s and O.D.-M.D.s in research, education, industry, and clinical practice. This unique program starts in March of each year, features small classes, and has 12 months devoted to clinical care.

Contact the **Admissions Office, telephone: 800-824-5526** at **The New England College of Optometry, 424 Beacon Street, Boston, MA 02115.** Additional information at **website: http://www.neco.edu. Email: admissions@neco.edu.**

POSITIONS OPEN

TENURE-TRACK POSITIONS
Georgia Institute of Technology

The School of Chemistry and Biochemistry of the Georgia Institute of Technology seeks to fill multiple tenure-track faculty positions. Exceptional candidates at all levels and in all areas of chemistry are encouraged to apply. In organic and biochemistry, there is particular interest in candidates at the level of **ASSOCIATE** or **FULL PROFESSOR.** Candidates with interdisciplinary research programs may be considered for joint appointments with other departments. Further information is available at **website: http://www.chemistry.gatech.edu.** Candidates for appointment at the **ASSISTANT PROFESSOR** level should send an application letter, curriculum vitae, and a summary of research plans, and arrange for submission of three letters of reference. Candidates for advanced levels should send an application letter, curriculum vitae, and the names of three references. All materials and requests for information should be submitted electronically, as per the instructions found at **website: http://www.chemistry.gatech.edu.** Applications will be considered beginning 15 October 2010. Application review will continue until the positions are filled. *Georgia Tech is an Equal Education/Employment Opportunity Institution.*

TENURE-TRACK FACULTY POSITION
Molecular Microbiology
Washington University School of Medicine

The Center for Women's Infectious Disease Research (cWIDR, **website: http://cwidr.wustl.edu/**) and the Department of Molecular Microbiology invites applicants for **ASSISTANT PROFESSOR** in the pathogenesis of infectious diseases related to women's health. Led by **Scott J. Hultgren,** Ph.D., the cWIDR seeks applicants with Ph.D., M.D., or M.D.-Ph.D. degrees and a strong desire to create high-impact programs in microbial pathogenesis and engage in interdisciplinary, collaborative research that can improve female health and quality of life. We strongly encourage applications from investigators interested in the molecular basis of infectious diseases, interactions of commensal and pathogenic microbes, and/or differences in pathogenic mechanisms between males and females. Applicants not currently engaged in women's health research, but interested in applying their expertise to this emerging field are also encouraged to apply. Please send a detailed curriculum vitae and a two-page summary of current and planned research as a single PDF attachment and arrange for three signed reference letters to be sent as PDF by October 31, 2010, to **Dr. Michael Caparon**, Associate Director and Faculty Search Committee Chair, **e-mail: caparon@wustl.edu.** *Washington University School of Medicine and cWIDR are committed to building diversity. Women and members of underrepresented groups are strongly encouraged to apply.*

MARKETPLACE

RECOMBINANT PROTEINS

HIV, SIV, HCV, HBV, EBV, Influenza HA, Human Proteins[rh] Ag/Ab:TB, Malaria, Dengue, Chagas, Lepto, Toxo, Tp, Chickengunya,
Immunodx@immunodx.com 1800-573-1700

Promab Biotechnologies Inc.
Custom Monoclonal Antibody $4,200
>3,000 CLONES WILL BE SCREENED
1-866-339-0871
www.promab.com info@promab.com